

Modal methods for rehomogenization of nodal cross sections in nuclear reactor core analysis

Gamarino, Matteo

DOI

[10.4233/uuid:084a28c2-dacc-4c4d-9f61-8c9444a3dd4a](https://doi.org/10.4233/uuid:084a28c2-dacc-4c4d-9f61-8c9444a3dd4a)

Publication date

2018

Document Version

Publisher's PDF, also known as Version of record

Citation (APA)

Gamarino, M. (2018). Modal methods for rehomogenization of nodal cross sections in nuclear reactor core analysis DOI: [10.4233/uuid:084a28c2-dacc-4c4d-9f61-8c9444a3dd4a](https://doi.org/10.4233/uuid:084a28c2-dacc-4c4d-9f61-8c9444a3dd4a)

Important note

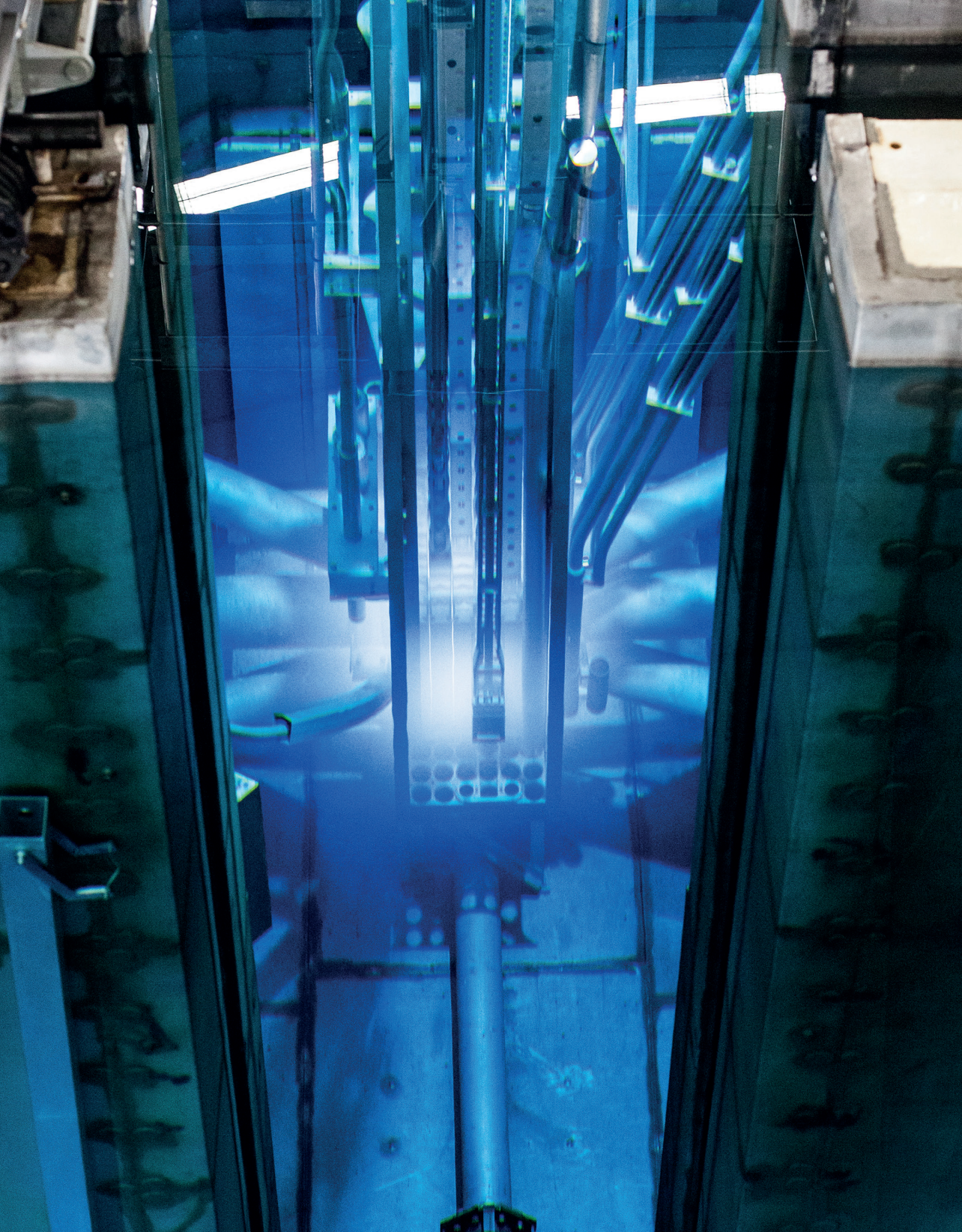
To cite this publication, please use the final published version (if applicable). Please check the document version above.

Copyright

Other than for strictly personal use, it is not permitted to download, forward or distribute the text or part of it, without the consent of the author(s) and/or copyright holder(s), unless the work is under an open content license such as Creative Commons.

Takedown policy

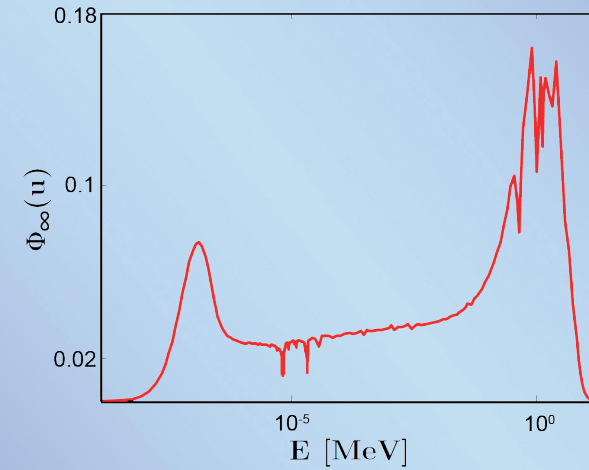
Please contact us and provide details if you believe this document breaches copyrights. We will remove access to the work immediately and investigate your claim.



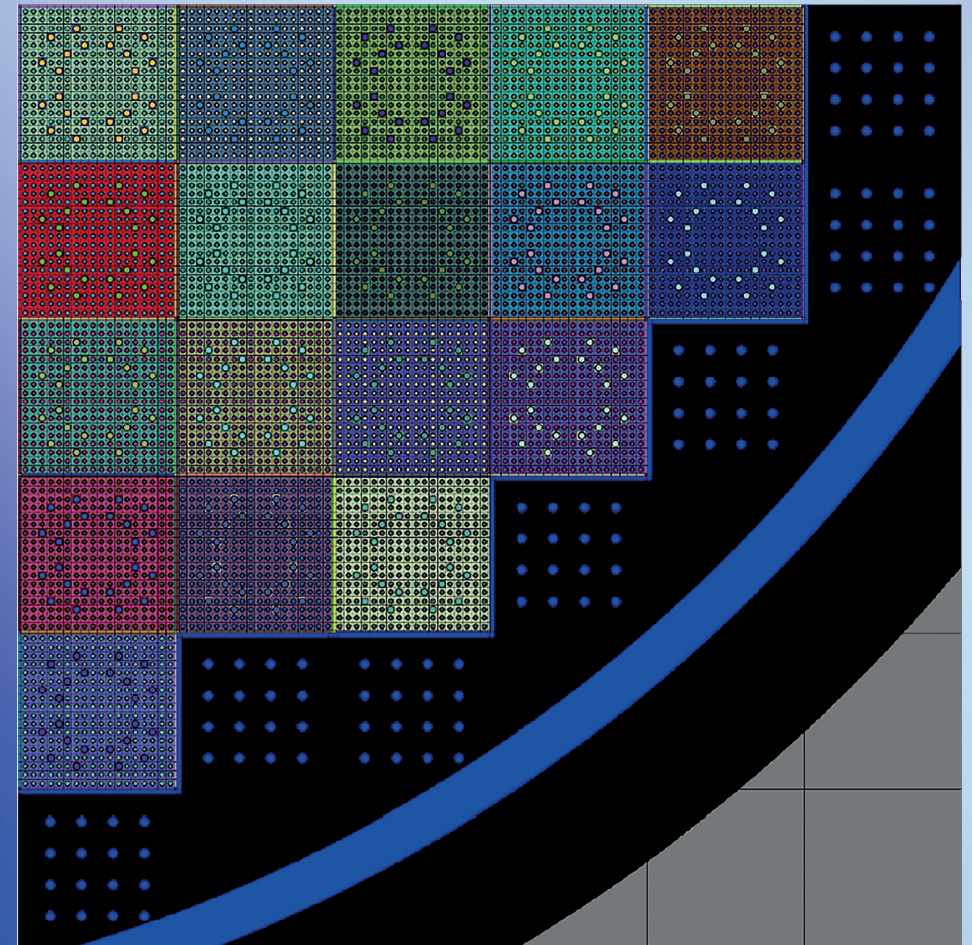
Modal methods for rehomogenization of nodal cross sections in nuclear reactor core analysis

Matteo Gamarino

Modal methods for rehomogenization of nodal cross sections in nuclear reactor core analysis



Matteo Gamarino



Propositions

Belonging to the Ph.D. thesis of Matteo Gamarino

MODAL METHODS FOR REHOMOGENIZATION OF NODAL CROSS SECTIONS IN NUCLEAR REACTOR CORE ANALYSIS

1. The accuracy of two-group nodal diffusion simulations with infinite-medium homogenization parameters relies on favorable error cancellation. (This thesis, Chapters 2 and 3)
2. Spectral rehomogenization of nodal cross sections makes the critical-buckling methodology redundant. (This thesis, Chapters 2 and 3)
3. Reactor analysts should not assess the accuracy of rehomogenization methods based only on the errors in the multiplication factor and assembly-averaged power. (This thesis, Chapters 2, 3, and 5)
4. The investment of research effort and funding would greatly benefit from peer-reviewed journals promoting the publication of negative results.
5. Recent major cold blasts (such as the early 2012 European cold wave) do not indicate a reversal of global warming and climate change. ¹
6. Locating nuclear research institutes in isolated areas hampers public acceptance of nuclear energy.
7. Only herd immunity can justify mandatory vaccination.
8. The absence of culturally-entrenched conservative religious beliefs is a necessary, yet not sufficient condition for full compliance with civil rights and gender equality.
9. A canteen providing good-quality and diverse food at subsidized rates is an important factor to improve employee workplace satisfaction and engagement.
10. The absence of symptoms of ‘numerical correctness bugs’ ² (wrong results, convergence failure, crashes and bad performance) does not prove that computer software is free of such bugs. The outcome of numerical simulations (including those presented in this thesis) must therefore be taken with a grain of salt.

These propositions are regarded as opposable and defensible, and have been approved as such by the promotor, Prof. dr. ir. J.L. Kloosterman.

¹European Environment Agency, “Global and European temperature”, 2018, <https://www.eea.europa.eu/data-and-maps/indicators/global-and-european-temperature-8/assessment>.

²A. Di Franco, H. Guo, and C. Rubio-González, “A comprehensive study of real-world numerical bug characteristics”, Proceedings of the 32nd IEEE/ACM International Conference on Automated Software Engineering, pp. 509-519, IEEE Press, 2017.

Stellingen

Behorende bij het proefschrift van Matteo Gamarino

MODAL METHODS FOR REHOMOGENIZATION OF NODAL CROSS SECTIONS IN NUCLEAR REACTOR CORE ANALYSIS

1. De nauwkeurigheid van twee-groep nodale diffusieberekeningen met oneindig-medium homogenisatieparameters is afhankelijk van gunstige foutenopheffing. (Dit proefschrift, Hoofdstukken 2 en 3)
2. Spectrale rehomogenisatie van nodale werkzame doorsneden maakt de kritische buckling methodiek overbodig. (Dit proefschrift, Hoofdstukken 2 en 3)
3. Reactoranalisten dienen de nauwkeurigheid van rehomogenisatiemethoden niet alleen op basis van fouten in de vermenigvuldigingsfactor en in de assemblage-gemiddelde vermogensproductie moeten beoordelen. (Dit proefschrift, Hoofdstukken 2, 3 en 5)
4. De investeringen van onderzoeksinspanning en financiering zouden gebaat zijn bij het stimuleren van publicatie van negatieve resultaten.
5. Recente intense koude perioden (zoals die van begin 2012 in Europa) zijn geen indicatie voor omkering van het broeikaseffect en klimaatverandering.¹
6. Het vestigen van nucleaire onderzoeksinstituten in geïsoleerde gebieden belemmert de publieke acceptatie van kernenergie.
7. Alleen groepsimmunitieit kan verplichte vaccinatie rechtvaardigen.
8. De afwezigheid van cultureel vervlochten conservatieve religieuze gedachten is een benodigde, maar niet voldoende, conditie voor volledige naleving van mensenrechten en geslachtsgelijkheid.
9. Een kantine die voorziet in hoge kwaliteit, divers voedsel tegen gesubsidieerde prijzen is een belangrijk element om werknemer tevredenheid en betrokkenheid te vergroten.
10. De afwezigheid van symptomen van ‘numerieke correctheid fouten’² (verkeerde resultaten, gebrek aan convergentie, slechte performance) is geen bewijs dat computersoftware vrij is van dergelijke fouten. De uitkomst van numerieke simulaties (inclusief die in dit proefschrift) moet dan ook met een korrel zout genomen worden.

Deze stellingen worden oponeerbaar en verdedigbaar geacht en zijn als zodanig goedgekeurd door de promotor, Prof. dr. ir. J.L. Kloosterman.

¹European Environment Agency, “Global and European temperature”, 2018, <https://www.eea.europa.eu/data-and-maps/indicators/global-and-european-temperature-8/assessment>.

²A. Di Franco, H. Guo, and C. Rubio-González, “A comprehensive study of real-world numerical bug characteristics”, Proceedings of the 32nd IEEE/ACM International Conference on Automated Software Engineering, pp. 509-519, IEEE Press, 2017.

**Modal methods
for rehomogenization of
nodal cross sections
in nuclear reactor core analysis**

**Modal methods
for rehomogenization of
nodal cross sections
in nuclear reactor core analysis**

Proefschrift

ter verkrijging van de graad van doctor
aan de Technische Universiteit Delft,
op gezag van de Rector Magnificus Prof. dr. ir. T.H.J.J. van der Hagen,
voorzitter van het College voor Promoties,
in het openbaar te verdedigen
op dinsdag 20 november 2018 om 12:30 uur
door

Matteo GAMARINO

Master of Science in Energy and Nuclear Engineering, Politecnico di Torino

geboren te Turijn, Italië

Dit proefschrift is goedgekeurd door de promotor:

Prof. dr. ir. J.L. Kloosterman

Copromotor:

Dr. ir. D. Lathouwers

Samenstelling promotiecommissie:

Rector Magnificus,

Prof. dr. ir. J.L. Kloosterman,

Dr. ir. D. Lathouwers,

Ir. A. Dall’Osso,

voorzitter

Technische Universiteit Delft, promotor

Technische Universiteit Delft, copromotor

Framatome

Onafhankelijke leden:

Prof. dr. A. Pautz,

Prof. dr. P. Ravetto,

Dr. L. van den Dурel,

Prof. dr. ir. A.W. Heemink,

Prof. dr. P. Dorenbos,

Ecole Polytechnique Fédérale de Lausanne

Politecnico di Torino

Nuclear-21

Technische Universiteit Delft

Technische Universiteit Delft, reservelid

© 2018, Matteo Gamarino

All rights reserved. No part of this book may be reproduced, stored in a retrieval system, or transmitted, in any form or by any means, without prior permission from the copyright owner.

ISBN 978-94-6186-961-6

Keywords: Neutron diffusion, Nodal methods, Homogenization, Core environment, Neutron leakage, Spectral and spatial effects, Cross-section model



The research work described in this thesis was performed in the Reactor Physics and Nuclear Materials (RPNM) section of the Department of Radiation, Science and Technology (RST) of Delft University of Technology (Delft, The Netherlands), and in the neutronics R&D department (DTIPD-F) of Framatome (Paris, France).

Financial support

This work was funded by the Framatome Ph.D. program.

Printed by: Ipskamp Printing (www.ipskampprinting.nl).

An electronic version of this dissertation is available at

<http://repository.tudelft.nl/>.

“In one world, effort is a bad thing. It, like failure, means you’re not smart or talented. If you were, you wouldn’t need effort. In the other world, effort is what makes you smart or talented.” – Carol Dweck

Thesis cover:

Front: Neutron flux energy spectrum per unit lethargy in a conventional UO_2 fuel assembly (top), and physical media for the computational mesh of an EPR^{TM} -like quarter-core geometry (bottom). Both figures have been obtained with the APOLLO2-A deterministic lattice transport code.

Back: Reactor pool of the Hoger Onderwijs Reactor (HOR) of Delft University of Technology (Reactor Institute Delft).

Contents

1	Introduction	1
1.1	Background and motivation	1
1.1.1	Nodal methods for reactor core analysis	1
1.1.2	Homogenization theory and the two-step procedure	3
1.1.3	Problem description: core-environment effects on the homogenization parameters	7
1.2	Review of state-of-the-art methodology	9
1.3	Research objectives and thesis structure	11
2	Modal synthesis of neutron spectrum changes	15
2.1	Introduction	15
2.2	Theory	16
2.2.1	The spectral rehomogenization algorithm	16
2.2.2	Modal approaches	20
2.2.3	Integration into the LWR two-step procedure	26
2.3	Validation	27
2.3.1	Procedure	27
2.3.2	Numerical results	29
2.4	Discussion	40
2.4.1	Approximations in the formulation of the method	41
2.4.2	Numerical features and computational efficiency	44
2.4.3	Comparison of the polynomial and POD approaches	45
2.4.4	Relation with the critical-spectrum correction	47
2.5	Summary	50
3	Modeling of the neutron leakage spectrum	51
3.1	Introduction	51
3.2	Theory	52
3.2.1	The diffusive leakage method	52
3.2.2	The fundamental-leakage approach	58
3.3	Numerical results	59

3.3.1	Validation of the diffusive leakage model	60
3.3.2	Comparison with the fundamental-leakage approach	77
3.4	Discussion	83
3.4.1	Numerical aspects and implementation features	83
3.4.2	On the approximate formulation of the diffusive method	85
3.4.3	Impact of the diffusion coefficient definition	86
3.4.4	Alternative leakage models	88
3.5	Summary	90
4	Modeling spectral effects of local nuclide density changes	93
4.1	Introduction	93
4.2	Description of the method	96
4.2.1	Reconstruction of the infinite-medium cross sections	96
4.2.2	Incorporation of neighbor effects	110
4.3	Numerical results	111
4.3.1	Single-assembly configurations	111
4.3.2	Application to a heterogeneous multiassembly configuration	123
4.4	Discussion	129
4.4.1	Numerical features and impact on the cross-section model	129
4.4.2	On the modal approach	132
4.4.3	Reconstruction of the diffusion coefficient	134
4.4.4	On the discontinuity factors and form functions	135
4.4.5	Reconstruction of the B^2 -corrected cross sections	137
4.4.6	Spectral effects of density changes on the rehomogenization coefficients	139
4.5	Summary	140
5	A two-dimensional model for spatial rehomogenization	143
5.1	Introduction	143
5.2	Description of the method	144
5.2.1	Equations for the environmental surface-averaged flux	146
5.2.2	Equations for the environmental surface-averaged current	147
5.2.3	Equations for the environmental corner-point flux	148
5.2.4	Weighted-residual balance equations	152
5.2.5	Summary of the procedure	154
5.3	Numerical results	155
5.4	Discussion	172
5.4.1	On the transverse-leakage approximation	172
5.4.2	Analysis on the discontinuity factors	174
5.4.3	Numerical features and implementation	183
5.4.4	Complementarity between the spatial and spectral effects of the environment	185
5.5	Summary	187

6	Conclusions and recommendations	189
6.1	Conclusions	189
6.2	Perspectives and recommendations	192
6.2.1	Spectral rehomogenization	192
6.2.2	Spatial rehomogenization	194
6.2.3	Validation on a broader spectrum of test cases	195
6.2.4	Coupled modeling of spatial and spectral effects	195
	Bibliography	197
A	The BRISINGR nodal code: description and validation	207
A.1	Fixed-source problems	208
A.1.1	Finite slab geometry	208
A.1.2	Three-dimensional geometry	209
A.2	Eigenvalue problems	210
B	Notation	213
B.1	Symbols	213
B.2	Acronyms	215
	Summary	217
	Samenvatting	219
	Acknowledgments	223
	List of Publications	225
	Curriculum Vitae	227

CHAPTER 1

INTRODUCTION

This thesis presents novel rehomogenization methods for Light Water Reactor (LWR) core analysis. In this chapter, a short introduction to nodal diffusion methods and core homogenization is provided. Practical difficulties arising from environmental effects on the nodal cross sections and discontinuity factors are discussed, and the need for rehomogenization is motivated. The main existing methods to correct homogenization errors are briefly reviewed. To conclude, the research objectives are outlined and an overview of the thesis contents is given.

1.1 Background and motivation

1.1.1 Nodal methods for reactor core analysis

Our capability to analyze nuclear reactor cores strongly relies on the numerical solution of the multigroup neutron transport and diffusion equations. The latter (which makes the assumption that the neutron flux only weakly depends on the angular variable) is the primary modeling tool in routine analyses for industrial calculations (Stacey, 2007). Core design, monitoring and safety analyses require thorough knowledge of physical quantities such as the effective multiplication factor, the reaction-rate and power distributions, control-rod worths and shutdown margins. Their determination calls for full three-dimensional (3-D) calculations of the neutron flux. The reactor core is a highly heterogeneous medium. Several levels of heterogeneity can be identified, ranging from the scale of the typical unit cell (made of a fuel pin, clad and coolant) to the intra- and inter-assembly variations in material composition. In conventional finite-difference diffusion tools, the mesh spacing is constrained by two requirements (Duderstadt and Hamilton, 1976): (*i*) it must be sufficiently fine to represent the spatial heterogeneity

adequately, and (ii) it must not be larger than the shortest (i.e., thermal) diffusion length in heterogeneous regions in order to avoid numerical inaccuracy. Consequently, an accurate finite-difference solution of the diffusion equation can only be achieved modeling explicitly every fuel pin, control rod, burnable-absorber rod, and water channel in the reactor core. In a few-group framework, this approach may result in more than 10^6 unknowns (the fluxes in each energy group at each mesh point). The magnitude of the problem increases considerably in reactor cycle analyses, in which a full-core spatial solution is needed at each fuel depletion step. In spite of the continuous advances in computer hardware, a direct numerical solution of this problem remains nowadays a prohibitive task due to practical limitations on memory storage and run time.

In the past, a number of solution strategies were developed as alternatives to fine-mesh approaches on a core-wide basis. Among them, coarse-mesh nodal diffusion methods are certainly the most successful and widely used tool (Lawrence, 1986; Stacey, 2007). In this class of methods, the reactor core is subdivided into relatively large subregions (referred to as nodes) in which the material composition is assumed uniform. A node usually consists of an entire fuel assembly or a quarter of fuel assembly in the radial plane. Each node is described by a set of equivalent few-group diffusion-theory parameters: the nodal cross sections (which are spatially constant over the cross-sectional area of the node) and the assembly discontinuity factors. The calculation of these parameters, which is based on General Equivalence Theory (GET) (Smith, 1986; Sanchez, 2009), is addressed in Section 1.1.2. With this coarse-mesh approach, the global (i.e., full-core) neutron flux distribution is computed at a significantly smaller number of mesh points. Moreover, the spatial detail of the geometry is reduced to a level where the diffusion approximation can be applied with a solid theoretical background, because the flux becomes a smoothly varying function of the spatial coordinates.

Early nodal methods, which appeared in the 1960s, were based on empirical relations and *ad hoc* approximations (Gupta, 1981; Lawrence, 1986; Smith, 1986). However, modern nodal schemes are consistently formulated (namely, the computed solution approaches the exact solution of the few-group diffusion equation if the spatial mesh is decreased or the approximation order is increased). Provided that reliable equivalent parameters are determined, they are comparable in accuracy to detailed pin-by-pin calculations, thus offering a trade-off between precision and computational efficiency. A detailed description of nodal methods is out of the scope of this thesis. The remainder of this section only summarizes the main solution strategies in advanced nodal schemes, to which the methods developed in this thesis are applied.

In most nodal codes, the 3-D diffusion equation is integrated over the two directions transverse to each coordinate axis (Lawrence, 1986). The so obtained one-dimensional (1-D) equations are coupled by the node-to-node transverse leakage, which is assumed to be in the shape of a quadratic polynomial. The leakage coefficients for a given direction are determined requiring that the volume-averaged values of the transverse leakage be preserved in three neighboring nodes. The most popular transverse-integrated

nodal approaches are the Nodal Expansion Method (NEM) and the Analytic Nodal Method (ANM). In the NEM (Finnemann et al., 1977; Langenbuch et al., 1977), the 1-D flux distributions are approximated by quartic polynomial expansions. In the ANM (Henry, 1972; Smith, 1979), the transverse-integrated equations are solved analytically, with no approximation other than the quadratic leakage fit. For more details about these methods, the interested reader may refer to: Lawrence (1986); Vogel and Weiss (1992); Bouamrine and Noceir (1994); Turinsky et al. (1995); Zimin et al. (1998); Joo et al. (1998); Fu and Cho (2002); Downar et al. (2006); Hébert (2008). Several acceleration techniques are available for the solution of the transverse-integrated equations, such as the Coarse Mesh Finite Difference (CMFD) iteration scheme (Smith, 1983; Sutton and Aviles, 1996) and Coarse Mesh Rebalancing (van Geemert, 2014). Since the nodal equations only provide volume-averaged and surface-averaged fluxes and reaction rates, dehomogenization techniques have been developed to reconstruct the heterogeneous pin-by-pin flux and power distributions using this average information (Rempe et al., 1989; Downar et al., 2006; Joo et al., 2009). In most reconstruction schemes, the two-dimensional (2-D) diffusion equation is solved locally (i.e., within each node) and independently in each energy group using the volume-averaged fluxes, the surface-averaged fluxes and currents, and the corner-point fluxes (for which additional approximations are introduced) as boundary conditions. The so obtained non-separable homogeneous flux distribution is modulated with a heterogeneous assembly flux shape.

1.1.2 Homogenization theory and the two-step procedure

Ideally, few-group nodal parameters (the homogenized cross sections and discontinuity factors) should be determined such that equivalence is kept between the homogenized-assembly diffusion-based representation of the reactor core and the exact solution of the heterogeneous transport equation (Smith, 1986; Sanchez, 2009). The most important quantities to be preserved are (i) the effective multiplication factor (or reactor eigenvalue), (ii) the volume-averaged few-group reaction rates in each homogenized region, and (iii) the surface-averaged few-group currents at the interfaces of each homogenized region. The reference angle-integrated transport equation in the energy group G reads

$$\nabla \cdot \mathbf{J}_G^{\text{het}}(\mathbf{r}) + \Sigma_{t,G}^{\text{het}}(\mathbf{r})\Phi_G^{\text{het}}(\mathbf{r}) = \sum_{G'=1}^{N_G} \left(\frac{\chi_G^{\text{het}}(\mathbf{r})}{k_{\text{eff}}} \nu \Sigma_{f,G'}^{\text{het}}(\mathbf{r}) + \Sigma_{s,G' \rightarrow G}^{\text{het}}(\mathbf{r}) \right) \Phi_{G'}^{\text{het}}(\mathbf{r}), \quad (1.1)$$

with the following definitions:

$$\mathbf{J}_G^{\text{het}}(\mathbf{r}) = \int_{4\pi} d\Omega \, \Omega \cdot \Phi_G^{\text{het}}(\mathbf{r}, \Omega), \quad (1.2a)$$

$$\Phi_G^{\text{het}}(\mathbf{r}) = \int_{4\pi} d\Omega \, \Phi_G^{\text{het}}(\mathbf{r}, \Omega), \quad (1.2b)$$

$$\Sigma_{s,G' \rightarrow G}^{\text{het}}(\mathbf{r}) = \frac{1}{2} \int_{-1}^1 d\mu_0 \Sigma_{s,G' \rightarrow G}^{\text{het}}(\mathbf{r}, \mu_0), \quad \mu_0 = \boldsymbol{\Omega} \cdot \boldsymbol{\Omega}'. \quad (1.2c)$$

In Eq. (1.1), k_{eff} is the effective multiplication factor, $\Phi_G^{\text{het}}(\mathbf{r})$ and $\mathbf{J}_G^{\text{het}}(\mathbf{r})$ are the 3-D angle-integrated heterogeneous flux and current densities in group G , and N_G is the number of energy groups. The cross-section notation is standard (Stacey, 2007). In Eq. (1.2), $\boldsymbol{\Omega}$ denotes the angular variable, $\Phi_G^{\text{het}}(\mathbf{r}, \boldsymbol{\Omega})$ is the group- G angular flux distribution, and μ_0 is the scattering angle cosine (Duderstadt and Hamilton, 1976). The homogenized diffusion equation with piecewise-constant (i.e., assembly-homogenized) cross sections is

$$\nabla \cdot \mathbf{J}_G^{\text{hom}}(\mathbf{r}) + \Sigma_{t,G}^{\text{hom}}(\mathbf{r})\Phi_G^{\text{hom}}(\mathbf{r}) = \sum_{G'=1}^{N_G} \left(\frac{\chi_G^{\text{hom}}(\mathbf{r})}{k_{\text{eff}}} \nu \Sigma_{f,G'}^{\text{hom}}(\mathbf{r}) + \Sigma_{s,G' \rightarrow G}^{\text{hom}}(\mathbf{r}) \right) \Phi_{G'}^{\text{hom}}(\mathbf{r}). \quad (1.3)$$

Given a node k with uniform cross sections, preservation of the volume-averaged reaction rate (for reaction type x) and surface-averaged currents is obtained with the relations

$$\Sigma_{x,G}^k = \frac{\int_{V_k} d\mathbf{r} \Sigma_{x,G}^{\text{het}}(\mathbf{r})\Phi_G^{\text{het}}(\mathbf{r})}{\int_{V_k} d\mathbf{r} \Phi_G^{\text{hom}}(\mathbf{r})} \quad (1.4)$$

and

$$\int_{S_k^i} d\mathbf{S} \nabla \cdot \mathbf{J}_G^{\text{hom}}(\mathbf{r}) = \int_{S_k^i} d\mathbf{S} \nabla \cdot \mathbf{J}_G^{\text{het}}(\mathbf{r}), \quad (1.5)$$

where V_k and S_k^i denote the volume and the i -th surface of node k , respectively. If Eqs. (1.4) and (1.5) are satisfied, k_{eff} is also preserved (Smith, 1986).

1.1.2.1 Spatial homogenization and energy condensation of cross sections

In Eq. (1.4), the spatially dependent cross sections are averaged within the node (i.e., the fuel assembly) by flux-volume weighting. Obviously, Eq. (1.4) cannot be used in practical applications, because neither the heterogeneous transport solution $\Phi_G^{\text{het}}(\mathbf{r})$ [Eq. (1.1)] nor the homogeneous diffusion solution $\Phi_G^{\text{hom}}(\mathbf{r})$ [Eq. (1.3)] is known *a priori*. This complexity is commonly circumvented approximating $\Phi_G^{\text{het}}(\mathbf{r})$ with the solution of the heterogeneous transport equation in the fuel assembly with reflective boundary conditions at its outer edges (Smith, 1986). In this calculation (referred to as single-assembly or infinite-medium calculation), the assembly is modeled in the most detailed geometry, and intra-assembly transport effects are taken into account. The zero-net-current boundary conditions are the only approximation. With the aforementioned assumption, Eq. (1.4) becomes

$$\Sigma_{x,G}^k \approx \Sigma_{x,G}^{\infty,k}, \quad \Sigma_{x,G}^{\infty,k} = \frac{\int_{V_k} d\mathbf{r} \Sigma_{x,G}^{\text{het}}(\mathbf{r})\Phi_{\infty,G}^{\text{het}}(\mathbf{r})}{\int_{V_k} d\mathbf{r} \Phi_{\infty,G}^{\text{het}}(\mathbf{r})}, \quad (1.6)$$

where $\Phi_{\infty,G}^{\text{het}}(\mathbf{r})$ denotes the heterogeneous flux from the single-assembly transport calculation. Moving from Eq. (1.4) to Eq. (1.6), the spatial integral of $\Phi_G^{\text{hom}}(\mathbf{r})$ has been replaced with the infinite-medium heterogeneous integral, thus introducing another approximation.

The single-assembly (or lattice) calculation is performed for each type of fuel assembly in a reactor core. It is commonly based on deterministic transport methods, such as collision probability, the method of characteristics, and discrete ordinates (Sanchez and McCormick, 1982; Lewis and Miller, 1984). The determination of the assembly-homogenized cross sections is usually split into two phases, as described below (Duderstadt and Hamilton, 1976; Smith, 1986; Stacey, 2007).

- The periodic lattice of the fuel assembly is first divided into a number of identical unit cells, each consisting of a fuel pin, its clad, the surrounding moderator, and the structural material. The transport equation is solved for every type of fuel cell, under the assumption of zero net leakage at the cell boundaries. More advanced lattice codes model clusters of cells (instead of each cell type independently) to account for cell-to-cell neutron exchange. The cell calculation is usually performed in 1-D cylindrical geometry and features (i) a very fine energy mesh (often hundreds of groups) to account for heterogeneous effects in resonance absorption and fast fission (such as energy self-shielding effects), and (ii) a detailed spatial discretization to model the strong variation in the neutron spectrum inside the cell (spatial self-shielding effects). Using the so obtained within-cell flux distribution as weighting function, the fine-group, fine-mesh cross sections are spatially averaged over the cell and collapsed to a smaller number of groups (usually between 6 and 40). Rather specialized techniques are applied for cells not containing fuel material, such as water holes, guide tubes hosting control rods, and burnable-poison rods.
- Collapsed cell-averaged cross sections are used in whole-assembly transport calculations that model all the homogenized fuel cells, control rods, water channels, and burnable-absorber rods. Modern lattice codes, such as APOLLO2 (Sanchez et al., 2010) and CASMO (Rhodes et al., 2006), adopt a detailed representation of the fuel cells also in this phase of the homogenization procedure. These codes use the method of characteristics (Sanchez and McCormick, 1982; Lewis and Miller, 1984) with an unstructured mesh and subdivide each fuel pin into octants of rings. The whole-assembly calculation must also be performed with a sufficient number of energy groups to account for spectral interactions between dissimilar cells (i.e., between pins having different fuel composition, between fuel cells and control rods, etc.). The resulting flux distribution is used to spatially average the pin-by-pin cross sections over the whole assembly and to collapse them further to few groups (usually two groups in LWR analysis).

The fine-group cross sections and the condensation spectrum used for energy collapsing

depend on the thermal-hydraulic conditions and material composition in the node (i.e., the reactor state parameters). Few-group homogenized cross sections for nodal routines must therefore be represented as a function of the local, instantaneous physical conditions. Lattice calculations are performed for a limited set of reactor states, from which a continuous representation (namely, the cross-section library) is built to cover the whole state-parameter phase space (Watson and Ivanov, 2002; Zimin and Semenov, 2005). In this way, the nodal cross sections can be reconstructed (usually via multivariate interpolation) at the exact, local conditions during the on-line core calculation. This solution strategy (based on single-assembly transport calculations for few-group constant generation and whole-core nodal diffusion simulations) is referred to as *two-step* procedure.

1.1.2.2 Assembly discontinuity factors

The transverse-integrated nodal equations (Section 1.1.1) are solved requiring continuity of the neutron flux and net current across nodal interfaces. A difficulty arising from the homogenization procedure is that the homogenized diffusion equation with the above continuity conditions lacks sufficient degrees of freedom to preserve simultaneously reaction rates and currents (Smith, 1986). This feature becomes apparent introducing Fick's diffusion law

$$\mathbf{J}_G^{\text{hom}}(\mathbf{r}) = -D_G^{\text{hom}}(\mathbf{r})\nabla\Phi_G^{\text{hom}}(\mathbf{r}) \quad (1.7)$$

into Eq. (1.5), which yields, for node k ,

$$D_{G,i}^k = \frac{-\int_{S_k^i} d\mathbf{S} \nabla \cdot \mathbf{J}_G^{\text{het}}(\mathbf{r})}{\int_{S_k^i} d\mathbf{S} \nabla^2 \Phi_G^{\text{hom}}(\mathbf{r})}. \quad (1.8)$$

If conventional flux and current continuity are imposed at the nodal interfaces, the values of the diffusion coefficient $D_{G,i}^k$ computed with Eq. (1.8) will be different on each surface S_k^i . Spatially constant values of the diffusion coefficient (preserving the quantities of Eqs. (1.4) and (1.5)) can only be found if additional degrees of freedom are introduced in the homogenized parameters. These degrees of freedom are the assembly-surface discontinuity factors, which allow the homogeneous surface fluxes to be discontinuous (Smith, 1986). These parameters relate the homogeneous surface flux $\Phi_{G,i}^{\text{hom},k}$ at a nodal interface i to the corresponding heterogeneous flux $\Phi_{G,i}^{\text{het},k}$, which is continuous and uniquely defined:

$$f_{G,i}^k = \frac{\Phi_{G,i}^{\text{het},k}}{\Phi_{G,i}^{\text{hom},k}}. \quad (1.9)$$

Assembly discontinuity factors can be viewed as additional homogenization parameters. As such, they are also computed in single-assembly transport calculations and stored in

the multiparameterized cross-section libraries. In the infinite lattice, the homogenized flux is spatially flat. Single-assembly discontinuity factors are, therefore, ratios of surface-averaged heterogeneous fluxes to volume-averaged fluxes:

$$f_{G,i}^k \approx f_{G,i}^{\infty,k}, \quad f_{G,i}^{\infty,k} = \frac{\Phi_{\infty,G,i}^{\text{het},k}}{\bar{\Phi}_{\infty,G}^{\text{het},k}} = \frac{\frac{1}{S_k^i} \int_{S_k^i} d\mathbf{S} \Phi_{\infty,G}^{\text{het}}(\mathbf{r})}{\frac{1}{V_k} \int_{V_k} d\mathbf{r} \Phi_{\infty,G}^{\text{het}}(\mathbf{r})}, \quad (1.10)$$

where S_k^i and V_k denote the values of the surface area and volume of the node, respectively.

1.1.3 Problem description: core-environment effects on the homogenization parameters

Equivalence between the homogeneous nodal model [Eq. (1.3)] and the heterogeneous fine-mesh global solution from transport [Eq. (1.1)] is only guaranteed if the neutron flux distribution in the fuel assembly is close to the infinite-medium one used for spatial homogenization and energy condensation of cross sections [Eq. (1.6)] and for the determination of the discontinuity factors [Eq. (1.10)]. If the assembly is far away from the reflector and surrounded by assemblies of the same type in a large medium compared to the neutron mean free path, the infinite-medium approximation is generally acceptable. However, this condition is seldom met in modern reactor cores, characterized by strongly heterogeneous configurations which aim to reduce the neutron leakage, to optimize the core power distribution, and to maximize fuel exploitation. Interassembly streaming effects induced by variations in material and fuel composition result in non-reflective boundary conditions at the assembly outer edges, thus invalidating the theoretical foundation of the homogenization procedure. Errors in the nodal cross sections and discontinuity factors due to deviations between the environmental and single-assembly flux distributions may have a much larger impact on the nodal calculation than spatial truncation errors. They become highly penalizing in configurations with significant node-to-node leakage and strong flux gradients near the assembly interfaces. Typical examples of such configurations are: fuel loading patterns combining low-enriched uranium-oxide (UOX) and mixed-oxide (MOX) assemblies (Palmtag, 1997; Downar et al., 2000); layouts with control-rod banks inserted or local, strong burnable absorbers (such as Pyrex and gadolinium); reflector boundaries; and elaborate depleted-assembly shuffling strategies. With these increasingly widespread complex core designs, few-group constants deriving from the standard homogenization paradigm may fail to reproduce accurate estimates of the reaction rates and multiplication factor. Eventually, even with default adjustments in the construction of parameterized tables (such as criticality by the fundamental-buckling correction), high-fidelity simulations of LWRs with environment-independent homogenization parameters are only possible for fresh fuel at start-up in weakly heterogeneous systems. Core-environment effects must therefore be modeled to provide more accurate inputs for nodal solvers.

1. Introduction

The impact of core heterogeneity on the neutron flux distribution is illustrated with an example. Fig. 1.1a shows the infinite-medium spatially averaged neutron spectra (normalized to unity) in a UO_2 and a MOX assemblies at zero burn-up. The two assemblies have substantially different spectra. Fig. 1.1b displays the variation in the spectra (computed with respect to the single-assembly configuration) when the two bundles are next to each other in the core environment. The perturbation in the neutron distribution is significant, especially at thermal energies. The spectrum in the UO_2 assembly is hardened (namely, the neutron density increases at high energies and decreases at low energies), whereas the spectrum in the MOX assembly is softened.

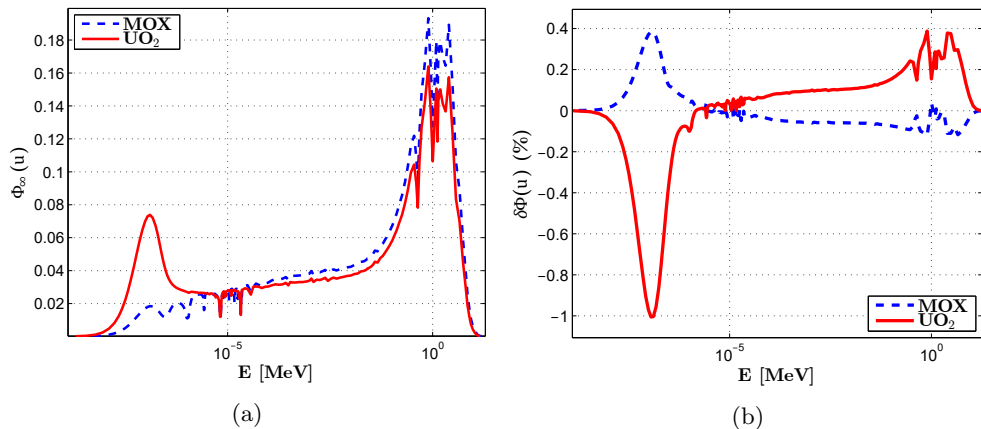


Fig. 1.1. Spectral effects at a UO_2/MOX interface: (a) infinite-medium assembly-averaged neutron flux spectra per unit lethargy u versus energy; (b) variation (in percentage) in the spatially homogenized spectra in the real environment, where the two fuel assemblies are next to each other. The spectra in the (a) quadrant are normalized to unity. Units of the non-normalized distributions are in neutrons/(square centimeters \cdot second).

Fig. 1.2 depicts the spatial distribution of the cell-homogenized heterogeneous thermal flux (normalized to unity) in the same UO_2 assembly under the infinite-lattice approximation (Fig. 1.2a) and when it neighbors the MOX assembly (Fig. 1.2b). In the second configuration, a steep flux gradient arises at the periphery of the assembly. Here, the flux magnitude decreases by about 20% compared to the single-assembly configuration.

It can be concluded that core heterogeneity has a relevant impact on the flux distribution in both space and energy.

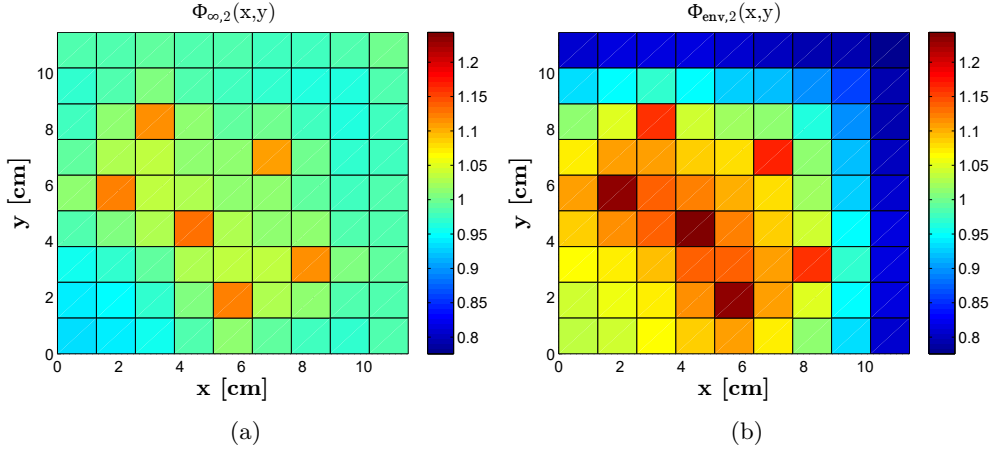


Fig. 1.2. Spatial effects at a UO_2/MOX interface: thermal-flux distribution (normalized to unity) in a UO_2 assembly quarter (a) within an infinite lattice and (b) adjacent to a MOX assembly. The non-normalized flux is in units of neutrons/(square centimeters \cdot second). The coordinates [0,0] (in cm) correspond to the assembly center. The six cells with flux peaking are empty guide tubes.

1.2 Review of state-of-the-art methodology

Since the formulation of consistent nodal methods, a number of strategies have been proposed to account for environmental effects on the homogenization parameters. Homogenization with the environmental boundary conditions, based on iterations between nodal and lattice calculations, turned out to be impractical because of its excessive computational burden (Smith, 1980; Colameco, 2012). Colorset (i.e., multiassembly) homogenization is also computationally unwieldy, because it calls for the simulation of each unique set of four assemblies which will appear in the reactor core life (Palmtag, 1997). Alternative methods have therefore been developed to preserve the high computational efficiency of the conventional two-step procedure. Even if the spatial and spectral effects of the environment are tightly coupled, for the sake of simplicity they are often addressed separately by reactor analysis methods. One of the early spectrum-correction methods was introduced by Becker (1976), who developed a simple analytical procedure to incorporate spectral effects into one-group nodal simulators. Palmtag and Smith (1998) found an empirical correlation with which to model local spectral interactions. This method, originally formulated for UO_2/MOX interfaces, is based on the observations that the fractional change in the fast-group cross sections is proportional to the leakage-to-removal ratio of fast neutrons and that the relative variation in the spectral index (raised to a power close to 1) accurately matches the relative variations in the cross sections (Palmtag, 1997). In a

similar approach proposed later by Ban and Joo (2016), called the Leakage Feedback Method, the cross-section functionalization is extended to the leakage fractions of both groups, and a separate formulation is proposed for peripheral fuel assemblies facing the reflector. Dall’Osso et al. (2010) applied a group-wise modal expansion to reconstruct the fine-energy spectrum change in the environment and to rehomogenize the nodal cross sections. Another modal approach, called *energy recondensation*, was developed at MIT (Zhu and Forget, 2011; Douglass and Rahnema, 2011). This method is based on the Discrete Generalized Multigroup (DGM) energy expansion theory (Rahnema et al., 2008; Zhu and Forget, 2010; Douglass and Rahnema, 2012).

Several methods have been proposed to take into account spatial effects. Spatial heterogeneity due to non-uniform intranodal depletion (i.e., gradients in the burn-up and nuclide concentrations) and fuel temperature is commonly modeled with a separable (along each coordinate axis) quadratic expansion of the nodal cross sections (Wagner et al., 1981; Forslund et al., 2001). A similar approach has been applied to represent design heterogeneity (Shatilla et al., 1996). However, these methods do not correct the spatial homogenization error due to deviations in the flux distribution between the environment and the infinite lattice. One of the first spatial rehomogenization techniques was proposed by Smith (1994). In his approach, the transverse-integrated intranodal cross sections are spatially (re)homogenized at each power iteration or thermal-feedback update with the computed 1-D heterogeneous flux shape. This shape is obtained via superposition of the heterogeneous infinite-lattice transverse-integrated flux form function and the homogeneous flux distribution from the transverse-integrated nodal calculation. This method uses single-assembly-generated rehomogenization coefficients and can be easily incorporated into existing codes. However, it does not correct the assembly discontinuity factors. A variant of it was later proposed by Palmtag (1997). In Dall’Osso (2014), the variation in the 1-D transverse-integrated flux between the real environment and the infinite lattice is evaluated with a modal expansion. This approach also corrects the discontinuity factors.

Another method for spatial rehomogenization is the 2-D submesh model that has been implemented in Studsvik’s nodal code SIMULATE (Bahadir et al., 2005; Bahadir and Lindahl, 2009). In this strategy, each radial node (i.e., fuel assembly or assembly quarter) is subdivided into $N \times N$ homogeneous rectangular subnodes (typically with $N = 5$). The 2-D diffusion equation is solved in every subregion with the corresponding infinite-medium homogenization parameters. The axial leakage (known from the global 3-D solution) is converted into an equivalent absorption cross section. The resulting intranodal flux distribution is used to rehomogenize the single-assembly cross sections over the submeshes and to estimate the environmental discontinuity factors at the assembly outer edges. The 2-D submesh calculation is combined with an axial homogenization model to handle axial heterogeneity. Radial zoning of fuel-assembly homogenization can also be used to reduce spatial errors. For example, EDF’s core simulator COCAGNE (Guillo et al., 2017) features a discretization of 2×2 subregions in each assembly quarter. Non-uniform nodes are used to model separately (*i*) the

four fuel pins in every external corner of the assembly, (*ii*) the outer and first inboard pin rows (at the assembly periphery), and (*iii*) the remainder of the fuel bundle. This meshing strategy has been chosen to minimize the level of heterogeneity in each subregion that is homogenized. In spite of their enhanced accuracy, refined-mesh approaches entail a somewhat higher computational effort than conventional nodal methods, which only use one or four nodes per fuel assembly.

Other methods do not specifically focus on spatial or spectral effects and try to model the global environmental effect. For example, in Rahnema and Nichita (1997), the corrections on the nodal cross sections and discontinuity factors are tabulated in the standard parameterized libraries versus the current-to-flux ratio (or other albedo parameters) at the node surfaces. These corrections are computed during the lattice calculation via parametric assembly simulations with varying albedo boundary conditions. They are interpolated during the nodal calculation just as the infinite-lattice group constants. Recently, a variant of this approach has been investigated (Kim et al., 2017). The drawback of this kind of method is that it demands multiple single-assembly calculations for each lattice state. Rahnema and McKinley (2002) developed high-order cross-section homogenization, which does not require additional lattice simulations. Using high-order boundary-condition perturbation theory (McKinley and Rahnema, 2000), the environmental homogenization parameters are expanded in terms of the surface current-to-flux ratio. The expansion coefficients are evaluated using the known unperturbed solution of the zero-leakage problem. This method requires two infinite-medium adjoint functions, which are precomputed and stored as additional parameters in the cross-section tables. Clarno and Adams (2005) proposed to capture neighbor effects during the single-assembly calculation via spatial superposition of typical four-assembly configurations. Recently, Groenewald et al. (2017) developed a semi-heterogeneous transport-embedded approach, in which the embedded transport calculations are performed with a simplified handling of spatial heterogeneity, energy discretization and solution operator. The computational burden of transport-nodal iterations is thus mitigated.

1.3 Research objectives and thesis structure

This thesis focuses on the development and implementation of new first-principle methods to improve the accuracy of cross sections and discontinuity factors used in nodal codes. The ultimate goal is to achieve more reliable estimates of the important quantities that influence reactor core design and operation, such as the multiplication factor, the fission-power distribution, and the worth of control rods. The primary motivation behind this work is that, despite the broad range of cross-section correction approaches formulated in the last few decades (Section 1.2), homogenization errors remain a partially unsolved issue in nodal analysis. To the author's knowledge, there exists no method that has given a comprehensive answer to the fundamental questions of homogenization theory. Although continuous advances in numerical methods and

large-scale massively parallel computers may in a near future make deterministic transport practical for 3-D whole-core calculations (Sanchez, 2012), nodal methods have reached industrial maturity and will most likely be used for many years to come. Further research on this topic, therefore, not only is of scientific interest, but also has practical relevance.

This thesis builds upon and extends previous work conducted at Framatome (Paris, France) in the area of rehomogenization (Dall’Osso et al., 2010; Dall’Osso, 2014). In this research, modeling of core-environment effects is addressed separating their spectral and spatial components. The spectral and spatial rehomogenization methods investigated in this dissertation share a common feature: they both consist of projection-based modal syntheses of variations in the flux distribution (in energy or space) between the real environment and the infinite lattice. The dissertation is structured as follows.

Chapter 2 is about spectral rehomogenization. The method is derived and described in detail. Focus is given to the choice of the basis and weighting functions for the modal synthesis of the neutron flux spectrum variation. Two tracks are investigated: a combination of polynomial basis functions and a physically oriented mode, and a fully mathematical approach based on Proper Orthogonal Decomposition (POD). The method is applied to relevant Pressurized-Water-Reactor (PWR) benchmark problems. Several aspects of this approach are discussed, such as its capability to model not only spectral interactions between dissimilar neighbor assemblies but also spectral effects due to different reactivity in the environment and in the infinite medium.

In **Chapter 3**, a method is developed to approximate the spectrum of interassembly neutron leakage in the core environment. The proposed approach applies Fick’s diffusion law to the environmental flux spectra determined by the rehomogenization algorithm. The accuracy and robustness of the method are tested on several multi-assembly configurations, and the impact of its non-linearity is discussed. This diffusive strategy is compared with an alternative approach, which uses the fundamental-mode leakage spectrum obtained from the solution of the homogeneous B_1 equations.

Chapter 4 presents an original application of spectral rehomogenization. The method described in Chapters 2 and 3 is adapted to model the spectral effects of local density changes (i.e., changes in the moderator density, the concentration of diluted boron, and the xenon atomic density) on the nodal macroscopic and microscopic cross sections. The cross-section dependence on these three state parameters is thus resolved without the standard multidimensional interpolation in parameterized libraries. The method is validated on a broad range of reactor states, in both single-assembly and multi-assembly configurations. It is illustrated that spectral rehomogenization inherently reproduces the combined spectrum changes due to perturbations in the local physical conditions and interassembly neutron leakage.

In **Chapter 5**, a two-dimensional modal method is formulated for spatial rehomogenization of cross sections and discontinuity-factor correction. The method is validated on the same PWR assembly configurations analyzed in Chapter 3. Its accuracy is assessed on both nodal and pin-by-pin quantities. A comparison with an already

existing 1-D rehomogenization approach is made, and the contribution of the various environmental effects to homogenization errors is quantified.

Concluding remarks and recommendations for future research follow in **Chapter 6**.

MODAL SYNTHESIS OF NEUTRON SPECTRUM CHANGES

2.1 Introduction

This chapter ¹ introduces the spectral rehomogenization method developed at Framatome (Dall’Osso et al., 2010). In this approach, the difference between the environmental and infinite-medium node-averaged flux spectra is estimated at the core-calculation level with a modal synthesis. The energy-condensation defects are evaluated on the fly and added to the nodal cross sections provided by the standard lattice calculation. The accuracy of the computed spectral corrections depends on the choice of the basis and weighting functions for the modal expansion and on the approximation of the energy distribution of the internodal neutron leakage. This chapter presents original work on the first subject. Two modal approaches are investigated and compared: a semi-analytic strategy, which combines polynomial basis functions and a physical mode (the neutron emission spectrum from fission), and a method based on Proper Orthogonal Decomposition (POD).

This chapter is structured as follows. Section 2.2 presents the spectral rehomogenization algorithm with the latest developments. Section 2.2.2 discusses the two sets of basis and weighting functions in the energy domain for the modal synthesis of the spectrum change. The incorporation of the rehomogenization approach into the LWR two-step procedure is also illustrated. Section 2.3 shows numerical results for some PWR sample problems that are representative of the spectral effects observed in a reactor core. Section 2.4 addresses several aspects of rehomogenization, such as

¹The content of this chapter has been published in *Nuclear Science and Engineering* **190**, 1, 2018 (Gamarino et al., 2018a).

numerical features, the impact of the approximations in the derivation of the method, and the interplay with the critical-buckling spectrum correction. A summary follows in Section 2.5.

2.2 Theory

2.2.1 The spectral rehomogenization algorithm

The spectral rehomogenization method considered in this thesis is part of a more general cross-section correction model that aims to reproduce environmental effects of various nature. In Gamarino et al. (2016), an analytic expression was determined for the few-group nodal cross section Σ_G^{env} homogenized in the real environment:

$$\Sigma_G^{\text{env}} = \Sigma_G^\infty + \delta\Sigma_G^{(r)} + \delta\Sigma_G^{(xs)}, \quad (2.1)$$

where

- Σ_G^∞ is the single-assembly cross section (interpolated in the libraries at the current values of the local state parameters);
- $\delta\Sigma_G^{(r)}$ is the homogenization defect due to the flux variation $\delta\Phi(\mathbf{r}, E)$ between the real environment and the infinite-medium conditions;
- $\delta\Sigma_G^{(xs)}$ is the homogenization error due to variations in the cross-section distribution caused by the depletion in the real environment; this term encompasses the corrections described in Wagner et al. (1981) and Forslund et al. (2001).

In the same work (Gamarino et al., 2016), a flux factorization was used to decouple the spatial and spectral components of the homogenization-flux defect. It was shown that the following approximation holds:

$$\delta\Sigma_G^{(r)} \approx \delta\Sigma_G^{\text{spat}} + \delta\Sigma_G^{\text{spectr}} + \delta\Sigma_G^{\text{cross}}, \quad (2.2)$$

where the cross correction $\delta\Sigma_G^{\text{cross}}$ represents the contribution of mixed space-energy terms. This component of the homogenization error accounts for the fact that the spatial and spectral effects of the environment are not separable.

We estimate the spectral cross-section correction $\delta\Sigma_{x,G}$ for the reaction type x within the coarse energy group G in a generic node as (from now on we drop the superscript *spectr* for the sake of lightness of the notation):

$$\delta\Sigma_{x,G} = \frac{1}{\Phi_G} \int_{E_G^-}^{E_G^+} dE \Sigma_{x,\infty}(E) \delta\Phi_G(E), \quad (2.3)$$

where E_G^+ and E_G^- denote the G^{th} -group upper and lower energy boundaries, respectively; $\Sigma_{x,\infty}(E)$ is the distribution in energy of the infinite-medium spatially averaged cross section; $\bar{\Phi}_G$ is the nodal volume-averaged integral flux; and $\delta\Phi_G(E)$ is the variation in the node-averaged neutron flux spectrum due to environmental effects. The nodal flux $\bar{\Phi}_G$ is defined as

$$\bar{\Phi}_G = \frac{1}{V} \int_V d\mathbf{r} \Phi_G(\mathbf{r}), \quad (2.4)$$

where V is the volume of the node. We solve for $\delta\Phi_G(E)$ with a modal expansion. We consider the neutron continuous-energy balance equation in the real environment in a generic homogenized node:

$$\Sigma_{t,\text{env}}(E)\Phi_{\text{env}}(E) + L_{\text{env}}(E) = \frac{\chi_{\text{env}}(E)}{k_{\text{eff}}} \int_0^\infty dE' \nu \Sigma_{f,\text{env}}(E') \Phi_{\text{env}}(E') + \int_0^\infty dE' \Sigma_{s,\text{env}}(E' \rightarrow E) \Phi_{\text{env}}(E'). \quad (2.5)$$

In Eq. (2.5), $\Phi_{\text{env}}(E)$ and $L_{\text{env}}(E)$ represent the environmental neutron flux spectrum and leakage energy distribution, respectively. The meaning of the remaining symbols corresponds to common notation in reactor physics literature (Stacey, 2007). We neglect the dependence of the cross-section distributions and of the fission spectrum on the environment [i.e., $\Sigma_{x,\text{env}}(E) \approx \Sigma_{x,\infty}(E)$, $\chi_{\text{env}}(E) \approx \chi_\infty(E)$]. This assumption is the main approximation in the formulation of the method and will be the subject of a thorough discussion in Section 2.4.1. From now on, the subscript referring to the type of environment is dropped from the cross-section notation. We replace the energy variable E with a lethargy-like quantity $u_G(E)$, which is defined separately in each coarse energy group as

$$u_G(E) = \frac{\ln\left(\frac{E}{E_G^-}\right)}{\ln\left(\frac{E_G^+}{E_G^-}\right)}. \quad (2.6)$$

This change of variable is made to ease the search of the basis and weighting functions of the modal expansion. The quantity u (we omit the subscript G) is bounded between 0 and 1 in each macrogroup. It is remarked that this *ad hoc* variable does not correspond to the definition of lethargy commonly found in reactor physics textbooks (namely, $u = \ln(E_0/E)$, with E_0 usually set to 10 MeV for reactor calculations). According to Eq. (2.6), u increases with E .

Replacing E with u , Eq. (2.5) can be rewritten, for group G , as

$$\Sigma_{t,G}(u)\Phi_{\text{env},G}(u) + L_{\text{env},G}(u) = \sum_{G'=1}^{N_G} \left(\frac{\chi_{G'}(u)}{k_{\text{eff}}} \int_0^1 du' \nu \Sigma_{f,G'}(u') \Phi_{\text{env},G'}(u') + \int_0^1 du' \Sigma_{s,G' \rightarrow G}(u' \rightarrow u) \Phi_{\text{env},G'}(u') \right). \quad (2.7)$$

In each coarse group, the environmental spectrum is formulated as the sum of the reference condensation spectrum in the infinite-medium conditions and the sought spectrum variation in the environment $\delta\Phi_G(u)$:

$$\Phi_{\text{env},G}(u) = \bar{\Phi}_G \varphi_{\infty,G}(u) + \delta\Phi_G(u). \quad (2.8)$$

In Eq. (2.8), the G^{th} -group single-assembly spectrum $\varphi_{\infty,G}(u)$ is normalized to unity, and $\delta\Phi_G(u)$ has zero average. Therefore, the following normalization condition is satisfied:

$$\int_0^1 du \Phi_{\text{env},G}(u) = \bar{\Phi}_G. \quad (2.9)$$

The spectrum difference is expanded in terms of the modal components $Q_{G,i}(u)$:

$$\delta\Phi_G(u) = \sum_{i=1}^{N_{Q_G}} \alpha_{G,i} Q_{G,i}(u), \quad (2.10)$$

where N_{Q_G} is the group-dependent number of basis functions. We choose basis functions having zero average within each coarse group to satisfy the condition of Eq. (2.9). An estimate of $\bar{\Phi}_G$ and of the multiplication factor k_{eff} [Eqs. (2.7) and (2.8)] is known from the nodal solution. We assume that these estimates satisfy the balance equation integrated in energy. This is another approximation of the method.

If the leakage energy distribution $L_{\text{env},G}(u)$ is known, the expansion coefficients $\alpha_{G,i}$ [Eq. (2.10)] are the only unknowns of the spectral rehomogenization problem. In order to solve for them, we define a linear system of algebraic equations by applying a standard weighted-residual technique to Eq. (2.7). The use of a fully mathematical approach to determine the equations of the system is justified by the local distortion in the shape of the computed spectrum perturbation that has been observed when physically justified conditions are imposed. These include the continuity of the environmental spectrum and of its first derivative at the boundary between the two energy groups, and the condition $\delta\Phi_1(u=1) = 0$ within the fast group (that is, no spectrum variation at the upper energy boundary of the fast group, as observed in Fig. 1.1b). After substitution of Eqs. (2.8) and (2.10), Eq. (2.7) is projected on a set of weighting functions $W_{G,j}(u)$ (with $j = 1, \dots, N_{Q_G}$) and integrated in u within each coarse group. After some algebraic manipulation, the projection term corresponding to the reaction rate x reads

$$\int_0^1 du W_{G,j}(u) \Sigma_{x,G}(u) \Phi_{\text{env},G}(u) = \bar{\Phi}_G h_{R,x,G,j} + \sum_{i=1}^{N_{Q_G}} \alpha_{G,i} h_{V,x,G,i,j}, \quad (2.11)$$

with the rehomogenization parameters $h_{R,x,G,j}$ and $h_{V,x,G,i,j}$ defined as

$$h_{R,x,G,j} = \int_0^1 du W_{G,j}(u) \Sigma_{x,G}(u) \varphi_{\infty,G}(u) \quad (2.12a)$$

and

$$h_{V,x,G,i,j} = \int_0^1 du W_{G,j}(u) \Sigma_{x,G}(u) Q_{G,i}(u). \quad (2.12b)$$

The reference coefficients $h_{R,x,G,j}$ carry the information of the reference collapsing spectrum in the infinite lattice, whereas the variational coefficients $h_{V,x,G,i,j}$ are defined in terms of the components of the spectrum perturbation. With the aforementioned assumption $\Sigma_{x,G}^{\text{env}}(u) \approx \Sigma_{x,G}^{\infty}(u)$, the coefficients in Eq. (2.12) only depend on infinite-medium quantities [$\Sigma_{x,G}^{\infty}(u)$, $\varphi_{\infty,G}(u)$] and on the basis and weighting functions chosen for the modal synthesis of $\delta\Phi_G(u)$. They do not depend on environmental quantities. Therefore, they can be computed for each fuel-assembly type during the lattice calculation.

If the above procedure is applied to all terms in Eq. (2.7), the rehomogenization problem can be cast in the following form:

$$\begin{aligned} \bar{\Phi}_G h_{R,t,G,j} + \sum_{i=1}^{N_{Q_G}} \alpha_{G,i} h_{V,t,G,i,j} + c_{G,j} &= \sum_{G'=1}^{N_G} \bar{\Phi}_{G'} \left(h_{R,s,G' \rightarrow G,j} + \right. \\ &\left. \frac{\chi_{G,j}}{k_{\text{eff}}} h_{R,f,G'} \right) + \sum_{G'=1}^{N_G} \sum_{i=1}^{N_{Q_{G'}}} \alpha_{G',i} \left(h_{V,s,G' \rightarrow G,i,j} + \frac{\chi_{G,j}}{k_{\text{eff}}} h_{V,f,G',i} \right), \end{aligned} \quad (2.13)$$

where $c_{G,j}$, $\chi_{G,j}$ and the coefficients h_R , h_V are the rehomogenization parameters corresponding to the fine-group neutron leakage, fission-emission spectrum, and various reaction rates. The variables in Eq. (2.13) are formulated as follows:

$$c_{G,j} = \int_0^1 du W_{G,j}(u) L_{\text{env},G}(u), \quad (2.14a)$$

$$\chi_{G,j} = \int_0^1 du W_{G,j}(u) \chi_G(u), \quad (2.14b)$$

$$h_{R,t,G,j} = \int_0^1 du W_{G,j}(u) \Sigma_{t,G}(u) \varphi_{\infty,G}(u), \quad (2.14c)$$

$$h_{V,t,G,i,j} = \int_0^1 du W_{G,j}(u) \Sigma_{t,G}(u) Q_{G,i}(u), \quad (2.14d)$$

$$h_{R,f,G} = \int_0^1 du \nu \Sigma_{f,G}(u) \varphi_{\infty,G}(u), \quad (2.14e)$$

$$h_{V,f,G,i} = \int_0^1 du \nu \Sigma_{f,G}(u) Q_{G,i}(u), \quad (2.14f)$$

$$h_{R,s,G' \rightarrow G,j} = \int_0^1 du W_{G,j}(u) \int_0^1 du' \Sigma_{s,G' \rightarrow G}(u' \rightarrow u) \varphi_{\infty,G'}(u'), \quad (2.14g)$$

$$h_{V,s,G' \rightarrow G,i,j} = \int_0^1 du W_{G,j}(u) \int_0^1 du' \Sigma_{s,G' \rightarrow G}(u' \rightarrow u) Q_{G',i}(u'). \quad (2.14h)$$

The matrix of the linear system of Eq. (2.13) has rank $r = N_G N_Q^{max}$, with $N_Q^{max} = \max_{G=1,\dots,N_G} \{N_{Q_G}\}$. This system is solved for each node following a non-linear iteration of the nodal solution. The quantities $\bar{\Phi}_G$ and k_{eff} are taken as input from the prior, partially converged power iteration of the eigenvalue calculation, whereas the precomputed rehomogenization coefficients [Eq. (2.14)] are interpolated in the parameterized libraries as a function of the local physical conditions. No additional lattice calculation is needed, neither when updating the cross sections throughout the nodal simulation nor when building the parameterized libraries.

After determining the coefficients $\alpha_{G,i}$, the spectral cross-section correction for reaction type x in a generic node is computed as

$$\delta \Sigma_{x,G} = \frac{1}{\bar{\Phi}_G} \int_0^1 du \Sigma_{x,G}^\infty(u) \delta \Phi_G(u) = \frac{1}{\bar{\Phi}_G} \sum_{i=1}^{N_{Q_G}} \alpha_{G,i} h_{V,x,G,i,0}, \quad (2.15)$$

where we have used the fact that $W_{G,0}(u) = 1$.

In the derivation presented here, no assumption has been made about the spectral distribution of the neutron leakage $L_{\text{env},G}(u)$. In order for the rehomogenization model to be applicable, this quantity must be determined based on nodal information. In this chapter, the best-estimate shape is taken as an input quantity from the reference transport simulation, even if this is not possible in routine calculations. This allows us to keep the validation of the methodology unaffected by the inaccuracy unavoidably introduced adopting a leakage spectrum other than the exact one. It is thereby possible to focus on the effect of the chosen sets of basis/weighting functions on the accuracy and performance of the method. The development of a model for the leakage spectrum is addressed in Chapter 3.

The methodology described above can be applied to an arbitrary number of groups. In this thesis we consider a two-group energy structure ($N_G = 2$). This is the most common choice in nodal codes for LWR analysis. The upper energy boundary of the fast group is set to $E_1^+ = 19.6$ MeV, and the lower energy boundary of the thermal group is set to $E_2^- = 1.1 \cdot 10^{-10}$ MeV. The thermal cut-off energy is $E_1^- \equiv E_2^+ = 0.625$ eV.

2.2.2 Modal approaches

The successful application of spectral rehomogenization relies on the modal components $Q_{G,i}(u)$ and $W_{G,j}(u)$ used to derive Eq. (2.13).

Two kinds of basis functions have been investigated. The first approach (to which we refer as polynomial or semi-analytic) adopts Chebyshev polynomials, in combination with a physically oriented mode (the neutron emission spectrum from fission) in the fast group. The use of the latter is justified by the peak observed in the spectrum

deformation at high energies (see Fig. 1.1b). Moreover, the fission spectrum is an appropriate trial function because it is mostly insensitive to the environmental conditions. An attempt has been made to find other modes having physical insight into the nature of the sought solution. This feature is highly desirable, as it commonly requires a reasonably low number of basis functions to reproduce the solution to a satisfactory accuracy (Stacey, 1967). The behavior of neutrons in the epithermal and thermal parts of the spectrum can be described by the $1/E$ -type slowing-down distribution and the Maxwellian distribution that characterizes thermal equilibrium with the moderator (Dall'Osso, 2003). However, a superposition of these migration modes can only be used to synthesize the neutron spectrum, not a spectrum perturbation. For instance, since the neutron temperature defining the Maxwellian distribution changes when moving from the infinite medium to the real environment, the thermal-spectrum variation cannot be described by such a function. Due to the difficulty of finding physical modes other than the fission spectrum, an alternative strategy has been formulated building upon POD. This choice is inspired by the search of basis functions capturing some information on the phenomenon under study (i.e., spectral interactions in a reactor core).

The two approaches are presented separately below.

2.2.2.1 A polynomial approach

Thermal-group basis functions In the thermal group, Chebyshev polynomials of the first kind $[T_i(u)]$ have been selected. These polynomials are defined with the following recursive formula:

$$\begin{aligned} T_0(u) &= 1, \\ T_1(u) &= u, \\ T_i(u) &= 2uT_{i-1}(u) - T_{i-2}(u), \quad i \geq 2. \end{aligned} \tag{2.16}$$

In the pseudo lethargy domain introduced in Section 2.2 [Eq. (2.6)], the thermal-group spectrum variation has value of zero for $u < b$, with $b \approx 0.5$ (which corresponds to about 5.85 meV). Therefore, a modification of Eq. (2.16) must be introduced in order for the basis functions to have zero average value in the interval $[b,1]$ and to be null in the interval $[0,b)$. The polynomials $T_i(u)$ are first shifted to have zero average between 0 and 1:

$$T'_i(u) = T_i(u) - \int_0^1 du T_i(u), \quad i \geq 1. \tag{2.17}$$

They are then multiplied by a unitary Heaviside function $H(u - b)$ that vanishes for $u < b$. According to the fine-group structure adopted in this thesis (see Section 2.2.2.2), a value of 0.52167 (corresponding to $E = 7.15$ meV) is chosen for b . This value matches the upper boundary of one of the fine-energy groups g . After these changes, the thermal basis functions read

$$Q_{2,i}(u) = T'_i(u')H(u - b), \quad i \geq 1, \tag{2.18}$$

where the shifted variable u' is defined as

$$u' = \frac{u - b}{1 - b}. \quad (2.19)$$

The first four basis functions computed with Eq. (2.18) are shown in Fig. 2.1. The superposition of the Heaviside function introduces a discontinuity in the modes at $u = b$.

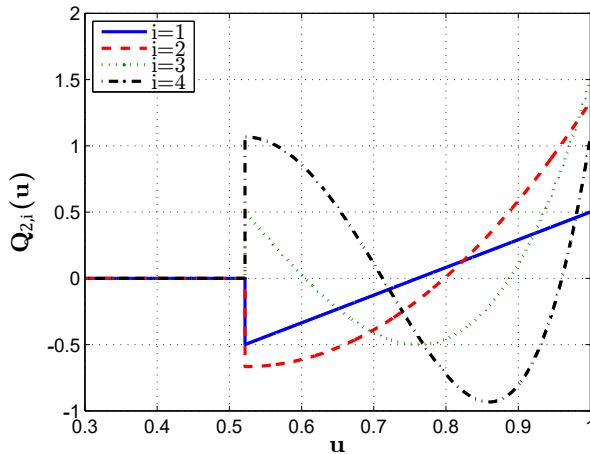


Fig. 2.1. Thermal-group polynomial basis functions.

Fast-group basis functions In the fast group, the first trial function is the already mentioned fission-spectrum migration mode $\chi(u)$. Several expressions can be found in the literature for this function. In this thesis, we use the formulation reported in Lamarsh's textbook (Lamarsh, 1966). In the energy domain, this reads

$$\chi(E) = n_f \sqrt{E} e^{-a_f E}, \quad (2.20)$$

with E expressed in mega-electron-volts (MeV). Eq. (2.20) is derived under the assumption that the fission-emission distribution does not vary with the energy of the incident neutron. The coefficient a_f and the normalization constant n_f depend on the fissioning nuclides. We consider $a_f = 0.776$ and $n_f = 0.771$. These numerical values correspond to uranium fuel enriched at less than 10%. We assume that the inaccuracy caused by using Eq. (2.20) for other enrichments or different types of fuel material (such as MOX assemblies) is reasonably small and acceptable in the context of this work.

After moving from E to u and subtracting the average value of $\chi(E)$, the sought basis function reads

$$Q_{1,1}(u) = ce^{-a_f E_1^- r_1^u} \ln(r_1)(r_1^u)^{3/2} - \chi_{\text{avg}}, \quad (2.21)$$

where

$$\chi_{\text{avg}} = \int_0^\infty dE \chi(E) = n_f \frac{\sqrt{\pi}}{2a_f^{3/2}}, \quad c = n_f (E_1^-)^{3/2}, \quad r_1 = \frac{E_1^+}{E_1^-}. \quad (2.22)$$

The remaining trial functions are, as in the thermal group, Chebyshev polynomials of the first kind, modified to have zero average value between 0 and 1:

$$Q_{1,i}(u) = T'_{i-1}(u), \quad i \geq 2. \quad (2.23)$$

The fast-group basis functions are plotted in Fig. 2.2 for $i \in [1, 4]$.

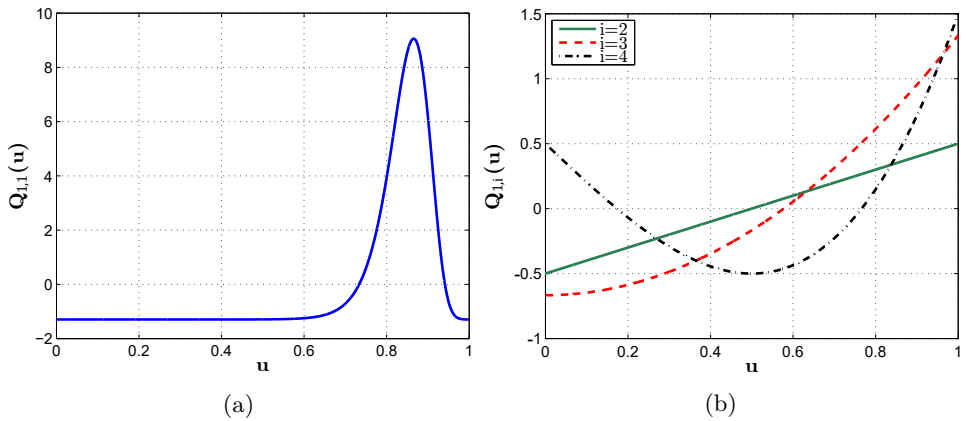


Fig. 2.2. Fast-group semi-analytic basis functions: (a) the neutron emission spectrum from fission and (b) Chebyshev polynomials of the first kind.

Weighting functions The achievement of satisfactory results with the above polynomial modes strongly depends on the weighting functions. Although their choice is in principle arbitrary, the weighting operators can be opted for to minimize the error in some sense (Stacey, 1967). For instance, the use of quasi-contiguous double step functions (i.e., 1 inside certain intervals and 0 outside) has the physical interpretation of requiring that the neutron balance be satisfied in an integral sense over certain regions of the energy domain. However, the importance of the various energy intervals can be sensitive to the specific assembly configuration and, hence, lack generality. Since we could not find a rigorous justification of the choice of the steps, this option has been discarded.

An attempt has been made to use the adjoint spectrum and the generalized importance functions computed at the lattice-calculation level. The physical meaning of this approach is to minimize the error on some characteristic spectrum-dependent integral quantity. Typical observables are, in this sense, the multiplication factor, the

spectral index, the breeding ratio, resonance integrals, the ^{235}U and ^{238}U absorption probabilities per fission-emitted neutron, and the ^{135}Xe worth, but other functionals of the spectrum can be defined (Gandini, 1967). This approach could not be implemented as a final solution because it produced an ill-conditioned matrix of the rehomogenization problem. Moreover, the adjoint and importance-function spectra in the real environment can differ from the infinite-medium ones. Hence, their use as test functions might not be rigorous.

On the basis of these considerations, the most natural choice is Galerkin weighting (that is, using weighting functions equal to the basis functions).

2.2.2.2 The POD approach

Proper Orthogonal Decomposition is a mathematical technique that has been widely used in the last decades in many scientific and engineering fields (Chatterjee, 2000; Kunisch and Volkwein, 2001) and to which a growing interest has been recently shown also in the nuclear community (Wols, 2010; Sartori, 2015; Buchan et al., 2013, 2015; Gamarino et al., 2017). In the framework of our rehomogenization method, the proposed approach is based on the calculation of the optimal (in a least-squares sense) orthonormal basis functions for the space spanned by a set of snapshots of the reference spectrum variation. A snapshot is the solution of the equation modeling the problem of interest for a specific configuration or state of the system. The shape of the so obtained modes is determined by the energy (namely, the information) carried within the retained snapshots and can thus capture some relevant features of the spectral changes. Even if the POD approach has a mathematical connotation and not a physical one, its underpinning idea is to describe the spectrum variation as a modulation of functions synthesizing its main components. This is, to some extent, the same principle of the Migration Mode Method for the approximation of the neutron spectrum (Dall’Osso, 2003).

As mentioned in Section 1.1.3, interassembly heterogeneity is the main source of spectral effects, which mostly occur at the interfaces between different neighbor regions. We therefore simulate several assembly-interface types to generate snapshots of the spectrum variation between the environmental and infinite-medium conditions. We simplify our analysis by considering 2-D colorsets (i.e., four-assembly sets). The idea behind the generation of snapshots can be illustrated with an example. Fig. 2.3 depicts the fast-group spectrum variation in a UO_2 assembly next to another UO_2 assembly hosting a bank of twenty-four black control rods. Three different curves are shown as a function of the ^{235}U fuel enrichment in the rodded bundle (1.8%, 2.4%, and 3.1%). The enrichment in the unrodded assembly (1.8 %) is fixed. Both assemblies have zero burn-up. In the epithermal range (that is, for approximately $u_1 < 0.6$ or $E < 18.6$ keV), the curves exhibit a very much alike outline with roughly a simple shift among them. Also, a peak is found at high energies in the three cases. However, if the enrichment in the rodded assembly increases, a distortion of such peak occurs, with a sign-changing bulge becoming apparent in the pseudo lethargy

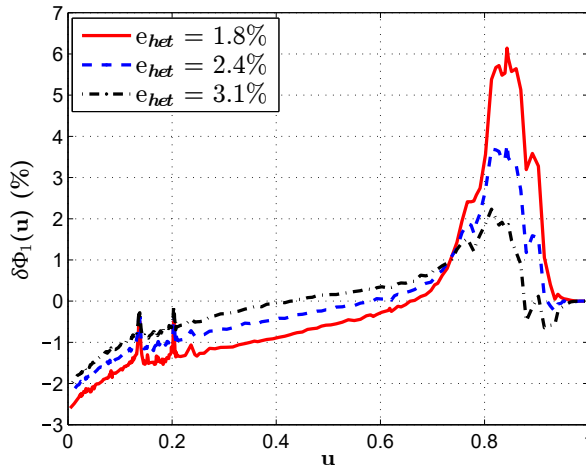


Fig. 2.3. Fast-group spectrum perturbation in a 1.8%-enriched UO_2 assembly as a function of the enrichment e_{het} in the adjacent rodged UO_2 bundle.

range $[0.85, 0.95]$ (i.e., between 1.4 and 8.2 MeV). This suggests that interassembly enrichment differences trigger a characteristic component of the spectrum variation. Spectral interactions between adjacent assemblies can be driven by differences in a broad range of parameters other than the enrichment, such as the fuel composition and burn-up, and by the presence of burnable poison and control elements. In order to cover the parameter space of spectral interfaces and to capture as many components of the spectrum variation as possible, multiple values of these heterogeneity variables must be sampled.

For a given test problem (corresponding to a certain set of the aforementioned parameters), we generate a snapshot by solving the neutron transport equation in the colorset and single-assembly configurations. The environmental and infinite-medium spatially averaged spectra are computed for each fuel bundle, together with the corresponding variation. In order to determine the detailed spectrum change, the numbers of fine energy groups g used in the fast and thermal coarse groups are 247 and 34, respectively. For both macrogroups, the matrix of snapshots A_G is obtained collecting the spectrum variation test solutions determined for different problems. The searched POD modes ensue from the Singular Value Decomposition (SVD) of A_G (Chatterjee, 2000; Kunisch and Volkwein, 2001). This mathematical tool returns the following matrix decomposition:

$$A_G = U_G S_G V_G^T, \quad (2.24)$$

where S_G is a diagonal matrix of size $n_G \times N_s$ (n_G is the number of fine groups in the coarse group G and N_s is the number of snapshots), whereas U_G and V_G have dimensions $n_G \times n_G$ and $N_s \times N_s$, respectively. The columns of the matrix

U_G are referred to as proper orthonormal modes and form the sought POD basis. The elements of S_G , which are non-negative and sorted in descending order, are the singular values of A_G . These are proportional to the energy of each mode, that is, its importance in the modal approximation of the vector space spanned by A_G . If all n_G eigenvectors produced by the SVD are used, the error in the approximation of the original snapshot data goes to zero. The POD basis for our rehomogenization method, consisting of N_{Q_G} modes, is built from a reduced form of Eq. (2.24), taking the first N_{Q_G} columns of U_G . The corresponding array provides a modal approximation of the snapshot set that minimizes the error in the L_2 -norm compared to all the other approximations. Also in this case, the rehomogenization problem is solved using the achieved POD modes as weighting functions as well (Galerkin projection).

2.2.3 Integration into the LWR two-step procedure

Fig. 2.4 shows how the rehomogenization method is integrated into the nodal core calculation and, more in general, into the two-step procedure commonly adopted in LWR analysis.

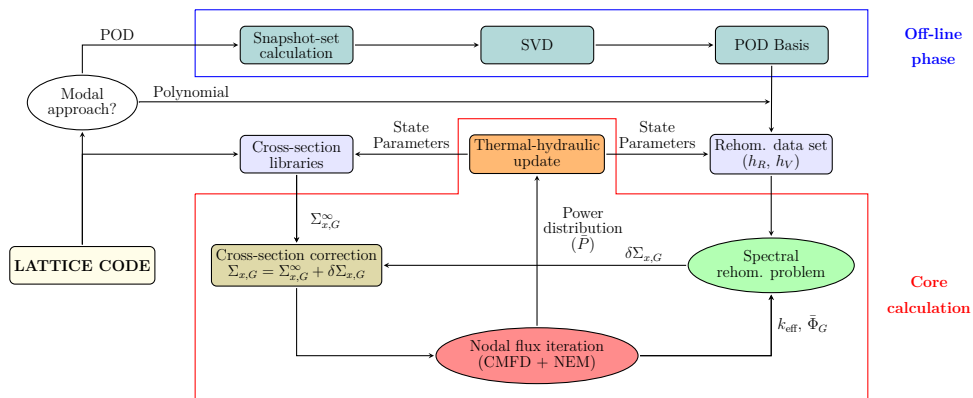


Fig. 2.4. Flow diagram of spectral rehomogenization within the LWR two-step calculation.

The rehomogenization coefficients are computed [via Eq. (2.14)] at the cross-section library level by post-processing the results of the fine-group lattice transport simulation. Their calculation merely requires the solution of further integrals in the energy domain. The only change in the parameterized tables is the storage of the additional homogenization parameters. If the POD approach is used for the modal synthesis of spectrum perturbations, a supplementary step is needed. Snapshots of the spectrum deformation have to be collected for various sample assembly configurations. These are then used to extract, via the SVD, the set of POD basis vectors with which the rehomogenization parameters are to be computed. The POD-basis calculation (to

which we refer as off-line phase) is to be performed prior to the lattice calculation. During the core calculation, a steady-state nodal flux iteration of the core eigenvalue problem is first performed with the infinite-medium cross sections interpolated in the libraries at the current values of the state parameters in the various nodes. At the end of the non-linear iteration, the nodal information ($\bar{\Phi}_G$ and k_{eff}) is used to solve the spectral rehomogenization problem [Eq. (2.13)] in each homogenized region. Since this is done locally sweeping all the nodes of the system, the algorithm is easily parallelizable. Depending on the coupled neutronics/thermal-hydraulics iteration control criterion, the following may be stated:

- If no thermal-feedback calculation is performed after the nodal flux iteration, the single-assembly cross sections are updated with the spectral correction computed by rehomogenization.
- If the thermal-feedback update is activated, the thermal-hydraulic calculation is performed using as input the nodal power (\bar{P}) distribution from the prior flux iteration. After interpolation in the parameterized tables at the new values of the state parameters, the cross sections are updated with the spectral correction previously computed by rehomogenization.

Alternatively, the rehomogenization update can be implemented at an intermediate step between the nodal flux and thermal-feedback iterations. The calculation continues until convergence of all the coupled fields. Note that the flux solver is not changed by the rehomogenization module. Therefore, the method can be easily integrated into already existing core simulators.

2.3 Validation

In this section, the results of spectral rehomogenization are presented for some benchmark problems. The analysis is made on 2-D colorset configurations, consisting of checkerboard-loaded four-assembly sets with reflective boundary conditions at the assembly centerlines. Both polynomial-based and POD-based approaches are considered. The analysis of the results is introduced by a description of the procedure followed for the validation.

2.3.1 Procedure

We apply spectral rehomogenization to three test cases exhibiting significant heterogeneity: a UO_2 colorset with burnable-poison rods (example 1), a UO_2 colorset hosting silver-indium-cadmium (AIC) control rods (example 2), and a UO_2/MOX colorset (example 3). Nodal calculations are performed with BRISINGR, a Delft University of Technology in-house-developed code. The solution strategy in BRISINGR is based on the conventional non-linear coupling between a Coarse Mesh Finite Difference

(CMFD) solver and the Nodal Expansion Method (NEM), with fourth-order polynomial synthesis of the two-group intranodal transverse-integrated flux. More details about this nodal code and its validation can be found in Appendix A. Two-group homogenization parameters are computed by the SERPENT continuous-energy Monte Carlo neutron transport code (Leppänen et al., 2015). Version 2.1.28 of SERPENT is used, in combination with the JEFF3.1 nuclear data library (Koning et al., 2006). Single-assembly calculations for group-constant generation are run with 750 active cycles of $7.5 \cdot 10^5$ source neutrons (50 inactive cycles are discarded to allow the initial fission-source distribution to converge). This choice results in $5.63 \cdot 10^8$ active neutron histories. A standard deviation lower than 2.5% has been found for all the input cross sections and discontinuity factors. Therefore, an uncertainty-propagation analysis is deemed not to be necessary for the scope of this thesis work. No critical-buckling correction is applied to the two-group cross sections. As clarified later, this choice is consistent with the calculation of the snapshots in the framework of the POD approach. We use two-group diffusion coefficients computed with the Cumulative Migration Method (CMM) (Liu et al., 2016). The simulations are made for initial-core isothermal conditions (i.e., without thermal-hydraulic feedback and fuel depletion). The values of the main state parameters correspond to standard hot full-power conditions (namely, $T_{\text{fuel}} = 846$ K, $T_{H_2O} = 582$ K, and $p = 158$ bar). We adopt a nodalization of 2×2 nodes per fuel assembly.

The results of the nodal calculations are compared to the reference solution from SERPENT, which is determined solving the neutron transport equation in the colorset environment with full geometric details and a very fine energy mesh (281 groups). In this analysis, we only address the errors in the node-averaged quantities. For each benchmark problem, we show the results of nodal simulations with:

- standard infinite-medium cross sections (*a*);
- cross sections rehomogenized with the reference spectral correction (*b*);
- polynomial-based spectral rehomogenization of cross sections (*c*);
- POD-based spectral rehomogenization of cross sections (*d*).

The reference spectral correction (calculation *b*) is evaluated, in line with Eq. (2.15), collapsing the fine-group cross sections $\Sigma_{x,G}^\infty(u)$ with the reference spectrum variation $\delta\Phi_G^{\text{ref}}(u)$ from SERPENT:

$$\delta\Sigma_{x,G}^{\text{spec,ref}} = \frac{1}{\bar{\Phi}_G} \int_0^1 du \Sigma_{x,G}^\infty(u) \delta\Phi_G^{\text{ref}}(u). \quad (2.25)$$

The cross-section correction computed with Eq. (2.25) does not take into account the spatial effects of the environment (i.e., it does not correct the spatial homogenization error). For this reason, it is only a partial correction. However, it fully corrects the

energy condensation error. We therefore consider calculation *b* as the reference for our method. For both modal approaches (calculations *c* and *d*), rehomogenization is applied with $N_{Q_G} = 4$ in each coarse group. The rehomogenization coefficients [Eq. (2.14)] are computed with the same 281-group energy structure defined in Section 2.2.2.2. In the analysis, the errors in the nodal cross sections are computed as

$$\Delta\Sigma_{x,G} = \frac{\Sigma_{x,G} - \Sigma_{x,G}^{\text{ref}}}{\Sigma_{x,G}^{\text{ref}}} \cdot 100\%, \quad (2.26)$$

where $\Sigma_{x,G}$ is the infinite-medium or rehomogenized cross section and $\Sigma_{x,G}^{\text{ref}}$ is the reference cross section (i.e., the cross section condensed and homogenized in the colorset environment).

The snapshots for the calculation of the POD modes are also computed with SERPENT. Each 281-group spectrum variation solution is obtained running $5.25 \cdot 10^6$ active neutron histories. This value is a reasonably good compromise between statistical accuracy and computational effort. For reasons related to the computing time of fine-group calculations, the B_1 critical-spectrum calculation is not performed. More details about the procedure for the generation of snapshots are given for each test case in Section 2.3.2.

2.3.2 Numerical results

2.3.2.1 Example 1 - UO₂ colorset with Pyrex rods

The first colorset is made of four 17×17 PWR fuel assemblies of fresh UO₂ having two different compositions: the former with 1.8% enrichment, the latter with 3.1% enrichment and 16 rods containing burnable poison. The absorber elements are made of borosilicate glass (Pyrex). The colorset and assembly layouts are depicted in Fig. 2.5. The concentration of diluted boron in the moderator is 700 parts per million (ppm).

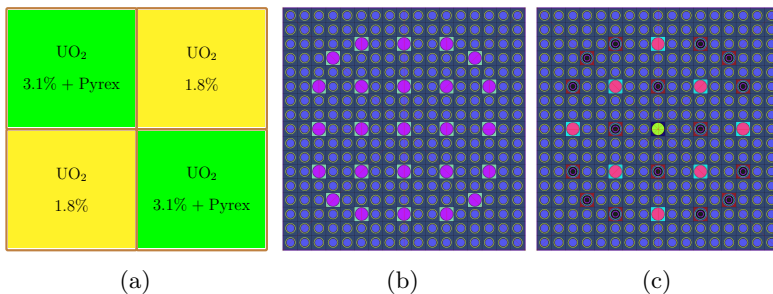


Fig. 2.5. (a) Assembly set of example 1. Layout of the UO₂ fuel assemblies: (b) with 1.8% enrichment, (c) with 3.1% enrichment and 16 Pyrex rods. The mass composition of the Pyrex glass is: Al₂O₃ (2.25%), B₂O₃ (12.7%), K₂O (1.15%), Na₂O (3.5%), SiO₂ (80.0%), and impurities (0.4%). The two bundles host 24 and 8 empty Zircaloy-4 guide tubes, respectively.

In this configuration, interassembly spectral effects are driven by differences in the enrichment and by the local presence of burnable-poison elements. In order to determine a set of POD modes, we generate 100 snapshots by means of a single-parameter analysis, with the Pyrex content in the heterogeneous assembly (namely, the assembly with poison rods) as the parametric variable. Solutions of the spectrum variation are computed sampling uniformly the target range $[5.9 \cdot 10^{-5}, 1.8 \cdot 10^{-3}]$ atoms/cm³ for the concentration of boron in the burnable-absorber rods $N_{B_{10}}^{bp}$. The snapshots are taken at the critical boron concentration (1465 ppm). In the nodal calculation, we simulate the colorset for one of the values of $N_{B_{10}}^{bp}$ spanned by the snapshot matrix (i.e., $9.3 \cdot 10^{-4}$ atoms/cm³). This is done in order to test capability of the POD modes to accurately reproduce the solutions used to build the original snapshot set. The chosen absorber concentration corresponds to $k_{\text{eff}} = 1.08733$ and to normalized values of the assembly-averaged total fission power of 0.93 in the 1.8%-enriched assembly and 1.07 in the 3.1%-enriched assembly with Pyrex (reference values from SERPENT). Fig. 2.6 shows the best-fit curves of the reference spectrum variation in the heterogeneous assembly. These have been computed with the polynomial basis functions and with the first four POD modes generated by the above procedure. The latter are plotted in Fig. 2.7. The POD operators fit very well the reference curves.

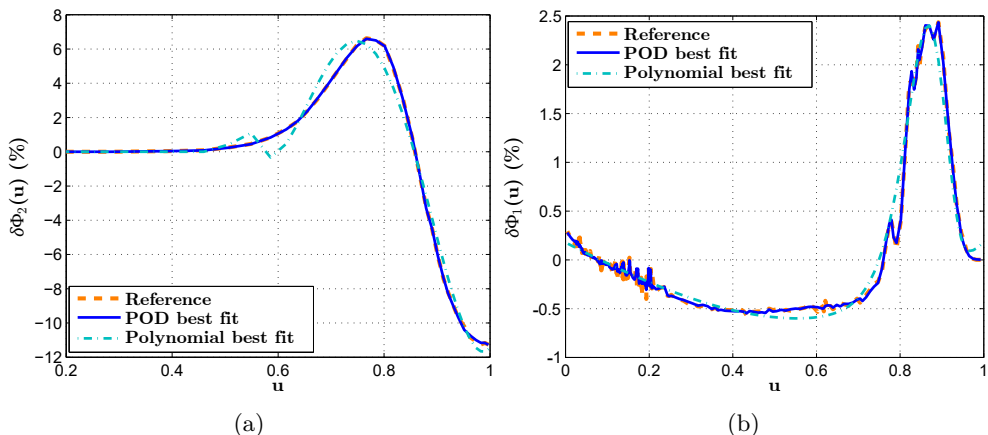


Fig. 2.6. Example 1: best fit of the (a) thermal-group and (b) fast-group reference spectrum deformation (per unit u) in the assembly hosting burnable-absorber rods. The perturbation (in percentage) is computed with respect to the assembly-averaged two-group flux from the reference transport calculation.

Comparing Figs. 2.6 and 2.7, it appears that the first and second POD basis functions retrieve the global shape of the reference spectrum perturbation. The spiky profiles observable in the higher-order modes, especially in the epithermal region, contribute to the reconstruction of the fine details of $\delta\Phi_G(u)$, including those associated to the resonances. Obviously, Chebyshev polynomials cannot reproduce such fine details due

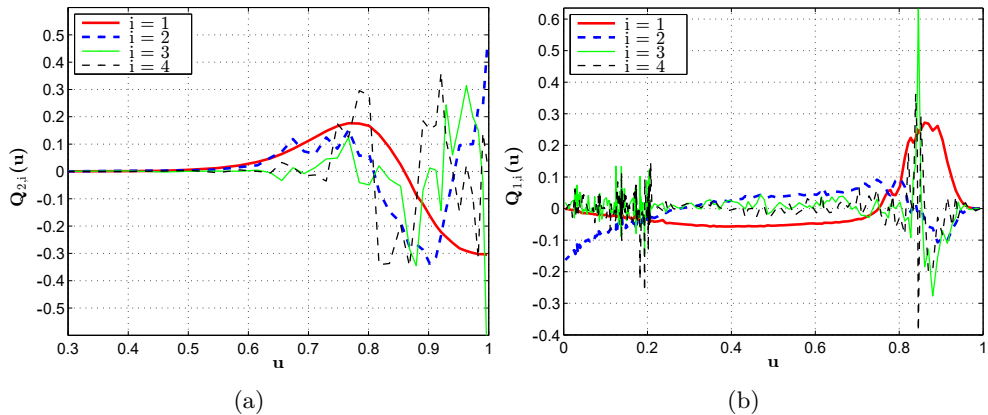


Fig. 2.7. (a) Thermal-group and (b) fast-group POD basis functions computed via the method of snapshots and the SVD for a one-parameter analysis of example 1.

to their smoothness. However, they fit the average outline of the reference curves precisely. The POD modes also inherit the property of the $\delta\Phi_G(u)$ snapshots to have zero average within each macrogroup.

The spectrum change estimated by rehomogenization with the two modal strategies is plotted in Fig. 2.8. The percent relative perturbation is computed with respect to the two-group assembly-averaged flux from the nodal calculation.

Table 2.1 reports the errors in the multiplication factor and assembly-averaged fission power (\bar{P}_{fiss}) for nodal calculations *a*, *b*, *c* and *d*. The number of power iterations for the convergence of the eigenvalue problem is also given. The power errors within parentheses correspond to the fast (first value) and thermal (second value) groups. The effectiveness of rehomogenization in improving the nodal fission power is apparent, while the gain in accuracy in the multiplication factor is somewhat limited. This is because the effects of changes in the flux spatial distribution are not accounted for by the present method. Tables 2.2 and 2.3 show the errors in the nodal cross sections of the two assemblies. With both modal approaches, the cross-section corrections computed by rehomogenization reproduce almost exactly the reference ones (calculation *b*). No significant difference is found between the two sets of basis and weighting functions, despite the higher accuracy of the POD strategy observed in Fig. 2.8, especially within the thermal group.

As seen in Table 2.1, rehomogenization causes an increase in the number of non-linear iterations by a factor of 1.9 with Chebyshev polynomials and by a factor of 2.8 with the POD modes. The numbers of power iterations reported in Table 2.1 correspond to a tolerance of 10^{-5} for the relative variations in the k_{eff} estimate and in the two-norm of the nodal flux distribution between two successive iterations.

An analysis is now carried out on the impact of the diffusion-coefficient spectral correction (δD_G). The diffusion coefficient can be rehomogenized in a similar fashion

2. Modal synthesis of neutron spectrum changes

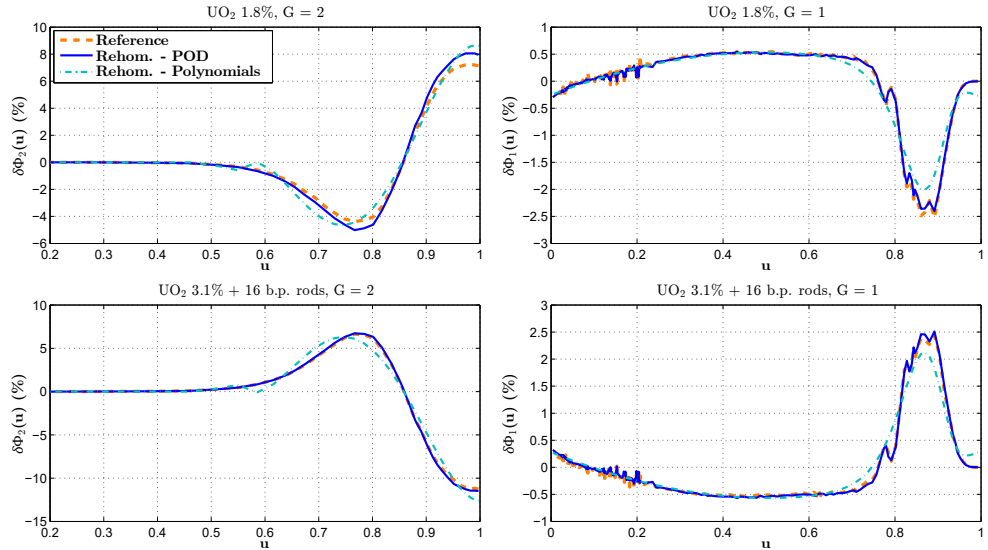


Fig. 2.8. Example 1: spectrum variation per unit u computed by rehomogenization. The abbreviation *b.p.* stands for burnable poison.

Table 2.1. Example 1: errors in the multiplication factor (Δk_{eff}) and nodal fission power.

Simulation	Number of power iterations	Δk_{eff} [pcm]	UO ₂ 1.8%	UO ₂ 3.1% + 16 b.p. rods
			Error in \bar{P}_{fiss} (%)	Error in \bar{P}_{fiss} (%)
No rehom. (a)	8	-403	0.55 (0.68, 0.53)	-0.48 (-0.49, -0.49)
Ref. $\delta\Sigma_G^{\text{spec}}$ (b)	8	-373	0.03 (0.37, -0.04)	-0.02 (-0.26, 0.04)
Spectr. rehom. - Cheb. (c)	15	-369	-0.02 (0.37, -0.09)	0.01 (-0.26, 0.09)
Spectr. rehom. - POD (d)	22	-369	-0.01 (0.36, -0.09)	0.01 (-0.26, 0.08)

Table 2.2. Example 1: errors in the nodal cross sections of the assembly without Pyrex rods.

UO ₂ 1.8%	$\Sigma_{a,1}$	$\Sigma_{a,2}$	$\nu\Sigma_{f,1}$	$\nu\Sigma_{f,2}$	$\Sigma_{t,1}$	$\Sigma_{t,2}$	$\Sigma_{s,1\rightarrow 1}$	$\Sigma_{s,1\rightarrow 2}$	$\Sigma_{s,2\rightarrow 2}$
Reference [cm ⁻¹]	0.00858	0.0621	0.00485	0.0825	0.539	1.310	0.513	0.0179	1.246
Simulation	Errors (%)								
No rehom. (a)	-0.25	0.73	0.40	0.82	-0.25	0.27	-0.27	0.13	0.25
Ref. $\delta\Sigma_G^{\text{spec}}$ (b)	0.04	0.17	0.14	0.24	0.0	-0.05	0.0	-0.03	-0.06
Spectr. rehom. - Cheb. (c)	0.06	0.11	0.15	0.17	-0.01	-0.07	-0.01	-0.04	-0.08
Spectr. rehom. - POD (d)	0.0	0.10	0.14	0.17	0.0	-0.08	0.0	-0.05	-0.09

to the other cross sections by defining its zeroth-order variational coefficient:

$$h_{V,D,G,i,0} = \int_0^1 du D_G^\infty(u) Q_{G,i}(u). \quad (2.27)$$

Table 2.3. Example 1: errors in the nodal cross sections of the assembly with Pyrex rods.

UO ₂ 3.1% + 16 b.p. rods	$\Sigma_{a,1}$	$\Sigma_{a,2}$	$\nu\Sigma_{f,1}$	$\nu\Sigma_{f,2}$	$\Sigma_{t,1}$	$\Sigma_{t,2}$	$\Sigma_{s,1\rightarrow 1}$	$\Sigma_{s,1\rightarrow 2}$	$\Sigma_{s,2\rightarrow 2}$
Reference [cm ⁻¹]	0.00997	0.09777	0.00660	0.1333	0.526	1.297	0.4997	0.016	1.198
Simulation	Errors (%)								
No rehom. (<i>a</i>)	0.27	-0.49	-0.22	-1.11	0.26	-0.49	0.27	-0.17	-0.50
Ref. $\delta\Sigma_G^{\text{spec}}$ (<i>b</i>)	-0.02	0.33	-0.11	-0.21	0.0	0.0	0.0	0.0	-0.02
Spectr. rehom. - Cheb. (<i>c</i>)	-0.03	0.33	-0.10	-0.21	0.0	0.0	0.0	0.05	-0.02
Spectr. rehom. - POD (<i>d</i>)	0.01	0.34	-0.09	-0.20	0.0	0.02	0.0	0.06	0.0

Hence, the following relation holds for δD_G :

$$\delta D_G = \frac{1}{\Phi_G} \sum_{i=1}^{N_{Q_G}} \alpha_{G,i} h_{V,D,G,i,0} \cdot \quad (2.28)$$

We consider as example the calculation with the reference spectral corrections (calculation *b*). In the version of SERPENT used in this thesis, the CMM can only be applied when the homogenized region covers the entire geometry. We therefore repeat the simulation with the outflow transport approximation (Choi et al., 2015) for the calculation of the diffusion coefficients. In this way, a comparison between the environmental and infinite-medium values is possible. For this option, Table 2.4 reports the main results of the simulations with (*e*) the reference corrections on the cross sections and the infinite-medium values of the diffusion coefficients, and (*f*) the reference corrections on the cross sections and diffusion coefficients. In calculation *f*, the correction δD_G is also computed with Eq. (2.25).

Table 2.4. Example 1: impact of diffusion-coefficient rehomogenization. The errors in the nodal power ($\Delta\bar{P}_{\text{fiss}}$) and diffusion coefficients (ΔD_G) are expressed in percentage.

Simulation	Δk_{eff} [pcm]	UO ₂ 1.8%				UO ₂ 3.1% + 16 b.p. rods		
		$\Delta\bar{P}_{\text{fiss}}$	ΔD_1	ΔD_2	$\Delta\bar{P}_{\text{fiss}}$	ΔD_1	ΔD_2	
Ref. $\delta\Sigma_G^{\text{spec}}$ (<i>e</i>)	-376	0.42 (0.52, 0.40)	0.29	-0.48	-0.37 (-0.37, -0.37)	-0.28	0.72	
Ref. $\delta\Sigma_G^{\text{spec}}$ and δD_G^{spec} (<i>f</i>)	-376	0.42 (0.52, 0.41)	-0.05	0.03	-0.37 (-0.37, -0.37)	0.05	-0.02	

Rehomogenization with the reference spectrum variation nullifies the errors in the diffusion coefficients. However, the δD_G corrections have clearly no impact on the integral parameters. This is due to the fact that they are not large enough to bring about appreciable changes in the neutron flux distribution. Such consideration can be justified as follows. If Tables 2.1 (calculation *b*) and 2.4 (calculation *e*) are compared, it appears that the outflow transport approximation produces a significant variation in the error in the thermal power with respect to the CMM. Since the other input parameters of the nodal calculation are unchanged, this variation is only caused by the differences between the values of D_G computed with the two approaches, which

are quite large. For instance, in the assembly with Pyrex rods the fast-group diffusion coefficient from the outflow-transport approximation is 6.2% higher than the one from the CMM, whereas the thermal-group value is nearly 10% lower. On the other hand, the corrections δD_G computed by rehomogenization are much smaller: -0.33% ($G = 1$) and 0.51% ($G = 2$) in the 1.8%-enriched assembly; 0.33% ($G = 1$) and -0.73% ($G = 2$) in the 3.1%-enriched one. The errors in the integral parameters are thus unaffected. This feature has been systematically observed also in the other benchmark problems. It can be concluded that diffusion-coefficient rehomogenization does not bring any substantial benefit to the accuracy of the nodal calculation.

2.3.2.2 Example 2 - UO₂ colorset with AIC-type control rods

The second colorset is made of four 17×17 UO₂ bundles (Fig. 2.9). The ²³⁵U enrichment is uniform (1.8% in all fuel pins). Two clusters of twenty-four black control rods each are inserted into two of the four bundles. The type of the control elements is AIC (silver-indium-cadmium), with the following mass percent composition: 80% ⁴⁷Ag, 15% ⁴⁸Cd, and 5% ⁴⁹In. No boron is present in the moderator ($C_{B_{10}} = 0$ ppm). The reference multiplication factor is 0.98860, and the reference values of the fission power are 1.22 in the unrodded assembly and 0.78 in the rodded one.

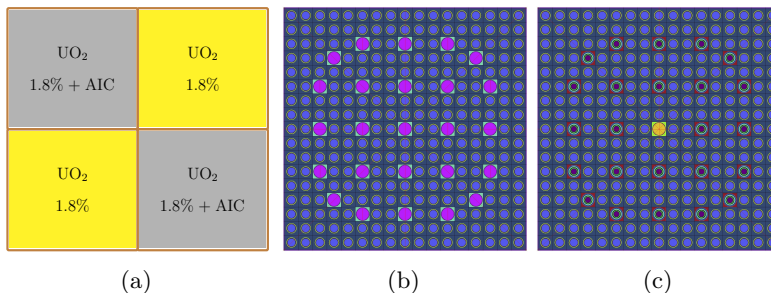


Fig. 2.9. (a) Assembly set of example 2. Layout of the UO₂ fuel assemblies: (b) unrodded, and (c) rodded. The former hosts 24 guide tubes and an instrumentation tube in the center, all of which are empty. In the latter, only the central instrumentation tube is free of control elements.

We now aim to build a set of snapshots representative of the spectral effects induced by control elements and, for the sake of generality, different enrichment. We therefore parameterize the variation in the flux spectrum using three variables:

- the fuel enrichment, which is homogeneously sampled in the interval [2.1%, 3.6%] for both the rodded and unrodded assemblies (20 combinations are selected);
- the number of control rods inserted in each heterogeneous fuel bundle (4, 8, 12, 16, 24, and 28), which is changed keeping the symmetry in the assembly layout;

- the type of control rods (AIC and B₄C).

A total number of 240 snapshots are computed. In order to verify whether the POD approach can accurately predict the spectrum deformation in unseen problems (i.e., problems whose solution was not included in the snapshot array), rehomogenization is also applied with the set of modes determined for example 1. In the analysis, we refer to the nodal simulations with the POD modes of examples 1 and 2 as $d1$ and $d2$, respectively.

The spectrum deformation computed by rehomogenization is reported in Fig. 2.10.

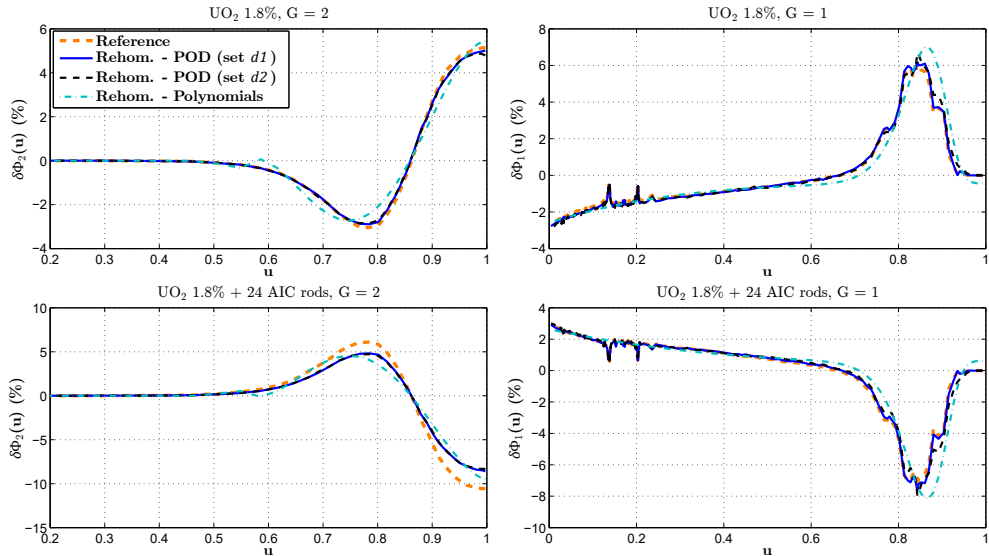


Fig. 2.10. Example 2: spectrum variation per unit u computed by rehomogenization.

With the three calculations, the magnitude of the thermal-group spectrum variation is underestimated in the rodded assembly. This result can be explained as follows. In the rodded assembly, the reference spectral correction $\delta\Sigma_{a,2}^{\text{spec,ref}}$ [Eq.(2.25)] is 0.59% of the infinite-medium cross section $\Sigma_{a,2}^{\infty}$. However, the global cross-section variation $\delta\Sigma_{a,2}^{\text{tot,ref}}$ (computed as the relative difference between the cross section condensed and homogenized in the colorset environment and $\Sigma_{a,2}^{\infty}$) is -0.71%. This means that the reference spatial correction $\delta\Sigma_{a,2}^{\text{spat,ref}}$ must go in the opposite direction of the spectral one and constitutes a significant part of the homogenization defect. Under the hypothesis of full separability of the two corrections (i.e., no cross term), it would be $\delta\Sigma_{a,2}^{\text{spat,ref}} \approx -1.31\%$. Since the thermalizing effect of the spatial term is not taken into account by spectral rehomogenization, the method predicts a harder spectrum (that is, it underestimates the magnitude of $\delta\Phi_2(u)$ as previously highlighted). In the

2. Modal synthesis of neutron spectrum changes

unrodded assembly, $\delta\Sigma_{a,2}^{\text{spec,ref}}$ is -0.37% of $\Sigma_{a,2}^{\infty}$, whereas the global variation $\delta\Sigma_{a,2}^{\text{tot,ref}}$ is -0.56%. Hence, the spatial correction is $\delta\Sigma_{a,2}^{\text{spat,ref}} \approx -0.19\%$. Since in this case the mismatch between the spectral and spatial corrections is significantly smaller, the differences between the simulated and reference curves are less evident.

The errors in the integral parameters and nodal cross sections are reported in Tables 2.5, 2.6 and 2.7.

Table 2.5. Example 2: errors in the multiplication factor and nodal fission power.

Simulation	Number of power iterations	Δk_{eff} [pcm]	UO ₂ 1.8%	UO ₂ 1.8% + 24 AIC rods
			Error in \bar{P}_{fiss} (%)	Error in \bar{P}_{fiss} (%)
No rehom. (a)	10	58	3.03 (0.98, 3.41)	-4.70 (-1.17, -5.61)
Ref. $\delta\Sigma_G^{\text{spec}}$ (b)	10	-486	1.14 (0.47, 1.28)	-1.77 (-0.56, -2.10)
Spectr. rehom. - Cheb. (c)	17	-513	1.25 (0.73, 1.36)	-1.94 (-0.87, -2.24)
Spectr. rehom. - POD (d1)	25	-543	1.14 (0.60, 1.25)	-1.77 (-0.71, -2.06)
Spectr. rehom. - POD (d2)	20	-524	1.16 (0.50, 1.29)	-1.80 (-0.60, -2.13)

Table 2.6. Example 2: errors in the nodal cross sections of the unrodded assembly.

UO ₂ 1.8%	$\Sigma_{a,1}$	$\Sigma_{a,2}$	$\nu\Sigma_{f,1}$	$\nu\Sigma_{f,2}$	$\Sigma_{t,1}$	$\Sigma_{t,2}$	$\Sigma_{s,1\rightarrow 1}$	$\Sigma_{s,1\rightarrow 2}$	$\Sigma_{s,2\rightarrow 2}$
Reference [cm ⁻¹]	0.00827	0.0557	0.00485	0.0837	0.534	1.313	0.509	0.0174	1.256
Simulation	Errors (%)								
No rehom. (a)	1.61	0.56	0.51	0.60	0.68	0.16	0.56	3.80	0.14
Ref. $\delta\Sigma_G^{\text{spec}}$ (b)	0.05	0.20	-0.12	0.23	-0.02	-0.05	-0.02	-0.07	-0.06
Spectr. rehom. - Cheb. (c)	-0.53	0.21	0.05	0.24	-0.14	-0.04	-0.13	-0.23	-0.05
Spectr. rehom. - POD (d1)	-0.08	0.21	-0.07	0.24	-0.08	-0.04	-0.07	-0.38	-0.05
Spectr. rehom. - POD (d2)	-0.04	0.20	-0.14	0.24	-0.06	-0.04	-0.05	-0.29	-0.06

Table 2.7. Example 2: errors in the nodal cross sections of the rodded assembly.

UO ₂ 1.8% + 24 AIC rods	$\Sigma_{a,1}$	$\Sigma_{a,2}$	$\nu\Sigma_{f,1}$	$\nu\Sigma_{f,2}$	$\Sigma_{t,1}$	$\Sigma_{t,2}$	$\Sigma_{s,1\rightarrow 1}$	$\Sigma_{s,1\rightarrow 2}$	$\Sigma_{s,2\rightarrow 2}$
Reference [cm ⁻¹]	0.0116	0.0817	0.00474	0.0853	0.534	1.286	0.507	0.0153	1.203
Simulation	Errors (%)								
No rehom. (a)	-1.71	0.71	-0.64	-0.93	-0.80	-0.38	-0.66	-4.77	-0.46
Ref. $\delta\Sigma_G^{\text{spec}}$ (b)	0.60	1.28	0.19	-0.12	0.02	0.05	0.0	0.01	-0.04
Spectr. rehom. - Cheb. (c)	1.02	1.15	-0.09	-0.30	0.13	-0.05	0.12	-0.17	-0.14
Spectr. rehom. - POD (d1)	0.66	1.15	0.0	-0.30	0.08	-0.05	0.07	0.07	-0.13
Spectr. rehom. - POD (d2)	0.58	1.15	0.10	-0.30	0.04	-0.05	0.03	-0.06	-0.13

The unexpectedly small error in k_{eff} of the standard calculation (calculation *a*) is the result of fortuitous error compensation as evidenced by the high deviations in the nodal power. This error cancellation vanishes when spectral rehomogenization is applied. The simulation with the reference corrections is well reproduced by the calculations with the rehomogenized cross sections. It still exhibits a somewhat high

error in the multiplication factor and thermal power, which confirms the need for spatial rehomogenization to fully take into account the environmental effects. We found that when applying the POD-based spectral rehomogenization (calculation *d2*) to the cross sections rehomogenized with the reference spatial corrections, the error in k_{eff} drops from -524 pcm to -3 pcm. In the rodded assembly, the error in $\Sigma_{a,2}$ increases when the reference $\delta\Sigma_{a,2}$ is added to the infinite-medium value (calculation *b*). This is also due to the exclusion of spatial effects (see Chapter 5 for more details). Fast-absorption corrections are overestimated with Chebyshev polynomials. This is because the polynomial basis functions do not capture the resonance peaks in the epithermal region (for $u_1 \in [0.05, 0.25]$, namely, $E \in [1.5 \text{ eV}, 46 \text{ eV}]$), where the magnitude of the reference curve is moderately overestimated. Since the fine-group absorption cross sections are considerably high in proximity of the resonance energies, an overestimated $\delta\Sigma_{a,1}$ is found in the rodded assembly (the opposite occurs in the unrodded one). In the framework of the POD analysis, the modes computed for example 1 approximate the spectrum perturbation about as accurately as those computed *ad hoc* for rodded configurations.

In this test case, the gap between the two modal approaches in terms of additional non-linear iterations is much less substantial.

2.3.2.3 Example 3 - UO₂/MOX colorset

The third colorset, which is shown in Fig. 2.11, consists of two 18×18 UO₂ assemblies and two 18×18 MOX assemblies. The UO₂ assemblies have 2.1% enrichment. The MOX bundle contains three different types of fuel pins: with low Pu content (1.78% ²³⁹Pu, 0.22% ²³⁵U) at the assembly corners, with intermediate Pu content (2.53% ²³⁹Pu, 0.21% ²³⁵U) along the assembly outer edges, and with high Pu content (3.86% ²³⁹Pu, 0.20% ²³⁵U) in the remainder of the fuel bundle. The concentration of diluted boron in the moderator is 2907 ppm. The reference multiplication factor is 1.00194, and the reference values of the nodal fission power are 0.86 in the UO₂ assembly and 1.14 in the MOX assembly.

Semi-analytic rehomogenization is applied with four (calculation *c1*) and seven (calculation *c2*) modes in the fast group. In the latter case, the fission spectrum and Chebyshev polynomials of order 1 to 6 are used. The POD-based rehomogenization is applied making use of three sets of basis functions:

- the POD modes computed for example 1 (set *d1*);
- the POD modes obtained from a multiparameter analysis of the present configuration (set *d2*);
- the POD modes obtained assembling all the snapshots computed for the three benchmark problems investigated in this chapter (set *d3*).

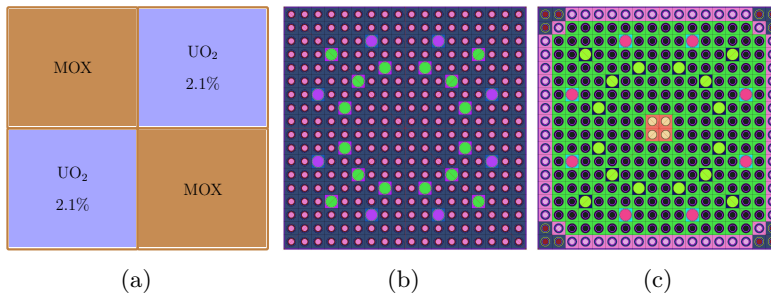


Fig. 2.11. (a) Assembly set of example 3. Layout of the (b) UO₂ and (c) MOX fuel assemblies. The MOX assembly is made of three fuel-pin types differing in plutonium content and ²³⁵U enrichment and hosts 4 water rods in the center.

We refer to the nodal simulations with these three sets of basis functions as $d1$, $d2$ and $d3$, respectively. The snapshots for the UO₂/MOX interface are generated following an approach similar to that of test cases 1 and 2, namely, considering the ²³⁵U enrichment and the Pu content in the three MOX-assembly pin types as parametric variables. The purpose of calculation $d3$ is to verify whether rehomogenization, applied with few modes, can still synthesize effectively the spectrum deformations of various assembly-interface types, that exhibit a considerably unlike behavior (especially in the fast range). This property of the POD modes is essential for the feasibility of the methodology at an industrial level, in which the use of modes not depending on the type of fuel assembly would be highly desirable.

Fig. 2.12 shows the fast-group spectrum variation in the UO₂ assembly computed with the set of modes $d1$. In this case, rehomogenization has been applied with the basis functions resulting from the SVD of high-order Legendre-polynomial best fits of the original snapshots. This strategy eliminates the noise caused by a different pattern of the spectrum change fine details in the two configurations, still preserving the global shape of the snapshots. Although the accuracy of the calculation is acceptable in the epithermal range, the method is not capable of recreating the bump observable at the end of the pseudolethargy domain (within $u_1 \in [0.87, 1.0]$, which corresponds to [2.2 MeV, 19.6 MeV]). This is expected, because the POD basis functions computed for the colorset with Pyrex rods have not been trained to reproduce such a localized, abruptly sign-changing feature of the spectrum deformation.

The spectrum variation computed with calculations $c1$, $c2$ and $d3$ is shown in Fig. 2.13. Since the results obtained with simulation $d2$ are almost identical to those of simulation $d3$, they are not reported for the sake of brevity. Rehomogenization with the set of modes $d3$ faithfully reproduces the bulge observed in the fast group. Such outcome can only be achieved with a proper *training* of the POD modes, that is, if solutions exhibiting this particular feature are included in the snapshot array. This can be deduced from Fig. 2.14a, which shows the fast-group POD basis functions

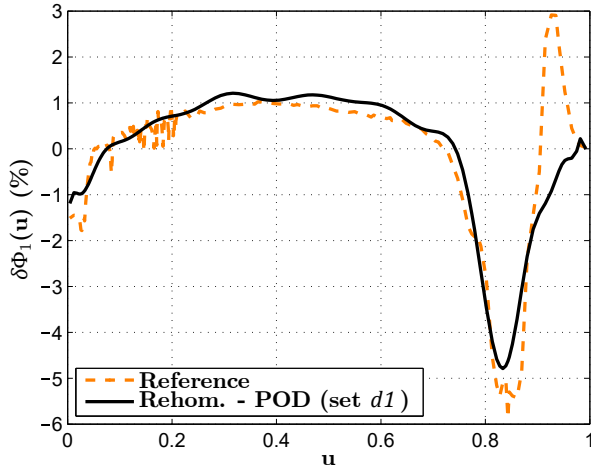


Fig. 2.12. Example 3: fast-group spectrum variation in the UO₂ assembly computed with the POD modes derived for example 1.

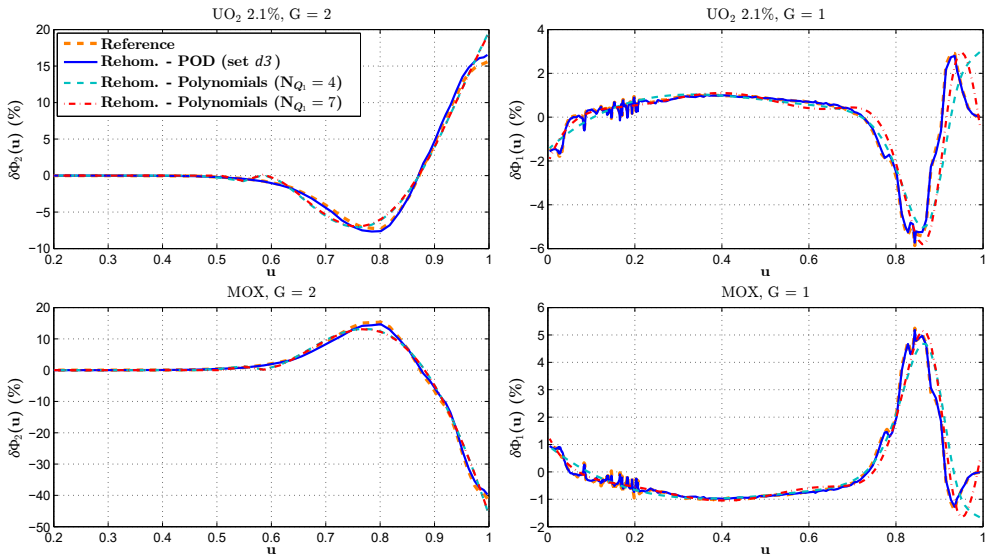


Fig. 2.13. Example 3: spectrum variation per unit u computed by rehomogenization.

computed from the snapshot set $d3$. Apparently, the shape of the high-energy bulge is retained by the second, third, and fourth modes. The second mode also inherits the step profile of $\delta\Phi_1(u)$ observed in the epithermal range (within $u_1 \in [0, 0.1]$, i.e., $E \in [0.625 \text{ eV}, 3.54 \text{ eV}]$) in both assemblies (see Fig. 2.13). The behavior of the singular

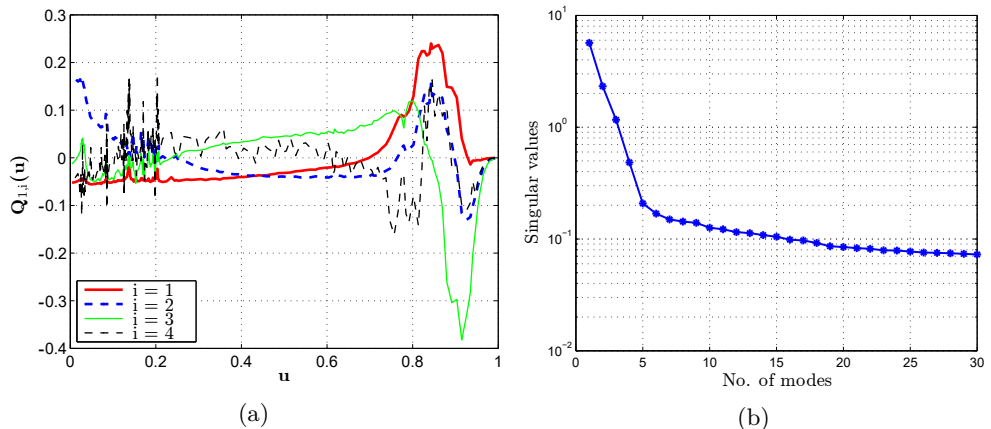


Fig. 2.14. (a) Fast-group POD modes computed by the SVD of the ensemble of snapshot sets built for examples 1, 2 and 3. (b) Singular values of the basis functions.

values of the computed modes is depicted in Fig. 2.14b. The first four basis functions have significantly higher singular values than the remaining ones. This suggests that they retain most of the information carried by the original snapshot set and that they are sufficient for an accurate reconstruction of the solution.

The polynomial-based rehomogenization with only four modes in the fast group cannot fit the steep bulge shape (Fig. 2.13). A significantly better prediction is achieved increasing the number of fast-group basis functions to seven.

The errors in the integral parameters and nodal cross sections are shown in Tables 2.8, 2.9 and 2.10. Also in this case, a limitation of the method due to the exclusion of spatial effects is apparent: in the MOX assembly, the error in $\nu\Sigma_{f,2}$ corrected with the reference $\delta\nu\Sigma_{f,2}$ increases compared to the infinite-medium value. The same occurs for fast fission in both assemblies and for thermal absorption in the MOX bundle. We verified that the errors in $\Sigma_{a,2}$ and $\nu\Sigma_{f,2}$ in the MOX assembly vanish when spectral rehomogenization is combined with the reference spatial cross-section corrections. The overestimation of $\delta\nu\Sigma_{f,1}$ in the two assemblies with calculation *c1* is caused by the inaccurate prediction of $\delta\Phi_1(u)$ at high energies. Because of the fast fissions of ^{238}U , the fine-group fission and production cross sections usually assume their highest values (if one does not consider the epithermal resonance spikes) at $u_1 > 0.8$ (that is, $E > 0.7$ MeV). Hence, the error in $\delta\Phi_1(u)$ at $u_1 \in [0.9, 1.0]$ ($E \in [4.0$ MeV, 19.6 MeV]) observed in Fig. 2.13 has more weight in the calculation of the few-group correction.

2.4 Discussion

This section addresses the following topics: the approximations in the derivation of the spectral rehomogenization algorithm (Section 2.4.1), the main numerical features

Table 2.8. Example 3: errors in the multiplication factor and nodal fission power.

Simulation	Number of power iterations	Δk_{eff} [pcm]	UO ₂ 2.1%	MOX
			Error in \bar{P}_{fiss} (%)	Error in \bar{P}_{fiss} (%)
No rehom. (<i>a</i>)	10	30	0.73 (0.26, 0.86)	-0.55 (-0.15, -0.71)
Ref. $\delta\Sigma_G^{\text{spec}}$ (<i>b</i>)	10	-7	-0.21 (0.53, -0.45)	0.15 (-0.30, 0.38)
Spectr. rehom. - Cheb. (<i>c1</i>)	19	21	-0.21 (0.92, -0.59)	0.16 (-0.53, 0.49)
Spectr. rehom. - Cheb. (<i>c2</i>)	17	24	-0.29 (0.53, -0.57)	0.21 (-0.31, 0.47)
Spectr. rehom. - POD (<i>d1</i>)	27	-18	-0.16 (0.31, -0.34)	-0.12 (-0.18, 0.28)
Spectr. rehom. - POD (<i>d3</i>)	22	-21	-0.25 (0.51, -0.50)	0.18 (-0.29, 0.42)

Table 2.9. Example 3: errors in the nodal cross sections of the UO₂ assembly.

UO ₂ 2.1%	$\Sigma_{a,1}$	$\Sigma_{a,2}$	$\nu\Sigma_{f,1}$	$\nu\Sigma_{f,2}$	$\Sigma_{t,1}$	$\Sigma_{t,2}$	$\Sigma_{s,1\rightarrow 1}$	$\Sigma_{s,1\rightarrow 2}$	$\Sigma_{s,2\rightarrow 2}$
Reference [cm ⁻¹]	0.00927	0.0894	0.00547	0.0979	0.534	1.302	0.508	0.0171	1.211
Simulation	Errors (%)								
No rehom. (<i>a</i>)	-0.61	1.12	0.07	1.27	-0.33	0.53	-0.37	1.18	0.50
Ref. $\delta\Sigma_G^{\text{spec}}$ (<i>b</i>)	0.11	0.18	0.35	0.30	0.01	0.01	0.01	-0.05	0.0
Spectr. rehom. - Cheb. (<i>c1</i>)	0.28	0.13	0.76	0.24	0.0	0.0	0.0	-0.1	-0.02
Spectr. rehom. - Cheb. (<i>c2</i>)	0.17	0.23	0.34	0.33	0.02	0.07	0.02	-0.08	0.06
Spectr. rehom. - POD (<i>d1</i>)	0.23	0.11	0.05	0.22	0.16	-0.03	0.16	0.24	-0.04
Spectr. rehom. - POD (<i>d3</i>)	0.05	0.12	0.31	0.24	0.0	-0.02	0.0	-0.10	-0.03

Table 2.10. Example 3: errors in the nodal cross sections of the MOX assembly.

MOX	$\Sigma_{a,1}$	$\Sigma_{a,2}$	$\nu\Sigma_{f,1}$	$\nu\Sigma_{f,2}$	$\Sigma_{t,1}$	$\Sigma_{t,2}$	$\Sigma_{s,1\rightarrow 1}$	$\Sigma_{s,1\rightarrow 2}$	$\Sigma_{s,2\rightarrow 2}$
Reference [cm ⁻¹]	0.0142	0.260	0.00990	0.375	0.526	1.517	0.498	0.0131	1.254
Simulation	Errors (%)								
No rehom. (<i>a</i>)	0.02	0.42	0.02	0.58	0.39	-0.64	0.43	-0.87	-0.90
Ref. $\delta\Sigma_G^{\text{spec}}$ (<i>b</i>)	-0.08	0.88	-0.25	1.08	-0.01	0.34	-0.01	0.04	0.23
Spectr. rehom. - Cheb. (<i>c1</i>)	-0.22	0.91	-0.47	1.13	0.0	0.26	0.0	0.20	0.13
Spectr. rehom. - Cheb. (<i>c2</i>)	-0.19	0.82	-0.30	1.04	-0.01	0.16	-0.01	0.20	0.03
Spectr. rehom. - POD (<i>d1</i>)	-0.24	0.81	-0.26	0.98	-0.10	0.30	-0.10	-0.02	0.20
Spectr. rehom. - POD (<i>d3</i>)	0.0	0.90	-0.25	1.11	0.0	0.30	0.0	0.08	0.17

of the method (Section 2.4.2), the comparison of the polynomial and POD approaches (Section 2.4.3), and the interplay between spectral rehomogenization and the critical-spectrum correction (Section 2.4.4).

2.4.1 Approximations in the formulation of the method

As mentioned in Section 2.2, the rehomogenization coefficients are computed with the infinite-medium, fine-group cross sections [Eq. (2.14)]. This is an approximation because Eqs. (2.5) and (2.7) are rigorously valid in the real environment, where the fine-energy cross sections may differ from the corresponding infinite-medium distributions. Deviations can exist due to (*i*) variations in the fuel, fission-product and

burnable-absorber isotopic concentrations N_i with respect to the infinite-medium depletion, and (ii) variations in the fine-group microscopic cross sections $\sigma_i(E)$. The latter are influenced by self-shielding effects in the heterogeneous arrangement of the fuel elements inside the assembly. In the core environment, the flux distribution obviously changes not only at the assembly level but also at the cell and fuel-pin levels, especially in the surroundings of the interface with a dissimilar region. Strong spatial perturbations in the spectrum inside the cell can cause variations in the ratio between the flux in the fuel rod and in the moderator. This results in a change in the resonance escape probability. In view of these considerations, a method has been developed to account for variations in the nuclide content N_i when computing the rehomogenization parameters. This method uses isotopic rehomogenization coefficients and is addressed in Chapter 4. In this section, we briefly investigate the impact of using the infinite-medium microscopic cross-section distributions in Eq. (2.14). We consider the UO_2/MOX colorset (example 3), in which the effects of within-cell flux distribution are expected to be more relevant due to the high flux gradient at the interface between these two types of assemblies. As shown in Fig. 2.15, in the MOX assembly, deviations up to 1.5% are found between the environmental and infinite-medium fine-group absorption cross sections in the thermal range and at the highest energies of the fast group. The nuclide densities are the same in the single-assembly and colorset calculations. The observed differences are therefore only due to the fine-group microscopic cross sections. The aforementioned deviations are comparable, in terms of magnitude, to the errors in the two-group single-assembly cross sections (Tables 2.9 and 2.10).

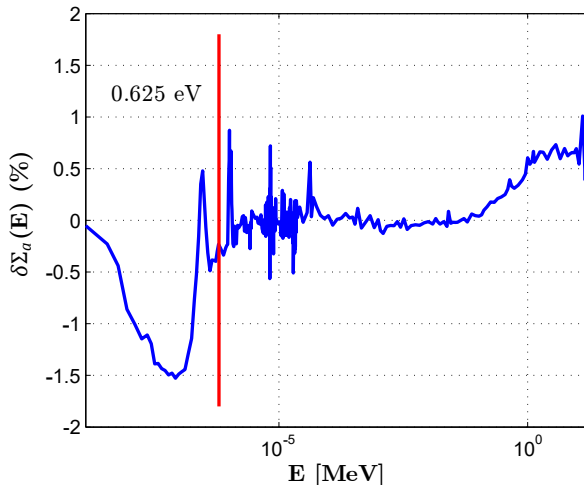


Fig. 2.15. Example 3: variation in the absorption cross-section energy distribution in the MOX assembly between the environmental and infinite-medium conditions.

Table 2.11 shows the results of the calculations with POD-based rehomogenization in which the $h_{R,x,G,j}$ and $h_{V,x,G,i,j}$ parameters (other than the $h_{V,x,G,i,0}$ coefficients) of Eq. (2.14) have been computed with the environmental and single-assembly fine-group cross sections.

Table 2.11. Example 3: application of the POD-based spectral rehomogenization with the infinite-medium and environmental rehomogenization coefficients. The latter are computed with the colorset fine-group cross sections. The errors Δ in the two-group cross sections (b) are expressed in percentage.

		UO ₂ 2.1%	MOX
Simulation	Δk_{eff} [pcm]	$\Delta \bar{P}_{\text{fiss}}$ (%)	$\Delta \bar{P}_{\text{fiss}}$ (%)
h_R, h_V from $\Sigma_{x,G}^\infty(u)$	-21	-0.25 (0.51, -0.50)	0.18 (-0.29, 0.42)
h_R, h_V from $\Sigma_{x,G}^{\text{env}}(u)$	-39	-0.30 (0.48, -0.58)	0.23 (-0.28, 0.48)

(a)

	UO ₂ 2.1%				MOX			
Simulation	$\Delta \Sigma_{a,1}$	$\Delta \Sigma_{a,2}$	$\Delta \nu \Sigma_{f,1}$	$\Delta \nu \Sigma_{f,2}$	$\Delta \Sigma_{a,1}$	$\Delta \Sigma_{a,2}$	$\Delta \nu \Sigma_{f,1}$	$\Delta \nu \Sigma_{f,2}$
h_R, h_V from $\Sigma_{x,G}^\infty(u)$	0.05	0.12	0.31	0.24	0.0	0.90	-0.25	1.11
h_R, h_V from $\Sigma_{x,G}^{\text{env}}(u)$	0.20	0.14	0.41	0.25	0.29	0.85	-0.12	1.04

(b)

The differences in the nodal cross sections between the two simulations are negligible in the thermal range and small in the fast one. They mostly affect fast-group absorption. The deviations in the integral parameters are also not relevant. This result is because variations in the fine-group microscopic cross sections are considerably smaller than variations in the condensation spectrum, which have a larger effect. A similar outcome has been found in the remaining test cases considered in this chapter. Hence, it may be concluded that the use of the infinite-lattice $\sigma_i(E)$ distributions in the calculation of the $h_{R,x,G,j}$ and $h_{V,x,G,i,j}$ coefficients (with $j \neq 0$) does not affect the performance of the method. We remark that, according to the derivation presented in Gamarino et al. (2016), it is mathematically consistent to use the infinite-medium distributions in Eq (2.15) (i.e., for $j = 0$).

Another approximation of the method is that the cross-section corrections are averaged over the node, whereas in reality the magnitude of spectral effects is significantly higher at the interfaces with neighbor assemblies. For the UO₂/MOX interface of example 3, Fig. 2.16 shows the reference spectrum variation (per unit of standard lethargy) in the UO₂ bundle quarter as a function of the distance from the assembly outer edge. The magnitude of the node-averaged perturbation corresponds to that observed approximately 3 centimeters away from the assembly border (that is, within the third inboard row of fuel cells). The strong spatial gradient in the spectrum change

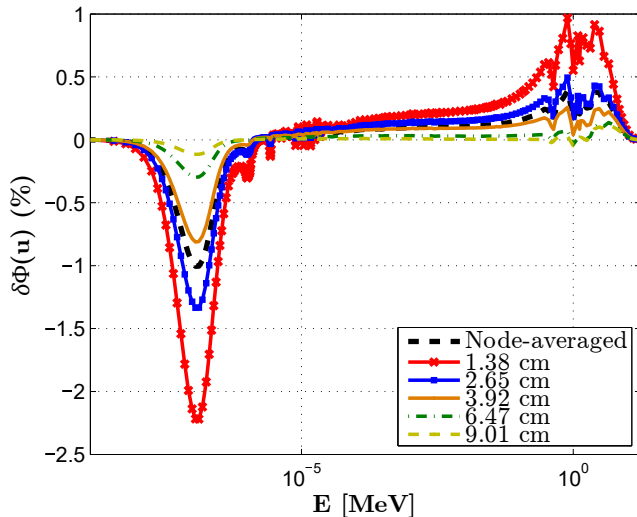


Fig. 2.16. UO₂/MOX interface: spectrum perturbation (per unit of standard lethargy $u = \ln(E_0/E)$, with $E_0 = 10$ MeV) in the UO₂ bundle quarter as a function of the distance from the assembly outer edge. The percent variation is referred to the assembly-averaged total (i.e., one-group) flux.

suggests that mixed space-energy terms (currently neglected by the method) can be important and should be modeled.

As a final remark, this rehomogenization approach does not correct the few-group discontinuity factors, which depend by definition on heterogeneous spatial form functions (Section 1.1.2.2). Since our approach relies on assembly-averaged distributions, a rigorous way has not been found so far to determine a spectral correction on this kind of homogenization parameter. However, a correction on the discontinuity factors is computed by the spatial rehomogenization method that has been developed in parallel to the spectral one (Chapter 5).

2.4.2 Numerical features and computational efficiency

In order to dampen numerical oscillations observed with Galerkin projection, an under-relaxation factor θ has been introduced for the spectrum variation. Hence, at each rehomogenization update m , the computed expansion coefficients $\alpha_{G,i}^m$ are corrected as follows:

$$\alpha_{G,i}^{m'} = \theta \alpha_{G,i}^m + (1 - \theta) \alpha_{G,i}^{(m-1)'}, \quad (2.29)$$

where $\alpha_{G,i}^{(m-1)'}$ is the estimate from the previous iteration. An optimal under-relaxation factor $\theta = 0.5$ has been found. Eq. (2.29) demands to store the coefficients $\alpha_{G,i}$ for each node of the computational domain. This is the only significant memory requirement

of the method at the on-line calculation level.

As shown in Section 2.3.2, in the case with no thermal-hydraulics feedback and when the reference leakage energy distribution is used, rehomogenization produces an increase in the number of non-linear iterations by a factor between 1.7 and 1.9 with the polynomial synthesis, and between 2 and 2.8 with the POD approach. The computational efficiency of the method is discussed more thoroughly in Chapter 3, which presents its final implementation (i.e., with a model for the neutron leakage spectrum).

The memory requirement for the storage of the h_R and h_V coefficients in the cross-section libraries can be easily quantified. We consider $\chi(u) = 0$ along the whole thermal-group energy domain (which trivially results in $\chi_{2,j} = 0, \forall j$), and we define the removal coefficients $h_{R,r,G,j} = h_{R,t,G,j} - h_{R,s,G \rightarrow G,j}$ and $h_{V,r,G,i,j} = h_{V,t,G,i,j} - h_{V,s,G \rightarrow G,i,j}$. With this choice, for a generic point in the state-parameter space, the total number of rehomogenization entries to be tabulated is given by $\sum_{G=1}^{N_G} (2N_{Q_G}^2 + 7N_{Q_G}) + N_{Q_1} + N_G$. In a two-group framework and using four basis functions in each coarse group ($N_{Q_G} = 4$), this translates into 126 coefficients. In order to limit the library growth, a method has been developed to store the rehomogenization parameters only as a function of the burn-up, the fuel temperature and the moderator temperature. This method consists of an on-the-fly update to account for the differences between the local values of the remaining state parameters (the moderator density and the soluble-boron and xenon concentrations) and the predetermined table-point values at which the spectral coefficients are computed. This method is described in Section 4.4.6.

2.4.3 Comparison of the polynomial and POD approaches

The results presented in Section 2.3.2 showed that the POD modes reconstruct the reference spectrum variation very accurately. Because of their capability of inheriting properties of the snapshots, they can faithfully reproduce the details of the transport solution, such as resonance-absorption spikes in the epithermal region. In the thermal group, the spectrum perturbation is a smooth function and has a weak dependence on the type of spectral interface, as well as on the local physical conditions (Gamarino et al., 2017). As a result, the thermal POD modes computed with a limited set of snapshots (namely, for a few test cases) can be easily generalized to other core configurations, even if samples of their solutions have not been included in the snapshot array. On the other hand, in the fast group the spectrum deformation strongly depends on the type of assembly interface and, as it will be clearer in Section 3.3.1.5, on the burn-up. The POD basis functions have to be trained to capture a number of components of $\delta\Phi_1(u)$. The accuracy of fast-group rehomogenization with POD is therefore tied to an extensive sampling of heterogeneous assembly configurations and fuel evolutions.

Polynomial modes can only fit the global behavior of the spectrum change. When local (energy-wise), strongly varying components are present (such as at a UO₂/MOX interface), they fail to reconstruct satisfactorily the shape of the perturbation in the

fast group. The use of more polynomial basis functions in this energy range can attenuate such deficiency. However, in some test cases this option has been found to cause unphysical oscillations in the $\delta\Phi$ -solution when leakage form functions other than the reference one are used. Limiting the number of modes to four is thus advisable. In all the benchmark problems examined in Section 2.3.2, the nodal calculation with POD-based rehomogenization converges more slowly than that with the polynomial approach.

Another feature of interest of the comparison between the two strategies is the conditioning of the spectral rehomogenization problem. For the simulations of example 1, Table 2.12 reports the condition number C_A of the solving matrices corresponding to the two assemblies. The problem formulated with the POD modes is significantly better conditioned thanks to their orthonormality properties. In order to avoid numerical instabilities, the polynomial basis functions should be orthonormalized by the stabilized Gram-Schmidt process (Golub and Van Loan, 2012). With this transformation, the corresponding rehomogenization linear system has a condition number of the same order of magnitude as that achieved with the POD operators.

Table 2.12. Example 1: condition number of the assembly-rehomogenization linear system.

	UO ₂ 1.8%	UO ₂ 3.1% + 16 b.p. rods
Modal approach		C_A
Chebyshev	437792	439739
POD	91	96
Chebyshev (Gram-Schmidt)	324	341

In this work, we have limited our analysis on the POD approach to the calculation of sets of modes for a few relevant configurations. In order to exploit the POD-based rehomogenization at an industrial level, one has to find a set of proper orthonormal basis functions effectively usable for several types of assembly interfaces. The number of snapshots fixes the computational burden of the POD off-line phase and, on the other hand, limits the achievable knowledge of the spectrum-change components. An effective sampling strategy must thus be developed to (i) reduce the amount of costly off-line computations and (ii) to boost the capability of the POD basis to reproduce the solution of problems not included in the snapshot set. In Gamarino et al. (2017), it was illustrated that some helpful insight into the snapshot selection process can be given by the analysis of the singular values of the snapshot matrices A_1 and A_2 [Eq. (2.24)]. We believe that the search of a more general set of modes can be tackled by combining an adaptive approach for the retention of snapshots (based on the singular-value decreasing importance) with a suitable numerical technique for the representation of high-dimensional functions, such as sparse grids (Bungartz and Griebel, 2004).

2.4.4 Relation with the critical-spectrum correction

In this section, an analysis is made on the interplay between spectral rehomogenization and another type of spectral cross-section correction: the critical-buckling (B_{crit}^2) correction.

In single-assembly transport calculations, it is common practice to adjust the neutron leakage rate in the homogenized assembly to enforce a multiplication factor equal to unity (Hebert, 2009). In this way, the fine-energy cross sections are collapsed with a more realistic spectrum, i.e., a spectrum closer to that of the critical core. Criticality is achieved adding an artificial leakage cross section $\Sigma_{\text{leak},g}$ to the fine-group absorption cross section. This additional cross section is defined as

$$\Sigma_{\text{leak},g} = D_g B_{\text{crit}}^2, \quad (2.30)$$

where D_g is the leakage coefficient of group g and B_{crit}^2 is the critical buckling (i.e., the buckling coefficient B^2 fulfilling the condition $k_\infty = 1$). The calculation of B_{crit}^2 is based on the fundamental-mode assumption and is usually performed using a B_1 homogeneous method (Hebert, 2009). Refined approaches consider the space and energy dependence of the buckling coefficient (Benoist et al., 1994; Smith, 2017). Even if this type of correction is meant to reduce the spectral differences between the infinite medium and the core environment, it cannot reproduce in any way spectral effects caused by unlike neighbors. It is therefore of interest to verify whether or not a relation of complementarity exists between this kind of cross-section correction and the one computed by rehomogenization.

We consider a rodded configuration similar to that modeled in example 2 (Section 2.3.2.2), consisting of a UO_2 assembly with 1.8% enrichment next to a UO_2 assembly with 2.4% enrichment and 24 AIC-type control rods. In order to be consistent with the fundamental-buckling approach, we study the critical colorset configuration, achieved with a diluted-boron concentration of 222 ppm. We compare the results of the nodal calculations having the following cross-section inputs (we omit the subscript *crit* in B_{crit}^2 for the sake of lightness of the notation):

- infinite-medium cross sections without the B^2 correction (*a*);
- infinite-medium cross sections with the B^2 correction (*b*);
- cross sections rehomogenized by the $\delta\Sigma_G$ computed with the reference spectrum variation $\delta\Phi_G(u) = \Phi_{\text{env},G}(u) - \Phi_{\infty,G}(u)$ (*c*);
- cross sections rehomogenized by the $\delta\Sigma_G$ computed with the reference spectrum variation $\delta\Phi_G^{B^2}(u) = \Phi_{\text{env},G}(u) - \Phi_{\infty,G}^{B^2}(u)$ (*d*).

We have denoted with $\Phi_{\infty,G}(u)$ and $\Phi_{\infty,G}^{B^2}(u)$ the non-critical and critical (i.e., B^2 -corrected) infinite-medium spectra, respectively. The single-assembly and colorset

transport calculations for the present analysis are performed with the APOLLO2-A deterministic lattice transport code (Martinolli et al., 2010). This choice allows us to avoid the computational burden of a 281-group B_1 spectrum calculation in SERPENT. APOLLO2-A features two approaches for the calculation of the diffusion coefficient: the outflow transport approximation (Choi et al., 2015) and the B_1 method (Hebert, 2009). The former is the only available option when single-assembly calculations are performed without critical buckling and is therefore chosen for this analysis. If no B^2 correction is performed, the values of k_∞ in the unrodded and rodded assemblies are 1.16433 and 0.82913, respectively. Criticality is achieved with $B^2 = 0.002608 \text{ cm}^{-2}$ in the former and with $B^2 = -0.003083 \text{ cm}^{-2}$ in the latter.

Fig. 2.17 shows, for the unrodded assembly, the overall spectrum variation (per unit of standard lethargy) between the critical colorset environment and the critical and non-critical infinite lattices. The environmental and infinite-lattice spectra are normalized to unity.

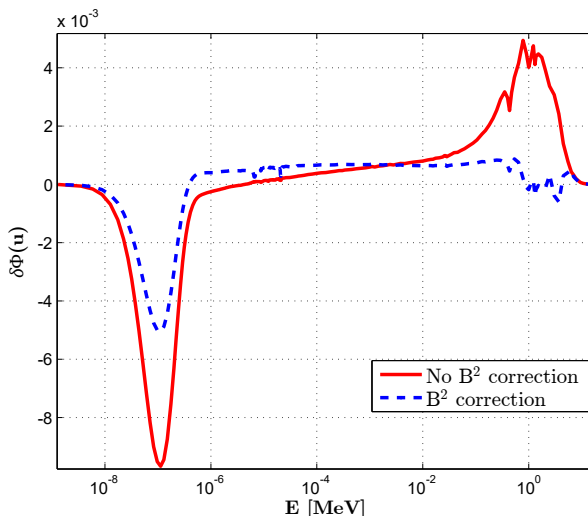


Fig. 2.17. Critical colorset UO_2 (1.8%-enriched) / UO_2 (2.4%-enriched) with 24 AIC control rods: difference in the spectrum of the unrodded assembly between the real environment and the critical (dashed line) and non-critical (solid line) infinite lattices. The neutron spectra [in units of neutrons/(square centimeters \cdot second)] are normalized to unity.

Clearly, the perturbation has lower magnitude when it is computed with respect to the buckling-corrected spectrum, especially at high energies. This can be explained by observing that given a positive value of B^2 (i.e., an outgoing neutron flow), the differences between the critical and non-critical infinite-medium spectra depend on two effects going in opposite directions: the higher leakage rate in the fast range (which tends to thermalize the spectrum), and the lower number of fast neutrons available for being scattered to thermal energies (which hardens the spectrum). The second effect

is preminent: with the B^2 correction, the spectral index in the unrodded assembly increases from 3.304 to 3.482. Since the environmental spectrum is hardened by the assembly with control rods, the spectrum variation is attenuated by the B^2 correction. Table 2.13 shows the errors in the integral parameters and nodal cross sections for calculations a , b , c , and d .

Table 2.13. Effect of the critical-spectrum correction on the nodal calculations without and with rehomogenization: errors in the (a) integral parameters and (b) nodal cross sections. The errors in the nodal power and cross sections are expressed in percentage. The power errors within parentheses correspond to the fast- and thermal-group power (in this order).

Simulation	Δk_{eff} [pcm]	UO ₂ 1.8%		UO ₂ 2.4% + 24 AIC rods	
		$\Delta \bar{P}_{\text{fiss}}$	$\Delta \bar{P}_{\text{fiss}}$	$\Delta \bar{P}_{\text{fiss}}$	$\Delta \bar{P}_{\text{fiss}}$
No rehom., no B^2 correction	-171	3.28 (1.34, 3.67)	-4.19 (-1.28, -5.02)		
No rehom., B^2 correction	-617	1.42 (0.48, 1.63)	-1.81 (-0.46, -2.23)		
Ref. $\delta \Sigma_G^{\text{spec}}$, no B^2 correction	-453	1.31 (0.49, 1.49)	-1.68 (-0.47, -2.04)		
Ref. $\delta \Sigma_G^{\text{spec}}$, B^2 correction	-458	1.27 (0.44, 1.45)	-1.61 (-0.42, -1.98)		

(a)

Simulation	UO ₂ 1.8%				UO ₂ 2.4% + 24 AIC rods			
	$\Delta \Sigma_{a,1}$	$\Delta \Sigma_{a,2}$	$\Delta \nu \Sigma_{f,1}$	$\Delta \nu \Sigma_{f,2}$	$\Delta \Sigma_{a,1}$	$\Delta \Sigma_{a,2}$	$\Delta \nu \Sigma_{f,1}$	$\Delta \nu \Sigma_{f,2}$
No rehom., no B^2 correction	1.06	0.77	0.66	0.85	-1.19	0.54	-0.93	-1.33
No rehom., B^2 correction	-0.72	0.66	0.11	0.72	1.31	0.63	0.10	-1.21
Ref. $\delta \Sigma_G^{\text{spec}}$, no B^2 correction	0.06	0.24	-0.05	0.29	0.30	1.43	0.05	-0.14
Ref. $\delta \Sigma_G^{\text{spec}}$, B^2 correction	0.06	0.21	0.12	0.26	0.34	1.45	-0.09	-0.11

(b)

Comparing simulations a and b , it appears that the B^2 correction significantly reduces the errors in the fast production and fast-to-thermal scattering cross sections, whereas it considerably overcorrects the fast absorption and total cross sections. Since thermal neutrons are much less leakage-prone, the correction has little influence on the thermal cross sections. The calculation with buckling exhibits significantly lower errors in the nodal power, but a much higher error in k_{eff} . The errors of calculations c and d are very close. The differences in the nodal cross sections between the two simulations (observable, for instance, in the error in fast fission) lie within the range of accuracy of the calculation. The same holds for the errors in k_{eff} and in the nodal power. This suggests that rehomogenization is not influenced by the fact that the infinite-medium cross sections are generated at conditions very far from criticality (16433 pcm off criticality in the unrodded assembly, -17087 pcm off criticality in the rodded one). The method can reproduce both neighbor effects (which cannot be modeled by the B^2 correction) and spectral effects due to different reactivity (i.e., different multiplicative properties) in the core environment and in the infinite lattice. Therefore, the two

corrections are not complementary.

Although the fundamental-buckling correction is widely adopted in the preparation of cross-section libraries, its application is notoriously not rigorous when simulating non-critical conditions, in which the neutron spectrum may differ from the critical one (Dall’Osso, 2015a,b; Demazière, 2016). These include reactor core transients and subcritical states during power outage. For example, Demazière (2016) showed that the use of B^2 -tweaked cross sections can have a large impact on the nodal simulation of transients strongly deviating from criticality. The results of our analysis demonstrate that spectral rehomogenization also carries out the task of the critical-spectrum correction, which can thus be discarded in the preparation of cross-section libraries. In this way, no bias is introduced in the simulation of non-critical conditions. One of the limitations in the cross-section model is therefore removed, with an advantage also in terms of the computational cost of the lattice calculation (namely, the absence of critical-spectrum iterations).

2.5 Summary

In this chapter, focus has been given to the definition of effective sets of basis and weighting functions for a modal reconstruction of the spectrum variation in the real environment. Both polynomial and POD-based strategies proved to be suitable candidates, with the latter synthesizing the spectrum perturbation to a higher degree of accuracy.

Spectral rehomogenization has been validated on multiassembly configurations typically encountered in PWR cores. The case without thermal feedback or fuel depletion has been considered. The rehomogenization algorithm can reproduce very accurately the spectral effects on nodal cross sections when the reference leakage energy distribution is used. Another benefit is that the B_1 critical-spectrum correction is no longer needed. A limitation of this approach is that it can only correct a part of the homogenization error. In order to fully capture core-environment effects, it cannot be decoupled from an effective spatial rehomogenization.

MODELING OF THE NEUTRON LEAKAGE SPECTRUM

3.1 Introduction

This chapter ¹ addresses the calculation of the neutron leakage spectral distribution. As mentioned in Section 2.2.1, this is the second pillar of spectral rehomogenization. The leakage rate in a fuel assembly is dominated by two factors (Hebert, 2009): scattering anisotropy and interassembly neutron exchange. The former has an important effect in PWRs due to the presence of hydrogen in the moderator and is usually taken into account via transport corrections (such as the consistent B_1 and P_1 approximations) at the lattice-calculation level. The latter depends inherently on the core environment. The inaccurate results achieved with a flat-leakage approximation (i.e., considering the leakage spectral distribution uniform and equal to the coarse-group nodal estimate) highlighted the importance of finding a realistic energy shape for streaming effects (Gamarino et al., 2018a). The aim of the work described in this chapter is therefore to develop a physically grounded model for the leakage spectrum. Two approaches are proposed and investigated. The first of these applies Fick's diffusion law to the node-averaged environmental spectra estimated by the rehomogenization algorithm. We refer to it as *diffusive* leakage model. The second uses the homogenized-assembly critical-leakage spectrum from the fundamental-mode B_1 calculation. The two strategies are tested on a wide range of heterogeneous PWR configurations, including those considered in Chapter 2. Both isothermal fresh-fuel conditions and configurations with fuel depletion are analyzed. Focus is given to the

¹Most of the content of this chapter has been published in *Annals of Nuclear Energy* **116**, 2018 (Gamarino et al., 2018b).

more promising diffusive approach.

This chapter is structured as follows. In Section 3.2 the diffusive and fundamental-mode leakage methods are described. Section 3.3 shows the numerical results of several PWR benchmark problems. In Section 3.4 we discuss various features of interest of the diffusive model. Concluding remarks follow in Section 3.5.

3.2 Theory

The leakage spectrum $L_{\text{env},G}(u)$ in Eq. (2.7) is expressed as

$$L_{\text{env},G}(u) = \bar{L}_G f_{L,G}(u), \quad (3.1)$$

where \bar{L}_G is the few-group node-averaged leakage and $f_{L,G}(u)$ is a form function describing the leakage energy dependence. The distribution $f_{L,G}(u)$ is normalized to unity so as to satisfy the condition

$$\int_0^1 du L_{\text{env},G}(u) = \bar{L}_G. \quad (3.2)$$

We define \bar{L}_G as

$$\bar{L}_G = \sum_{d=x,y,z} \frac{J_{G,d+} - J_{G,d-}}{\Delta d}, \quad (3.3)$$

where Δd is the node width along the coordinate axis d , while $J_{G,d+}$ and $J_{G,d-}$ are the surface-averaged directional net currents at the node boundaries $d+$ and $d-$. An estimate of these is available from the latest non-linear flux iteration. Using Eq. (3.1), Eq. (2.14a) becomes

$$c_{G,j} = \bar{L}_G h_{L,G,j}, \quad h_{L,G,j} = \int_0^1 du W_{G,j}(u) f_{L,G}(u). \quad (3.4)$$

In the following, we formulate $f_{L,G}(u)$ and $h_{L,G,j}$ for the two aforementioned leakage models.

3.2.1 The diffusive leakage method

We consider two adjacent nodes k and l separated by a surface ΔS along the generic direction x (Fig. 3.1). The two nodes have size Δx^k and Δx^l along x . We apply the discrete (in space) Fick's diffusion law to compute the spectral distribution of the neutron current $J_G^S(u)$ through the surface ΔS :

$$J_G^S(u) = -D_G^k(u) \frac{\Phi_{\text{env},G}^S(u) - \Phi_{\text{env},G}^{k_c}(u)}{\Delta x^k/2}, \quad (3.5)$$

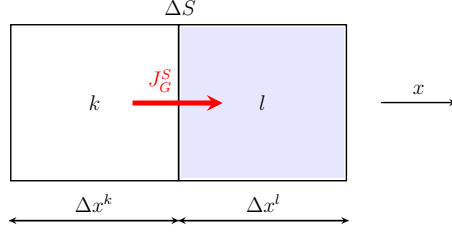


Fig. 3.1. One-dimensional layout of a generic nodal interface.

where $D_G^k(u)$ denotes the distribution in energy of the spatially averaged diffusion coefficient in node k , $\Phi_{\text{env},G}^S(u)$ is the environmental flux spectrum at the interface between the two facing nodes, and $\Phi_{\text{env},G}^{k_c}(u)$ is the environmental flux spectrum at the center of node k . A similar equation can be written for node l :

$$J_G^S(u) = -D_G^l(u) \frac{\Phi_{\text{env},G}^{l_c}(u) - \Phi_{\text{env},G}^S(u)}{\Delta x^l/2}. \quad (3.6)$$

We make the approximation that the spectrum at the center of a given node is equal to the node-averaged spectrum:

$$\Phi_{\text{env},G}^{m_c}(u) \approx \Phi_{\text{env},G}^m(u), \quad m = k, l. \quad (3.7)$$

The discrete formulation of Fick's law [Eqs. (3.5) and (3.6)] and Eq. (3.7) are based on a linear flux spatial distribution. This hypothesis is not consistent with the quartic polynomial expansion commonly adopted in advanced nodal codes. Because of the lack of information for a more rigorous spatial discretization of spectral distributions, we make the assumption that this approximation is acceptable within the range of accuracy of the proposed methodology.

As done for the cross-section distributions in Section 2.2.1, the dependence of the fine-energy diffusion coefficient on the environment is neglected:

$$D_G^m(u) \approx D_{G,\infty}^m(u), \quad m = k, l. \quad (3.8)$$

Continuity of the current distribution $J_G^S(u)$ is imposed by equating Eqs. (3.5) and (3.6). The following expression is found for the environmental spectrum at the surface ΔS :

$$\Phi_{\text{env},G}^S(u) = \frac{\tilde{D}_G^k(u)\Phi_{\text{env},G}^k(u) + \tilde{D}_G^l(u)\Phi_{\text{env},G}^l(u)}{\tilde{D}_G^k(u) + \tilde{D}_G^l(u)}, \quad (3.9)$$

where the quantity $\tilde{D}_G^m(u)$ reads

$$\tilde{D}_G^m(u) = \frac{2D_G^m(u)}{\Delta x^m}, \quad m = k, l. \quad (3.10)$$

3. Modeling of the neutron leakage spectrum

Substituting Eqs. (3.9) and (3.10) into Eq. (3.5) or Eq. (3.6) yields

$$J_G^S(u) = -\hat{D}_G^{k,l}(u)(\Phi_{\text{env},G}^l(u) - \Phi_{\text{env},G}^k(u)), \quad (3.11)$$

with the harmonic-averaged diffusion parameter $\hat{D}_G^{k,l}(u)$ defined as

$$\hat{D}_G^{k,l}(u) = \frac{\tilde{D}_G^k(u)\tilde{D}_G^l(u)}{\tilde{D}_G^k(u) + \tilde{D}_G^l(u)}. \quad (3.12)$$

We refer to $\hat{D}_G^{k,l}(u)$ as the fine-energy nodal-coupling diffusion coefficient.

Moving to a more general multi-dimensional framework, the node-averaged leakage spectrum for the homogenized region k is determined applying Eq. (3.11) to all the interfaces with the surrounding nodes:

$$L_{\text{env},G}^k(u) = \sum_{m=1}^{N_{nb}} \frac{\hat{D}_G^{k,m}(u)}{\Delta d^{k,m}} \left(\Phi_{\text{env},G}^k(u) - \Phi_{\text{env},G}^m(u) \right). \quad (3.13)$$

In Eq. (3.13), the superscript m cycles over the number of neighbor nodes N_{nb} , and $\Delta d^{k,m}$ is the width of node k along the direction perpendicular to the interface with node m . Combining Eqs. (3.1) and (3.13) yields the nodal leakage form function $f_{L,G}^k(u)$:

$$f_{L,G}^k(u) = \sum_{m=1}^{N_{nb}} w_G^{k,m} \frac{\hat{D}_G^{k,m}(u)}{\Delta d^{k,m}} \left(\Phi_{\text{env},G}^k(u) - \Phi_{\text{env},G}^m(u) \right). \quad (3.14)$$

The N_{nb} normalization constants $w_G^{k,m}$ in Eq. (3.14) are introduced to fulfill Eq. (3.2). They are computed imposing the preservation of the few-group leakage $L_G^{k,m}$ through each nodal interface:

$$\frac{w_G^{k,m}}{\Delta d^{k,m}} \int_0^1 du \hat{D}_G^{k,m}(u) \left(\Phi_{\text{env},G}^k(u) - \Phi_{\text{env},G}^m(u) \right) = \frac{L_G^{k,m}}{\bar{L}_G^k}, \quad (3.15)$$

where $L_G^{k,m}$ is defined in terms of the few-group surface-averaged net current $J_G^{k,m}$ (known from the nodal calculation) across the interface between the homogenized regions k and m :

$$L_G^{k,m} = \frac{J_G^{k,m}}{\Delta d^{k,m}}. \quad (3.16)$$

In Eq. (3.15), dividing by the node-averaged leakage \bar{L}_G^k is required to scale $f_{L,G}^k(u)$ to unity [see Eq. (3.2)]. After introducing Eqs. (2.8) and (2.10), Eq. (3.14) becomes

$$f_{L,G}^k(u) = \sum_{m=1}^{N_{nb}} w_G^{k,m} \frac{\hat{D}_G^{k,m}(u)}{\Delta d^{k,m}} \left[\bar{\Phi}_G^k \varphi_{\infty,G}^k(u) + \sum_{i=1}^{N_{Q_G}} \alpha_{G,i}^k Q_{G,i}(u) - \left(\bar{\Phi}_G^m \varphi_{\infty,G}^m(u) + \sum_{i=1}^{N_{Q_G}} \alpha_{G,i}^m Q_{G,i}(u) \right) \right]. \quad (3.17)$$

The projection of Eq. (3.17) over the weighting functions $W_{G,j}(u)$ (with $j = 1, \dots, N_{Q_G}$) results in the following expression for the j -th leakage rehomogenization coefficient of node k :

$$h_{L,G,j}^k = \sum_{m=1}^{N_{nb}} \frac{w_G^{k,m}}{\Delta d^{k,m}} \left[\bar{\Phi}_G^k h_{R,\hat{D},G,j}^{k*,m} + \sum_{i=1}^{N_{Q_G}} \alpha_{G,i}^k h_{V,\hat{D},G,i,j}^{k,m} - \left(\bar{\Phi}_G^m h_{R,\hat{D},G,j}^{k,m*} + \sum_{i=1}^{N_{Q_G}} \alpha_{G,i}^m h_{V,\hat{D},G,i,j}^{k,m} \right) \right]. \quad (3.18)$$

In Eq. (3.18), a new type of rehomogenization parameter has been introduced for the nodal-coupling diffusion coefficient:

$$h_{R,\hat{D},G,j}^{k*,m} = \int_0^1 du W_{G,j}(u) \hat{D}_G^{k,m}(u) \varphi_{\infty,G}^k(u), \quad (3.19a)$$

$$h_{R,\hat{D},G,j}^{k,m*} = \int_0^1 du W_{G,j}(u) \hat{D}_G^{k,m}(u) \varphi_{\infty,G}^m(u), \quad (3.19b)$$

$$h_{V,\hat{D},G,i,j}^{k,m} = \int_0^1 du W_{G,j}(u) \hat{D}_G^{k,m}(u) Q_{G,i}(u). \quad (3.19c)$$

The normalization condition of Eq. (3.15) results in the following expression for $w_G^{k,m}$:

$$w_G^{k,m} = \frac{J_G^{k,m} / \bar{L}_G^k}{\bar{\Phi}_G^k h_{R,\hat{D},G,0}^{k*,m} + \sum_{i=1}^{N_{Q_G}} \alpha_{G,i}^k h_{V,\hat{D},G,i,0}^{k,m} - \left(\bar{\Phi}_G^m h_{R,\hat{D},G,0}^{k,m*} + \sum_{i=1}^{N_{Q_G}} \alpha_{G,i}^m h_{V,\hat{D},G,i,0}^{k,m} \right)}, \quad (3.20)$$

where, as in Eq. (2.15), we have used the fact that $W_{G,0}(u)$ is equal to unity to define the rehomogenization coefficients for $j = 0$.

As observed in Eq. (3.19), the coefficients $h_{R,\hat{D}}$ and $h_{V,\hat{D}}$ for a certain node k are not uniquely defined. This is because they also depend on the reference collapsing spectrum $[\varphi_{\infty,G}^m(u)]$ and on the diffusion-coefficient distribution $[D_G^m(u)]$ in the adjacent node m . The information on the former is carried by the coefficient $h_{R,\hat{D},G,j}^{k,m*}$, whereas the information on the latter is present in the coefficients $h_{R,\hat{D},G,j}^{k*,m}$, $h_{R,\hat{D},G,j}^{k,m*}$ and $h_{V,\hat{D},G,i,j}^{k,m}$. For a given fuel assembly, these ‘‘mixed’’ rehomogenization parameters must be computed during the lattice calculation for each spectral interface (namely, for each dissimilar adjacent assembly). Nevertheless, information on the neighbor bundles is not easily achievable in the single-assembly simulation, because the lattice code has no knowledge of the bordering regions that the fuel assembly will encounter during its operating life in the reactor core. Although the cross-section generation procedure could be modified to add such a feature, this would demand to redefine

3. Modeling of the neutron leakage spectrum

the architecture of the lattice code. Moreover, the simulated unit assembly and its neighbor elements can experience different operating conditions and burn-up. Thus, the coefficients of Eq. (3.19) should be computed for several combinations of values of the state parameters in adjacent assemblies, with the fuel exposure being the most relevant quantity to be sampled. In the light of the complex assembly-shuffling strategies adopted in modern core designs, the growth of the cross-section libraries caused by the storage of the rehomogenization parameters for the nodal-coupling diffusion coefficient would be significant. In conclusion, the formulation of the diffusive leakage model presented above is not suitable for a practical integration into lattice-physics codes. In order to circumvent this difficulty, an alternative version of the method is proposed. This variant is based on the assumption that the diffusion-coefficient spectral distribution does not change significantly in two adjacent assemblies:

$$D_G^k(u) \approx D_G^m(u). \quad (3.21)$$

Under this approximation, Eq. (3.9) for the neutron spectrum at the surface ΔS reduces to

$$\Phi_{\text{env},G}^S(u) \approx \frac{\Phi_{\text{env},G}^k(u) + \Phi_{\text{env},G}^l(u)}{2}. \quad (3.22)$$

Furthermore, Eq. (3.11) can be rewritten as

$$J_G^S(u) \approx 2 \frac{D_G^k(u)}{\Delta x^k + \Delta x^l} \left(\Phi_{\text{env},G}^k(u) - \Phi_{\text{env},G}^l(u) \right). \quad (3.23)$$

Using Eq. (3.21) again, the following expression holds for $J_G^S(u)$:

$$J_G^S(u) \approx \frac{2}{\Delta x^k + \Delta x^l} \left(D_G^k(u) \Phi_{\text{env},G}^k(u) - D_G^l(u) \Phi_{\text{env},G}^l(u) \right). \quad (3.24)$$

The values of $J_G^S(u)$ computed for nodes k and l with Eq. (3.24) are equal and opposite. Hence, the continuity of the neutron-current spectrum at the interface ΔS is satisfied. We emphasize that, although the approximate definition of Eq. (3.24) has not a rigorous foundation, it is justified by the observation that $D_G(u)$ almost does not vary with the assembly composition. In Sections 3.3 and 3.4, we discuss further the validity of this approximation and its impact on the calculation of the leakage spectrum.

Based on Eq. (3.24), the following approximation for $f_{L,G}^k(u)$ is derived:

$$f_{L,G}^k(u) \approx \sum_{m=1}^{N_{nb}} s^{k,m} \frac{w_G^{k,m}}{\Delta d^{k,m}} \left(D_G^k(u) \Phi_{\text{env},G}^k(u) - D_G^m(u) \Phi_{\text{env},G}^m(u) \right). \quad (3.25)$$

In Eq. (3.25), the spatial coefficient $s^{k,m}$ is given by

$$s^{k,m} = \frac{2}{\Delta d^{k,m} + \Delta d^{m,k}}. \quad (3.26)$$

After some algebraic manipulation, the leakage projection parameter becomes

$$h_{L,G,j}^k \approx \sum_{m=1}^{N_{nb}} s^{k,m} \frac{w_G^{k,m}}{\Delta d^{k,m}} \left[\bar{\Phi}_G^k h_{R,D,G,j}^k + \sum_{i=1}^{N_{QG}} \alpha_{G,i}^k h_{V,D,G,i,j}^k - \left(\bar{\Phi}_G^m h_{R,D,G,j}^m + \sum_{i=1}^{N_{QG}} \alpha_{G,i}^m h_{V,D,G,i,j}^m \right) \right], \quad (3.27)$$

where the coefficients $h_{R,D,G,j}^k$ and $h_{V,D,G,i,j}^k$ for node k read

$$h_{R,D,G,j}^k = \int_0^1 du W_{G,j}(u) D_G^k(u) \varphi_{\infty,G}^k(u), \quad (3.28a)$$

$$h_{V,D,G,i,j}^k = \int_0^1 du W_{G,j}(u) D_G^k(u) Q_{G,i}(u). \quad (3.28b)$$

An analogous equation can be written for the same coefficients in the generic neighbor node m . The normalization constant $w_G^{k,m}$ is now

$$w_G^{k,m} = \frac{J_G^{k,m} / (\bar{L}_G^k s^{k,m})}{\bar{\Phi}_G^k h_{R,D,G,0}^k + \sum_{i=1}^{N_{QG}} \alpha_{G,i}^k h_{V,D,G,i,0}^k - \left(\bar{\Phi}_G^m h_{R,D,G,0}^m + \sum_{i=1}^{N_{QG}} \alpha_{G,i}^m h_{V,D,G,i,0}^m \right)}. \quad (3.29)$$

The variables detailed in Eq. (3.28) are the standard rehomogenization parameters for the diffusion coefficient [see Eq. (2.27)]. They only depend on the local infinite-medium neutron spectrum and diffusion-coefficient distribution. No information on fine-group quantities in the neighbor nodes is required. Therefore, these coefficients can be easily computed during the lattice calculation, in a similar manner to the rehomogenization parameters for the cross sections and the fission spectrum [Eq. (2.14)].

Despite the heuristic connotation of Fick's law, the diffusive approach has a physical justification. This can be illustrated with an example. We consider a 3.1%-enriched UO_2 assembly with burnable-absorber (Pyrex) rods adjacent to a 1.8%-enriched UO_2 assembly (example 1 of Section 2.3.2.1). Both fuel bundles are at zero burn-up. For the assembly with poison, Fig. 3.2 shows the leakage form functions computed by Eqs. (3.14) and (3.25) (that is, the original and approximate formulations of the method) using the reference environmental flux spectra $\Phi_{\text{env},G}^{k,\text{ref}}(u)$ and $\bar{\Phi}_{\text{env},G}^{m,\text{ref}}(u)$. The comparison with the reference environmental leakage reveals that the diffusive definition provides a very accurate estimate and that the differences between the two formulations are negligible.

From a numerical point of view, the diffusive approach translates into the dependence of the leakage parameter $h_{L,G,j}$ [Eqs. (3.18) and (3.27)] on the spectrum-variation modal expansion coefficients $\alpha_{G,i}$, which are the unknowns of the rehomogenization algorithm. Therefore, a non-linearity is introduced. In addition, the spectral-correction

3. Modeling of the neutron leakage spectrum

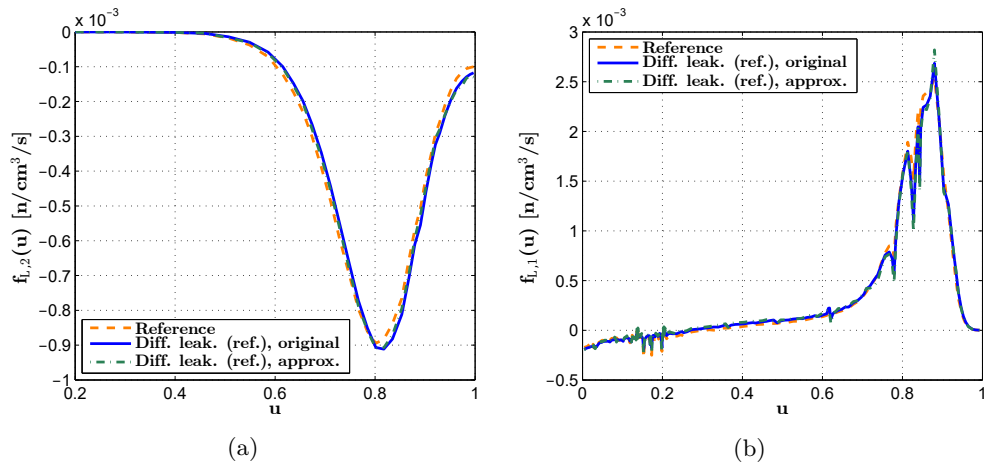


Fig. 3.2. (a) Thermal-group and (b) fast-group reference diffusive leakage (i.e., computed with the reference environmental flux spectra) in a 3.1%-enriched UO_2 assembly with Pyrex rods next to a 1.8%-enriched UO_2 assembly. Units are in neutrons/(cubic centimeters · second).

problem is no longer local, because the spectrum variation solution in a given node depends on the spectrum perturbation (i.e., on the coefficients $\alpha_{G,i}$) in the neighbor nodes. More details about numerical aspects of the method are given in Section 3.4.1.

3.2.2 The fundamental-leakage approach

The second approach consists of using the fundamental-leakage spectrum determined at the single-assembly calculation level.

We make the approximation

$$f_{L,G}^k(u) \approx f_{L,G}^{\infty,k}(u), \quad (3.30)$$

where $f_{L,G}^{\infty,k}(u)$ is the leakage distribution making the infinite lattice critical (i.e., $k_{\infty} = 1$). This function is computed in most lattice-physics codes, in which the unit assembly is simulated under critical conditions (Hebert, 2009). As mentioned in Section 2.4.4, in the absence of information on the exact operating conditions and on the materials surrounding the assembly, this assumption provides the most realistic representation of the core environment. The critical-leakage calculation is commonly based on the homogeneous fundamental-mode B_1 approximation. An exhaustive description of the corresponding theory can be found in Hebert (2009). In this thesis,

we adopt the following formulation of $f_{L,G}^\infty(u)$ (the superscript k is omitted):

$$f_{L,G}^\infty(u) = \frac{D_G(u)B^2\varphi_{\infty,G}^{B^2}(u)}{\int_0^1 du D_G(u)B^2\varphi_{\infty,G}^{B^2}(u)}, \quad (3.31)$$

where B^2 is the critical buckling and $D_G(u)$ is the G^{th} -group leakage-coefficient energy distribution, which is also a function of B^2 . Both quantities come from the solution of the homogeneous B_1 equations (Hebert, 2009). Their product $D_G(u)B^2$ is the critical-leakage cross-section distribution. In Eq. (3.31), $\varphi_{\infty,G}^{B^2}(u)$ denotes the B^2 -corrected infinite-medium spectrum, which has the same shape in energy as the fundamental mode computed by the B_1 model. The normalization of $f_{L,G}^\infty(u)$ to unity satisfies Eq. (3.2). After substitution of Eqs. (3.30) and (3.31) into Eq. (3.4), the leakage projection coefficient for a generic node reads

$$h_{L,G,j} = \frac{\int_0^1 du W_{G,j}(u) D_G(u) B^2 \varphi_{\infty,G}^{B^2}(u)}{\int_0^1 du D_G(u) B^2 \varphi_{\infty,G}^{B^2}(u)}. \quad (3.32)$$

With this approach, $h_{L,G,j}$ can be computed on the basis only of lattice information. Therefore, its calculation is performed directly during the single-assembly simulation, as for the other rehomogenization parameters [Eq. (2.14)]. No complexity is added to the on-line solution of the spectral rehomogenization problem.

Despite its straightforwardness, this method presents some significant limitations. Even if the B_1 model provides the best possible representation of the critical lattice surrounding the assembly, the infinite-medium shape formulated in Eq. (3.31) might not capture the streaming effects occurring in the real environment in the presence of strong interassembly heterogeneity. Moreover, as discussed in Section 2.4.4, the theoretical foundation of the B_1 spectrum correction fades when non-critical conditions are simulated. In reactor core transients and subcritical states (Dall’Osso, 2015a,b; Demazière, 2016), the B^2 -corrected spectrum and the fundamental-leakage distribution may deviate from those in the non-critical core environment even in homogeneous systems (i.e., in the absence of streaming effects). Another drawback of this approach is its lack of generality, because it can only be applied if the cross-section libraries are built with the fundamental-buckling paradigm.

3.3 Numerical results

In this section, the methodology is applied to two-group nodal simulations of several PWR colorset configurations, as done in Chapter 2. In the first part, the diffusive leakage model is validated. In the second part, the fundamental-leakage approach is tested and the two strategies are compared.

3.3.1 Validation of the diffusive leakage model

Reactor configurations at zero burn-up and isothermal conditions are first addressed. We consider the following benchmark problems: a UO_2 colorset with burnable-poison (Pyrex) rods (example 1), a UO_2 colorset hosting silver-indium-cadmium (AIC) control rods (example 2), a UO_2/MOX colorset (example 3), and a UO_2 colorset with gadolinium-bearing fuel pins (example 4). Examples 1, 2 and 3 have been used in Chapter 2 (Section 2.3.2) to validate the modal synthesis of the spectrum variation. For these test cases, in the analysis that follows we only focus on the accuracy of the leakage prediction (for other aspects of the calculation, the reader may refer to Section 2.3.2). In this part of the investigation, nodal simulations are run with BRISINGR (Appendix A). Single-assembly cross sections and discontinuity factors are computed with SERPENT (Leppänen et al., 2015). The details about their calculation can be found in Section 2.3.1. The fine-group [Eqs. (3.19) and (3.28)] and two-group diffusion coefficients are formulated with the CMM (Liu et al., 2016). For the sake of generality, the homogenization parameters are generated without the critical-buckling correction. This approach is of particular interest in the light of the findings reported in Section 2.4.4, which show that rehomogenization can also reproduce spectral effects due to different reactivity in the core environment and in the infinite lattice.

As further validation of the methodology, we also simulate a test case with fuel depletion (example 5). This benchmark problem consists of a UO_2 colorset with Pyrex rods and is modeled with ARTEMIS (Hobson et al., 2013), the core simulator of Framatome's code platform ARCADIA (Curca-Tivig et al., 2007; Porsch et al., 2012). The cross-section libraries used by ARTEMIS are generated with APOLLO2-A (Martinolli et al., 2010).

In all the example problems, the spatial discretization and the values of the main state parameters are the same as in Section 2.3.1. We present the results of the following calculations:

- with infinite-medium cross sections (*a*);
- with cross sections corrected by the reference spectral defect [Eq. (2.25)] (*b*);
- with spectral rehomogenization of cross sections using the reference environmental-leakage spectrum (*c*);
- with spectral rehomogenization of cross sections using the original formulation of the diffusive leakage model [Eqs. (3.17) and (3.18)] (*d*);
- with spectral rehomogenization of cross sections using the approximate variant of the diffusive leakage model [Eqs. (3.25) and (3.27)] (*e*).

Unless stated otherwise, rehomogenization is applied with the polynomial (or semi-analytic) synthesis in the fast group and the POD-based one in the thermal group

(Section 2.2.2). This hybrid approach has been chosen because, as discussed in Section 2.4.3, at the current stage of development of the methodology a universal POD basis has not been achieved yet for the fast group. The semi-analytic strategy is therefore deemed to have a more general validity in this energy range. In all the test cases, we use the POD modes computed with the ensemble of snapshots of examples 1, 2 and 3, as explained in Chapter 2 (i.e., the $d\mathcal{B}$ set defined in Section 2.3.2.3).

Numerical results of calculations b and c are also reported in this chapter to ease a comprehensive evaluation of the methodology for the leakage spectrum. Calculation c provides the reference solution to assess the performance of the leakage model, whereas calculation b provides the reference solution for the rehomogenization method as a whole. We underscore that the cross-section corrections used in calculation b only correct the node-averaged spectral component of the homogenization defect. They do not remove spatial homogenization errors. Therefore, the results of calculation b are not the best estimates that may be achieved with the nodal calculation if the input cross sections were fully condensed and homogenized in the colorset environment. They only serve as a reference to assess the accuracy of spectral rehomogenization. In calculation c , the reference environmental leakage is computed by Eq. (3.31) with the assembly-averaged, fine-group leakage cross sections and flux spectra obtained from a 281-group transport simulation of the whole colorset.

3.3.1.1 Example 1 - UO_2 colorset with Pyrex rods

The colorset and assembly layouts have been shown in Fig. 2.5. In this analysis, we simulate the critical configuration (i.e., $k_{\text{eff}}^{\text{ref}} = 1.0$), obtained with a concentration of diluted boron of 1465 ppm. The reference (normalized) total fission power is 0.92 in the 1.8%-enriched assembly and 1.08 in the 3.1%-enriched assembly with Pyrex.

Fig. 3.3 shows the leakage spectrum in the assembly without burnable absorber computed by rehomogenization with the diffusive model. All curves are normalized to the few-group assembly-averaged leakage from the nodal calculation e . The reference environmental leakage from the transport simulation is accurately reproduced in the fast group. Minor deviations only occur in the high-energy peak range (at $u_1 \in [0.7, 0.95]$, i.e., approximately between 0.12 and 8.2 MeV) and in the epithermal region (at $u_1 < 0.1$, i.e., $E < 3.5$ eV). In the thermal group the result is also satisfactory, even if a slight shift of the bell-shaped curve towards higher values of u is observed. Differences between the original and approximate definitions of the leakage spectrum are negligible.

Fig. 3.4 depicts the flux spectrum variation in the two assemblies. The curves computed with the diffusive approach have the same level of accuracy as those obtained with the reference leakage input. The slight overestimation of the absolute value of the reference perturbation in the epithermal region is a consequence of the aforementioned discrepancy in the predicted leakage spectrum in this energy range. The shift found in the computed thermal leakage has no appreciable effect on the spectrum deformation. For the sake of comparison, Fig. 3.5 shows the fast-group spectrum variation in the

3. Modeling of the neutron leakage spectrum

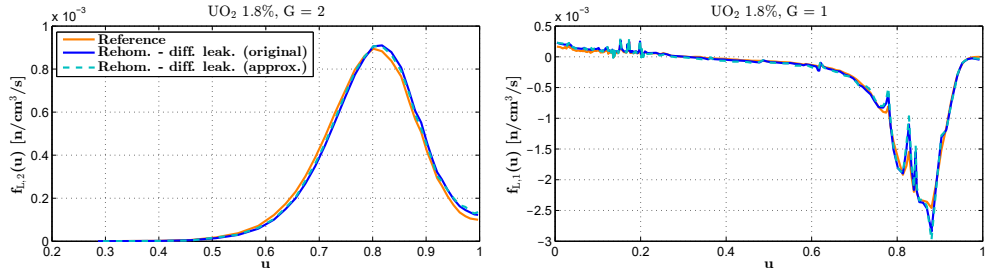


Fig. 3.3. Example 1: leakage spectrum (per unit u) in the 1.8%-enriched UO_2 assembly, as computed by rehomogenization with the diffusive model and the hybrid modal approach (namely, the POD basis in the thermal group and the semi-analytic one in the fast group). The group-wise curves have the same norm. The labels “original” and “approx.” refer to Eqs. (3.17) and (3.25), respectively. Units are in neutrons/(cubic centimeters \cdot second).

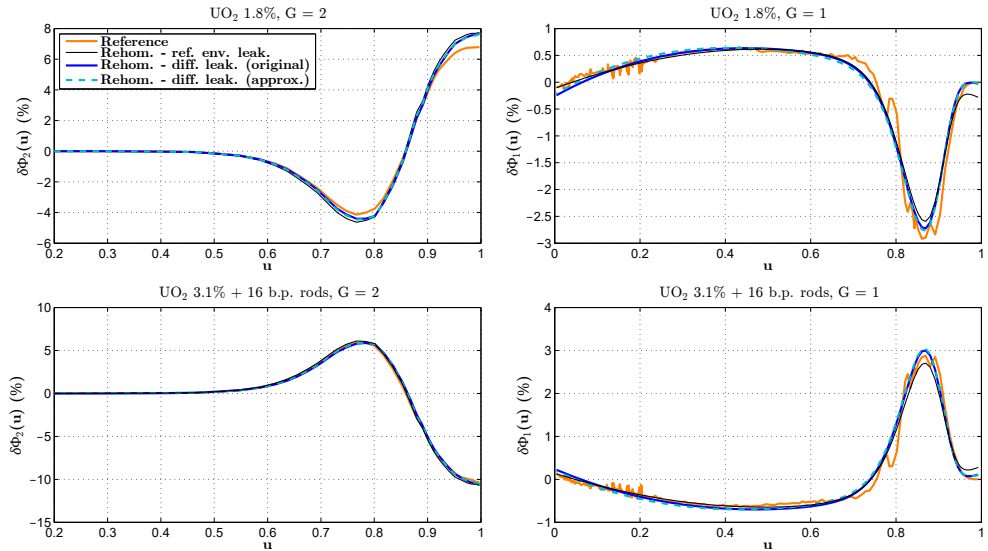


Fig. 3.4. Example 1: spectrum variation (per unit u) computed by rehomogenization with the diffusive leakage model and the hybrid modal approach.

assembly with Pyrex rods computed with the diffusive approximation and the POD modes.

The errors in the nodal cross sections are reported in Tables 3.1 and 3.2 for the two assemblies. The corrections computed with the diffusive leakage model reproduce very accurately those obtained with calculation *c*. A slight miscorrection is only found in fast-to-thermal scattering with the original formulation (calculation *d*). Table 3.3 shows the errors in the multiplication factor (Δk_{eff}), the few-group nodal

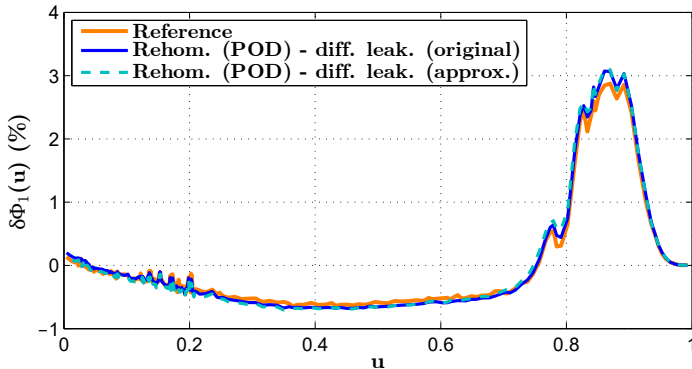


Fig. 3.5. Example 1: fast-group spectrum variation in the assembly with Pyrex rods, as computed by rehomogenization with the POD modes and the diffusive leakage approximation.

flux ($\Delta\bar{\Phi}_G$), and the nodal fission power ($\Delta\bar{P}_{\text{fiss}}$). Also for these parameters, the results of simulations *d* and *e* match those of the reference calculations (*b* and *c*). The errors in the fission power drop to zero. Table 3.3 also indicates the number of non-linear power iterations (N_{iter}) for the convergence of the eigenvalue calculation. Also in this case, we used a tolerance $\epsilon_{\text{iter}} = 10^{-5}$ for the relative variation in the k_{eff} estimate and in the nodal-flux-array two-norm between two successive iterations. Compared to the simulation without rehomogenization, the number of iterations increases by a factor of 2.3 in calculation *d* and of 1.9 in calculation *e*.

Table 3.1. Example 1: errors in the nodal cross sections of the assembly without Pyrex rods. Rehomogenization is applied with the hybrid modal approach.

UO ₂ 1.8%	$\Sigma_{a,1}$	$\Sigma_{a,2}$	$\nu\Sigma_{f,1}$	$\nu\Sigma_{f,2}$	$\Sigma_{t,1}$	$\Sigma_{t,2}$	$\Sigma_{s,1\rightarrow 1}$	$\Sigma_{s,1\rightarrow 2}$	$\Sigma_{s,2\rightarrow 2}$
Reference [cm ⁻¹]	0.00877	0.0690	0.00485	0.0815	0.540	1.308	0.513	0.0178	1.238
Simulation	Errors (%)								
No rehom. (<i>a</i>)	-0.39	0.66	0.39	0.77	-0.32	0.25	-0.32	-0.11	0.24
Ref. $\delta\Sigma_G^{\text{spec}}$ (<i>b</i>)	0.03	0.13	0.16	0.22	0.01	-0.04	0.01	-0.01	-0.05
Rehom. - ref. env. leak. (<i>c</i>)	0.07	0.06	0.15	0.15	-0.01	-0.08	-0.01	-0.05	-0.09
Rehom. - diff. leak., original (<i>d</i>)	0.11	0.09	0.22	0.19	-0.01	-0.06	0.0	-0.19	-0.07
Rehom. - diff. leak., approx. (<i>e</i>)	0.17	0.09	0.25	0.18	0.0	-0.07	0.0	-0.12	-0.08

3.3.1.2 Example 2 - UO₂ colorset with AIC-type control rods

The colorset layout has been shown in Fig. 2.9. Other properties (such as the reference eigenvalue and fission power) can be found in Section 2.3.2.2.

Figs. 3.6 and 3.7 show the leakage distribution and the spectrum variation determined by rehomogenization. In the thermal group, for both quantities the computed curves almost overlap with those corresponding to the reference leakage. In the fast group,

3. Modeling of the neutron leakage spectrum

Table 3.2. Example 1: errors in the nodal cross sections of the assembly with Pyrex rods. Rehomonization is applied with the hybrid modal approach.

UO ₂ 3.1% + 16 b.p. rods	$\Sigma_{a,1}$	$\Sigma_{a,2}$	$\nu\Sigma_{f,1}$	$\nu\Sigma_{f,2}$	$\Sigma_{t,1}$	$\Sigma_{t,2}$	$\Sigma_{s,1\rightarrow 1}$	$\Sigma_{s,1\rightarrow 2}$	$\Sigma_{s,2\rightarrow 2}$
Reference [cm ⁻¹]	0.0101	0.104	0.00659	0.132	0.525	1.296	0.499	0.0158	1.190
Simulation	Errors (%)								
No rehom. (a)	0.41	-0.47	-0.17	-1.01	0.32	-0.45	0.33	0.10	-0.46
Ref. $\delta\Sigma_G^{\text{spec}}$ (b)	-0.03	0.27	-0.13	-0.20	0.0	0.0	0.0	0.01	-0.02
Rehom. - ref. env. leak. (c)	-0.07	0.30	-0.11	-0.17	0.0	0.02	0.0	0.07	-0.01
Rehom. - diff. leak., original (d)	-0.12	0.25	-0.15	-0.22	-0.02	-0.01	-0.02	0.16	-0.04
Rehom. - diff. leak., approx. (e)	-0.19	0.26	-0.19	-0.21	-0.03	0.0	-0.03	0.08	-0.03

Table 3.3. Example 1: number of power iterations and errors in the multiplication factor, nodal flux, and fission power. The two values of $\Delta\bar{\Phi}_G$ refer to the fast and thermal groups, respectively. The value of $\Delta\bar{P}_{\text{fiss}}$ out of parentheses refers to the total power, whereas the two values within parentheses correspond to the fast- and thermal-group contributions, respectively. Rehomonization is applied with the hybrid modal approach.

Simulation	N_{iter}	Δk_{eff} [pcm]	UO ₂ 1.8%		UO ₂ 3.1% + 16 b.p. rods	
			$\Delta\bar{\Phi}_G$ (%)	$\Delta\bar{P}_{\text{fiss}}$ (%)	$\Delta\bar{\Phi}_G$ (%)	$\Delta\bar{P}_{\text{fiss}}$ (%)
No rehom. (a)	8	-338	0.2, -0.84	0.40 (0.69, 0.33)	-0.12, 0.73	-0.34 (-0.48, -0.30)
Ref. $\delta\Sigma_G^{\text{spec}}$ (b)	9	-310	0.14, -0.58	0.05 (0.42, -0.03)	-0.04, 0.27	-0.05 (-0.29, 0.03)
Rehom. - ref. env. leak. (c)	13	-306	0.14, -0.57	0.0 (0.40, -0.10)	-0.05, 0.29	0.0 (-0.28, 0.09)
Rehom. - diff. leak., original (d)	18	-303	0.16, -0.68	-0.04 (0.46, -0.16)	-0.06, 0.36	0.04 (-0.33, 0.14)
Rehom. - diff. leak., approx. (e)	15	-303	0.15, -0.63	0.0 (0.50, -0.11)	-0.05, 0.31	0.0 (-0.35, 0.10)

the leakage prediction is very precise in the epithermal range, whereas some inaccuracy arises in the high-energy region (at $u_1 \in [0.7, 1.0]$, that is, between 0.12 and 19.6 MeV). The fast-group spectrum deformation computed with the POD modes is plotted in Fig. 3.8 for the unrodded assembly. Only the result of the approximate version of the leakage model is shown. Compared to the polynomial approach, the outcome is more accurate in the epithermal region, with the resonance spikes being fitted precisely.

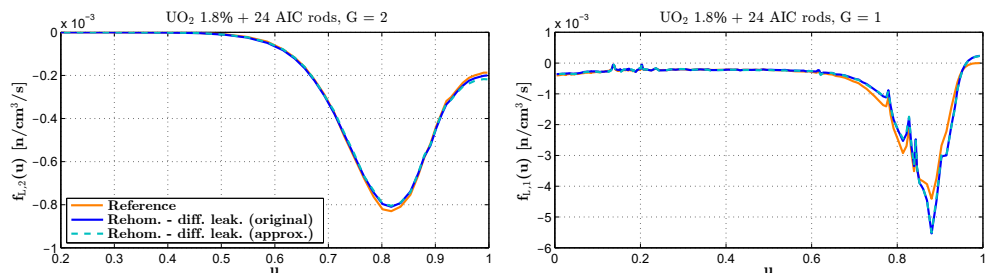


Fig. 3.6. Example 2: leakage spectrum in the rodged assembly computed by rehomogenization with the diffusive model and the hybrid modal approach.

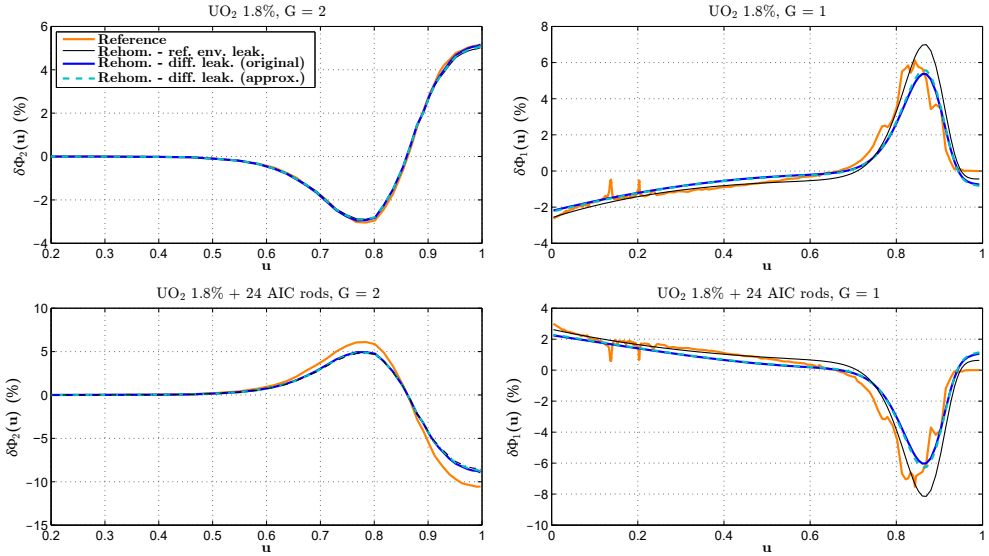


Fig. 3.7. Example 2: spectrum variation computed by rehomogenization with the diffusive leakage model and the hybrid modal approach.

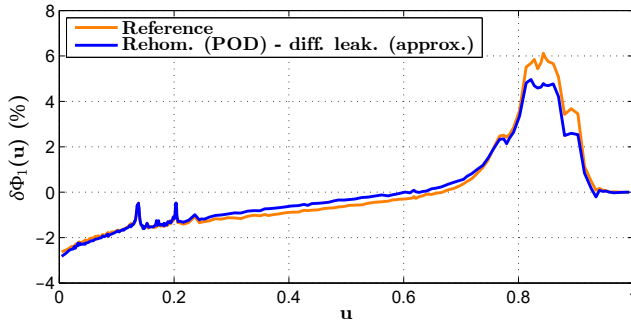


Fig. 3.8. Example 2: fast-group spectrum variation in the unrodded assembly, as computed by rehomogenization with the POD modes and the approximate formulation of the diffusive leakage model.

The errors in the nodal cross sections, multiplication factor, nodal flux and fission power are shown in Tables 3.4, 3.5, and 3.6. Since the results achieved with the two formulations of the diffusive leakage model are equivalent, they are only reported for the approximate one. With the diffusive approach, the deviations in the thermal cross sections are very close to those found with calculation *b*. In the fast group, for all the reaction types the computed corrections go in the right direction and

3. Modeling of the neutron leakage spectrum

approach the reference ones. The main differences between calculations *e1* and *e2* are in the $\delta\Sigma_{a,1}$ and $\delta\Sigma_{s,1\rightarrow 2}$ estimates. The corrections on k_{eff} , the nodal flux and the fission power are also in good agreement with the reference values. The errors in the last two quantities are significantly lower than those found with infinite-medium homogenization parameters.

Table 3.4. Example 2: errors in the nodal cross sections of the unrodded assembly. The abbreviation ‘‘Hybr.’’ refers to the hybrid modal approach.

UO ₂ 1.8%	$\Sigma_{a,1}$	$\Sigma_{a,2}$	$\nu\Sigma_{f,1}$	$\nu\Sigma_{f,2}$	$\Sigma_{t,1}$	$\Sigma_{t,2}$	$\Sigma_{s,1\rightarrow 1}$	$\Sigma_{s,1\rightarrow 2}$	$\Sigma_{s,2\rightarrow 2}$
Reference [cm ⁻¹]	0.00827	0.0557	0.00485	0.0837	0.534	1.313	0.509	0.0174	1.256
Simulation	Errors (%)								
No rehom. (<i>a</i>)	1.61	0.56	0.51	0.60	0.68	0.16	0.56	3.80	0.14
Ref. $\delta\Sigma_G^{\text{spec}}$ (<i>b</i>)	0.05	0.20	-0.12	0.23	-0.02	-0.05	-0.02	-0.07	-0.06
Rehom. (Hybr.) - ref. env. leak. (<i>c</i>)	-0.53	0.20	0.05	0.23	-0.14	-0.05	-0.13	-0.24	-0.06
Rehom. (Hybr.) - diff. leak., approx. (<i>e1</i>)	-0.25	0.20	-0.12	0.23	0.05	-0.05	0.05	0.25	-0.06
Rehom. (POD) - diff. leak., approx. (<i>e2</i>)	0.12	0.21	-0.25	0.24	0.08	-0.04	0.09	-0.34	-0.05

Table 3.5. Example 2: errors in the nodal cross sections of the rodded assembly.

UO ₂ 1.8% + 24 AIC rods	$\Sigma_{a,1}$	$\Sigma_{a,2}$	$\nu\Sigma_{f,1}$	$\nu\Sigma_{f,2}$	$\Sigma_{t,1}$	$\Sigma_{t,2}$	$\Sigma_{s,1\rightarrow 1}$	$\Sigma_{s,1\rightarrow 2}$	$\Sigma_{s,2\rightarrow 2}$
Reference [cm ⁻¹]	0.0116	0.0817	0.00474	0.0853	0.534	1.286	0.507	0.0153	1.203
Simulation	Errors (%)								
No rehom. (<i>a</i>)	-1.71	0.71	-0.64	-0.93	-0.80	-0.38	-0.66	-4.77	-0.46
Ref. $\delta\Sigma_G^{\text{spec}}$ (<i>b</i>)	0.60	1.28	0.19	-0.12	0.02	0.05	0.0	0.01	-0.04
Rehom. (Hybr.) - ref. env. leak. (<i>c</i>)	1.02	1.16	-0.09	-0.29	0.13	-0.04	0.12	-0.16	-0.13
Rehom. (Hybr.) - diff. leak., approx. (<i>e1</i>)	0.65	1.16	0.17	-0.28	-0.11	-0.04	-0.11	-0.71	-0.12
Rehom. (POD) - diff. leak., approx. (<i>e2</i>)	0.38	1.14	0.23	-0.31	-0.13	-0.06	-0.15	0.18	-0.14

Table 3.6. Example 2: number of power iterations and errors in the multiplication factor, nodal flux and fission power.

Simulation	N_{iter}	Δk_{eff} [pcm]	UO ₂ 1.8%		UO ₂ 1.8% + 24 AIC rods	
			$\Delta\bar{\Phi}_G$ (%)	$\Delta\bar{P}_{\text{fiss}}$ (%)	$\Delta\bar{\Phi}_G$ (%)	$\Delta\bar{P}_{\text{fiss}}$ (%)
No rehom. (<i>a</i>)	10	58	-0.56, 2.08	3.03 (0.98, 3.41)	0.69, -3.50	-4.70 (-1.17, -5.61)
Ref. $\delta\Sigma_G^{\text{spec}}$ (<i>b</i>)	10	-486	-0.06, 0.19	1.14 (0.47, 1.28)	0.29, -1.46	-1.77 (-0.56, -2.10)
Rehom. (Hybr.) - ref. env. leak. (<i>c</i>)	15	-512	-0.02, 0.06	1.25 (0.74, 1.36)	0.30, -1.52	-1.94 (-0.87, -2.24)
Rehom. (Hybr.) - diff. leak., approx. (<i>e1</i>)	16	-435	-0.09, 0.33	1.38 (0.49, 1.56)	0.35, -1.78	-2.15 (-0.58, -2.57)
Rehom. (POD) - diff. leak., approx. (<i>e2</i>)	25	-517	-0.01, 0.04	1.08 (0.38, 1.22)	0.27, -1.34	-1.67 (-0.45, -2.01)

3.3.1.3 Example 3 - UO₂/MOX colorset

This colorset has been described in Section 2.3.2.3 (see Fig. 2.11). Figs. 3.9 and 3.10 depict the leakage distribution and the spectrum perturbation estimated by rehomogenization with the hybrid and POD modal approaches. Also in this case, the results

are only shown for the approximate formulation of the leakage model. The computed fast-group distributions suffer from some inaccuracy in the higher part of the energy domain (at $u_1 > 0.85$, corresponding to $E > 1.5$ MeV). Here, the bulge-shaped outline featured by the spectrum variation is not reproduced by the polynomial approach and is amplified by the POD-based one. The result is instead satisfactory in the epithermal region.

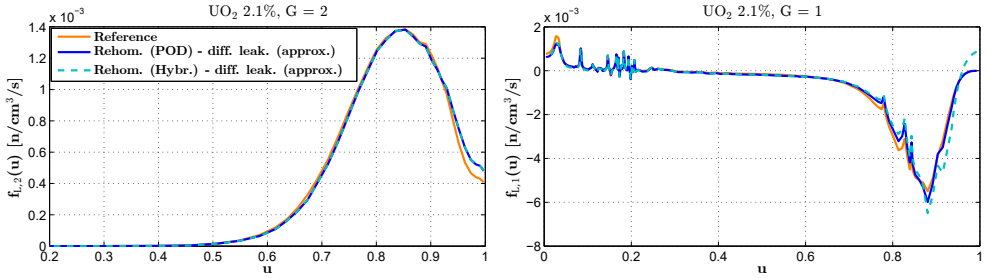


Fig. 3.9. Example 3: leakage spectrum in the UO_2 assembly computed by rehomogenization with the diffusive model.

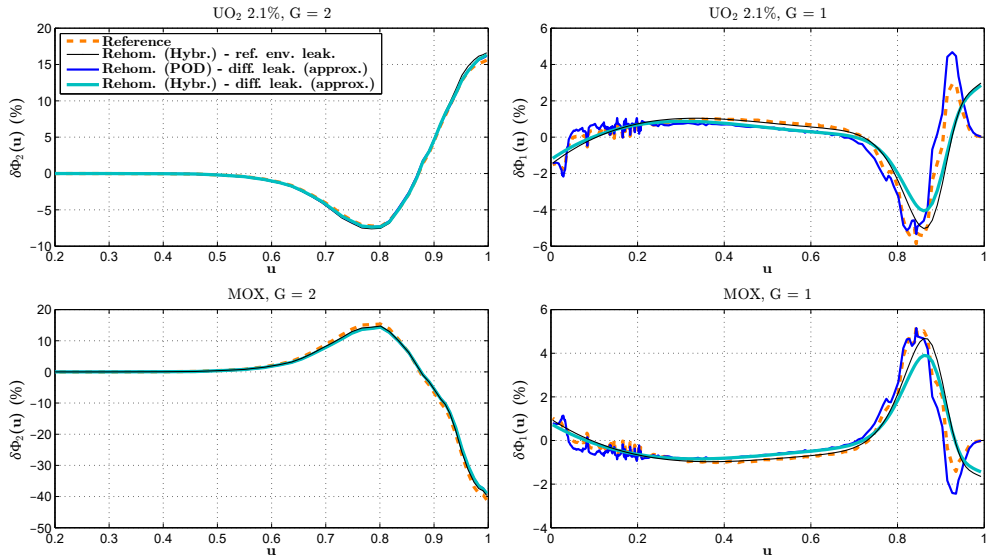


Fig. 3.10. Example 3: spectrum variation computed by rehomogenization with the diffusive leakage model.

Tables 3.7, 3.8 and 3.9 show the errors in the nodal cross sections and in the integral parameters. As in the previous examples, the performance of the method is excellent

3. Modeling of the neutron leakage spectrum

in the thermal group. In the fast group, all the cross-section corrections go in the right direction. The simulation with the POD modes (calculation *e2*) reproduces the reference value of $\delta\Sigma_{a,1}$ almost exactly, whereas both calculations *c* and *e1* overestimate it, especially in the MOX assembly. This difference depends on the reconstruction of the epithermal resonances, which is achieved to a high level of accuracy only with the POD basis. Because of the aforementioned flaws in the prediction of $\delta\Phi_1(u)$ at high energies, the three calculations overcorrect significantly the production cross section $\nu\Sigma_{f,1}$ and, as a result, the fast-group nodal power. Nevertheless, due to the small contribution of the latter and to the considerable improvement in the thermal-power estimate, the error in the total power decreases appreciably. The correction on k_{eff} is overestimated (calculation *e2*) or mispredicted (calc. *e1*), but the errors remain low.

Table 3.7. Example 3: errors in the nodal cross sections of the UO₂ assembly.

UO ₂ 2.1%	$\Sigma_{a,1}$	$\Sigma_{a,2}$	$\nu\Sigma_{f,1}$	$\nu\Sigma_{f,2}$	$\Sigma_{t,1}$	$\Sigma_{t,2}$	$\Sigma_{s,1\rightarrow 1}$	$\Sigma_{s,1\rightarrow 2}$	$\Sigma_{s,2\rightarrow 2}$
Reference [cm ⁻¹]	0.00927	0.0894	0.00547	0.0979	0.534	1.302	0.508	0.0171	1.211
Simulation	Errors (%)								
No rehom. (<i>a</i>)	-0.61	1.12	0.07	1.27	-0.33	0.53	-0.37	1.18	0.50
Ref. $\delta\Sigma_G^{\text{spec}}$ (<i>b</i>)	0.11	0.18	0.35	0.30	0.01	0.01	0.01	-0.05	0.0
Rehom. (Hybr.) - ref. env. leak. (<i>c</i>)	0.28	0.11	0.76	0.23	0.0	-0.03	0.0	-0.11	-0.04
Rehom. (Hybr.) - diff. leak., approx. (<i>e1</i>)	0.22	0.15	0.82	0.27	-0.08	0.0	-0.10	0.20	-0.01
Rehom. (POD) - diff. leak., approx. (<i>e2</i>)	0.16	0.15	0.71	0.26	-0.14	-0.01	-0.15	0.15	-0.02

Table 3.8. Example 3: errors in the nodal cross sections of the MOX assembly.

MOX	$\Sigma_{a,1}$	$\Sigma_{a,2}$	$\nu\Sigma_{f,1}$	$\nu\Sigma_{f,2}$	$\Sigma_{t,1}$	$\Sigma_{t,2}$	$\Sigma_{s,1\rightarrow 1}$	$\Sigma_{s,1\rightarrow 2}$	$\Sigma_{s,2\rightarrow 2}$
Reference [cm ⁻¹]	0.0142	0.260	0.00990	0.375	0.526	1.517	0.498	0.0131	1.254
Simulation	Errors (%)								
No rehom. (<i>a</i>)	0.02	0.42	0.02	0.58	0.39	-0.64	0.43	-0.87	-0.90
Ref. $\delta\Sigma_G^{\text{spec}}$ (<i>b</i>)	-0.08	0.88	-0.25	1.08	-0.01	0.34	-0.01	0.04	0.23
Rehom. (Hybr.) - ref. env. leak. (<i>c</i>)	-0.21	0.90	-0.47	1.11	0.0	0.29	0.0	0.21	0.16
Rehom. (Hybr.) - diff. leak., approx. (<i>e1</i>)	-0.33	0.89	-0.49	1.09	0.05	0.26	0.07	-0.16	0.12
Rehom. (POD) - diff. leak., approx. (<i>e2</i>)	-0.10	0.89	-0.52	1.09	0.07	0.26	0.08	-0.29	0.13

Table 3.9. Example 3: number of power iterations and errors in the multiplication factor, nodal flux and fission power.

Simulation	N_{iter}	Δk_{eff} [pcm]	UO ₂ 2.1%		MOX	
			$\Delta\Phi_G$ (%)	$\Delta\bar{P}_{\text{fiss}}$ (%)	$\Delta\Phi_G$ (%)	$\Delta\bar{P}_{\text{fiss}}$ (%)
No rehom. (<i>a</i>)	10	30	0.03, -0.15	0.73 (0.26, 0.86)	0.04, -0.69	-0.55 (-0.15, -0.71)
Ref. $\delta\Sigma_G^{\text{spec}}$ (<i>b</i>)	10	-7	0.09, -0.56	-0.21 (0.53, -0.45)	0.02, -0.39	0.15 (-0.30, 0.38)
Rehom. (Hybr.) - ref. env. leak. (<i>c</i>)	16	16	0.09, -0.56	-0.19 (0.93, -0.57)	0.02, -0.28	0.15 (-0.53, 0.47)
Rehom. (Hybr.) - diff. leak., approx. (<i>e1</i>)	12	34	0.06, -0.36	0.04 (0.99, -0.28)	0.03, -0.49	-0.03 (-0.57, 0.23)
Rehom. (POD) - diff. leak., approx. (<i>e2</i>)	20	-51	0.07, -0.40	0.07 (0.96, -0.22)	0.03, -0.60	-0.05 (-0.55, 0.19)

3.3.1.4 Example 4 - UO_2 colorset with gadolinium-bearing fuel rods

In this example (Fig. 3.11), the checkerboard layout consists of two 17×17 UO_2 assemblies with 1.8% enrichment and two 17×17 UO_2 assemblies with 3.9% enrichment and 12 fuel rods containing gadolinium (Gd). The pins with burnable poison are located at the periphery of the assemblies, in the outer and first inboard rows. They have 0.25% ^{235}U enrichment and 8% mass content of gadolinium oxide (Gd_2O_3), with the isotopic composition of naturally occurring gadolinium. The concentration of boron in the moderator is 1830 ppm, and the reference multiplication factor is 1.00303. The reference fission power is 0.82 in the 1.8%-enriched assembly and 1.18 in the 3.9%-enriched one.

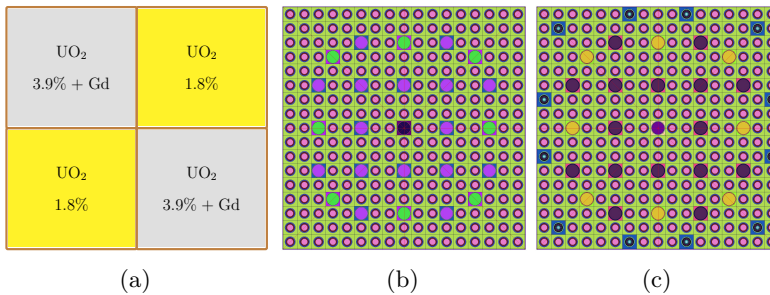


Fig. 3.11. (a) Assembly set of example 4. Layout of the UO_2 fuel assemblies: (b) with 1.8% enrichment, (c) with 3.9% enrichment and 12 gadolinium-bearing fuel rods in the periphery of the assembly. Both assemblies host 24 empty guide tubes and an empty tube for the instrumentation in the center.

Figs. 3.12 and 3.13 portray the leakage distribution and the spectrum variation. In the fast group, the spectrum change from the diffusive approach exhibits a tilt with respect to the curve obtained with the reference leakage input. The magnitude of the reference spectrum deformation is overestimated in the epithermal region. As in the colorset with control rods (Sections 2.3.2.2 and 3.3.1.2), the computed $\delta\Phi_2(u)$ deviates from the reference because of spatial effects. This behavior can be justified as follows. In the assembly with gadolinium, the variation in the flux spatial distribution is positive at the periphery and exceeds 15% in the outer cell rows (see Fig. 5.15), where the fuel pins with burnable poison are located and neutron absorption is higher. Hence, the average spatial correction $\delta\Sigma_{a,2}^{\text{spat,ref}}$ in the node is positive. Since the hardening effect of the spatial term is not accounted for by spectral rehomogenization, the method predicts a softer spectrum (that is, the amplitude of the thermal spectrum change is overestimated).

Tables 3.10, 3.11 and 3.12 report the numerical errors. Simulations *b* and *c* differ most clearly in their prediction of $\delta\nu\Sigma_{f,2}$ in the gadolinium-bearing assembly and of $\delta\Sigma_{a,1}$ in both fuel bundles. In the thermal group, the corrections computed with the diffusive model match those of calculation *c*. The cross sections $\Sigma_{a,1}$ and $\Sigma_{s,1\rightarrow 2}$

3. Modeling of the neutron leakage spectrum

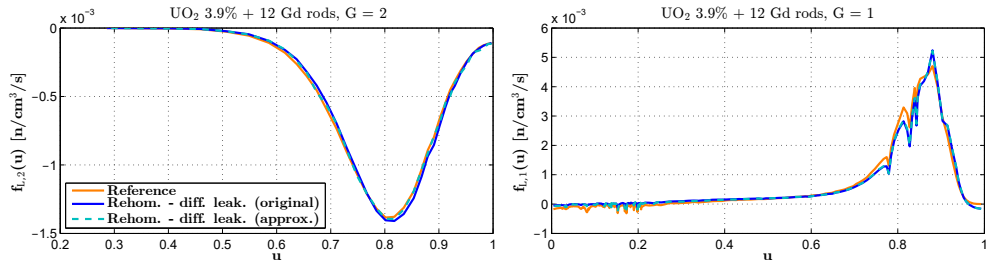


Fig. 3.12. Example 4: leakage spectrum in the UO_2 assembly with gadolinium-bearing fuel rods, as computed by rehomogenization with the diffusive model and the hybrid modal approach.

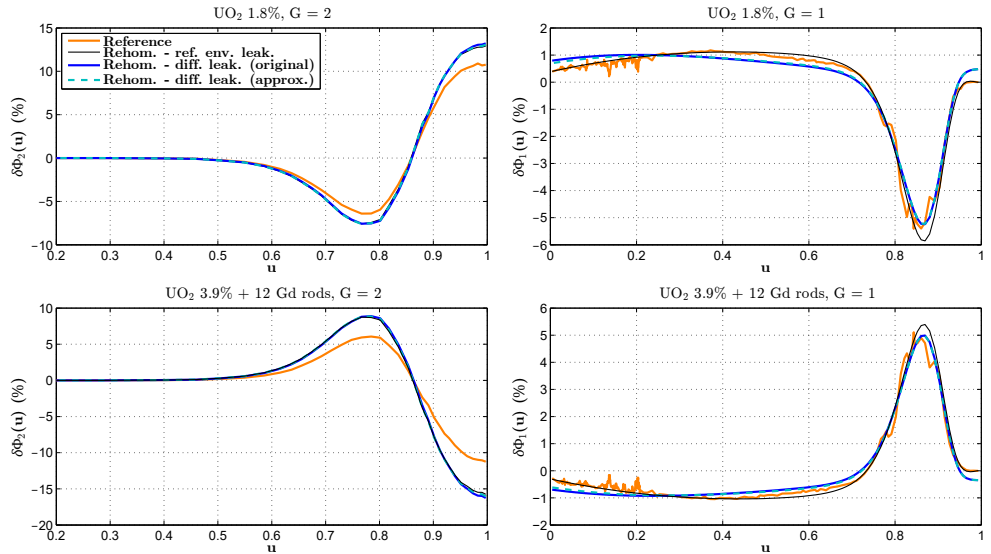


Fig. 3.13. Example 4: spectrum variation computed by rehomogenization with the diffusive leakage model and the hybrid modal approach.

are overcorrected due to the overestimation of $\delta\Phi_1(u)$ in the epithermal range. The correction on $\nu\Sigma_{f,1}$ is larger than the reference value in the assembly with poison, whereas it goes in the wrong direction in the low-enriched bundle. These inaccuracies are due to the misprediction of the spectrum change in the epithermal region and in the range $[0.95, 1.0]$ (i.e., $E \in [8.2 \text{ MeV}, 19.6 \text{ MeV}]$), where a non-zero $\delta\Phi_1(u)$ is computed. The errors in k_{eff} and fission power do not decrease significantly if only the spectral effects are accounted for.

Table 3.10. Example 4: errors in the nodal cross sections of the assembly without gadolinium.

UO ₂ 1.8%	$\Sigma_{a,1}$	$\Sigma_{a,2}$	$\nu\Sigma_{f,1}$	$\nu\Sigma_{f,2}$	$\Sigma_{t,1}$	$\Sigma_{t,2}$	$\Sigma_{s,1\rightarrow 1}$	$\Sigma_{s,1\rightarrow 2}$	$\Sigma_{s,2\rightarrow 2}$
Reference [cm ⁻¹]	0.00889	0.0721	0.00486	0.0806	0.540	1.310	0.513	0.0180	1.237
Simulation	Errors (%)								
No rehom. (a)	-0.99	1.06	0.31	1.30	-0.59	0.36	-0.57	-0.96	0.32
Ref. $\delta\Sigma_G^{\text{spec}}$ (b)	0.02	0.23	0.22	0.44	0.02	-0.11	0.02	-0.01	-0.13
Rehom. (Hybr.) - ref. env. leak. (c)	0.29	0.07	0.15	0.28	0.08	-0.20	0.07	0.03	-0.22
Rehom. (Hybr.) - diff. leak., original (d)	0.44	0.08	0.51	0.29	0.0	-0.19	-0.03	0.59	-0.21
Rehom. (Hybr.) - diff. leak., approx. (e)	0.39	0.07	0.48	0.28	-0.01	-0.20	-0.03	0.45	-0.22

Table 3.11. Example 4: errors in the nodal cross sections of the assembly with gadolinium.

UO ₂ 3.9% + 12 Gd rods	$\Sigma_{a,1}$	$\Sigma_{a,2}$	$\nu\Sigma_{f,1}$	$\nu\Sigma_{f,2}$	$\Sigma_{t,1}$	$\Sigma_{t,2}$	$\Sigma_{s,1\rightarrow 1}$	$\Sigma_{s,1\rightarrow 2}$	$\Sigma_{s,2\rightarrow 2}$
Reference [cm ⁻¹]	0.0103	0.119	0.00740	0.152	0.531	1.349	0.504	0.0164	1.228
Simulation	Errors (%)								
No rehom. (a)	0.93	-2.46	0.11	-0.90	0.55	-0.59	0.53	0.91	-0.42
Ref. $\delta\Sigma_G^{\text{spec}}$ (b)	-0.03	-1.71	-0.21	-0.10	-0.01	-0.13	-0.01	0.02	0.02
Rehom. (Hybr.) - ref. env. leak. (c)	-0.28	-1.36	-0.21	0.28	-0.08	0.09	-0.07	-0.02	0.23
Rehom. (Hybr.) - diff. leak., original (d)	-0.45	-1.36	-0.45	0.27	-0.03	0.09	0.0	-0.61	0.23
Rehom. (Hybr.) - diff. leak., approx. (e)	-0.40	-1.36	-0.42	0.28	-0.02	0.09	0.0	-0.48	0.23

Table 3.12. Example 4: number of power iterations and errors in the multiplication factor, nodal flux and fission power.

Simulation	N_{iter}	Δk_{eff} [pcm]	UO ₂ 1.8%		UO ₂ 3.9% + 12 Gd rods	
			$\Delta\bar{\Phi}_G$ (%)	$\Delta\bar{P}_{\text{fss}}$ (%)	$\Delta\bar{\Phi}_G$ (%)	$\Delta\bar{P}_{\text{fss}}$ (%)
No rehom. (a)	9	712	0.48, -2.15	-1.74 (0.18, -2.25)	-0.49, 3.30	1.20 (-0.11, 1.63)
Ref. $\delta\Sigma_G^{\text{spec}}$ (b)	9	698	0.27, -1.24	-1.65 (0.15, -2.13)	-0.36, 2.42	1.14 (-0.09, 1.55)
Rehom. (Hybr.) - ref. env. leak. (c)	13	717	0.26, -1.17	-1.79 (0.06, -2.28)	-0.32, 2.16	1.24 (-0.04, 1.66)
Rehom. (Hybr.) - diff. leak., original (d)	12	698	0.19, -0.85	-1.36 (0.44, -1.84)	-0.27, 1.85	0.94 (-0.26, 1.34)
Rehom. (Hybr.) - diff. leak., approx. (e)	12	704	0.21, -0.93	-1.45 (0.41, -1.94)	-0.28, 1.91	1.0 (-0.24, 1.41)

3.3.1.5 Example 5 (fuel depletion)

We consider a colorset with three 1.8%-enriched UO₂ assemblies and a 3.1%-enriched UO₂ assembly hosting 16 Pyrex rods. The composition and the internal layout of the fuel bundles are the same as those displayed in Fig. 2.5. The fuel elements are burnt at a power volumetric density of 107.03 kW/l until an average colorset exposure of 12.0 GWd/t, which corresponds to about 303 days. The depletion is performed with 50 burn-up steps of gradually increasing size. The values of the state parameters are kept constant during the evolution. The diluted-boron concentration (1000 ppm) is chosen so as to make the configuration critical during the first part of the depletion (Fig. 3.14).

In this test case, the two-group cross-section libraries are generated with the critical-buckling correction, which is the default option in the ARTEMIS nodal code. Rehomogenization is applied with the Chebyshev basis functions also in the thermal group, and with the approximate variant of the diffusive leakage method. In APOLLO2-A,

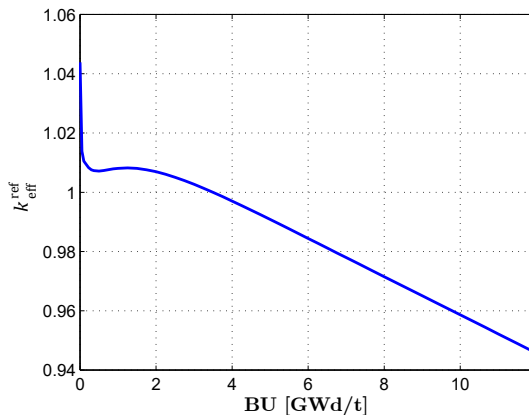


Fig. 3.14. Example 5: reference multiplication factor versus burn-up.

the rehomogenization coefficients are only parameterized versus the burn-up, the fuel temperature and the moderator temperature. They are computed at predetermined nominal values of the moderator density and of the concentrations of diluted boron and xenon. During the nodal calculation, they are updated to account for differences between the actual values of these three state parameters in each node and the nominal ones. As mentioned in Section 2.4.2, this choice is made to minimize the memory requirement for the storage of the additional rehomogenization entries in the cross-section tables. The full details of the algorithm developed for the update are given in Section 4.4.6. In the framework of the present analysis, we have verified that the error introduced using updated rehomogenization coefficients (instead of computing them at the exact, local conditions) is negligible or small.

Fig. 3.15 shows the spectrum variation in the 1.8%-enriched assembly next to the assembly with Pyrex rods at the beginning and at the end of the depletion. In the fast group, the reference curve exhibits a change of sign and a significant deformation with the burn-up, especially at high energies. As observed in the UO_2/MOX test case (example 3), rehomogenization succeeds in predicting the average behavior of the distribution in the epithermal and intermediate regions of the spectrum, but it fails to reproduce rigorously its strongly varying outline in the upper part of the energy domain. The comparison with the reference-leakage-input curve reveals that the leakage spectrum is accurately estimated by the diffusive model and that the above inaccuracy is mostly due to the inherent limitations of a polynomial synthesis in the fast group. In the thermal range, neither the shape nor the magnitude of the spectrum perturbation changes appreciably with the fuel exposure, and the reconstruction remains accurate throughout the evolution.

Figs. 3.16 and 3.17 depict the errors in the absorption and production cross sections of the fuel assembly with Pyrex rods and the poison-free bundle next to it as a

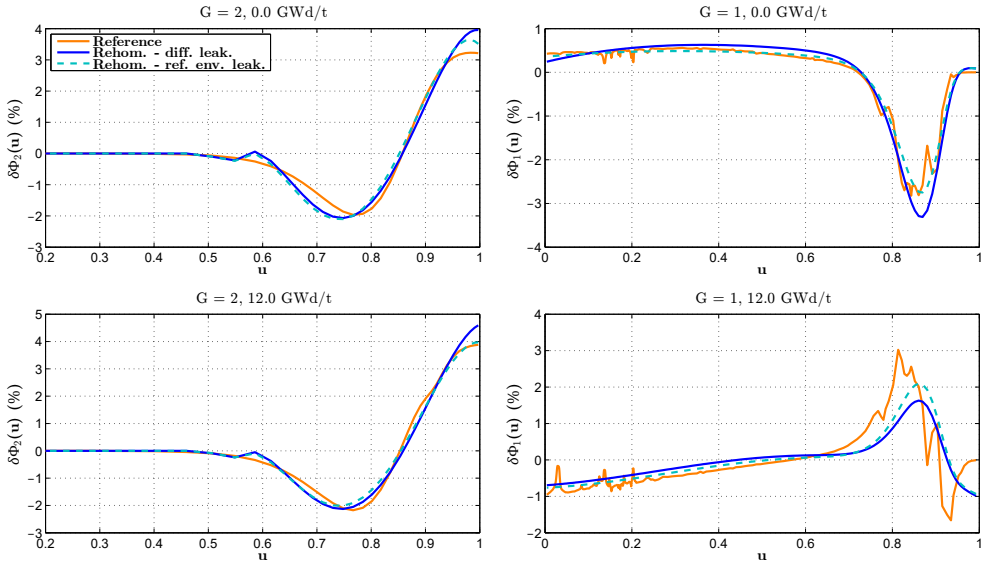


Fig. 3.15. Example 5: spectrum variation in the 1.8%-enriched assembly adjacent to the 3.1%-enriched poisoned bundle, at 0 GWd/t (top) and 12.0 GWd/t (bottom).

function of the burn-up. In the plots the zero-error bar is highlighted. The corrections computed with the diffusive model are in good agreement with those obtained with the reference-leakage input. A significant overcorrection is only found for fast absorption in the assembly with burnable absorber. For both reaction types, a considerable improvement is achieved in the thermal group of the heterogeneous (i.e., poisoned) assembly, above all in $\nu\Sigma_{f,2}$, and in the fast group of the assembly without Pyrex. In the poison-free bundle, the errors in $\Sigma_{a,2}$ are significantly reduced in the first part of the depletion. However, they increase with burn-up and ultimately overcome in magnitude the homogenization defect, which slowly decreases with the fuel exposure. No gain in accuracy is found for fast absorption in the heterogeneous assembly.

The errors in the nodal flux are shown in Fig. 3.18 for the aforementioned two assemblies and in Fig. 3.19 for the 1.8%-enriched assembly next to an assembly of the same type. The improvement produced by rehomogenization is evident in the thermal group, where in the absence of spectral corrections the errors increase significantly with the burn-up (up to 2% in the assembly with Pyrex rods and about 1% in the remaining two bundles). With the diffusive-leakage-based rehomogenization, the errors are bounded below 0.5% in the dissimilar adjacent assemblies and 0.2% in the third bundle. Furthermore, they do not change significantly with the fuel exposure, whereas in the calculation with infinite-medium cross sections they exhibit a monotonically increasing behavior during the second part of the depletion.

Fig. 3.20 shows the evolution of the error in the nodal fission power of the dissimilar

3. Modeling of the neutron leakage spectrum

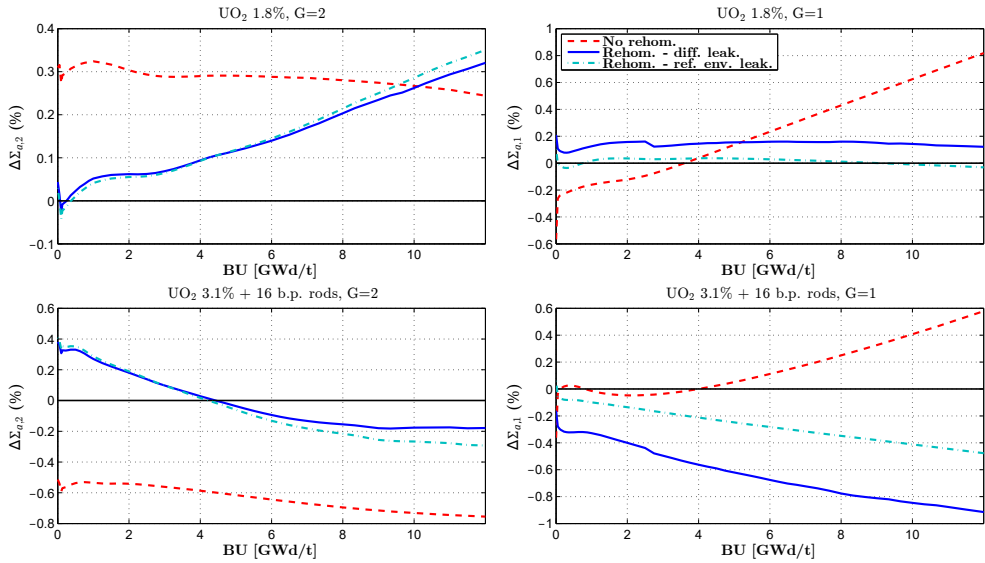


Fig. 3.16. Example 5: error in the two-group absorption cross section as a function of burn-up in the two adjacent dissimilar assemblies.

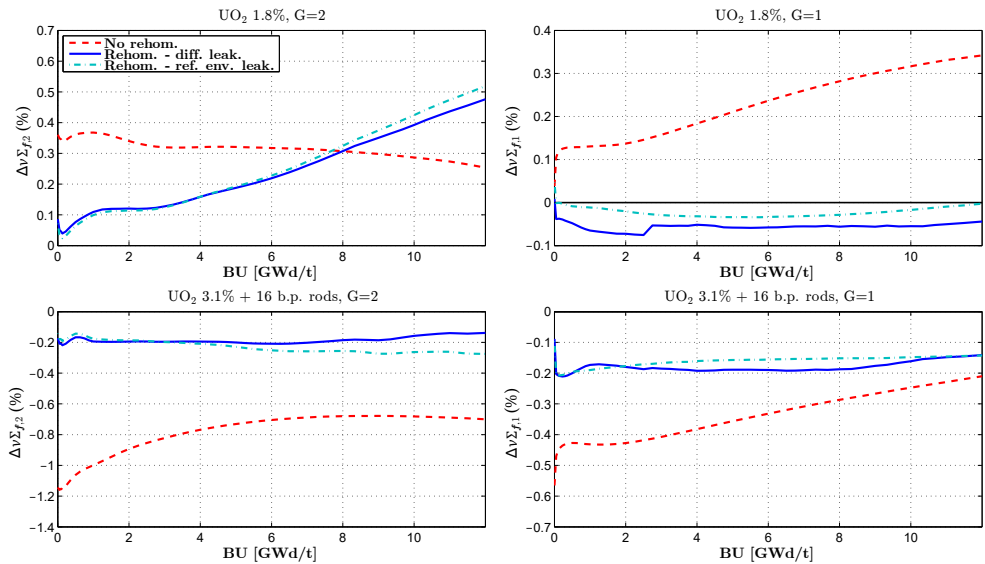


Fig. 3.17. Example 5: error in the two-group production cross section as a function of burn-up in the two adjacent dissimilar assemblies.

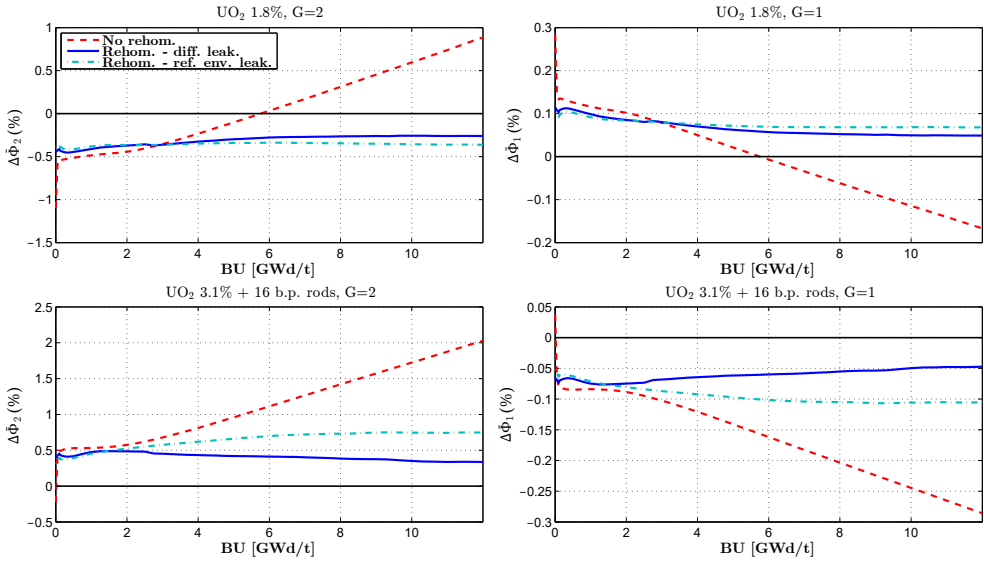


Fig. 3.18. Example 5: error in the two-group nodal flux as a function of burn-up in the two adjacent dissimilar assemblies.

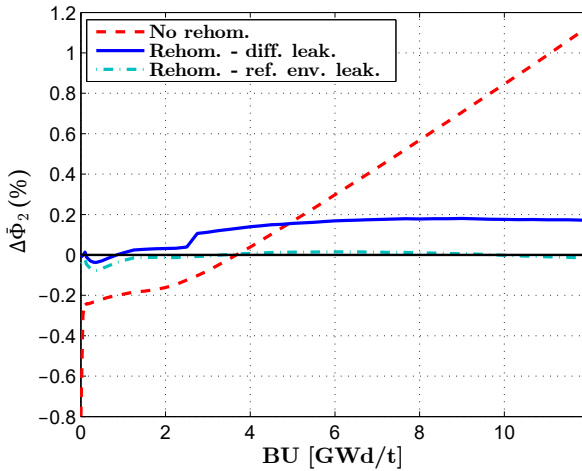


Fig. 3.19. Example 5: error in the thermal-group nodal flux as a function of burn-up in the UO_2 assembly adjacent to an identical assembly.

neighboring assemblies. The benefits of rehomogenization are apparent, especially in the first part of the depletion. The behavior of the curves can be interpreted as follows. When infinite-medium cross sections are used, the power is underestimated in the more

3. Modeling of the neutron leakage spectrum

reactive assembly (i.e., the 3.1%-enriched one). This is due to the underestimation of its thermal production cross section (see Fig. 3.17). Therefore, the fuel initially burns less and loses reactivity more slowly, which goes in the direction of an increase in the power with burn-up. The opposite occurs in the least reactive assembly type (the low-enriched one), in which the power is overestimated. A consequence of this evolution is that the power deviations tend to decrease with burn-up in the three assemblies. As shown in Fig. 3.21, the error in the multiplication factor (which is initially negative) also becomes lower for increasing values of the fuel exposure and approaches a constant value. When rehomogenization is applied, the deviations in the power are considerably lower, especially in the assembly with Pyrex rods at the beginning of the depletion. However, with the error pattern introduced by the spectral corrections, the self-healing effect discussed above vanishes. This might be the cause (or one of the causes) of the monotonically increasing behavior of the errors in the power and in k_{eff} (Fig. 3.21) when rehomogenization is applied.

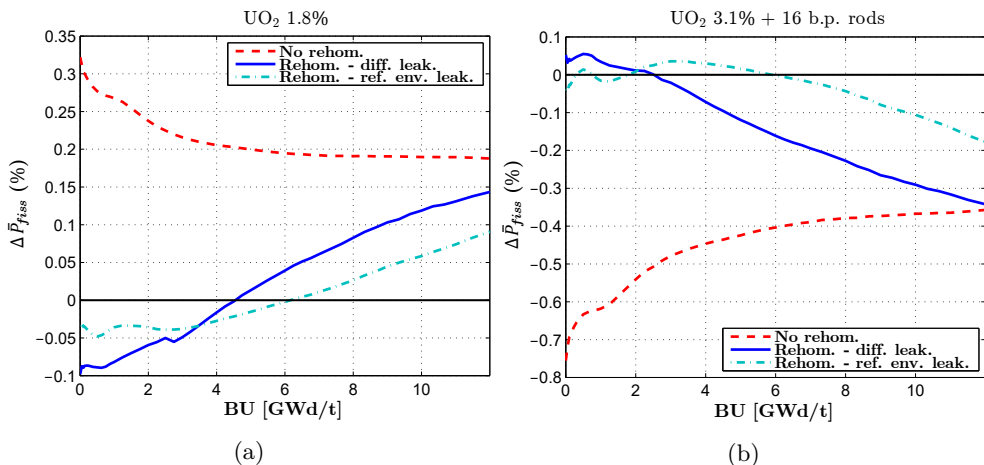


Fig. 3.20. Example 5: error in the nodal fission power as a function of burn-up in the two adjacent dissimilar assemblies.

Another possible source of inaccuracy in the depletion is that, in this analysis, the spectral corrections are only computed for the macroscopic cross sections. Few-group microscopic cross sections are not rehomogenized. Therefore, the solution of Bateman's equations for the depletion of fissile isotopes, fission products and burnable poison benefits from rehomogenization only in part, namely, via the improved accuracy in the few-group nodal flux as observed in Figs. 3.18 and 3.19. This source of error could be removed introducing isotopic rehomogenization coefficients to correct the microscopic cross sections. Based on Eq. (2.12), the reference and variational isotopic parameters

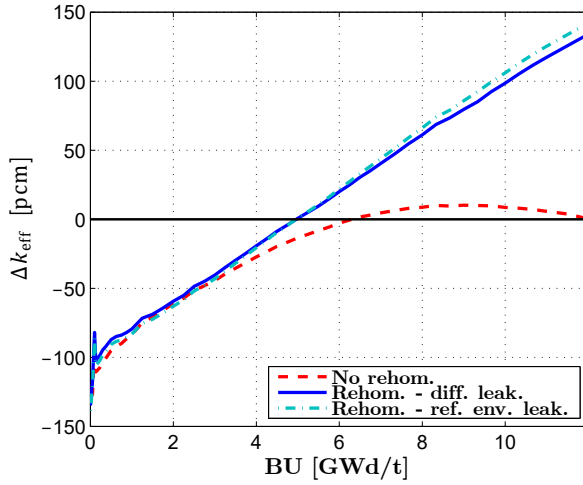


Fig. 3.21. Example 5: error in the multiplication factor as a function of burn-up.

for the generic nuclide c and the reaction type x can be defined as

$$h_{R,x,c,G,j} = \int_0^1 du W_{G,j}(u) \sigma_{x,c,G}(u) \varphi_{\infty,G}(u), \quad (3.33a)$$

$$h_{V,x,c,G,i,j} = \int_0^1 du W_{G,j}(u) \sigma_{x,c,G}(u) Q_{G,i}(u). \quad (3.33b)$$

A relation similar to Eq. (2.15) holds for the microscopic cross section $\sigma_{x,c,G}$:

$$\delta\sigma_{x,c,G} = \frac{1}{\bar{\Phi}_G} \sum_{i=1}^{N_{Q_G}} \alpha_{G,i} h_{V,x,c,G,i,0}. \quad (3.34)$$

Rehomogenization of microscopic cross sections is addressed more in detail in Chapter 4.

3.3.2 Comparison with the fundamental-leakage approach

In this part of the analysis, the fundamental-leakage approach is investigated and compared to the diffusive method for some test cases without feedback or depletion. Nodal calculations are performed with BRISINGR (Appendix A). The infinite-medium cross sections and discontinuity factors and the rehomogenization coefficients are computed with APOLLO2-A (Martinolli et al., 2010). This choice has been made to avoid a computationally demanding fine-group B_1 spectrum calculation in SERPENT (Leppänen et al., 2015). The diffusion coefficients are obtained from the homogeneous B_1 model. This approach makes the assumption that the leakage coefficient $D_G(u)$,

3. Modeling of the neutron leakage spectrum

which defines the critical leakage [Eq. (3.31)], can be used as diffusion coefficient (Hebert, 2009). The results are briefly presented for examples 1 and 2, which are now simulated using single-assembly input data generated with the critical-buckling procedure. An additional test case (a non-critical UO_2/MOX colorset) is also considered. Rehomogenization is applied with the hybrid modal approach.

For the assembly of example 1 hosting Pyrex rods (Section 3.3.1.1), Fig. 3.22 compares (i) the fundamental-mode leakage computed with APOLLO2-A single-assembly-generated data and (ii) the leakage predicted by rehomogenization with the diffusive model. The spectrum perturbation determined with the two approaches is also depicted.

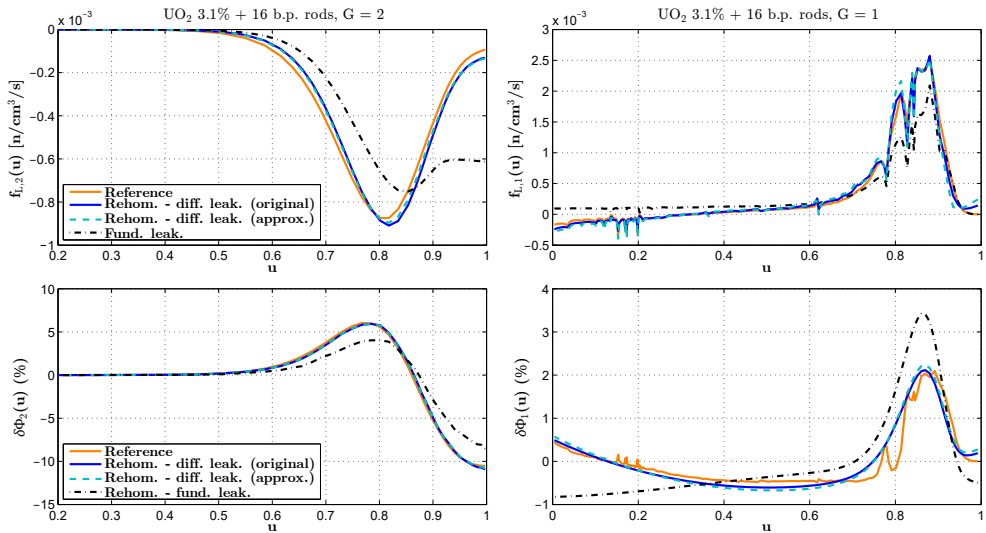


Fig. 3.22. Example 1: fundamental-mode and diffusive leakage distributions (top), and corresponding spectrum variation (bottom) in the assembly with Pyrex rods for the calculation with B^2 -corrected input data.

In the thermal group, the critical-leakage spectrum significantly overestimates the amplitude of the reference for $u_2 \in [0.85, 1.0]$ ($E \in [0.15 \text{ eV}, 0.625 \text{ eV}]$) and underestimates it in the remaining part of the domain ($u_2 \in [0.5, 0.85]$, corresponding to $E \in [6 \text{ meV}, 0.15 \text{ eV}]$). As a consequence, the magnitude of the spectrum change is underestimated in the two lethargy ranges. In the epithermal region ($u_1 \in [0, 0.3]$, $E \in [0.625 \text{ eV}, 110 \text{ eV}]$), the environmental leakage is negative (i.e., there is an incoming flow of neutrons), whereas the fundamental-mode leakage is positive. Therefore, the fast-group spectrum deformation computed with the latter deviates significantly from the reference in this lethargy range and eventually has opposite sign near the thermal cut-off. Since in this region the fine-group cross sections are higher than in the remainder of the fast-group domain, an error in the prediction of

the spectrum variation has more weight. In the high-energy region ($u_1 \in [0.75, 0.85]$, that is, $E \in [0.27 \text{ MeV}, 1.5 \text{ MeV}]$), the underestimation of the environmental leakage causes a considerable overprediction of $\delta\Phi_1(u)$. Analogous results are found for the assembly without Pyrex rods. The effect of the aforementioned mispredictions in the fast group can be observed in Table 3.13, which shows the deviations in the integral parameters and in the main nodal cross sections. With the fundamental-leakage approach (calculation f), $\Sigma_{a,1}$ is overcorrected, whereas the corrections on $\nu\Sigma_{f,1}$ go in the wrong direction. For both reaction types, the errors become higher than in the calculation without rehomogenization. In the thermal group the corrections have the right sign, but their magnitude is underestimated. The error in the fission power increases notably. Also in this case, with the diffusive leakage approach the reference cross-section corrections are accurately predicted, and the errors in k_{eff} and in the fission power match the expected values (calculations b and c).

Table 3.13. Example 1: errors in the integral parameters and main nodal cross sections for the simulation with B^2 -corrected input data. Errors are in pcm for the multiplication factor and in percentage for the fission power and cross sections.

Simulation	UO ₂ 1.8%						UO ₂ 3.1% + 16 b.p. rods				
	Errors (%)										
	Δk_{eff} [pcm]	$\Delta \bar{P}_{\text{fiss}}$	$\Delta \Sigma_{a,1}$	$\Delta \Sigma_{a,2}$	$\Delta \nu \Sigma_{f,1}$	$\Delta \nu \Sigma_{f,2}$	$\Delta \bar{P}_{\text{fiss}}$	$\Delta \Sigma_{a,1}$	$\Delta \Sigma_{a,2}$	$\Delta \nu \Sigma_{f,1}$	$\Delta \nu \Sigma_{f,2}$
No rehom. (a)	-189	0.85	-0.04	0.69	0.51	0.81	-0.72	0.10	-0.50	-0.33	-1.03
Ref. $\delta\Sigma_G^{\text{spec}}$ (b)	-158	0.14	0.04	0.14	0.13	0.24	-0.12	-0.03	0.27	-0.10	-0.20
Rehom. - ref. env. leak. (c)	-154	0.11	-0.01	0.08	0.15	0.17	-0.09	0.0	0.28	-0.11	-0.19
Rehom. - diff. leak., original (d)	-155	0.11	0.13	0.12	0.20	0.22	-0.10	-0.13	0.23	-0.17	-0.25
Rehom. - diff. leak., approx. (e)	-154	0.04	0.15	0.12	0.13	0.21	-0.03	-0.15	0.23	-0.12	-0.24
Rehom. - fund. leak. (f)	-177	1.43	0.90	0.24	0.79	0.33	-1.22	-0.98	-0.02	-0.82	-0.52

The same analysis is performed for the colorset of example 2 (Section 3.3.1.2). Fig. 3.23 depicts the leakage distribution and the spectrum variation in the rodded assembly. Compared to the case without critical-buckling correction (Fig. 3.7), the change in shape and sign of the fast-group spectrum deformation is apparent. The reconstruction of the perturbation with the fundamental-leakage approach still lacks accuracy. In the thermal group, similar conclusions can be drawn as for the previous test case. The deviations in the nodal cross sections and integral parameters are in Table 3.14. Calculation e accurately corrects $\Sigma_{a,1}$, which is instead largely undercorrected with simulation f . The error in k_{eff} is reduced by rehomogenization, especially with the diffusive leakage model, whereas the impact on the fission power is quite small (most of the error is due to spatial effects).

In the examples considered so far, homogenization errors in the fast-group infinite-medium cross sections are mostly due to spectral effects, rather than spatial ones. Hence, a last benchmark problem has been tailored to achieve very high errors in the fast-group cross sections. In this way, we can better evaluate the capability of spectral rehomogenization to correct them. The example consists of a UO₂/MOX colorset. The colorset layout is similar to that illustrated in Fig. 2.11a, with one of the two MOX

3. Modeling of the neutron leakage spectrum

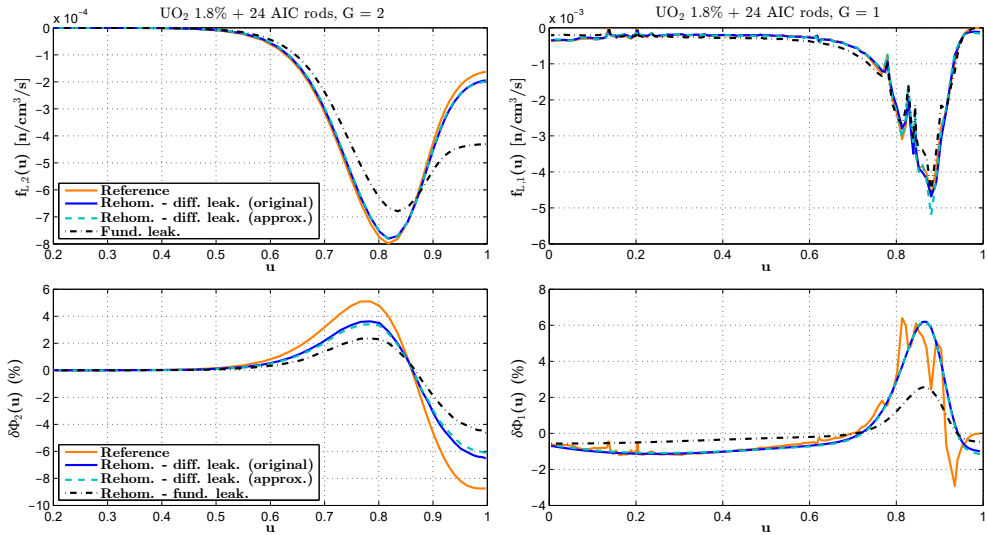


Fig. 3.23. Example 2: fundamental-mode and diffusive leakage distributions (top), and corresponding spectrum variation (bottom) in the rodded assembly for the calculation with B^2 -corrected input data.

Table 3.14. Example 2: errors in the integral parameters and main nodal cross sections for the simulation with B^2 -corrected input data.

Simulation	UO ₂ 1.8%						UO ₂ 1.8% + 24 AIC rods				
	Errors (%)										
	Δk_{eff} [pcm]	$\Delta \bar{P}_{\text{fiss}}$	$\Delta \Sigma_{a,1}$	$\Delta \Sigma_{a,2}$	$\Delta \nu \Sigma_{f,1}$	$\Delta \nu \Sigma_{f,2}$	$\Delta \bar{P}_{\text{fiss}}$	$\Delta \Sigma_{a,1}$	$\Delta \Sigma_{a,2}$	$\Delta \nu \Sigma_{f,1}$	$\Delta \nu \Sigma_{f,2}$
No rehom. (a)	-540	0.94	-0.72	0.43	-0.13	0.46	-1.46	1.83	0.83	0.46	-0.76
Ref. $\delta \Sigma_{\text{G}}^{\text{spec}}$ (b)	-337	1.14	0.05	0.17	0.05	0.20	-1.77	0.47	1.32	-0.02	-0.07
Rehom. - ref. env. leak. (c)	-381	1.12	0.07	0.18	0.02	0.21	-1.74	0.32	1.19	-0.1	-0.27
Rehom. - diff. leak., approx. (e)	-357	1.17	0.12	0.19	-0.13	0.22	-1.82	0.23	1.17	0.08	-0.29
Rehom. - fund. leak. (f)	-434	1.07	-0.51	0.25	-0.08	0.28	-1.66	1.03	1.06	0.22	-0.45

assemblies replaced by another UO₂ assembly. The three UO₂ assemblies are identical and have 3.5% ²³⁵U enrichment, whereas the MOX assembly has 8.0% ²³⁹Pu content. The internal loading of the fuel bundles corresponds to that of Figs. 2.11b and 2.11c. The diluted-boron concentration is 700 ppm, and the reference multiplication factor is 1.26257. The reference values of the fission power are 0.87 in the MOX assembly, 1.03 in the UO₂ assembly next to it and 1.10 in the third UO₂ bundle.

Figs. 3.24 and 3.25 show the spectrum variation in the adjacent UO₂ and MOX assemblies (heterogeneous interface) and in the UO₂ assembly next to two UO₂ bundles (homogeneous interface). Compared to the previous test cases, the fundamental-leakage spectrum provides a better approximation in the fast group. In particular, the prediction is reasonably accurate for the UO₂ assembly next to the MOX assembly.

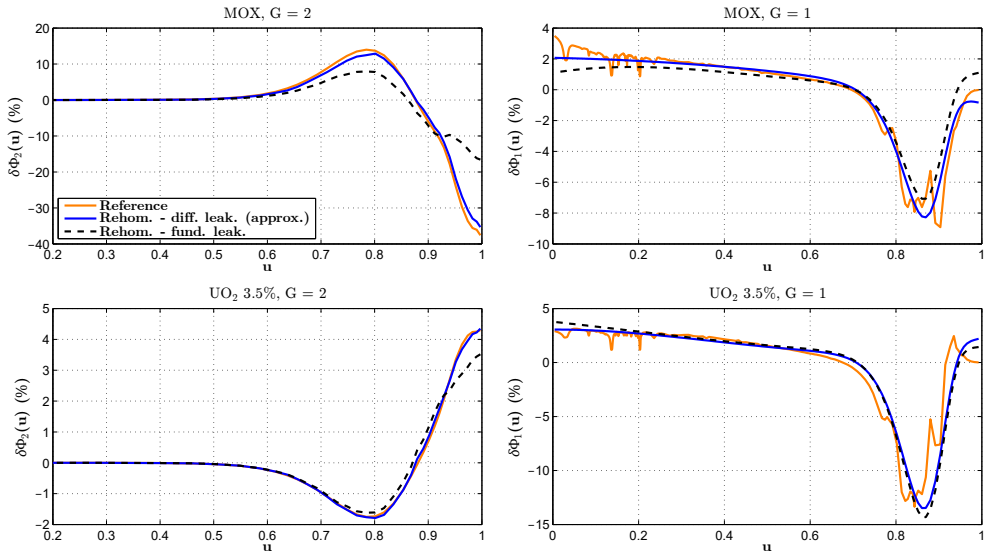


Fig. 3.24. Non-critical UO_2/MOX example: spectrum variation in the adjacent UO_2 and MOX assemblies (heterogeneous interface).

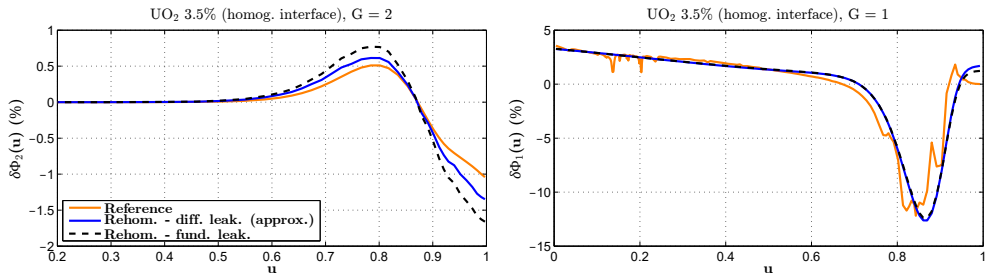


Fig. 3.25. Non-critical UO_2/MOX example: spectrum variation in the UO_2 assembly next to two assemblies of the same type (homogeneous interface).

However, the spectrum perturbation in the latter is considerably underestimated in the epithermal region. In the UO_2 assembly bordering an identical assembly, the two leakage models produce a similarly accurate outcome. In this case, due to the low interassembly heterogeneity the fundamental-leakage approach provides a satisfactory approximation of the environmental leakage. In the thermal group, the infinite-medium leakage strategy is still inadequate, especially in the MOX assembly. Table 3.15 shows the errors in the nodal cross sections and integral parameters. Their magnitude is relevant in the fast-group cross sections (up to 4% in absorption in the MOX assembly). A considerable part of these errors is due to the use of a B^2 -

3. Modeling of the neutron leakage spectrum

Table 3.15. Non-critical UO₂/MOX example: errors in the (a) integral parameters and (b) main nodal cross sections of the three assemblies.

	MOX	UO ₂ 3.5% (next to MOX)	UO ₂ 3.5% (next to UO ₂)
Simulation	Δk_{eff} [pcm]	$\Delta \bar{P}_{\text{fiss}}$ (%)	$\Delta \bar{P}_{\text{fiss}}$ (%)
No rehom. (a)	-26	1.16	0.0
Ref. $\delta \Sigma_G^{\text{spec}}$ (b)	76	1.31	-0.28
Rehom. - ref. env. leak. (c)	-223	0.86	-0.07
Rehom. - diff. leak., approx. (e)	-164	0.40	0.07
Rehom. - fund. leak. (f)	-60	-0.70	0.59

(a)

	MOX				UO ₂ 3.5% (next to MOX)				UO ₂ 3.5% (next to UO ₂)			
	Errors (%)											
Simulation	$\Delta \Sigma_{a,1}$	$\Delta \Sigma_{a,2}$	$\Delta \nu \Sigma_{f,1}$	$\Delta \nu \Sigma_{f,2}$	$\Delta \Sigma_{a,1}$	$\Delta \Sigma_{a,2}$	$\Delta \nu \Sigma_{f,1}$	$\Delta \nu \Sigma_{f,2}$	$\Delta \Sigma_{a,1}$	$\Delta \Sigma_{a,2}$	$\Delta \nu \Sigma_{f,1}$	$\Delta \nu \Sigma_{f,2}$
No rehom. (a)	-3.97	0.60	-1.67	0.57	-3.32	0.31	-2.03	0.33	-3.20	-0.08	-2.06	-0.08
Ref. $\delta \Sigma_G^{\text{spec}}$ (b)	-0.08	0.90	0.19	1.04	0.02	0.08	0.23	0.09	0.0	0.02	0.16	-0.03
Rehom. - ref. env. leak. (c)	-0.03	0.87	-0.13	1.0	0.71	0.06	0.24	0.07	0.45	0.0	-0.1	-0.01
Rehom. - diff. leak., approx. (e)	-0.27	0.90	-0.22	1.04	0.72	0.08	0.23	0.09	0.59	0.0	0.03	0.0
Rehom. - fund. leak. (f)	-1.35	0.49	-0.33	0.52	1.02	0.11	0.28	0.12	0.57	0.02	-0.06	0.02

(b)

corrected condensation spectrum in an environment very far from criticality (26257 pcm of positive reactivity). The benefits of rehomogenization in combination with the diffusive leakage model are apparent. The errors in the fast-group cross sections are significantly reduced and become very close to those of calculation *c*. An improvement in the power prediction is also found. With the fundamental-leakage approach, the errors also decrease but to a smaller extent. Moreover, deficiencies in the calculation of the thermal corrections cause a considerable misprediction of the power in the MOX assembly. If no spectral correction is performed, the errors in the thermal flux (not shown in Table 3.15) are relevant : -6.67% in the MOX assembly, -4.88% in the adjacent UO₂ assembly, and -4.92% in the remaining UO₂ bundle. These discrepancies are reduced to -1.88%, 0.17% and 0.03% with calculation *e*, and to -2.88%, 0.87% and 0.15% with calculation *f*. With the fundamental-leakage approach, in the UO₂ assembly next to the MOX one, the somewhat high residual error in $\bar{\Phi}_2$ deteriorates the estimate of the total power, even if the deviations in $\Sigma_{a,2}$ and $\nu \Sigma_{f,2}$ are close to the ones of calculation *c* due to fortuitous error cancellation. The variation in k_{eff} observed with calculation *c* (i.e., our reference for the leakage model) goes in the opposite direction with respect to that of calculation *b* (our global reference for spectral rehomogenization). This is found, to a lesser extent, also for the fission power in the MOX assembly. Such outcome is again a side effect of the use of smoothly varying basis functions, which cannot reproduce in any way the fine details of the spectrum perturbation (in particular, the resonance spikes).

The same UO₂/MOX colorset has been simulated in critical conditions, obtained

with a soluble-boron concentration of 4392 ppm. Fig. 3.26 shows the corresponding spectrum variation in the adjacent UO_2 and MOX assemblies. As in the example with Pyrex rods (Fig. 3.22), the critical-leakage approach provides a poor approximation of the reference, especially in the fast group. A comparison between the non-critical and critical results (Figs. 3.24 and 3.26, respectively) reveals that the fundamental-leakage approximation does not necessarily perform better in a critical environment.

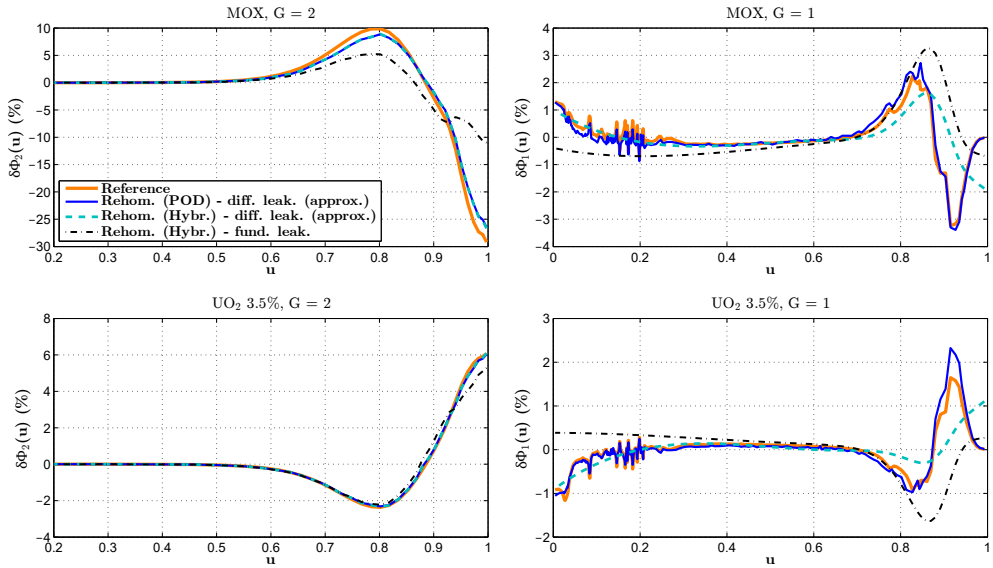


Fig. 3.26. UO_2/MOX example: spectrum variation in the adjacent UO_2 and MOX assemblies in a critical environment.

3.4 Discussion

In this section we discuss various aspects of the diffusive leakage model. Focus is given to its numerical features and computational efficiency and to the validity of the assumption underpinning the approximate formulation of the method [Eq. (3.21)]. We also address the influence of the fine-group diffusion coefficient definition on the accuracy of the leakage spectrum prediction. To conclude, we briefly mention another track for leakage modeling that has been investigated in this thesis work.

3.4.1 Numerical aspects and implementation features

As mentioned in Section 3.2.1, the diffusive leakage method is non-linear and non-local. Non-linearity is tackled computing the leakage parameter $h_{L,G,j}$ [Eqs. (3.18) and (3.27)] with the spectrum-variation expansion coefficients $\alpha_{G,i}$ from the previous

3. Modeling of the neutron leakage spectrum

rehomogenization iteration. The spectral correction problem cannot be solved independently for each node, as in the case of the fundamental-leakage approach. This requires to store the coefficients $\alpha_{G,i}$ for all the nodes of the system. However, with the Galerkin-based modal synthesis this must be done irrespective of the leakage model to dampen numerical oscillations observed in the convergence process (see Section 2.4.2). Therefore, non-local features of the diffusive approach add no further complexity to the rehomogenization problem.

When the normalization factor $w_G^{k,m}$ is computed for the leakage spectrum at the interface between nodes k and m , numerical instability can arise if the denominator of Eq. (3.20) or Eq. (3.29) has a value close to zero. This can occur, for instance, in adjacent fresh-fuel nodes with the same composition. In order to avoid undesired convergence issues in the nodal simulation, the diffusive approach is only applied if the following approximate threshold condition is met:

$$\frac{|\bar{\Phi}_G^k - \bar{\Phi}_G^m|}{\bar{\Phi}_G^{\text{avg},km}} \leq \epsilon_{\text{tol}}, \quad (3.35)$$

where ϵ_{tol} is a given tolerance and $\bar{\Phi}_G^{\text{avg},km}$ is the arithmetic average of the coarse-group flux in nodes k and m . Otherwise, no action is performed (i.e., the assumption is made that there is no leakage through the given interface) or the fundamental-leakage shape is used for that surface, if available from the lattice calculation. Values of ϵ_{tol} in the range 0.1%-1.0% proved to be a suitable choice. A similar threshold condition should be applied to the node-averaged leakage \bar{L}_G^k , that divides $J_G^{k,m}$ in Eqs. (3.20) and (3.29). However, this second control is not necessary if we use the notation of Eq. (3.13) with normalization to $J_G^{k,m}$, instead of the notation of Eqs. (3.1) and (3.14) with normalization to $J_G^{k,m}/\bar{L}_G^k$.

Due to the non-linearity of the diffusive approach, the spectrum perturbation and the leakage distribution computed by rehomogenization are intimately coupled. In order to reduce oscillations in the convergence of the calculation, numerical damping is performed on the leakage coefficients at each assembly interface. We define the few-group leakage parameter $q_{G,j}^{k,m}$ for the edge of node k bordering with node m (we take as example the approximate formulation of the method):

$$q_{G,j}^{k,m(n)} = \left\{ w_G^{k,m} \left[\bar{\Phi}_G^k h_{R,D,G,j}^k + \sum_{i=1}^{N_{QG}} \alpha_{G,i}^k h_{V,D,G,i,j}^k - \left(\bar{\Phi}_G^m h_{R,D,G,j}^m + \sum_{i=1}^{N_{QG}} \alpha_{G,i}^m h_{V,D,G,i,j}^m \right) \right] \right\}^{(n)}. \quad (3.36)$$

In Eq. (3.36), the superscript (n) refers to the n -th rehomogenization iteration. At each iteration, the parameter $q_{G,j}^{k,m(n)}$ is updated as follows:

$$q_{G,j}^{k,m(n)'} = \theta q_{G,j}^{k,m(n)} + (1 - \theta) q_{G,j}^{k,m(n-1)'}, \quad (3.37)$$

where $q_{G,j}^{k,m^{(n-1)'}}$ denotes the estimate of Eq. (3.36) from the previous rehomogenization iteration, and θ is the damping factor (taken as 0.5). Under-relaxation has been found to strongly increase the stability of the computation. Without it, a significantly lower rate of convergence is observed for most test cases. The drawback of this procedure is that the coefficients $q_{G,j}^{k,m^{(n)'}}$ must be saved in memory for each internodal surface. For a 3-D, two-group simulation with four basis functions per group, the memory requirement is 48 coefficients per node.

When the polynomial-based spectral rehomogenization is combined with the diffusive leakage model, the number of non-linear flux iterations increases by a factor of 1.2 to 1.9. Slower convergence (up to a factor of 2.5) is found with the POD approach. We deem that this loss of computational efficiency is fully compensated for by the observed gain in accuracy. Moreover, the benchmark problems presented in this work have been simulated without thermal-hydraulic feedback. This choice has been made to validate spectral rehomogenization against the reference solutions from SERPENT and APOLLO2-A, in which the thermal feedback cannot be easily included. In an actual core calculation, the method would be nested in the iterations between the flux solver and the thermal-feedback calculation (see Section 2.2.3). Its cost in terms of additional iterations would therefore be amortized.

In all test cases, the fundamental-leakage approach exhibits a somewhat faster convergence than the diffusive one. The increase in the number of flux iterations is always well below a factor of 2. This can be explained by the absence of non-linearity.

3.4.2 On the approximate formulation of the diffusive method

The results presented in Section 3.3 show that the differences between the original and approximate formulations of the diffusive method [Eqs. (3.17) and (3.25)] are negligible. This confirms that the approximation of Eq. (3.21) is generally acceptable. For example, Fig. 3.27 depicts the fine-group diffusion coefficient in the two assemblies of example 1. The deviations between the two distributions are negligible in the fast group, whereas they are more substantial in the thermal group, especially at very low energies. The rehomogenization method is, however, less sensitive to variations in the computed thermal leakage, which has smaller magnitude. The behavior observed in Fig. 3.27 can be justified by considering that the migration of fast neutrons is not significantly affected by differences in the enrichment or by the presence of thermal absorbers (such as burnable poison and control rods). These are only perceived when neutrons are slowed down to thermal energies. A similar outcome has been also found for adjacent assemblies with significantly different fuel composition, such as the UO_2 and MOX assemblies of example 3.

To conclude, we verified that environmental effects on the fine-energy diffusion coefficients are negligible and that the performance of the method is not influenced by the use of the infinite-medium $D_G(u)$ distributions instead of the environmental ones in Eqs. (3.19) and (3.28).

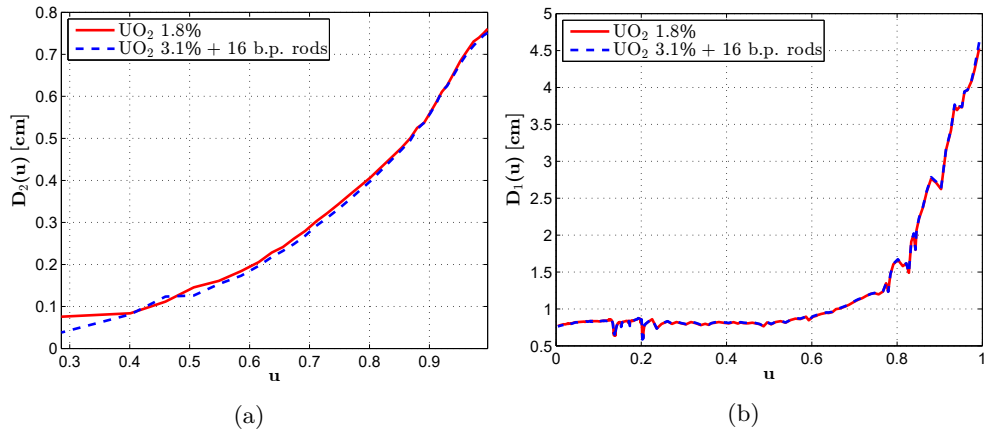


Fig. 3.27. Example 1: (a) thermal-group and (b) fast-group diffusion-coefficient energy distributions, computed with the CMM in SERPENT, in the two adjacent assemblies.

3.4.3 Impact of the diffusion coefficient definition

We now assess the sensitivity of the diffusive-leakage spectrum to the diffusion coefficient formulation and its effect on the performance of the method. The calculation of the diffusion coefficient in deterministic lattice-physics codes is usually based either on the B_1 methodology (Hebert, 2009) or on one of the conventional transport approximations (Choi et al., 2015): consistent P_N , outflow (or out-scatter), and inflow (or in-scatter). Several works (Smith, 2017; Choi et al., 2015, 2017) have highlighted the weaknesses of approaches other than the inflow transport approximation, which is unanimously credited to have the most rigorous foundation. For Monte Carlo codes, Liu et al. (2016) proved that the optimal method is the already mentioned CMM, which is equivalent to the inflow transport approximation in the limit of a homogeneous slab.

For the benchmark problems investigated in Section 3.3, we computed the $D_G(u)$ distributions with the options featured by the SERPENT and APOLLO2-A codes: the CMM for the former, the B_1 model for the latter, and the outflow transport approximation for both. We consider as illustrative case the assembly with gadolinium-bearing fuel pins of example 4, for which Fig. 3.28 shows the diffusion coefficient from the CMM and the outflow transport approximation computed with SERPENT data. The corresponding leakage spectra, determined with the approximate version of the diffusive model, are depicted in Fig. 3.29. In order to focus on the differences caused by the diffusion coefficient formulation, they have been computed using the reference environmental flux spectra. The spectrum variation predicted by rehomogenization with the diffusive method and the hybrid modal approach is also shown. The deviations between the CMM and the outflow transport approximation have an effect on

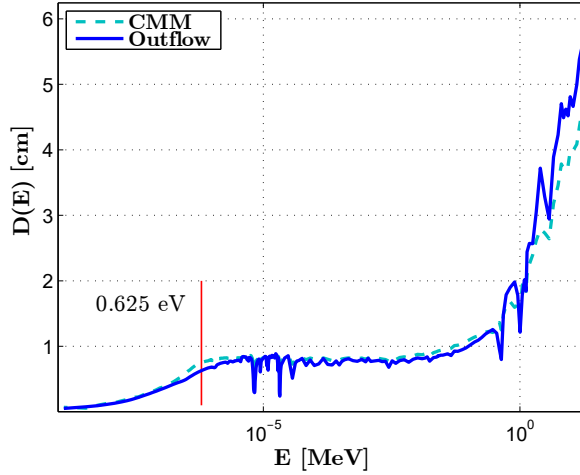


Fig. 3.28. Example 4: fine-group diffusion coefficient in the gadolinium-bearing fuel assembly, computed in SERPENT with the CMM and the outflow transport approximation.

the leakage especially in the higher-energy region of the fast group ($u_1 \geq 0.7$, i.e., $E \geq 0.12$ MeV). Here, the fine-energy diffusion coefficient computed with the CMM is significantly lower than that from the outflow transport approximation. When looking at the spectrum perturbation, the outflow approach is less accurate in the high-energy region. However, it results in a better approximation in the epithermal range, even if the leakage spectra corresponding to the two formulations exhibit negligible differences in this part of the energy domain. In the thermal group, the variations in the spectrum deformation driven by discrepancies in the diffusion coefficient are not significant.

If the outflow transport approximation is used instead of the CMM, the errors in $\Sigma_{a,1}$ and $\Sigma_{s,1 \rightarrow 2}$ decrease from -0.40% and -0.48% (see calculation e in Table 3.11) to -0.12% and -0.15% in the gadolinium-bearing assembly; from 0.39% and 0.45% (see calculation e in Table 3.10) to 0.1% and 0.07% in the assembly without poison. The error in the total fission power also becomes lower than that found with the CMM formulation: from -1.45% and 1.0% (see calc. e in Table 3.12) to -0.92% and 0.64% in the fuel bundles without and with gadolinium, respectively. Therefore, the approach used to compute the diffusion coefficient can have a relevant impact on the outcome of rehomogenization combined with the diffusive leakage method.

The analysis of the remaining benchmark problems showed that in the thermal group the outflow transport approximation generally provides a more accurate leakage reconstruction. However, as observed for the above sample problem, the impact of diffusion coefficient variations is small in this energy group. In the fast group, finding an evident trend is difficult and the accuracy of the various formulations depends on the specific test case.

3. Modeling of the neutron leakage spectrum

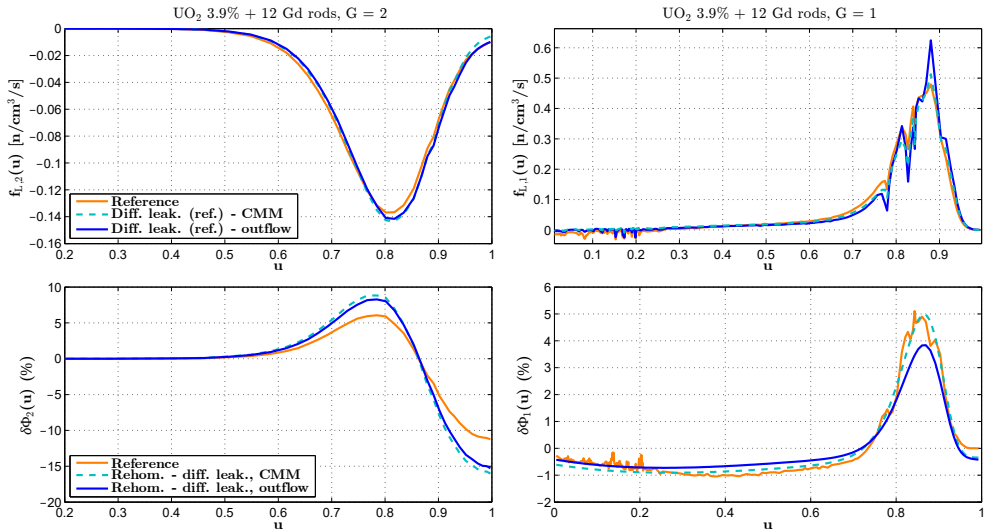


Fig. 3.29. Example 4: reference diffusive-leakage spectrum in the gadolinium-bearing assembly (top) and spectrum variation computed by rehomogenization (bottom) using the fine-group diffusion coefficients from the CMM and the outflow transport approximation (see Fig. 3.28).

3.4.4 Alternative leakage models

Other methods to model the neutron-leakage energy dependence have been examined in this thesis. For example, we have investigated a modal synthesis of the variation in the leakage spectrum between the core environment and the critical infinite lattice. This approach was suggested by the fact that, as observed in Fig. 3.22, the environmental leakage distribution may be approximated as the sum of the fundamental-mode distribution $f_{L,G}^\infty(u)$ and a function $\delta f_{L,G}(u)$:

$$L_{\text{env},G}(u) = \bar{L}_G f_{L,G}^\infty(u) + \delta f_{L,G}(u), \quad (3.38)$$

with

$$\delta f_{L,G}(u) = \sum_{i=1}^{N_{P_G}} \gamma_{G,i} P_{G,i}(u). \quad (3.39)$$

In view of the high accuracy of the diffusive model in the thermal group, the approach of Eqs. (3.38) and (3.39) has been only tested in the fast group. We limited the number of basis functions $P_{G,i}(u)$ to 2 ($N_{P_1} = 2$) and selected the first two modes used for the semi-analytic synthesis of the fast-group spectrum variation (i.e., the neutron fission-emission spectrum and the first-order Chebyshev polynomial). The additional equations to solve for the coefficients $\gamma_{1,i}$ were found projecting the neutron continuity equation

[Eq. (2.7)] over unit double-step functions (namely, 1 inside a given pseudo lethargy interval and 0 outside). Their pseudo lethargy range was determined with a heuristic procedure. For the set of benchmark problems considered in Section 3.3.1, which have been simulated again with B^2 -corrected homogenization parameters, we attempted to minimize the deviations of the computed leakage distribution from the reference one within the epithermal region, where the accuracy of the spectrum variation reconstruction is more important.

This approach provided a better leakage prediction than the fundamental-mode approximation in examples 1, 4 and, to a lesser extent, 3. However, in all cases it was less accurate than the diffusive approximation. The method failed to converge in example 2. Figs. 3.30 and 3.31 show the computed fast-group leakage variation $\delta f_{L,1}(u)$ and the corresponding leakage spectrum in the MOX and gadolinium-bearing assemblies of examples 3 and 4, respectively (see Sections 3.3.1.3 and 3.3.1.4). The computed $\delta f_{L,1}(u)$ is compared with a least-squares best fit of the reference leakage variation, which has been determined with the same basis functions used in the modal expansion. The reconstructed leakage spectrum is compared with the results of the fundamental-mode and diffusive approaches.

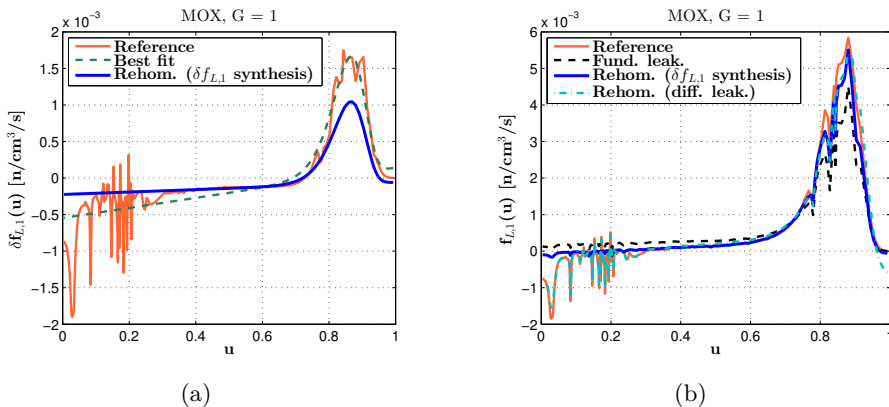


Fig. 3.30. Example 3: (a) fast-group leakage variation between the critical colorset and the critical infinite lattice, and (b) reconstructed fast-group leakage spectrum. The plots refer to the MOX assembly. The distributions are normalized to the node-averaged, coarse-group leakage \bar{L}_1 from the nodal calculation with modal synthesis of the leakage spectrum.

The leakage predicted with this alternative approach is satisfactory in the gadolinium-bearing assembly. However, compared to the diffusive leakage method the loss of accuracy is apparent in the MOX assembly.

Numerical instability was observed increasing the number of basis functions N_{P_1} to 3 or 4. Moreover, we found that this method is highly sensitive to the choice of the pseudo lethargy ranges of the step weighting functions. Small changes in their selection can result in significant perturbations in the leakage reconstruction. Eventually, the

3. Modeling of the neutron leakage spectrum

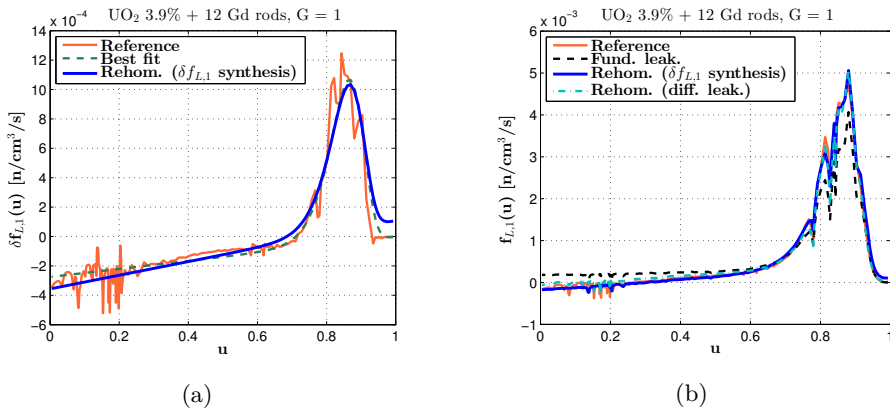


Fig. 3.31. Example 4: (a) fast-group leakage variation between the critical colorset and the critical infinite lattice, and (b) reconstructed fast-group leakage spectrum. The plots refer to the assembly with gadolinium-bearing fuel pins.

leakage modal synthesis approach (which can only be applied with the critical-buckling methodology) was abandoned because of the lack of robustness and of a rigorous theoretical basis supporting the definition of the domain of the step functions.

3.5 Summary

We presented a method to estimate the interassembly neutron-leakage spectrum in the real environment. This computational scheme completes the spectral rehomogenization technique originally developed at Framatome. The proposed approach applies Fick's diffusion law to the node-averaged environmental flux spectra computed by rehomogenization. Numerical results show that rehomogenization combined with this leakage model can capture spectral effects on the few-group nodal cross sections very accurately. In the thermal group, the diffusive approach matches the spectral corrections computed with the reference environmental leakage. In the fast group, more accurate cross-section inputs for nodal routines are also obtained, even though small deviations from the reference corrections are observed in some configurations. These can be due to: (i) minor inaccuracies in the prediction of the leakage distribution in the high-energy and epithermal regions, and (ii) the difficulty of the basis functions reproducing the resonance details of the spectrum perturbation and its strongly varying shape at high energies. A significant improvement in the estimates of the nodal power distribution and of the multiplication factor is found. The gain in accuracy is achieved at a moderate computational cost. The increase in the number of non-linear flux iterations, which depends on the modal approach, is generally below a factor of 2.

The method has been compared to a simpler approach that uses the fundamental-

mode leakage distribution computed by the lattice code in the framework of the B_1 critical-spectrum calculation. For all the test cases, the diffusive model outperforms the critical-leakage strategy. The latter only provides a satisfactory approximation of the environmental leakage in the presence of weak spectral interactions, that is, in assemblies surrounded by assemblies featuring a similar composition. When applied to heterogeneous fuel loading patterns, this method fails to accurately predict the leakage in the thermal and epithermal ranges of the energy spectrum.

Other leakage models were investigated. However, no gain in accuracy was found compared to the diffusive approach, which is the most robust option and remains the default method adopted in ARTEMIS.

MODELING SPECTRAL EFFECTS OF LOCAL NUCLIDE DENSITY CHANGES

4.1 Introduction

As introduced in Section 1.1.2.1, nodal cross sections must be represented as a function of the local, instantaneous physical conditions. For PWRs, the following variables (referred to as state parameters) are commonly chosen for the parameterization of cross sections in libraries: the burn-up, the fuel temperature, the moderator/coolant temperature, the moderator/coolant density, the concentration of boric acid (^{10}B) dissolved in the moderator, and the concentration of xenon (^{135}Xe). An additional parameter is the presence of control rods. Spectral effects due to deviations between the actual core depletion and the single-assembly base depletion may be accounted for with empirically-defined history variables (Watson and Ivanov, 2002; Bilodid and Mittag, 2010). These include the local concentration of ^{239}Pu , the spectral-history index, and the burnable-poison history. However, modern nodal codes make use of microscopic depletion models to track the evolution of a number of nuclides (Bilodid and Mittag, 2010), thus discarding history variables in the cross-section parameterization of PWRs. In Boiling Water Reactor (BWR) core analysis, the coolant density (or void) history and the control-blade history are commonly retained.

The generation of cross-section libraries depends on (*i*) the model chosen for the representation of multivariate dependences, and (*ii*) the state-parameter sampling strategy. These two aspects are briefly reviewed in the following.

It is common practice to represent the cross-section functional dependence by interpolation or approximation methods (Zimin and Semenov, 2005). In both approaches, the mesh for the multidimensional domain is composed of the linear subspaces of the

single independent variables (i.e., the axes or directions). For each axis, a functional basis is found. A generic multivariate function is built by a linear combination of tensor products of the 1-D basis functions. In the interpolation approach (Watson and Ivanov, 2002), the cross sections at a given state (i.e., a point inside the tensorized grid) are computed from the mesh-point values by a linear or higher-order (polynomial, spline) interpolation algorithm. For instance, in ARTEMIS (Hobson et al., 2013) the interpolation functions are based on combinations of cubic B-splines (for the burn-up and moderator density) and second-order polynomials (for the other state variables). Four triplets (namely, three-parameter cross terms) are used to build the multivariate dependence. The interpolation approach is very general, because it demands no knowledge of the functional dependence of the interpolated data. However, it suffers from three main downsides (Zimin and Semenov, 2005; Bokov, 2009): (i) it does not support a direct extrapolation of cross sections at operating points beyond the mesh boundaries, (ii) it requires a regular Cartesian mesh, and (iii) it is prone to the *curse of dimensionality*. The second point may hamper the definition of an optimal grid, because certain state parameters are more important than others in the cross-section representation. Regions of little or no physical interest may be included in the tabulation, causing a worthless increase in the number of lattice calculations and in the size of the cross-section library. The third drawback, typical of high-dimensional systems, is because the number of mesh points and the computational cost of library generation grow exponentially with the number of state parameters (Bokov, 2009). This aspect strongly penalizes the simulation of reactor transients and design basis accidents, for which cross-section libraries must span wider intervals of the state parameters than in ordinary operating conditions.

Approximation techniques aim to estimate cross-term dependences by functional forms (Zimin and Semenov, 2005). Since few-group homogenized cross sections mostly exhibit a smooth behavior versus the state parameters, polynomial functions are usually employed. Functional relations between the single cross sections and the state parameters are not known *a priori*. The main challenge is therefore finding an optimal multivariate polynomial for each cross-section type. Several strategies to identify suitable polynomials are described in the literature. Among them, we mention trial-and-error approaches (Turski et al., 1997), stepwise regression (Zimin and Semenov, 2005), quasi-regression (Bokov and Prinsloo, 2007; Bokov et al., 2008; Bokov, 2009), regression (Dufek, 2011), and the Tucker decomposition (Luu et al., 2017). With approximation techniques, there is no restriction on the type of grid. Unstructured multivariate domains are used, with an appreciable reduction in the number of mesh points and lattice simulations. Extrapolation outside the mesh boundaries is easily performed. Moreover, the so obtained cross-section libraries only contain the regression coefficients. They have therefore significantly smaller size than the parameterized tables ensuing from the interpolation approach (Zimin and Semenov, 2005; Dufek, 2011). However, this strategy is also affected by the curse of dimensionality, because the number of important polynomials increases dramatically if many state variables are considered. Furthermore, since a polynomial function must be determined for each

type of macroscopic and microscopic cross sections, the regression cost may be high. When building the cross-section model (by either interpolation or approximation), the sampling strategy is of great importance for the accuracy and effectiveness of the representation. Quasi-random sampling is used in several polynomial-regression approaches (Zimin and Semenov, 2005; Bokov et al., 2008; Bokov, 2009; Dufek, 2011). Sánchez-Cervera et al. (2014) employed first-order adjoint perturbation theory to evaluate the sensitivity of the infinite-medium multiplication factor (k_∞) to the distance between points in the interpolation grid. For each axis, they estimated the optimal intervals between samples and their minimum number to satisfy a given target accuracy in k_∞ . Recently, an increasing interest has been shown in sparse-grid methods (Botes and Bokov, 2011; Bokov et al., 2012; Botes and Bokov, 2014; Botes et al., 2017). This approach consists of sampling the state-parameter phase space on a reduced tensor-product grid. Sparse-grid sampling was investigated in the framework of both interpolation and regression approaches. For example, Botes and Bokov (2011) showed that, for a linear interpolation algorithm, a sparse grid requires orders of magnitude fewer points than a full tensor-product grid, while satisfying the same target accuracy.

The work presented in this chapter ¹ aims to mitigate some of the weaknesses of the cross-section methodology discussed hitherto. We describe a novel approach to model the spectral effects of three relevant state parameters: the moderator/coolant density (ρ_{H_2O}), the soluble-boron concentration ($C_{B_{10}}$), and the xenon concentration ($N_{Xe_{135}}$). The proposed method is an original development of the spectral rehomogenization technique described in Chapters 2 and 3, which is extended to compute the variation in the infinite-medium condensation spectrum due to local nuclide density perturbations. Changes in the fine-energy homogenized cross sections are incorporated by a heuristic approach. We show that the dependence of the few-group macroscopic and microscopic cross sections on the aforementioned state variables (ρ_{H_2O} , $C_{B_{10}}$, and $N_{Xe_{135}}$) can be accounted for directly. Neither multivariate interpolation in the parameterized libraries nor multidimensional polynomial approximation is needed along these three axes of the state-parameter phase space, which can be eliminated or sampled individually (namely, without cross terms) at far fewer points. This strategy reduces (i) the computational burden of the lattice-physics calculation (i.e., the number of reactor states to be simulated), (ii) the size of cross-section libraries, and (iii) the run time of the nodal-data reconstruction during the on-line calculation.

This chapter is organized as follows. The method is described in Section 4.2. In Section 4.3, we show the numerical results of various test cases. We first validate the methodology on single-assembly configurations. We consider a typical PWR UO₂ fuel assembly at zero burn-up. The accuracy of the cross-section reconstruction is tested for a broad range of the values of the three state parameters considered in this work. Afterwards, we investigate a heterogeneous PWR multiassembly configuration hosting control rods. In this benchmark problem, the method is applied to capture

¹The content of this chapter has been accepted for publication in *Annals of Nuclear Energy*.

the combined spectral effects of perturbations in the local physical conditions and interassembly neutron streaming. In Section 4.4 we discuss several aspects of interest of the methodology, such as its main numerical features and the benefits on the cross-section model. We also address the impact of variations in the state parameters on the assembly discontinuity factors and on the form functions for the pin-power reconstruction. A summary is given in Section 4.5.

4.2 Description of the method

In Section 4.2.1 we describe the method to reconstruct the infinite-medium macroscopic and microscopic nodal cross sections. In Section 4.2.2 we show how neighbor effects (see Chapters 2 and 3) can be incorporated into this procedure.

4.2.1 Reconstruction of the infinite-medium cross sections

The proposed reconstruction method can be applied to both types of cross-section models reviewed in Section 4.1. In this work, we focus on the interpolation technique. This is currently the most widely used approach in core simulators (Bahadir and Lindahl, 2009; Hobson et al., 2013; Guillo et al., 2017).

We define the following set of state parameters (for a PWR):

$$p = \left[Bu, T_{\text{fuel}}, T_{H_2O}, N_{H_2O}, N_{B_{10}}, N_{Xe_{135}} \right], \quad (4.1)$$

denoting, in order, the burn-up, the fuel temperature, the water temperature, the molecular number density of water, and the atomic number densities of diluted boron and xenon. The water mass density ρ_{H_2O} (in g/cm³) and the boron concentration $C_{B_{10}}$ (in parts per million - ppm) are linearly related to the corresponding number densities:

$$\rho_{H_2O} = N_{H_2O} m_{H_2O} \frac{10^{24}}{N_{Av}}, \quad C_{B_{10}} = \frac{N_{B_{10}}}{\rho_{H_2O}} \frac{m_{B_{10}}}{f_{B_{10}}} \frac{10^{24}}{N_{Av}} 10^6, \quad (4.2)$$

where m_{H_2O} is the water molecular weight, $m_{B_{10}}$ is the atomic weight of the isotope ¹⁰B, $f_{B_{10}}$ is the mass fraction of ¹⁰B in the boron mixture, and N_{Av} is the Avogadro number.

In standard approaches, the infinite-medium macroscopic cross section $\Sigma_{x,G}^\infty$ (for a given reaction type x and the coarse energy group G) is reconstructed at the local physical conditions in a node (p_{loc}) as follows:

$$\Sigma_{x,G}^\infty(p_{loc}) = \Sigma_{x,G}^{\infty,\text{res}}(p_{loc}) + \sum_{c=1}^{n_I} N_c^{\text{loc}} \sigma_{x,c,G}^\infty(p_{loc}). \quad (4.3)$$

In Eq. (4.3), n_I is the number of isotopes tracked by the cross-section model; N_c^{loc} is the local number density of isotope c ; $\sigma_{x,c,G}^\infty$ is the coarse-group microscopic cross

section of isotope c ; and $\Sigma_{x,G}^{\infty,\text{res}}$ is the *residual* (i.e., lumped) macroscopic cross section, carrying the contribution of the isotopes that are not modeled explicitly. All the quantities in Eq. (4.3) are spatially homogenized in the node. The cross sections $\sigma_{x,c,G}^{\infty}$ and $\Sigma_{x,G}^{\infty,\text{res}}$ are interpolated in the parameterized libraries at the local values of the variables listed in Eq. (4.1). The densities N_c^{loc} are taken as input from the thermal-hydraulic feedback and fuel depletion calculations (and, possibly, from a critical-boron search for $N_{B_{10}}$).

We introduce a reduced set of state parameters, p' :

$$p' = \left[Bu, T_{\text{fuel}}, T_{H_2O} \right]. \quad (4.4)$$

This subset defines a tensorized grid made of only three axes (instead of six), with the densities N_{H_2O} , $N_{B_{10}}$ and $N_{Xe_{135}}$ kept fixed at a reference nominal value ($N_{H_2O}^{\text{nom}}$, $N_{B_{10}}^{\text{nom}}$, and $N_{Xe_{135}}^{\text{nom}}$) when building the cross-section tables. Using this reduced set and introducing a correction term $\delta\Sigma_{x,G}^{\infty}$, Eq. (4.3) is rewritten as

$$\Sigma_{x,G}^{\infty}(p_{\text{loc}}) = \Sigma_{x,G}^{\infty,\text{res}}(p'_{\text{loc}}) + \sum_{c=1}^{n_I} N_c^{\text{loc}} \sigma_{x,c,G}^{\infty}(p'_{\text{loc}}) + \delta\Sigma_{x,G}^{\infty}. \quad (4.5)$$

The cross sections $\sigma_{x,c,G}^{\infty}$ and $\Sigma_{x,G}^{\infty,\text{res}}$ are now only interpolated at the local burn-up, fuel temperature and water temperature. The spectral effect of changes in N_{H_2O} , $N_{B_{10}}$ and $N_{Xe_{135}}$ from their nominal values is taken into account with the additional term $\delta\Sigma_{x,G}^{\infty}$. This correction is computed on the fly (namely, during the nodal calculation) by an iterative procedure, which we address below.

We define the local (p_{loc}) and nominal (p_{nom}) conditions as

$$p_{\text{loc}} = \left[p'_{\text{loc}}, N_{H_2O}^{\text{loc}}, N_{B_{10}}^{\text{loc}}, N_{Xe_{135}}^{\text{loc}} \right] \quad (4.6a)$$

and

$$p_{\text{nom}} = \left[p'_{\text{loc}}, N_{H_2O}^{\text{nom}}, N_{B_{10}}^{\text{nom}}, N_{Xe_{135}}^{\text{nom}} \right]. \quad (4.6b)$$

The following nominal values are chosen: $\rho_{H_2O}^{\text{nom}} = 0.7 \text{ g/cm}^3$, $C_{B_{10}}^{\text{nom}} = 700 \text{ ppm}$, and $N_{Xe_{135}}^{\text{nom}} = 4.0 \cdot 10^{-9} \text{ a/\AA}^3$ (i.e., atoms/cubic Ångström). The selected value of $N_{Xe_{135}}^{\text{nom}}$ is about twice as high as the the average xenon concentration in the depletion of a highly-enriched UO_2 fuel assembly. This choice is meant to consider an intermediate value between the equilibrium concentration in a standard power reactor and the peak values occurring at the extreme points of a spatial xenon oscillation (Duderstadt and Hamilton, 1976).

Changes in ρ_{H_2O} , $C_{B_{10}}$ and $N_{Xe_{135}}$ (i.e., transitions from p_{nom} to p_{loc}) have three different effects on $\Sigma_{x,G}^{\infty}$:

- a *direct* effect, due to variations in the corresponding number densities;

4. Modeling spectral effects of local nuclide density changes

- a spectral effect, due to variations in the infinite-medium condensation spectrum;
- a third effect, due to perturbations in the fine-energy microscopic cross-section distributions $[\sigma_{\infty,x,c}(E)]$ that are collapsed to few groups via spectrum weighting.

We refer to the third effect as *microscopic* effect. The direct effect is trivially taken into account using the actual local densities ($N_{H_2O}^{\text{loc}}$, $N_{B_{10}}^{\text{loc}}$ and $N_{Xe_{135}}^{\text{loc}}$) in Eq. (4.5). The spectral and microscopic effects act upon the few-group residual and isotopic cross sections. We search an analytic expression to model these effects starting from the definition of the generic isotopic cross section $\sigma_{x,c,G}^{\infty,\text{loc}}$ condensed in the exact, local conditions. This reads

$$\sigma_{x,c,G}^{\infty,\text{loc}} = \frac{1}{\bar{\Phi}_{\infty,G}^{\text{loc}}} \int_{E_G^-}^{E_G^+} dE \sigma_{\infty,x,c}^{\text{loc}}(E) \Phi_{\infty}^{\text{loc}}(E), \quad (4.7)$$

where $\bar{\Phi}_{\infty,G}^{\text{loc}}$ is the few-group flux, $\sigma_{\infty,x,c}^{\text{loc}}(E)$ is the microscopic cross-section energy distribution, and $\Phi_{\infty}^{\text{loc}}(E)$ is the condensation spectrum. All the quantities in Eq. (4.7) are homogenized in the infinite lattice. Using an approach similar to that of Section 2.2.1, we define the condensation spectrum in the local conditions in the domain of the pseudo lethargy u [Eq. (2.6)] as

$$\bar{\Phi}_{\infty,G}^{\text{loc}}(u) = \bar{\Phi}_{\infty,G}^{\text{loc}} \varphi_{\infty,G}^{\text{nom}}(u) + \delta\bar{\Phi}_{\infty,G}(u), \quad (4.8)$$

where $\varphi_{\infty,G}^{\text{nom}}(u)$ is the reference condensation spectrum (normalized to unity) in the nominal conditions, and $\delta\bar{\Phi}_{\infty,G}(u)$ is the spectrum change due to perturbations in ρ_{H_2O} , $C_{B_{10}}$ and $N_{Xe_{135}}$ (i.e., the spectrum change that occurs when moving from p_{nom} to p_{loc}). A similar equation is introduced for $\sigma_{\infty,x,c}^{\text{loc}}(E)$:

$$\sigma_{\infty,x,c,G}^{\text{loc}}(u) = \sigma_{\infty,x,c,G}^{\text{nom}}(u) + \delta\sigma_{\infty,x,c,G}(u). \quad (4.9)$$

Moving from E to u and introducing Eqs. (4.8) and (4.9) into Eq. (4.7), we obtain

$$\sigma_{x,c,G}^{\infty,\text{loc}} = \sigma_{x,c,G}^{\infty,\text{nom}} + \delta\sigma_{x,c,G}^{\infty,s} + \delta\sigma_{x,c,G}^{\infty,m} + \delta\sigma_{x,c,G}^{\infty,*}, \quad (4.10)$$

where we have defined

- the few-group isotopic cross section in the nominal conditions:

$$\sigma_{x,c,G}^{\infty,\text{nom}} = \int_0^1 du \sigma_{\infty,x,c,G}^{\text{nom}}(u) \varphi_{\infty,G}^{\text{nom}}(u); \quad (4.11a)$$

- the isotopic correction term due to the spectral effect:

$$\delta\sigma_{x,c,G}^{\infty,s} = \frac{1}{\bar{\Phi}_{\infty,G}^{\text{loc}}} \int_0^1 du \sigma_{\infty,x,c,G}^{\text{nom}}(u) \delta\bar{\Phi}_{\infty,G}(u); \quad (4.11b)$$

- the isotopic correction term due to the microscopic effect:

$$\delta\sigma_{x,c,G}^{\infty,m} = \int_0^1 du \delta\sigma_{\infty,x,c,G}(u) \varphi_{\infty,G}^{\text{nom}}(u); \quad (4.11c)$$

- a cross (i.e., spectral-microscopic) isotopic correction term:

$$\delta\sigma_{x,c,G}^{\infty,*} = \frac{1}{\bar{\Phi}_{\infty,G}^{\text{loc}}} \int_0^1 du \delta\sigma_{\infty,x,c,G}(u) \delta\Phi_{\infty,G}(u). \quad (4.11d)$$

During the nodal simulation, the nominal cross section $\sigma_{x,c,G}^{\infty,\text{nom}}$ [Eq. (4.11a)] is interpolated in the parameterized libraries at the local values of Bu , T_{fuel} and T_{H_2O} . The iterative calculation of the cross-section corrections of Eqs. (4.11b) to (4.11d) is addressed in Sections 4.2.1.1 and 4.2.1.2. In Section 4.2.1.3 we show how the macroscopic correction $\delta\Sigma_{x,G}^{\infty}$ [Eq. (4.5)] can be computed at each iteration step and provide a global overview of the methodology.

4.2.1.1 The spectral effect

The variation in the condensation spectrum due to local nuclide density changes is estimated following the approach described in Chapter 2 for the environmental spectrum correction, with some different assumptions.

We consider the continuous-energy neutron balance equation in the infinite lattice at the local conditions. In the pseudo lethargy domain, this reads

$$\Sigma_{\infty,t,G}^{\text{loc}}(u) \Phi_{\infty,G}^{\text{loc}}(u) = \sum_{G'=1}^{N_G} \left(\frac{\chi_G(u)}{k_{\infty}^{\text{loc}}} \int_0^1 du' \nu \Sigma_{\infty,f,G'}^{\text{loc}}(u') \Phi_{\infty,G'}^{\text{loc}}(u') + \int_0^1 du' \Sigma_{\infty,s,G' \rightarrow G}^{\text{loc}}(u' \rightarrow u) \Phi_{\infty,G'}^{\text{loc}}(u') \right), \quad (4.12)$$

where k_{∞}^{loc} is the single-assembly multiplication factor. We neglect the dependence of the neutron fission-emission spectrum $\chi_G(u)$ on the local conditions. This approximation is acceptable, because the fission spectrum is mainly determined by the fuel composition and enrichment (Lamarsh, 1966). Eq. (4.12) is valid for the general case without critical-buckling correction on the nodal cross sections. If a critical-spectrum search is made in the lattice-physics calculation, the following leakage rate must be added to the left-hand side of Eq. (4.12) (Hebert, 2009):

$$L_{\infty,G}^{\text{loc}}(u) = D_{\infty,G}^{\text{loc}}(u) B_{\text{crit,loc}}^2 \psi_{\infty,G}^{\text{loc}}(u), \quad (4.13)$$

where $B_{\text{crit,loc}}^2$ is the critical buckling in the local conditions, $D_{\infty,G}^{\text{loc}}(u)$ is the leakage-coefficient distribution, and $\psi_{\infty,G}^{\text{loc}}(u)$ is the critical spectrum. Moreover, k_{∞}^{loc} must

4. Modeling spectral effects of local nuclide density changes

be set to unity on the right-hand side of Eq. (4.12). The critical-buckling approach complicates the solution of the rehomogenization problem applied to Eq. (4.12), because the leakage function detailed in Eq. (4.13) also depends on the local conditions. Since in Section 2.4.4 we have showed that the B_{crit}^2 correction is unnecessary when spectral rehomogenization is applied, in the rest of the derivation we will consider the non-critical medium [Eq. (4.12)]. Some observations about the critical approach will be made in Section 4.4.5.

As in Eq. (2.10), we express the spectrum variation $\delta\Phi_{\infty,G}(u)$ [Eq. (4.8)] as a linear combination of basis functions $Q_{G,i}(u)$:

$$\delta\Phi_{\infty,G}(u) = \sum_{i=1}^{N_{Q_G}} \alpha_{\infty,G,i} Q_{G,i}(u). \quad (4.14)$$

The modal coefficients $\alpha_{\infty,G,i}$ are determined such that Eq. (4.12) is satisfied in a weighted-integral sense. Substituting Eqs. (4.8) and (4.14) into Eq. (4.12) and projecting Eq. (4.12) on the weighting operators $W_{G,j}(u)$ (with $j \in [1, N_{Q_G}]$) yields the following linear system of equations:

$$\begin{aligned} \bar{\Phi}_{\infty,G}^{\text{loc}} h_{R,r,G,j}^{\text{loc}} + \sum_{i=1}^{N_{Q_G}} \alpha_{\infty,G,i} h_{V,r,G,i,j}^{\text{loc}} &= \frac{\chi_{G,j}}{k_{\infty}^{\text{loc}}} \sum_{G'=1}^{N_G} \left(\bar{\Phi}_{\infty,G'}^{\text{loc}} h_{R,f,G'}^{\text{loc}} + \right. \\ &\left. \sum_{i=1}^{N_{Q_{G'}}} \alpha_{\infty,G',i} h_{V,f,G',i}^{\text{loc}} \right) + \sum_{\substack{G'=1 \\ G' \neq G}}^{N_G} \left(\bar{\Phi}_{\infty,G'}^{\text{loc}} h_{R,s,G' \rightarrow G,j}^{\text{loc}} + \sum_{i=1}^{N_{Q_{G'}}} \alpha_{\infty,G',i} h_{V,s,G' \rightarrow G,i,j}^{\text{loc}} \right), \end{aligned} \quad (4.15)$$

with the following expressions for

- the reference rehomogenization coefficients ($h_{R,x,G,j}^{\text{loc}}$):

$$h_{R,r,G,j}^{\text{loc}} = h_{R,t,G,j}^{\text{loc}} - h_{R,s,G \rightarrow G,j}^{\text{loc}}, \quad (4.16a)$$

$$h_{R,t,G,j}^{\text{loc}} = \int_0^1 du W_{G,j}(u) \Sigma_{\infty,t,G}^{\text{loc}}(u) \varphi_{\infty,G}^{\text{nom}}(u), \quad (4.16b)$$

$$h_{R,f,G}^{\text{loc}} = \int_0^1 du \nu \Sigma_{\infty,f,G}^{\text{loc}}(u) \varphi_{\infty,G}^{\text{nom}}(u), \quad (4.16c)$$

$$h_{R,s,G' \rightarrow G,j}^{\text{loc}} = \int_0^1 du W_{G,j}(u) \int_0^1 du' \Sigma_{\infty,s,G' \rightarrow G}^{\text{loc}}(u' \rightarrow u) \varphi_{\infty,G'}^{\text{nom}}(u'); \quad (4.16d)$$

- the variational rehomogenization coefficients ($h_{V,x,G,i,j}^{\text{loc}}$):

$$h_{V,r,G,i,j}^{\text{loc}} = h_{V,t,G,i,j}^{\text{loc}} - h_{V,s,G \rightarrow G,i,j}^{\text{loc}}, \quad (4.17a)$$

$$h_{V,t,G,i,j}^{\text{loc}} = \int_0^1 du W_{G,j}(u) \Sigma_{\infty,t,G}^{\text{loc}}(u) Q_{G,i}(u), \quad (4.17b)$$

$$h_{V,f,G,i}^{\text{loc}} = \int_0^1 du \nu \Sigma_{\infty,f,G}^{\text{loc}}(u) Q_{G,i}(u), \quad (4.17c)$$

$$h_{V,s,G' \rightarrow G,i,j}^{\text{loc}} = \int_0^1 du W_{G,j}(u) \int_0^1 du' \Sigma_{\infty,s,G' \rightarrow G}^{\text{loc}}(u' \rightarrow u) Q_{G',i}(u'); \quad (4.17d)$$

- and the fission-spectrum coefficient ($\chi_{G,j}$):

$$\chi_{G,j} = \int_0^1 du W_{G,j}(u) \chi_G(u). \quad (4.18)$$

The rehomogenization coefficients in Eqs. (4.16) and (4.17) have the same structure as those in Eq. (2.14). However, they depend on both local and nominal quantities, instead of only local quantities.

The few-group flux, the multiplication factor and the rehomogenization parameters must be known to solve Eq. (4.15) for the coefficients $\alpha_{\infty,G,i}$. We compute $\bar{\Phi}_{\infty,G}^{\text{loc}}$ and k_{∞}^{loc} solving the few-group homogenized balance equation in the infinite medium. In a two-group framework and for the practical case with fission emission only in the fast range (namely, $\chi_1 = 1$ and $\chi_2 = 0$), this can be written as

$$\begin{cases} \left(\Sigma_{a,1}^{\infty,\text{loc}} + \Sigma_{s,1 \rightarrow 2}^{\infty,\text{loc}} - \frac{1}{k_{\infty}^{\text{loc}}} \nu \Sigma_{f,1}^{\infty,\text{loc}} \right) \cdot \bar{\Phi}_{\infty,1}^{\text{loc}} = \left(\Sigma_{s,2 \rightarrow 1}^{\infty,\text{loc}} + \frac{1}{k_{\infty}^{\text{loc}}} \nu \Sigma_{f,2}^{\infty,\text{loc}} \right) \cdot \bar{\Phi}_{\infty,2}^{\text{loc}}, \\ \left(\Sigma_{a,2}^{\infty,\text{loc}} + \Sigma_{s,2 \rightarrow 1}^{\infty,\text{loc}} \right) \cdot \bar{\Phi}_{\infty,2}^{\text{loc}} = \Sigma_{s,1 \rightarrow 2}^{\infty,\text{loc}} \cdot \bar{\Phi}_{\infty,1}^{\text{loc}}. \end{cases} \quad (4.19)$$

From Eq. (4.19), the following expression is derived for the multiplication factor:

$$k_{\infty}^{\text{loc}} = \frac{\nu \Sigma_{f,1}^{\infty,\text{loc}}}{\Sigma_{a,1}^{\infty,\text{loc}} + \Sigma_{s,1 \rightarrow 2}^{\infty,\text{loc}}} + \frac{\Sigma_{s,1 \rightarrow 2}^{\infty,\text{loc}}}{\Sigma_{a,1}^{\infty,\text{loc}} + \Sigma_{s,1 \rightarrow 2}^{\infty,\text{loc}}} \cdot \frac{\nu \Sigma_{f,2}^{\infty,\text{loc}}}{\Sigma_{a,2}^{\infty,\text{loc}} + \Sigma_{s,2 \rightarrow 1}^{\infty,\text{loc}}}. \quad (4.20)$$

The two-group flux is computed as

$$\bar{\Phi}_{\infty,1}^{\text{loc}} = 1, \quad \bar{\Phi}_{\infty,2}^{\text{loc}} = \frac{\Sigma_{s,1 \rightarrow 2}^{\infty,\text{loc}}}{\Sigma_{a,2}^{\infty,\text{loc}} + \Sigma_{s,2 \rightarrow 1}^{\infty,\text{loc}}}. \quad (4.21)$$

The nodal cross sections in Eqs. (4.20) and (4.21) are determined with Eq. (4.5), using the value of $\delta \Sigma_{x,G}^{\infty}$ from the latest, partially converged iteration of the reconstruction procedure. In the first iteration, $\delta \Sigma_{x,G}^{\infty}$ is set to zero and only the direct effect of density variations is taken into account.

The rehomogenization parameters detailed in Eqs. (4.16) and (4.17) depend on the

4. Modeling spectral effects of local nuclide density changes

fine-energy macroscopic cross sections in the local conditions $[\Sigma_{\infty,x,G}^{\text{loc}}(u)]$. These can be defined as

$$\Sigma_{\infty,x,G}^{\text{loc}}(u) = \Sigma_{\infty,x,G}^{\text{nom}}(u) + \sum_{c=1}^{n_p} \delta N_c \sigma_{\infty,x,c,G}^{\text{loc}}(u) + \sum_{c=1}^{n_p} N_c^{\text{nom}} \delta \sigma_{\infty,x,c,G}(u), \quad (4.22)$$

where δN_c indicates the variation in the isotopic number density between the local and nominal conditions. To a first approximation, the summations on the right-hand side of Eq. (4.22) are limited to the contributions of H_2O , ^{10}B and ^{135}Xe (i.e., $n_p = 3$). We temporarily neglect perturbations in the isotopic cross-section distributions (namely, the aforementioned microscopic effect), that is

$$\delta \sigma_{\infty,x,c,G}(u) \approx 0, \quad \sigma_{\infty,x,c,G}^{\text{loc}}(u) \approx \sigma_{\infty,x,c,G}^{\text{nom}}(u). \quad (4.23)$$

This assumption is only justified if a sufficiently fine energy mesh is used and if the variation in the state parameters is mild. In Section 4.2.1.2 we will show how this approximation can be relaxed.

Substituting Eqs. (4.22) and (4.23) into Eqs. (4.16) and (4.17), the rehomogenization parameters in the local conditions are estimated as

$$h_{R,x,G,j}^{\text{loc}} \approx h_{R,x,G,j}^{\text{nom}} + \sum_{c=1}^{n_p} \delta N_c h_{R,x,c,G,j}^{\text{nom}} \quad (4.24a)$$

and

$$h_{V,x,G,i,j}^{\text{loc}} \approx h_{V,x,G,i,j}^{\text{nom}} + \sum_{c=1}^{n_p} \delta N_c h_{V,x,c,G,i,j}^{\text{nom}}, \quad (4.24b)$$

where $h_{R,x,c,G,j}^{\text{nom}}$ and $h_{V,x,c,G,i,j}^{\text{nom}}$ are the isotopic rehomogenization coefficients [Eq. (3.33)] evaluated in the nominal conditions:

$$h_{R,x,c,G,j}^{\text{nom}} = \int_0^1 du W_{G,j}(u) \sigma_{\infty,x,c,G}^{\text{nom}}(u) \varphi_{\infty,G}^{\text{nom}}(u), \quad (4.25a)$$

$$h_{V,x,c,G,i,j}^{\text{nom}} = \int_0^1 du W_{G,j}(u) \sigma_{\infty,x,c,G}^{\text{nom}}(u) Q_{G,i}(u). \quad (4.25b)$$

In Eq. (4.24), the macroscopic coefficients $h_{R,x,G,j}^{\text{nom}}$ and $h_{V,x,G,i,j}^{\text{nom}}$ are computed with Eqs. (4.16) and (4.17) using the nominal distributions $\Sigma_{\infty,x,G}^{\text{nom}}(u)$. These coefficients, and the microscopic ones detailed in Eq. (4.25), are interpolated at p_{nom} [Eq. (4.6b)] in the parameterized libraries obtained from the subset p' [Eq. (4.4)]. We use (i) the ^{10}B and ^{135}Xe isotopic coefficients to update the macroscopic coefficients for absorption and removal, and (ii) the H_2O coefficients to update the macroscopic coefficients for absorption, removal and scattering. For example, the macroscopic parameters for the removal cross section [Eqs. (4.16a) and (4.17a)] are evaluated as

$$h_{R,r,G,j}^{\text{loc}} \approx h_{R,r,G,j}^{\text{nom}} + \delta N_{\text{H}_2\text{O}} h_{R,r,\text{H}_2\text{O},G,j}^{\text{nom}} + \delta N_{B_{10}} h_{R,a,B_{10},G,j}^{\text{nom}} + \delta N_{Xe_{135}} h_{R,a,Xe_{135},G,j}^{\text{nom}} \quad (4.26a)$$

and

$$h_{V,r,G,i,j}^{\text{loc}} \approx h_{V,r,G,i,j}^{\text{nom}} + \delta N_{H_2O} h_{V,r,H_2O,G,i,j}^{\text{nom}} + \delta N_{B_{10}} h_{V,a,B_{10},G,i,j}^{\text{nom}} + \delta N_{Xe_{135}} h_{V,a,Xe_{135},G,i,j}^{\text{nom}}. \quad (4.26b)$$

The rehomogenization problem of Eq. (4.15) is solved at each iteration of the cross-section reconstruction algorithm. Also in this case, under-relaxation is performed on the coefficients $\alpha_{\infty,G,i}$ (with a factor $\theta = 0.5$) to dampen numerical oscillations in the convergence process (see Section 2.4.2). The spectral correction on the isotopic cross section $\sigma_{x,c,G}^{\infty}$ [Eq. (4.11b)] is computed as (we set again $W_{G,0}(u) = 1$)

$$\delta\sigma_{x,c,G}^{\infty,s} = \frac{1}{\bar{\Phi}_{\infty,G}^{\text{loc}}} \sum_{i=1}^{N_{Q_G}} \alpha_{\infty,G,i} h_{V,x,c,G,i,0}^{\text{nom}}. \quad (4.27)$$

4.2.1.2 The microscopic effect

Deviations in the fine-group isotopic cross sections between the local and nominal conditions are mainly induced by:

- variations in the energy self-shielding properties due to changes in the moderator/coolant density;
- variations in the average fuel-to-moderator thermal-flux ratio due to perturbations in the xenon concentration.

The first contribution mostly affects resonant isotopes (such as ^{238}U) and is preminent in the fast group. The second contribution acts on the cross-section distributions of the main thermal-neutron absorbers (such as ^{235}U) and is only relevant in the thermal group.

We introduce a new type of isotopic rehomogenization coefficients to estimate the microscopic-effect and cross correction terms [Eqs. (4.11c) and (4.11d)]:

$$s_{R,x,c,G,j} = \int_0^1 du W_{G,j}(u) \delta\sigma_{\infty,x,c,G}(u) \varphi_{\infty,G}^{\text{nom}}(u), \quad (4.28a)$$

$$s_{V,x,c,G,i,j} = \int_0^1 du W_{G,j}(u) \delta\sigma_{\infty,x,c,G}(u) Q_{G,i}(u). \quad (4.28b)$$

We refer to s_R and s_V as *self-shielding* coefficients. Combining Eqs. (4.14) and (4.28), Eqs. (4.11c) and (4.11d) become

$$\delta\sigma_{x,c,G}^{\infty,m} = s_{R,x,c,G,0} \quad (4.29a)$$

and

$$\delta\sigma_{x,c,G}^{\infty,*} = \frac{1}{\bar{\Phi}_{\infty,G}^{\text{loc}}} \sum_{i=1}^{N_{Q_G}} \alpha_{\infty,G,i} sV_{x,c,G,i,0} \cdot \quad (4.29b)$$

We determine the variation functions $\delta\sigma_{\infty,x,c,G}(u)$ and the self-shielding coefficients with a heuristic approach. Below, the procedure is addressed separately for the aforementioned effects of water density and xenon concentration.

For the UO_2 assembly with 1.8% enrichment considered in Chapters 2 and 3, Fig. 4.1 shows the energy distribution of the homogenized, fast-group absorption cross section of ^{238}U at different values of the moderator density. The values of $N_{Xe_{e135}}$ and C_{B10} are $0 \text{ a}/\text{\AA}^3$ and 700 ppm, respectively. The fuel exposure is zero.

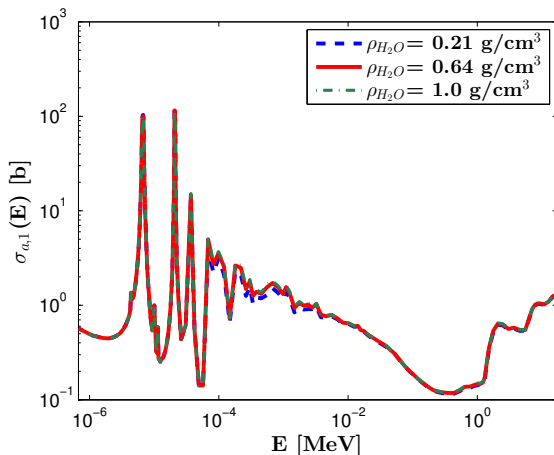


Fig. 4.1. Fine-group, homogenized absorption cross section of ^{238}U versus energy in the fast region (namely, between 0.625 eV and 19.6 MeV), at different values of the moderator density. The figure refers to a 1.8%-enriched UO_2 assembly. Units are in barn.

Changes in ρ_{H_2O} cause perturbations in the isotopic cross-section distribution in the epithermal region, which become significant at very low densities. In order to better appreciate the differences in the low-lying resonance region (namely, between 6.67 eV and 208.46 eV), Fig. 4.2 depicts the variation in the distribution at $\rho_{H_2O} = 0.21 \text{ g}/\text{cm}^3$ with respect to the previously defined nominal conditions. The perturbation is displayed for two values of soluble-boron concentration: 0 ppm and 2450 ppm. The xenon density varies from $4.0 \cdot 10^{-9} \text{ a}/\text{\AA}^3$ to $0 \text{ a}/\text{\AA}^3$. The overlap of the two curves suggests that neither the boron concentration nor the xenon density has an impact on fast-group absorption properties. The microscopic effect is thus only due to the water density. An increase in absorption of 4% and 9.7% is observed for the resonances at 6.67 eV and 20.9 eV, respectively. The impact of this variation on the group-one collapsed macroscopic cross section is relevant and must be taken into

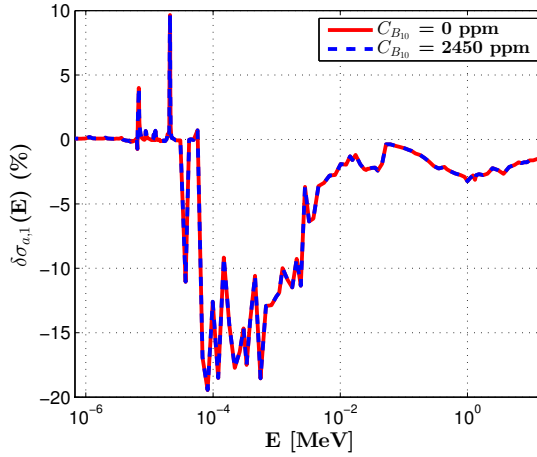


Fig. 4.2. Relative variation (compared to the nominal conditions) in the fine-group, homogenized absorption cross section of ^{238}U in the fast region. Local conditions correspond to $\rho_{\text{H}_2\text{O}} = 0.21 \text{ g/cm}^3$, $N_{\text{Xe}_{135}} = 0 \text{ a/\AA}^3$, $C_{\text{B}_{10}} = 0 \text{ ppm}$ (solid curve) and $C_{\text{B}_{10}} = 2450 \text{ ppm}$ (dashed curve).

account. The variation in the thermal group (not shown here) is less significant and reaches a maximum value of about 2% at 1 meV.

Since a simple relation between $\delta\sigma_{\infty,x,c,G}(u)$ and $\delta N_{\text{H}_2\text{O}}$ cannot be found, we use a regression-like approach to model the dependence of self-shielding coefficients on $N_{\text{H}_2\text{O}}$, without cross terms involving the boron and xenon concentrations. Due to the smoothness of the corresponding behavior, one-variable polynomial approximations of order 1 to 3 proved to be sufficiently accurate. This requires to perform four additional lattice simulations for each burn-up (and, possibly, fuel-temperature) point of the cross-section libraries built in the phase space p' [Eq. (4.4)]. For the type of fuel assembly considered in this work (i.e., UO_2 with neither control elements nor burnable absorbers), we compute the water-density self-shielding coefficients for ^{238}U , ^{235}U and natural zirconium (Zr). These nuclides have been selected based on (i) their contribution to the fast-group macroscopic absorption and fission cross sections and (ii) the amplitude of the variation in their isotopic cross sections with water density. Plutonium isotopes must be included in depletion calculations and for MOX assembly analyses.

The contribution of changes in the xenon concentration to $\delta\sigma_{\infty,x,c,G}(u)$ is a lattice effect and can be explained as follows. In the lattice calculation, the cross section of the absorbing nuclide c (for instance, ^{235}U) in the fine energy group g is spatially homogenized over the fuel assembly as (we omit the subscript x and the superscript

∞)

$$\bar{\sigma}_{c,g} = \frac{\sum_{i_f=1}^{n_{f_c}} N_{c,i_f} \sigma_{c,g,i_f} \Phi_{g,i_f} A_{i_f}}{\bar{N}_c \bar{\Phi}_g A_{fa}}, \quad (4.30)$$

where n_{f_c} is the number of fuel cells in the assembly, A_{i_f} is the cross-sectional area of the i_f -th cell, A_{fa} is the cross-sectional area of the whole assembly, \bar{N}_c is the assembly-averaged number density, and $\bar{\Phi}_g$ is the g^{th} -group assembly-averaged flux (with the water tubes and water gap included in the average). The quantities N_{c,i_f} and σ_{c,g,i_f} are invariant to the physical conditions in the node. If the level of xenon increases (or decreases) compared to its nominal value, the thermal flux becomes more (or less) depressed in the fuel rods. This causes an increase (or decrease) in the ratio of the average flux in the moderator to that in the fuel, commonly referred to as *thermal disadvantage factor* (Duderstadt and Hamilton, 1976). Hence, the ratio $\Phi_{g,i_f}/\bar{\Phi}_g$ in Eq. (4.30) decreases (or increases), and so does $\bar{\sigma}_{c,g}$. This change is less relevant when considering fuel assemblies without empty guide tubes, empty instrumentation tubes, and water channels in general. The correction term for such xenon-induced effect is also computed with a heuristic approach, based on the following observations for the variation function $\delta\sigma_{\infty,x,c,G}(u)$ within the thermal coarse group:

- for a given $\delta N_{Xe_{135}}$, the dependence of the variation function on the other state parameters is negligible (for $C_{B_{10}}$) or small (for ρ_{H_2O});
- the shape of the variation function does not vary with $\delta N_{Xe_{135}}$;
- the magnitude of the variation function scales linearly with $\delta N_{Xe_{135}}$.

The first property is apparent in Fig. 4.3, which shows the behavior of the thermal-absorption variation function of ^{235}U in the 1.8%-enriched UO_2 assembly considered before. The variation has been computed at $N_{Xe_{135}} = 0 \text{ a}/\text{\AA}^3$. Three curves are displayed, corresponding to different values of N_{H_2O} and $N_{B_{10}}$. The second and third properties can be observed in Fig. 4.4, which depicts the same variation function for different values of $N_{Xe_{135}}$ at $\rho_{H_2O}^{\text{nom}}$ and $C_{B_{10}}^{\text{nom}}$. The solid marked lines correspond to the reference distributions $\delta\sigma_{\infty,x,c,G}^{\text{ref}}(u)$ from APOLLO2-A, whereas the dashed lines correspond to the distributions computed with the following approximate relation of linearity:

$$\delta\sigma_{\infty,x,c,G}(u) \approx \left(\sigma_{\infty,x,c,G}^{\text{sample}}(u) - \sigma_{\infty,x,c,G}^{\text{nom}}(u) \right) \frac{\delta N_{Xe_{135}}}{\delta N_{Xe_{135}}^{\text{sample}}}. \quad (4.31)$$

In Eq. (4.31), $\sigma_{\infty,x,c,G}^{\text{sample}}(u)$ is the reference distribution evaluated at a sample concentration of xenon ($N_{Xe_{135}}^{\text{sample}} = 2.0 \cdot 10^{-9} \text{ a}/\text{\AA}^3$ in the example of Fig. 4.4) and at the nominal values of ρ_{H_2O} and $C_{B_{10}}$. We have $\delta N_{Xe_{135}}^{\text{sample}} = N_{Xe_{135}}^{\text{sample}} - N_{Xe_{135}}^{\text{nom}}$. Clearly, Eq. (4.31) provides a very accurate estimate of the reference variation. It can thus be used to model the dependence of the coefficients $s_{R,x,c,G,j}$ and $s_{V,x,c,G,i,j}$ [Eq. (4.28)]

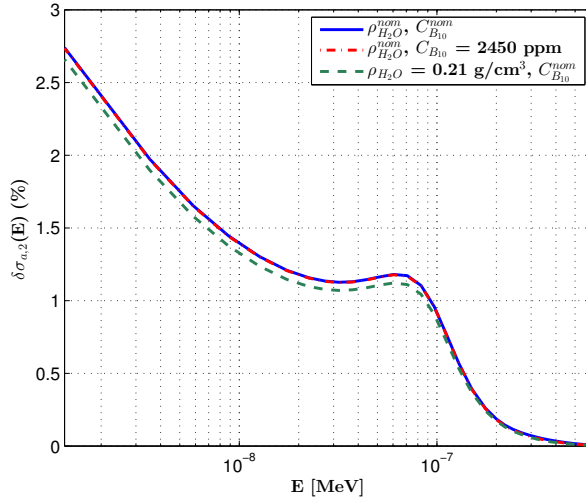


Fig. 4.3. Relative variation (compared to the nominal conditions) in the fine-group, homogenized absorption cross section of ^{235}U in the thermal region. The local conditions correspond to $N_{Xe_{135}} = 0 \text{ a}/\text{\AA}^3$ and different combinations of $\rho_{\text{H}_2\text{O}}$ and $C_{B_{10}}$.

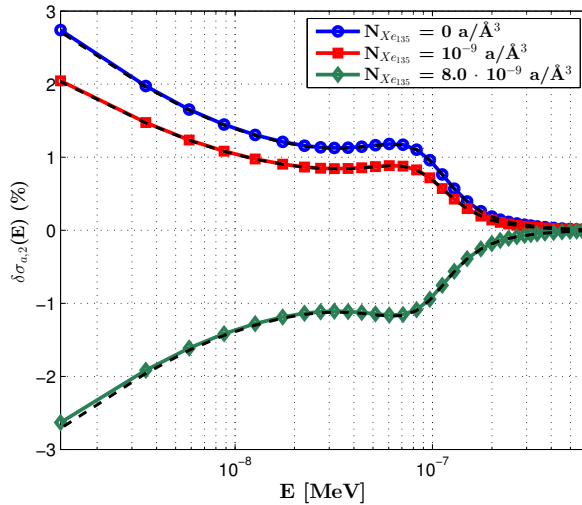


Fig. 4.4. Impact of $N_{Xe_{135}}$ on the variation in the fine-group, homogenized absorption cross section of ^{235}U in the thermal region. The values of $\rho_{\text{H}_2\text{O}}$ and $C_{B_{10}}$ are the nominal ones. The dashed curves have been computed using a linear approximation [Eq. (4.31)].

4. Modeling spectral effects of local nuclide density changes

on N_{Xe135} . This approach only requires, for each value of the burn-up, the simulation of an additional state during the lattice calculation to obtain the sample distribution $\sigma_{\infty,x,c,G}^{\text{sample}}(u)$. In the on-line calculation, the local coefficients are estimated as

$$s_{R,x,c,G,j} \approx s_{R,x,c,G,j}^{\text{sample}} \frac{\delta N_{Xe135}}{\delta N_{Xe135}^{\text{sample}}}, \quad s_{V,x,c,G,i,j} \approx s_{V,x,c,G,i,j}^{\text{sample}} \frac{\delta N_{Xe135}}{\delta N_{Xe135}^{\text{sample}}}. \quad (4.32)$$

In the analysis presented in this chapter, we compute the xenon-related correction terms of Eq. (4.29) for the thermal absorption in ^{235}U , ^{135}Xe , ^{10}B and H_2O , and for the thermal fission in ^{235}U . Since the spectrum variation $\delta\Phi_{\infty,2}(u)$ is zero at very low energies (where the variation function has higher magnitude), the cross correction $\delta\sigma_{x,c,G}^{\infty,*}$ is considerably smaller than the microscopic one $\delta\sigma_{x,c,G}^{\infty,m}$.

It should be noted that a lattice effect similar to that observed for xenon also occurs when the soluble-boron concentration changes. However, the corresponding variation in the fine-group cross sections is less relevant. For instance, the change in the thermal absorption of ^{235}U at 2450 ppm has a maximum value of about 0.15% at 1 meV. Since the corresponding impact on the collapsed cross sections is negligible, this kind of correction is not applied for perturbations in $C_{B_{10}}$.

As explained in Section 4.2.1.1, before solving the spectral rehomogenization problem [Eq. (4.15)] the standard macroscopic rehomogenization coefficients h_R and h_V are corrected with Eq. (4.24) to account for the direct effect of nuclide density changes. Using the self-shielding coefficients of Eq. (4.28), we introduce an additional correction to include the microscopic effects in the reconstruction of the spectrum deformation. For example, Eq. (4.24b) becomes

$$h_{V,x,G,i,j}^{\text{loc}} \approx h_{V,x,G,i,j}^{\text{nom}} + \sum_{c=1}^{n_p} \delta N_c \left(h_{V,x,c,G,i,j}^{\text{nom}} + s_{V,x,c,G,i,j} \right) + \sum_{q=1}^{n_s} N_q^{\text{loc}} s_{V,x,q,G,i,j}, \quad (4.33)$$

where the index q cycles over the aforementioned relevant isotopes other than ^{10}B , ^{135}Xe , and H_2O (namely, ^{238}U , ^{235}U , and Zr for the water-density self-shielding effect; ^{235}U for the xenon-variation effect). For burnable nuclides, the atomic density N_q^{loc} comes from the environmental depletion calculation in the local conditions. We have verified that only the xenon-variation component of this correction has an impact on the solution of Eq. (4.15). The accuracy of the computed spectrum perturbation does not vary if we neglect the water-density microscopic effect on the macroscopic h_R and h_V coefficients (namely, if Eq. (4.24) is used instead of Eq. (4.33)), even at very low values of $\rho_{\text{H}_2\text{O}}$. Hence, the high-order (i.e., with $j > 0$) $s_{R,x,c,G,j}$ and $s_{V,x,c,G,i,j}$ coefficients are only computed for the xenon-induced microscopic effect. This allows us to minimize the regression cost for the calculation of water-density self-shielding coefficients.

4.2.1.3 Overview

At each iteration step, the global isotopic cross-section correction is computed summing the contributions of Eqs. (4.27) and (4.29):

$$\delta\sigma_{x,c,G}^{\infty} = s_{R,x,c,G,0} + \frac{1}{\overline{\Phi}_{\infty,G}^{\text{loc}}} \sum_{i=1}^{N_{QG}} \alpha_{\infty,G,i} \left(h_{V,x,c,G,i,0}^{\text{nom}} + s_{V,x,c,G,i,0} \right). \quad (4.34)$$

The global macroscopic correction is determined as

$$\delta\Sigma_{x,G}^{\infty} = \frac{1}{\overline{\Phi}_{\infty,G}^{\text{loc}}} \sum_{i=1}^{N_{QG}} \alpha_{\infty,G,i} h_{V,x,G,i,0}^{\text{loc}}, \quad (4.35)$$

with the coefficients $h_{V,x,G,i,0}^{\text{loc}}$ defined according to Eq. (4.33). A similar expression holds for the correction of the diffusion coefficient δD_G^{∞} . Some considerations about its calculation are made in Section 4.4.3.

A flow diagram of the local cross-section reconstruction algorithm is depicted in Fig. 4.5.

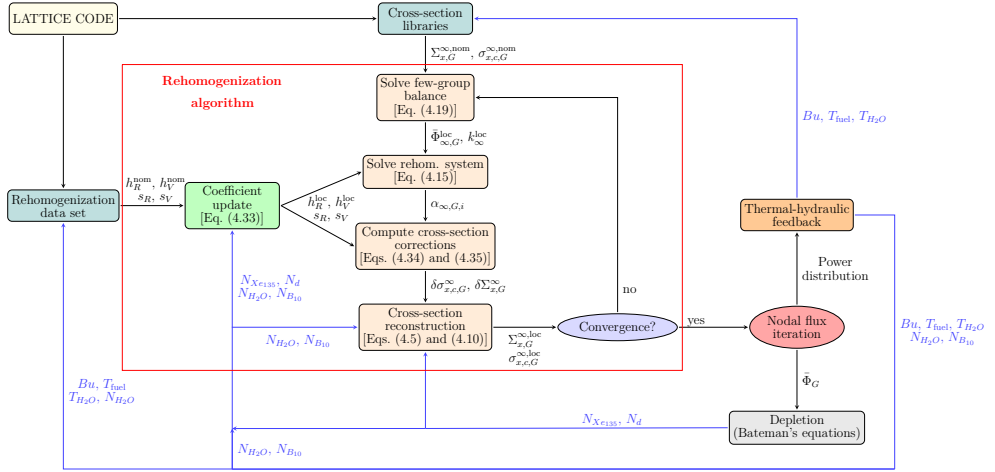


Fig. 4.5. Flow diagram of the rehomogenization-based algorithm for the reconstruction of the infinite-medium cross sections in a given node. The blue arrows represent the flow of state-parameter information (N_d denotes the number densities of the most relevant isotopes tracked in the fuel depletion calculation).

At the beginning of a new burn-up step or after a thermal-hydraulic update, the few-group cross sections and the rehomogenization coefficients are evaluated at the new values of Bu , T_{fuel} and T_{H_2O} in a given node and at the nominal values of ρ_{H_2O} , $C_{B_{10}}$

and $N_{Xe_{135}}$. The rehomogenization problem [Eq. (4.15)] is solved using (i) the values of $\bar{\Phi}_{\infty,G}^{\text{loc}}$ and k_{∞}^{loc} ensuing from the few-group infinite-medium balance [Eq. (4.19)], and (ii) the rehomogenization coefficients updated via Eq. (4.33) to account for the direct and microscopic effects of variations in ρ_{H_2O} , $C_{B_{10}}$ and $N_{Xe_{135}}$. The isotopic and macroscopic cross-section corrections are computed with Eqs. (4.34) and (4.35). The cross-section reconstruction follows with Eqs. (4.5) and (4.10). This procedure is repeated until convergence of $\bar{\Phi}_{\infty,G}^{\text{loc}}$ and k_{∞}^{loc} , upon which the so obtained cross sections can be used in the core nodal calculation. Homogenized cross sections are reconstructed independently in each node of the computational domain. Therefore, the algorithm can be easily parallelized.

4.2.2 Incorporation of neighbor effects

When a fuel assembly is simulated within the reactor core, the spectral effects of local nuclide density changes and interassembly neutron streaming cannot be separated. We now seek the spectrum deformation resulting from the combination of these two effects.

We compute the variation $\delta\Phi_G(u)$ between the real environment in the local physical conditions and the infinite lattice in the nominal conditions. Eq. (4.8) becomes

$$\Phi_{\text{env},G}^{\text{loc}}(u) = \bar{\Phi}_G \varphi_{\infty,G}^{\text{nom}}(u) + \delta\Phi_G(u), \quad (4.36)$$

where the few-group environmental flux $\bar{\Phi}_G$ (we have dropped the superscript *loc*) is now taken from the latest power iteration of the nodal calculation. The spectral rehomogenization problem [Eq. (4.15)] is rewritten replacing k_{∞}^{loc} with the core effective multiplication factor k_{eff} (which also comes from the previous nodal iteration) and adding the internodal-leakage term (Section 3.2.1):

$$\begin{aligned} \bar{\Phi}_G h_{R,r,G,j}^{\text{loc}} + \sum_{i=1}^{N_{Q_G}} \alpha_{G,i} h_{V,r,G,i,j}^{\text{loc}} + \bar{L}_G h_{L,G,j}^{\text{loc}} = \frac{\chi_{G,j}}{k_{\text{eff}}} \sum_{G'=1}^{N_G} \left(\bar{\Phi}_{G'} h_{R,f,G'}^{\text{loc}} + \right. \\ \left. \sum_{i=1}^{N_{Q_{G'}}} \alpha_{G',i} h_{V,f,G',i}^{\text{loc}} \right) + \sum_{\substack{G'=1 \\ G' \neq G}}^{N_G} \left(\bar{\Phi}_{G'} h_{R,s,G' \rightarrow G,j}^{\text{loc}} + \sum_{i=1}^{N_{Q_{G'}}} \alpha_{G',i} h_{V,s,G' \rightarrow G,i,j}^{\text{loc}} \right), \quad (4.37) \end{aligned}$$

where the leakage projection coefficient $h_{L,G,j}^{\text{loc}}$ is given by Eq. (3.27), with the rehomogenization parameters $h_{R,D,G,j}^{\text{loc}}$ and $h_{V,D,G,i,j}^{\text{loc}}$ defined as in Eqs. (4.16) and (4.17). Eq. (4.37) is structurally identical to Eq. (2.13), but the rehomogenization coefficients are defined in a different way. The microscopic and macroscopic cross-section corrections are computed with Eqs. (4.34) and (4.35), using the core-environment coefficients $\alpha_{G,i}$ and the rehomogenization parameters ensuing from Eqs. (4.25), (4.28) and (4.33).

Fig. 4.6 shows how the rehomogenization algorithm is nested in the core simulation

when modeling the combined spectral effects of local physical conditions and node-to-node neutron leakage. Compared to the infinite-medium reconstruction, multiple iterations after the interpolation at p_{nom} (see Fig. 4.5) are not necessary. Fig. 4.6 differs from Fig. 2.4 mostly in the flow of state-parameter information.

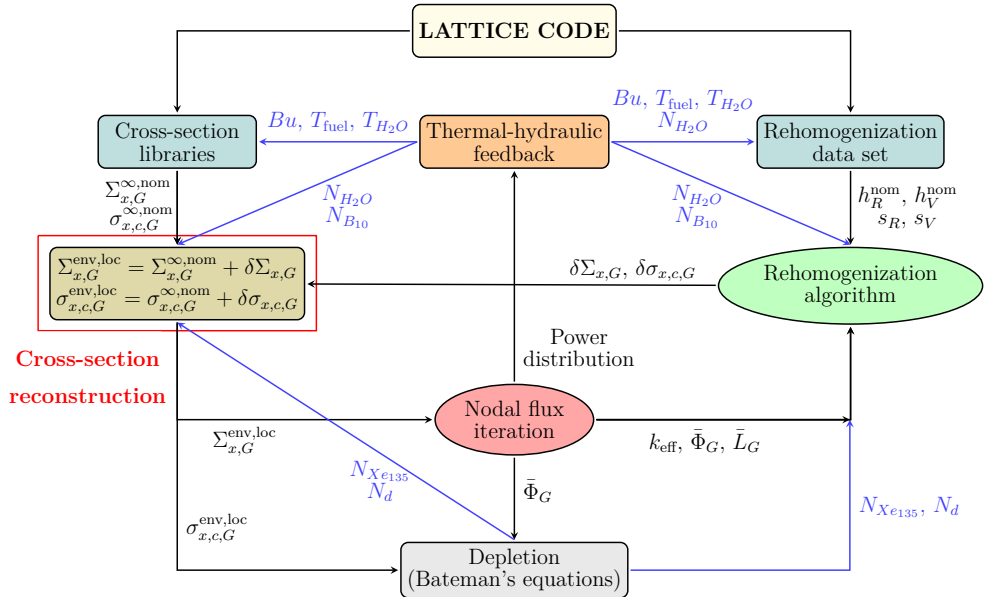


Fig. 4.6. Flow diagram of the core calculation when the nodal cross sections are directly reconstructed in the real environment at the local conditions.

4.3 Numerical results

In this section we apply the proposed method to several test cases. We first focus on the reconstruction of the local infinite-medium cross sections of a standard UO_2 fuel assembly (Section 4.3.1). Afterwards, we investigate a multiassembly benchmark problem and test the reconstruction of cross sections in the real environment at the local conditions (Section 4.3.2).

4.3.1 Single-assembly configurations

We consider a 17×17 UO_2 fuel assembly with 1.8% enrichment. This kind of assembly has already been simulated in examples 1 and 2 of Sections 2.3.2 and 3.3. The fuel bundle contains 24 empty guide tubes and an empty instrumentation tube made of

a Zircaloy-4 alloy. The assembly side has size 21.61 cm, with the cell pitch and the water gap measuring 1.26 cm and 0.8 mm, respectively. The assembly layout can be found in Fig. 2.5b.

The cross-section reconstruction algorithm as described in Section 4.2.1 has been implemented in the BRISINGR code (Appendix A). In the analysis that follows, infinite-lattice calculations for the generation of two-group cross sections in the nominal conditions are performed with APOLLO2-A (Martinolli et al., 2010). The critical-buckling correction is not applied ($B^2 = 0$). The spectrum-variation basis functions $Q_{G,i}(u)$ [Eq. (4.14)] are determined with the POD approach described in Section 2.2.2.2. The POD modes are extracted from the SVD of a set of 100 snapshots of the reference spectrum perturbation. The snapshots have been computed sampling the whole range of the values of ρ_{H_2O} , $C_{B_{10}}$ and $N_{Xe_{135}}$ that can be found in a reactor core. In both coarse energy groups, the spectrum perturbation is synthesized with the first four modes ensuing from the above procedure. These are shown in Fig. 4.7. The rank of the rehomogenization matrix [Eq. (4.15)] is 8.

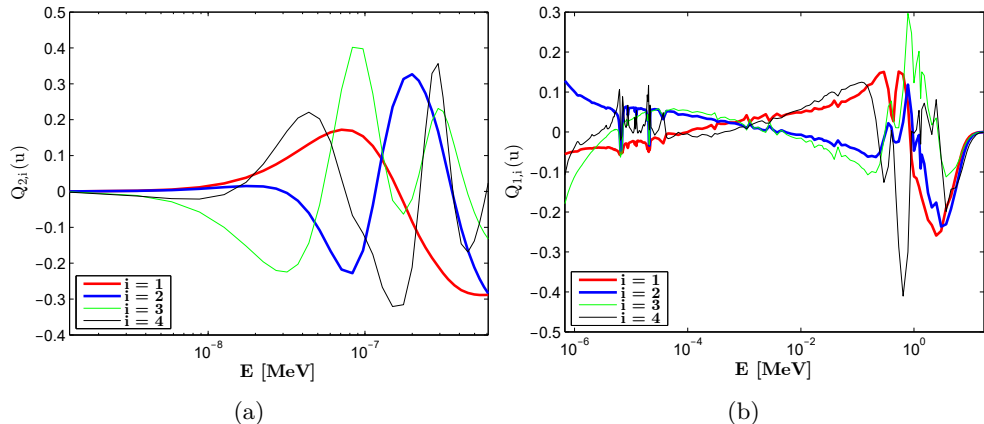


Fig. 4.7. (a) Thermal-group and (b) fast-group POD basis functions computed with the method of snapshots and the SVD.

The single-assembly cross sections are generated at zero burn-up. The nominal values of ρ_{H_2O} , $C_{B_{10}}$ and $N_{Xe_{135}}$ are those defined in Section 4.2.1. In order to keep the analysis unaffected by interpolation errors, we compute the nominal cross sections at the exact values of the fuel and moderator temperatures. When simulating normal operating conditions, we set $T_{\text{fuel}} = 851.5$ K and $T_{H_2O} = 586.1$ K. We consider variations in the boron concentration within the range [0 ppm, 3200 ppm]. The water density is spanned in the interval $[0.21 \text{ g/cm}^3, 1.0 \text{ g/cm}^3]$. Since we simulate fresh-fuel conditions, in all the test cases the local xenon density is set to 0 a/\AA^3 , which corresponds to a strong variation from its nominal value as seen in Section 4.2.1. The macroscopic and microscopic cross sections predicted with the rehomogenization-based

algorithm $(\Sigma_{x,G}^{\infty,\text{loc}}, \sigma_{x,c,G}^{\infty,\text{loc}})$ are compared to those obtained in APOLLO2-A at the exact, local conditions $(\Sigma_{x,G}^{\infty,\text{loc,ref}}, \sigma_{x,c,G}^{\infty,\text{loc,ref}})$. The errors in the reconstructed cross sections are computed as

$$\Delta\Sigma_{x,G}^{\infty} = \frac{\Sigma_{x,G}^{\infty,\text{loc}} - \Sigma_{x,G}^{\infty,\text{loc,ref}}}{\Sigma_{x,G}^{\infty,\text{loc,ref}}} \cdot 100\%, \quad \Delta\sigma_{x,c,G}^{\infty} = \frac{\sigma_{x,c,G}^{\infty,\text{loc}} - \sigma_{x,c,G}^{\infty,\text{loc,ref}}}{\sigma_{x,c,G}^{\infty,\text{loc,ref}}} \cdot 100\%. \quad (4.38)$$

The variation in the macroscopic cross sections between the local and nominal conditions is determined as

$$\delta\Sigma_{x,G}^{\infty} = \frac{\Sigma_{x,G}^{\infty,\text{loc}} - \Sigma_{x,G}^{\infty,\text{nom}}}{\Sigma_{x,G}^{\infty,\text{nom}}} \cdot 100\%. \quad (4.39)$$

Similar expressions hold for the errors and variations in the multiplication factor $(\Delta k_{\infty}, \delta k_{\infty})$, in the node-averaged two-group flux $(\Delta\bar{\Phi}_{\infty,G}, \delta\bar{\Phi}_{\infty,G})$, and in the node-averaged total fission power $(\Delta\bar{P}_{\text{fiss}}^{\infty}, \delta\bar{P}_{\text{fiss}}^{\infty})$.

Our target in terms of accuracy is to have:

- errors not exceeding 50 pcm in k_{∞} and 0.1% in the macroscopic cross sections in the most frequent conditions (namely, in the normal range of operation);
- errors not exceeding 100 pcm in k_{∞} and 0.5% in the macroscopic cross sections in abnormal operating points (such as very low moderator densities) that are typically reached in accidental conditions.

We include in the second category the transitions from cold to hot conditions during the reactor start-up and from hot to cold conditions when the reactor is shut down. We believe that the above error bounds are reasonably low considered the range of accuracy of nodal diffusion tools. For instance, the values chosen for normal operating conditions would be easily concealed by homogenization errors arising in heterogeneous core configurations (Chapters 2 and 3).

The convergence of the reconstruction algorithm (Fig. 4.5) is reached when the relative changes in k_{∞}^{loc} and in the nodal flux two-norm between two successive iterations drop below a tolerance $\epsilon_{\text{iter}} = 10^{-5}$.

The analysis is structured as follows. We first present sample results for variations in only one parameter. In this way, the accuracy of the method is assessed individually for the three variables considered in this work. When focusing on variations in the moderator density or boron concentration only, the nominal xenon density is set to 0 a/Å³. Afterwards, simultaneous perturbations in the three parameters are addressed.

4.3.1.1 Variation in the xenon concentration

We consider a perturbed configuration with $N_{Xe_{135}} = 0$ a/Å³ and $\delta N_{Xe_{135}} = -4.0 \cdot 10^{-9}$ a/Å³. The boron concentration and the water density are at their nominal values.

4. Modeling spectral effects of local nuclide density changes

The reference value of k_{∞}^{loc} is 1.08277.

Fig. 4.8 shows the thermal-group spectrum variation (per unit pseudo lethargy) due to this perturbation. The deformation in the fast group is negligible (its magnitude ranges from -0.01% to 0.05%) and is therefore not shown. The reference change is very accurately predicted by the method.

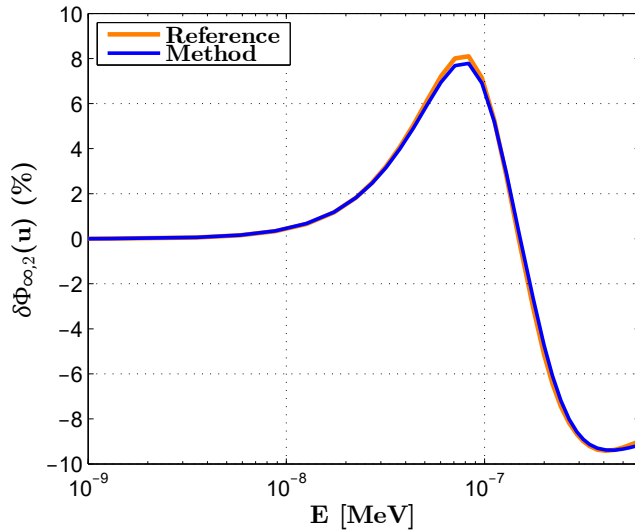


Fig. 4.8. Thermal-group spectrum variation (per unit u) versus energy due to a change in $N_{Xe_{135}}$ from $4.0 \cdot 10^{-9} \text{ a}/\text{\AA}^3$ to $0 \text{ a}/\text{\AA}^3$.

Table 4.1 reports the errors in the computed macroscopic cross sections and in the main integral parameters. The two flux-error values refer to the fast and thermal groups. The number of iterations (n_{iter}) of the reconstruction algorithm is also shown.

Table 4.1. Transition from $N_{Xe_{135}} = 4.0 \cdot 10^{-9} \text{ a}/\text{\AA}^3$ to $N_{Xe_{135}} = 0 \text{ a}/\text{\AA}^3$: errors in the reconstructed macroscopic cross sections and in the main integral parameters, and number of iterations.

$\Delta \Sigma_{a,1}^{\infty}$ (%)	$\Delta \Sigma_{a,2}^{\infty}$ (%)	$\Delta \nu \Sigma_{f,1}^{\infty}$ (%)	$\Delta \nu \Sigma_{f,2}^{\infty}$ (%)	$\Delta \Sigma_{s,1 \rightarrow 2}^{\infty}$ (%)	Δk_{∞} [pcm]	$\Delta \bar{\Phi}_{\infty,G}$ (%)	$\Delta \bar{P}_{\text{fiss}}^{\infty}$ (%)	n_{iter}
0.011	0.003	-0.009	0.008	0.01	-2	-0.002, 0.006	0.01	7

The deviations are negligible for all the quantities. If the xenon-variation microscopic effect (Section 4.2.1.2) is not taken into account, the errors in $\Sigma_{a,2}^{\infty}$ and $\nu \Sigma_{f,2}^{\infty}$ increase to -0.55% and -0.82%, respectively, and the error in k_{∞} becomes -249 pcm.

The interplay among the various effects (direct, spectral, and microscopic) of the xenon perturbation is quantified in Table 4.2, which shows the corresponding contributions to the reference global variation in the cross sections and integral parameters. For

this kind of perturbation, the spectral and microscopic effects play a secondary role compared to the direct one.

Table 4.2. Variation in the macroscopic cross sections and integral parameters due to a change in $N_{Xe_{135}}$ from $4.0 \cdot 10^{-9}$ a/Å³ to 0 a/Å³. The global variation and its spectral and microscopic components have been determined with the reference data from APOLLO2-A. The reference perturbed cross sections are $\Sigma_{a,2}^{\infty} = 0.066702$ cm⁻¹ and $\nu\Sigma_{f,2}^{\infty} = 0.080904$ cm⁻¹.

	$\delta\Sigma_{a,2}^{\infty}$ (%)	$\delta\nu\Sigma_{f,2}^{\infty}$ (%)	δk_{∞} [pcm]	$\delta\bar{\Phi}_{\infty,G}$ (%)	$\delta\bar{P}_{\text{fiss}}^{\infty}$ (%)
Direct	-8.94	0.0	7930	-1.92, 7.50	5.81
Spectr. + micr. (ref.)	1.49	1.95	311	0.31, -1.2	0.77
Global (ref.)	-7.44	1.95	8241	-1.62, 6.3	6.58

4.3.1.2 Variations in the concentration of diluted boron

We analyze two examples with varying concentration of diluted boron:

- a transition from 700 ppm to 2450 ppm, with $N_{Xe_{135}} = 0$ a/Å³ in both nominal and perturbed conditions (case *a*);
- a transition from 700 ppm to 0 ppm, with $N_{Xe_{135}} = 4.0 \cdot 10^{-9}$ a/Å³ in the nominal state and $N_{Xe_{135}} = 0$ a/Å³ in the perturbed one (case *b*).

The first perturbed value of $C_{B_{10}}$ (2450 ppm) may be representative of the beginning of the core life at hot full-power conditions, in the absence of burnable poisons and with control rods out. The second value (0 ppm) is typically found at the end of a fuel cycle. The reference values of k_{∞} in the two perturbed conditions are 0.87077 (case *a*) and 1.20541 (case *b*). In case *a*, in which there is no xenon variation, the microscopic effect and the corresponding corrections [Eqs. (4.11c) and (4.11d)] are not taken into account.

Fig. 4.9 depicts the spectrum perturbations in the two test cases. The deformation is significant in the thermal group, whereas the fast group is only affected in the epithermal range. The result is flawless in the thermal and epithermal regions. The deviations from the reference found at high energies (especially at $E > 100$ keV in case *b*) have negligible impact on the reconstruction of the fast-group cross sections, because in this range (*i*) the magnitude of $\delta\Phi_{\infty,1}(u)$ is low and (*ii*) only the fission cross sections are relatively high, due to the contribution of fast fissions of ²³⁸U.

The errors in the macroscopic cross sections and integral parameters are in Table 4.3. Table 4.4 shows the errors in the rehomogenized isotopic cross sections of some relevant nuclides. The deviations have the same order of magnitude as the errors found with the conventional multivariate interpolation. For case *a*, Table 4.5 reports the contributions of the various effects to the overall variation in the macroscopic cross sections and in

4. Modeling spectral effects of local nuclide density changes

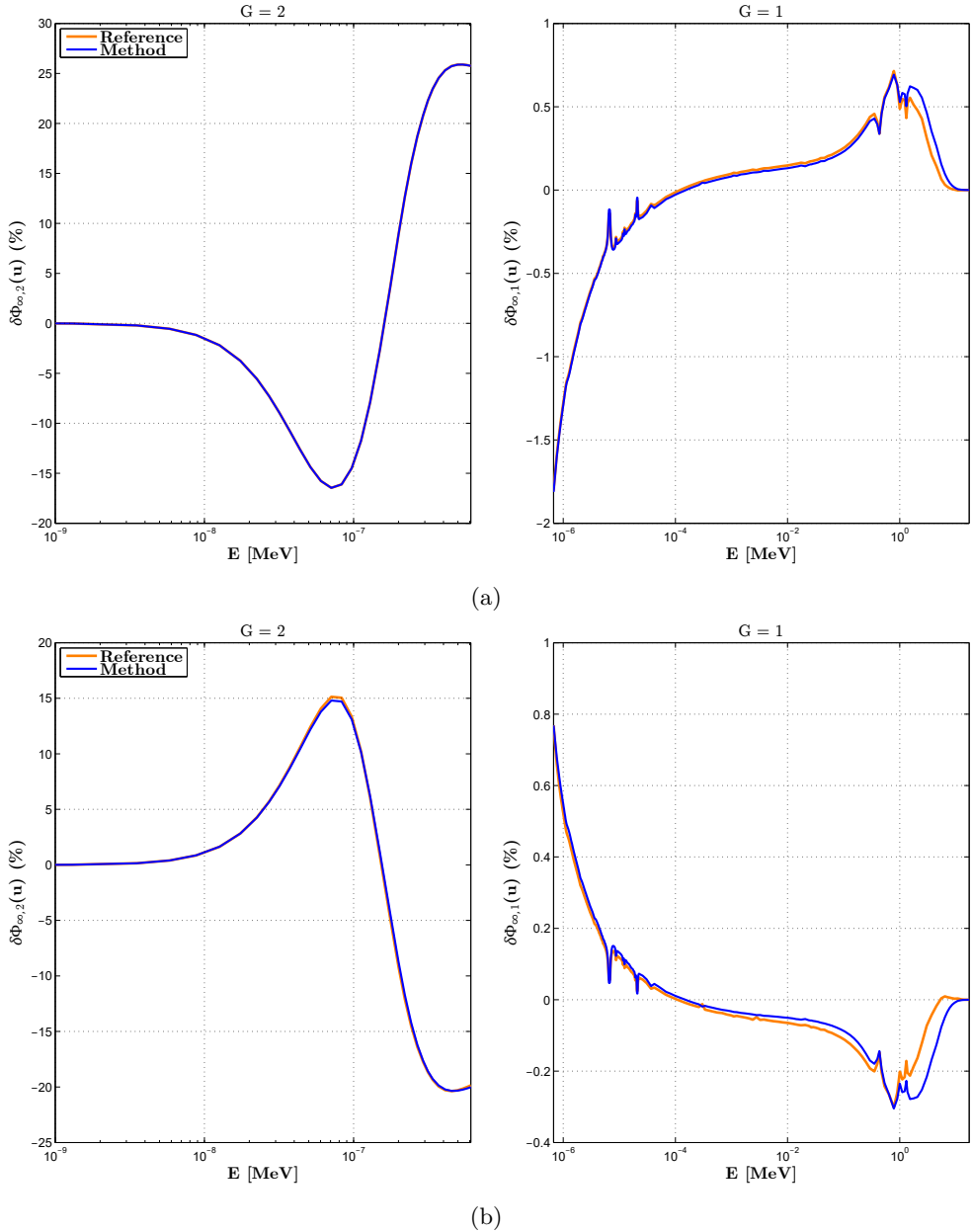


Fig. 4.9. Spectrum variations (per unit u) versus energy due to the following transitions: (a) from $C_{B_{10}} = 700$ ppm to $C_{B_{10}} = 2450$ ppm (both conditions have $N_{Xe_{135}} = 0$ a/Å³); (b) from $C_{B_{10}} = 700$ ppm and $N_{Xe_{135}} = 4.0 \cdot 10^{-9}$ a/Å³ to $C_{B_{10}} = 0$ ppm and $N_{Xe_{135}} = 0$ a/Å³.

the integral parameters. Also in this case, the direct effect is preeminent.

Table 4.3. Variations in the boron concentration: errors in the reconstructed macroscopic cross sections and in the main integral parameters, and number of iterations.

Case	$\Delta\Sigma_{a,1}^\infty$ (%)	$\Delta\Sigma_{a,2}^\infty$ (%)	$\Delta\nu\Sigma_{f,1}^\infty$ (%)	$\Delta\nu\Sigma_{f,2}^\infty$ (%)	$\Delta\Sigma_{s,1\rightarrow 2}^\infty$ (%)	Δk_∞ [pcm]	$\Delta\bar{\Phi}_{\infty,G}$ (%)	$\Delta\bar{P}_{\text{fiss}}^\infty$ (%)	n_{iter}
<i>a</i>	-0.007	-0.018	0.012	-0.039	-0.02	-13	0.0, -0.004	-0.033	8
<i>b</i>	0.016	0.03	-0.013	0.039	0.031	4	0.0, 0.001	0.033	7

Table 4.4. Variations in the boron concentration: errors (in %) in the reconstructed microscopic cross sections of some relevant isotopes.

Case	H ₂ O		¹⁰ B	¹³⁵ Xe	²³⁵ U				²³⁸ U		
	$\Delta\sigma_{a,2}^\infty$	$\Delta\sigma_{s,1\rightarrow 2}^\infty$	$\Delta\sigma_{a,2}^\infty$	$\Delta\sigma_{a,2}^\infty$	$\Delta\sigma_{a,1}^\infty$	$\Delta\sigma_{a,2}^\infty$	$\Delta\nu\sigma_{f,1}^\infty$	$\Delta\nu\sigma_{f,2}^\infty$	$\Delta\sigma_{a,1}^\infty$	$\Delta\sigma_{a,2}^\infty$	$\Delta\nu\sigma_{f,1}^\infty$
<i>a</i>	0.017	-0.016	0.017	-0.046	-0.021	-0.039	-0.021	-0.039	-0.004	-0.038	0.052
<i>b</i>	-0.035	0.030	-0.026	0.016	0.020	0.040	0.020	0.039	0.017	0.037	-0.054

Table 4.5. Variations in the macroscopic cross sections and integral parameters due to the transition from 700 ppm to 2450 ppm (case *a*). Since neither the water density nor the xenon level changes and the microscopic effect of boron concentration is neglected, only the direct and spectral effects are present. The reference values of the perturbed cross sections are: $\Sigma_{a,1}^\infty = 0.008891 \text{ cm}^{-1}$, $\Sigma_{a,2}^\infty = 0.076932 \text{ cm}^{-1}$, $\nu\Sigma_{f,1}^\infty = 0.004830 \text{ cm}^{-1}$, $\nu\Sigma_{f,2}^\infty = 0.080188 \text{ cm}^{-1}$, and $\Sigma_{s,1\rightarrow 2}^\infty = 0.017106 \text{ cm}^{-1}$.

	$\delta\Sigma_{a,1}^\infty$ (%)	$\delta\Sigma_{a,2}^\infty$ (%)	$\delta\nu\Sigma_{f,1}^\infty$ (%)	$\delta\nu\Sigma_{f,2}^\infty$ (%)	$\delta\Sigma_{s,1\rightarrow 2}^\infty$ (%)	δk_∞ [pcm]	$\delta\bar{\Phi}_{\infty,G}$ (%)	$\delta\bar{P}_{\text{fiss}}^\infty$ (%)
Direct	4.80	28.11	0.0	0.0	0.0	-20950	4.92, -17.76	-13.99
Spectr. (ref.)	-0.336	-3.50	-0.284	-2.78	-1.92	-250	-0.085, 0.306	-1.73
Global (ref.)	4.46	24.61	-0.284	-2.78	-1.92	-21200	4.83, -17.45	-15.72

We have made a parametric analysis by considering the whole range of variation of the boric-acid concentration in a reactor core. Fig. 4.10 shows the errors in k_∞ and in the node-averaged total fission power versus the boron concentration. The zero-error bar is highlighted. The errors in the macroscopic thermal absorption and production cross sections are plotted in Fig. 4.11. The results are shown for the cases with $N_{Xe_{135}}^{\text{nom}} = 0 \text{ a}/\text{\AA}^3$ and $N_{Xe_{135}}^{\text{nom}} = 4.0 \cdot 10^{-9} \text{ a}/\text{\AA}^3$. In the former (i.e., when $C_{B_{10}}$ is the only changing parameter), the deviations are negligible along the whole boron axis. In the latter (i.e., with a combined variation of the two variables), their magnitude is higher, yet remains within the target bounds (50 pcm for k_∞ , 0.1% for the macroscopic cross sections). Only at 3200 ppm, the errors in k_∞ and $\nu\Sigma_{f,2}^\infty$ (-45 pcm and -0.11%, respectively) are close to or slightly exceed the prescribed limits. However, values of $C_{B_{10}}$ higher than 3000 ppm are uncommon in modern PWR core design. The amount of chemical shim is limited (usually to 2000 or 2500 ppm) to avoid a positive moderator void coefficient of reactivity (Duderstadt and Hamilton, 1976).

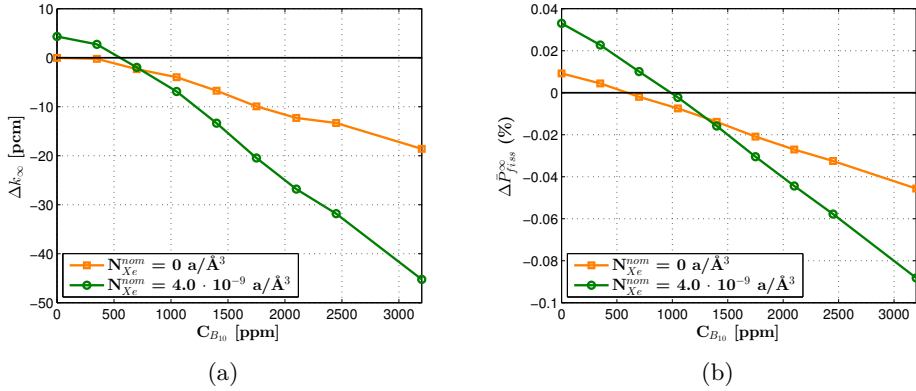


Fig. 4.10. Errors in the (a) multiplication factor and (b) total fission power versus the boron concentration. The case with $N_{Xe^{135}}^{nom} = 0 \text{ a}/\text{\AA}^3$ corresponds to a variation in $C_{B_{10}}$ only.

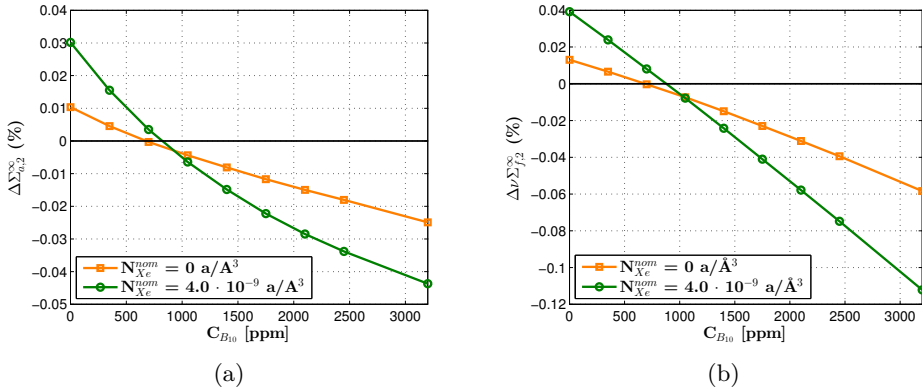


Fig. 4.11. Errors in the thermal-group (a) absorption and (b) production cross sections versus the boron concentration.

4.3.1.3 Variations in the water density

Following the same approach as for the boron concentration, we consider three examples with perturbations in the moderator density:

- a transition from 0.7 g/cm^3 to 0.76 g/cm^3 , with $N_{Xe^{135}} = 4.0 \cdot 10^{-9} \text{ a}/\text{\AA}^3$ in the nominal state (case a);
- a transition from 0.7 g/cm^3 to 0.91 g/cm^3 , with $N_{Xe^{135}} = 4.0 \cdot 10^{-9} \text{ a}/\text{\AA}^3$ in the nominal state (case b);

- a transition from 0.7 g/cm^3 to 0.21 g/cm^3 , with $N_{Xe_{135}} = 0 \text{ a/\AA}^3$ in both nominal and perturbed conditions (case *c*).

Case *a* is an example of mild fluctuation during normal operation. It corresponds to a change in the moderator temperature of about 30 K at the nominal pressure (158 bar). Cases *b* and *c* are instead examples of strong perturbations. The first value of ρ_{H_2O} (0.91 g/cm^3) is encountered in the transition from cold zero power to hot full power during the reactor start-up. The second value (0.21 g/cm^3) may occur in design basis accidents, such as loss-of-flow accidents. The reference values of k_∞ in the three perturbed states are 1.08028 (case *a*), 1.06777 (case *b*), and 0.93046 (case *c*).

Fig. 4.12 shows the spectrum perturbations of cases *b* and *c*. Compared to the previous examples, a significant deformation also takes place in the fast group. The shape of the variation features a double peak in the range 50 keV - 19.6 MeV, changing sign at about 1 MeV. This shape is somewhat similar to that observed (within the fission-emission energy region) in the spectrum variation triggered by internodal heterogeneity at UO_2/MOX interfaces (Figs. 3.10 and 3.26). At $\rho_{H_2O} = 0.21 \text{ g/cm}^3$, the magnitude of the perturbation becomes remarkable in both groups. The POD basis accurately reproduces the sharp outline of the high-energy deformation and the resonance spikes in the epithermal region.

The errors in the cross sections and integral parameters are presented in Tables 4.6 and 4.7. In case *a*, all the errors are negligible, except for the thermal absorption of ^{135}Xe . In case *b*, the target accuracy is achieved for all the macroscopic cross sections other than fast-to-thermal scattering, for which the error bound is slightly exceeded. Similarly, the isotopic cross sections of H_2O and ^{10}B and fast fission in ^{238}U have errors between 0.1% and 0.2%. In case *c*, the deviations in the thermal-group macroscopic cross sections are still negligible, whereas higher errors (between -0.35% and -0.51%) are observed in the fast group. These residual errors are caused by minor imperfections in the prediction of the epithermal spectrum perturbation [Fig. 4.12b]. For instance, at 6.67 eV (which corresponds to one of the main resonances of ^{238}U) the reference spectrum change is -17.3%, whereas the computed value is -18.0%. Since the magnitude of the deformation is very high, small discrepancies in the resonance region can result in non-negligible errors in the collapsed cross sections. We have verified that the fast-group errors drop to zero if the cross-section corrections are computed with the reference $\delta\Phi_{\infty,1}(u)$. Another feature of the low-density calculation is the increase in the number of iterations for the convergence of the reconstruction algorithm.

Table 4.6. Variations in the water density: errors in the reconstructed macroscopic cross sections and in the main integral parameters, and number of iterations.

Case	$\Delta\Sigma_{a,1}^\infty$ (%)	$\Delta\Sigma_{a,2}^\infty$ (%)	$\Delta\nu\Sigma_{f,1}^\infty$ (%)	$\Delta\nu\Sigma_{f,2}^\infty$ (%)	$\Delta\Sigma_{s,1\rightarrow 2}^\infty$ (%)	Δk_∞ [pcm]	$\Delta\Phi_{\infty,G}$ (%)	$\Delta\bar{P}_{\text{fiss}}^\infty$ (%)	n_{iter}
<i>a</i>	0.067	-0.002	-0.018	0.013	0.034	-9	-0.008, 0.027	0.031	7
<i>b</i>	0.065	-0.019	-0.05	0.025	0.115	26	-0.035, 0.1	0.098	6
<i>c</i>	-0.361	0.062	-0.374	0.046	-0.506	-35	0.044, -0.522	-0.434	17

4. Modeling spectral effects of local nuclide density changes

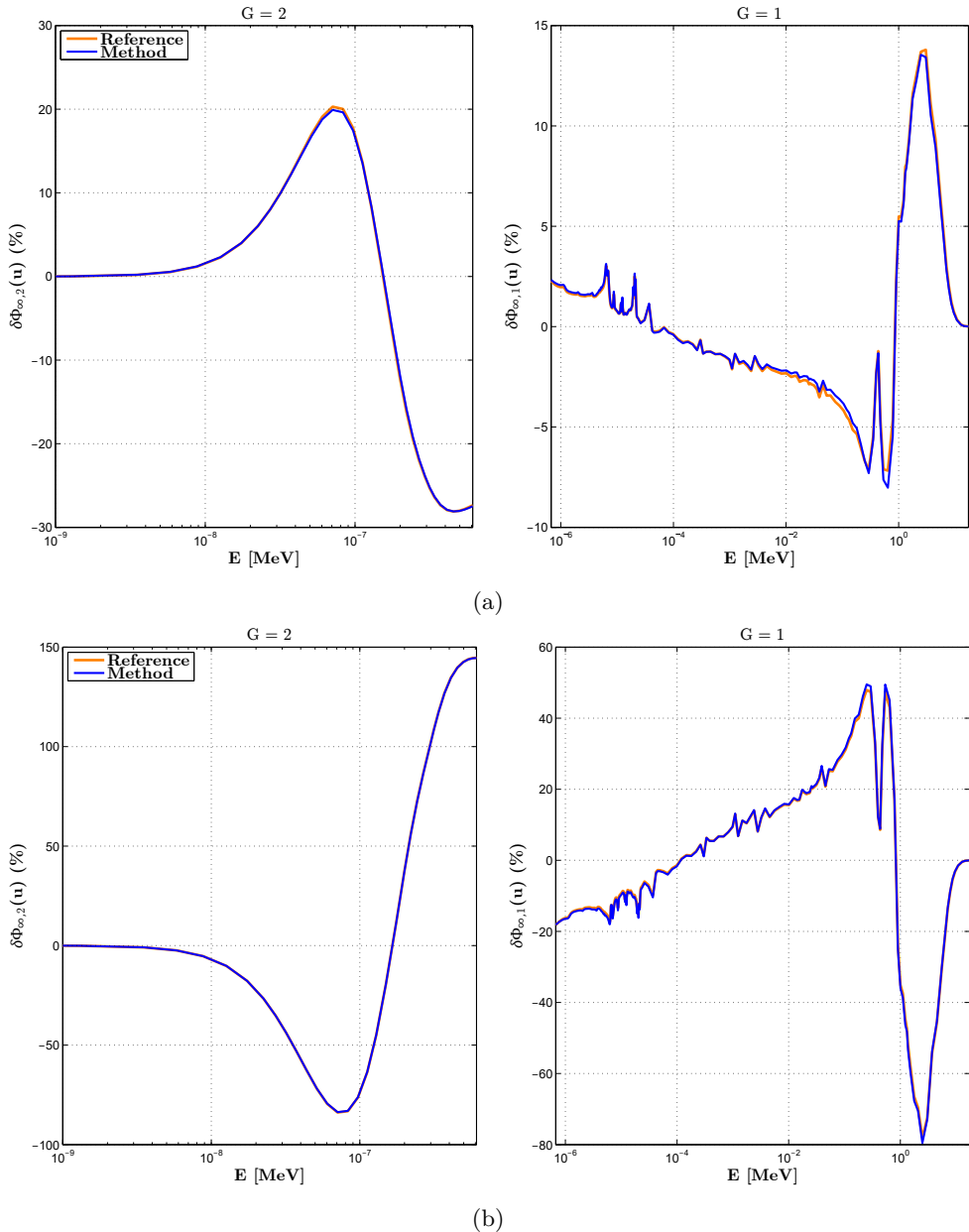


Fig. 4.12. Spectrum variations (per unit u) versus energy due to the following transitions: (a) from $\rho_{H_2O} = 0.7 \text{ g/cm}^3$ and $N_{Xe_{135}} = 4.0 \cdot 10^{-9} \text{ a/\AA}^3$ to $\rho_{H_2O} = 0.91 \text{ g/cm}^3$ and $N_{Xe_{135}} = 0 \text{ a/\AA}^3$; (b) from $\rho_{H_2O} = 0.7 \text{ g/cm}^3$ to $\rho_{H_2O} = 0.21 \text{ g/cm}^3$ (both conditions have $N_{Xe_{135}} = 0 \text{ a/\AA}^3$).

Table 4.7. Variations in the water density: errors (in %) in the reconstructed microscopic cross sections of some relevant isotopes.

Case	H ₂ O		¹⁰ B	¹³⁵ Xe	²³⁵ U				²³⁸ U		
	$\Delta\sigma_{a,2}^\infty$	$\Delta\sigma_{s,1\rightarrow 2}^\infty$	$\Delta\sigma_{a,2}^\infty$	$\Delta\sigma_{a,2}^\infty$	$\Delta\sigma_{a,1}^\infty$	$\Delta\sigma_{a,2}^\infty$	$\Delta\nu\sigma_{f,1}^\infty$	$\Delta\nu\sigma_{f,2}^\infty$	$\Delta\sigma_{a,1}^\infty$	$\Delta\sigma_{a,2}^\infty$	$\Delta\nu\sigma_{f,1}^\infty$
<i>a</i>	-0.053	0.034	-0.053	-0.263	0.019	0.014	0.018	0.013	0.087	0.012	-0.063
<i>b</i>	-0.148	0.115	-0.148	-0.098	0.071	0.025	0.065	0.025	0.072	0.021	-0.189
<i>c</i>	0.297	-0.538	0.297	-0.748	-0.64	0.046	-0.568	0.046	-0.306	0.041	-0.071

The contributions of the various effects to the cross-section variations are reported in Table 4.8 for case *c*. The perturbations computed by the method are compared to the reference ones. In this example, the spectral and microscopic effects give a relevant contribution to the global variation.

Table 4.8. Variations in the macroscopic cross sections and integral parameters due to the transition from 0.7 g/cm³ to 0.21 g/cm³ (case *c*). The reference values of the perturbed cross sections are: $\Sigma_{a,1}^\infty = 0.006768$ cm⁻¹, $\Sigma_{a,2}^\infty = 0.046244$ cm⁻¹, $\nu\Sigma_{f,1}^\infty = 0.003907$ cm⁻¹, $\nu\Sigma_{f,2}^\infty = 0.071230$ cm⁻¹, and $\Sigma_{s,1\rightarrow 2}^\infty = 0.004003$ cm⁻¹.

	$\delta\Sigma_{a,1}^\infty$ (%)	$\delta\Sigma_{a,2}^\infty$ (%)	$\delta\nu\Sigma_{f,1}^\infty$ (%)	$\delta\nu\Sigma_{f,2}^\infty$ (%)	$\delta\Sigma_{s,1\rightarrow 2}^\infty$ (%)	δk_∞ [pcm]	$\delta\tilde{\Phi}_{\infty,G}$ (%)	$\delta\tilde{P}_{\text{fiss}}^\infty$ (%)
Direct	-2.68	-13.72	0.0	0.0	-68.69	-11520	15.96, -57.60	-45.38
Spectr. + micr. (ref.)	-17.81	-11.38	-19.35	-13.64	-8.35	-3711	1.85, -6.68	-12.96
Spectr. + micr. (calc.)	-18.09	-11.33	-19.65	-13.60	-8.47	-3745	1.90, -6.86	-13.14
Global (ref.)	-20.48	-25.1	-19.35	-13.64	-77.05	-15230	17.81, -64.27	-58.34

A parametric analysis similar to that of Section 4.3.1.2 has been made for the water density. The errors versus the moderator density are shown in Figs. 4.13 to 4.16 for various quantities. At densities between 0.51 and 0.81 g/cm³, the absolute values of errors in the cross sections are below 0.1% in the fast group and 0.03% in the thermal one, and the absolute values of deviations in k_∞ are below 20 pcm. At 0.21 g/cm³, the highest error is found in fast-to-thermal scattering (-0.63% when the xenon concentration also varies).

4.3.1.4 Combined variations in the three parameters

We assess the performance of the method for simultaneous variations in the three parameters. From now on, we will only consider nominal conditions with $N_{Xe_{135}} = 4.0 \cdot 10^{-9}$ a/Å³. The perturbation $\delta N_{Xe_{135}}$ is therefore fixed at $-4.0 \cdot 10^{-9}$ a/Å³.

Table 4.9 reports the numerical errors for various perturbed states. A more general overview is given in Figs. 4.17 to 4.19, which show the deviations in k_∞ , $\Sigma_{a,2}^\infty$ and $\nu\Sigma_{f,2}^\infty$ along the whole range of variation of ρ_{H_2O} and $C_{B_{10}}$. At water densities between 0.51 and 0.81 g/cm³, the absolute values of the errors in k_∞ are (i) lower than 25 pcm if $C_{B_{10}}$ varies in the range [0 ppm, 1500 ppm], and (ii) lower than 40 pcm if $C_{B_{10}}$ varies in the range [1500 ppm, 2000 ppm]. The errors in $\Sigma_{a,2}^\infty$ are well below

4. Modeling spectral effects of local nuclide density changes

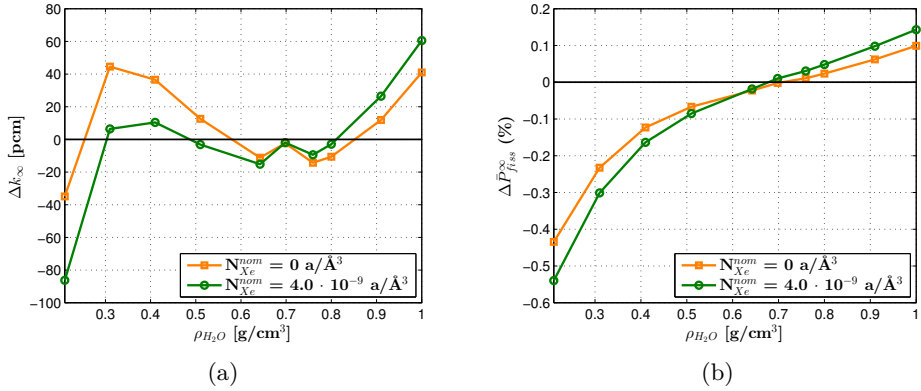


Fig. 4.13. Errors in the (a) multiplication factor and (b) total fission power versus the moderator density. The case with $N_{Xe135}^{nom} = 0 \text{ a}/\text{\AA}^3$ corresponds to a variation in ρ_{H_2O} only.

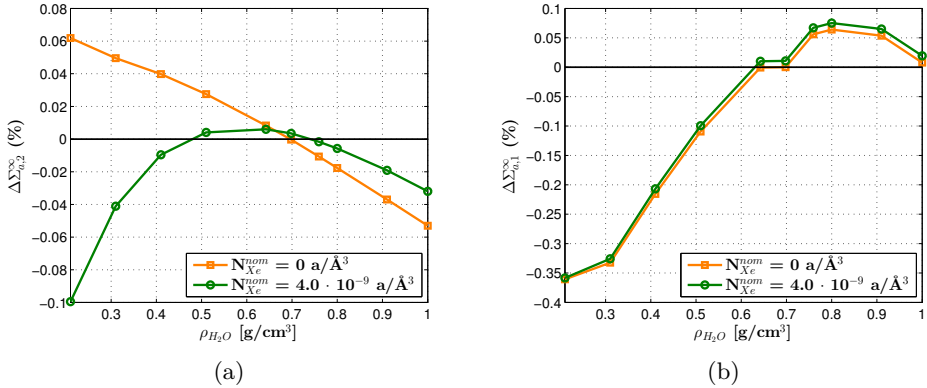


Fig. 4.14. Errors in the (a) thermal- and (b) fast-group absorption cross sections versus the moderator density.

0.1% in most of the state-parameter domain, whereas the deviations in $\nu \Sigma_{f,2}^{\infty}$ remain below this bound if $C_{B_{10}} < 2000 \text{ ppm}$ and $\rho_{H_2O} > 0.41 \text{ g/cm}^3$. The errors in the aforementioned quantities become negative for boron concentrations above a certain value. At $\rho_{H_2O} = 0.21 \text{ g/cm}^3$, the dependence on the boron concentration is negligible (especially in k_{∞} and $\Sigma_{a,2}^{\infty}$). Similarly, deviations in the fast group only depend on the moderator density and almost do not vary with the boron concentration. This can be observed in Fig. 4.20, which shows the behavior of the error in $\Sigma_{a,1}^{\infty}$.

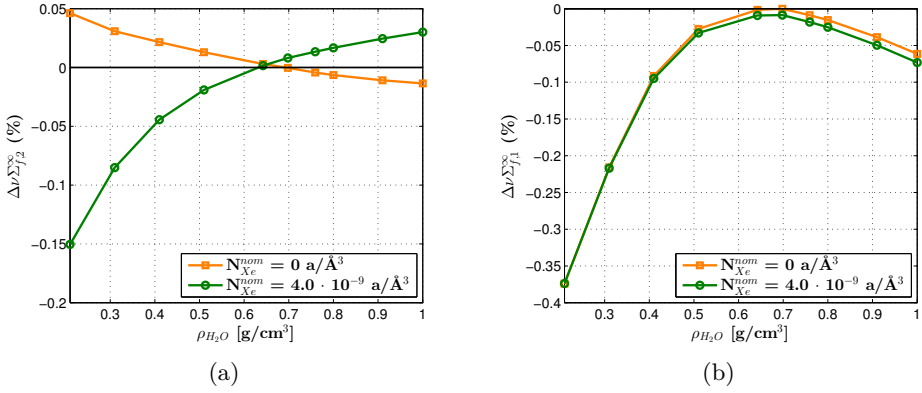


Fig. 4.15. Errors in the (a) thermal- and (b) fast-group production cross sections versus the moderator density.

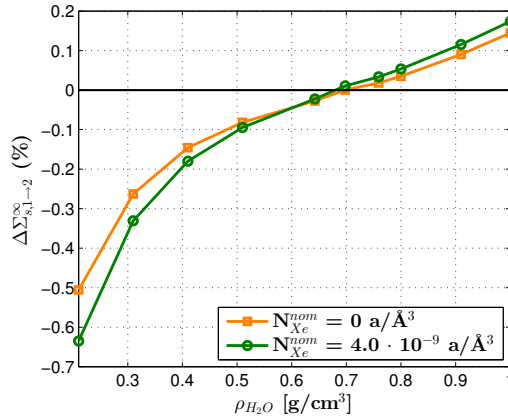


Fig. 4.16. Error in the fast-to-thermal scattering cross section versus the moderator density.

4.3.2 Application to a heterogeneous multiassembly configuration

We now apply the method to predict the combined effects of perturbations in the state parameters and interassembly neutron leakage on the node-averaged spectrum. The analysis is made on the colorset benchmark problem with control rods described in Section 2.3.2.2. The fuel assemblies in the colorset, made of 1.8%-enriched UO_2 , are of the same type as that simulated in Section 4.3.1 for the reconstruction of the infinite-medium cross sections. Two banks of twenty-four AIC control elements each are inserted into two of the four bundles. The arrangement of the assemblies in the colorset and their internal layout can be found in Fig. 2.9.

4. Modeling spectral effects of local nuclide density changes

Table 4.9. Three-parameter variations: errors in the reconstructed macroscopic cross sections and in the main integral parameters, and number of iterations. The perturbed xenon concentration is $0 \text{ a}/\text{\AA}^3$ in all the test cases.

ρ_{H_2O} [g/cm ³]	$C_{B_{10}}$ [ppm]	$\Delta\Sigma_{a,1}^\infty$ (%)	$\Delta\Sigma_{a,2}^\infty$ (%)	$\Delta\nu\Sigma_{f,1}^\infty$ (%)	$\Delta\nu\Sigma_{f,2}^\infty$ (%)	$\Delta\Sigma_{s,1\rightarrow 2}^\infty$ (%)	Δk_∞ [pcm]	$\Delta\Phi_{\infty,G}$ (%)	$\Delta\bar{P}_{\text{fiss}}^\infty$ (%)	n_{iter}
0.41	0	-0.198	-0.001	-0.102	-0.015	-0.154	26	0.024, -0.129	-0.132	9
0.51	1200	-0.104	-0.004	-0.028	-0.041	-0.111	-13	-0.018, -0.09	-0.107	9
0.64	800	0.009	0.004	-0.008	-0.003	-0.026	-15	0.006, -0.022	-0.021	7
0.76	1600	0.061	-0.028	-0.012	-0.030	0.012	-23	-0.008, 0.031	-0.002	7
0.81	200	0.079	0.018	-0.027	0.04	0.066	0	-0.012, 0.037	0.062	7
0.81	1400	0.071	-0.029	-0.021	-0.017	0.038	-13	-0.015, 0.053	0.024	6
0.91	2000	0.063	-0.065	-0.044	-0.044	0.095	-1	-0.034, 0.125	0.056	6
1.0	2600	0.026	-0.098	-0.067	-0.075	0.154	7	-0.053, 0.198	0.084	7

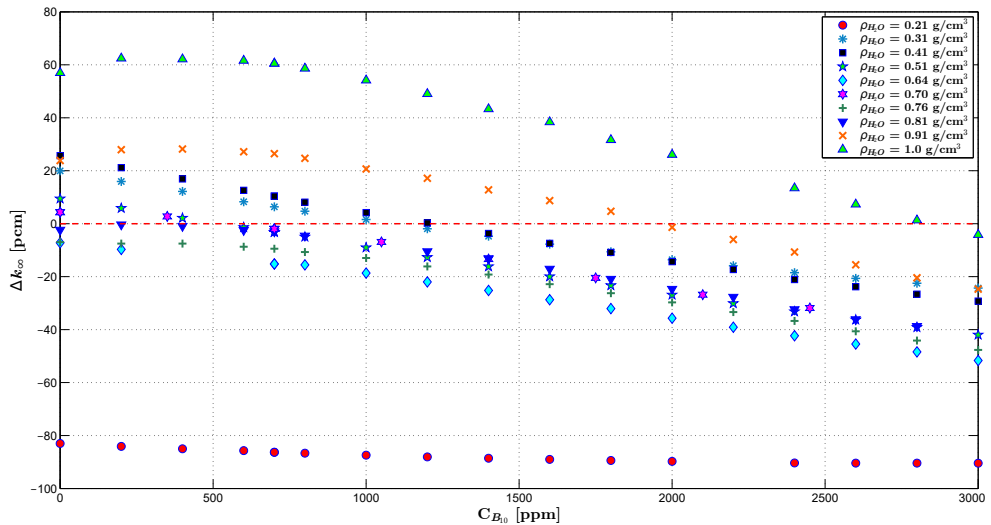


Fig. 4.17. Error in the infinite-medium multiplication factor as a function of the boron concentration (on the x-axis) and of the moderator density (markers). In all the simulated states, the variation in the xenon density is $\delta N_{Xe_{135}} = -4.0 \cdot 10^{-9} \text{ a}/\text{\AA}^3$.

As in Sections 2.3.2.2 and 3.3.1.2, the multiassembly set is simulated at zero burn-up and at normal operating conditions ($T_{\text{fuel}} = 851.5 \text{ K}$, $T_{H_2O} = 586.1 \text{ K}$, $\rho_{H_2O} = 0.71 \text{ g/cm}^3$), without thermal-hydraulic feedback or fuel depletion. Since there is no boron diluted in the moderator ($C_{B_{10}} = 0 \text{ ppm}$), the deviations of the local conditions from the nominal ones are $\delta C_{B_{10}} = -700 \text{ ppm}$ and $\delta N_{Xe_{135}} = -4.0 \cdot 10^{-9} \text{ a}/\text{\AA}^3$. The change in the water density is negligible. The reference effective multiplication factor and control-rod bank worth computed with APOLLO2-A are $k_{\text{eff}} = 0.98847$ and $w_{CR} = 21840 \text{ pcm}$, respectively. The reference assembly-averaged fission power \bar{P}_{fiss} is 1.216 in the unrodded assembly and 0.784 in the rodded one.

The nodal simulations of the colorset are performed with the ARTEMIS code (Hobson

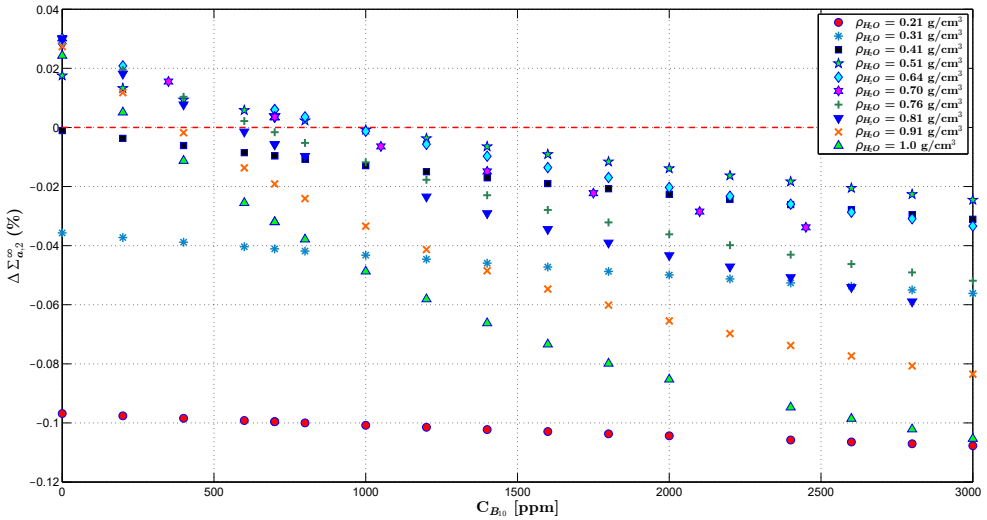


Fig. 4.18. Error in the thermal-group absorption cross section as a function of the boron concentration (on the x-axis) and of the moderator density (markers).

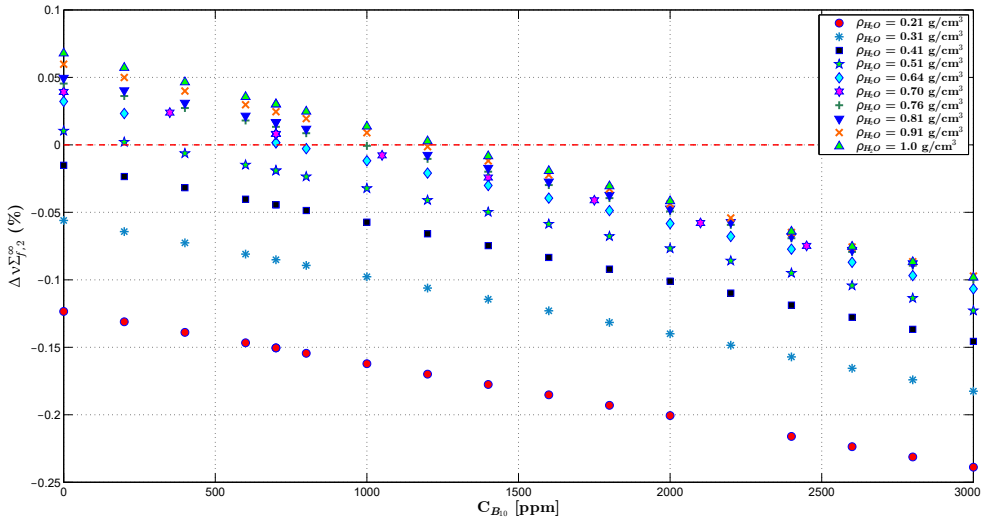


Fig. 4.19. Error in the thermal-group production cross section as a function of the boron concentration (on the x-axis) and of the moderator density (markers).

et al., 2013), in which a beta-testing version of the rehomogenization-based cross-section model has been implemented. Also in this case, the parameterized libraries are generated with APOLLO2-A. We present the results of the following calculations:

4. Modeling spectral effects of local nuclide density changes

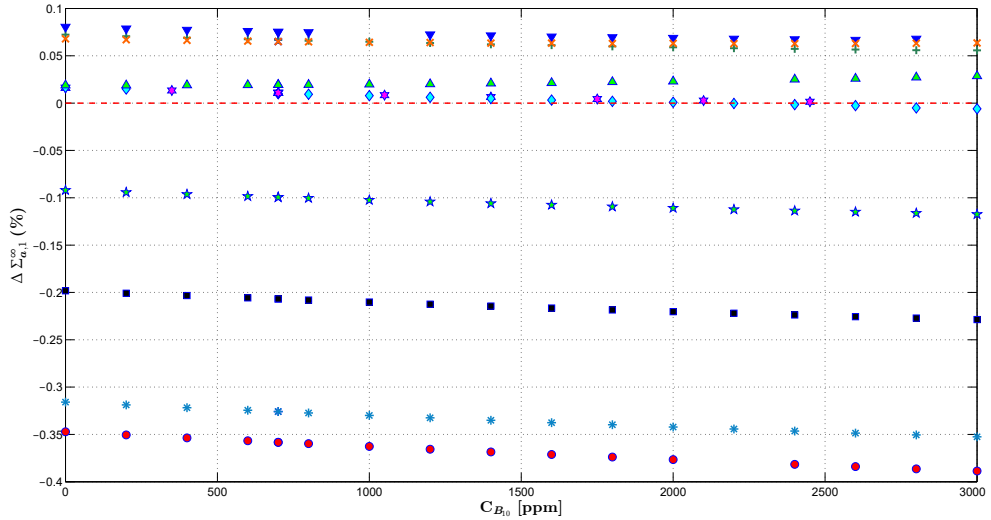


Fig. 4.20. Error in the fast-group absorption cross section as a function of the boron concentration (on the x-axis) and of the moderator density (markers). The legend is the same as in Figs. 4.17 to 4.19.

- with infinite-medium cross sections computed without the critical-buckling correction (*a*);
- with standard infinite-medium cross sections and the critical-buckling correction (*b*);
- with cross sections corrected by the reference spectral defect (*c*);
- with spectral rehomogenization of the infinite-medium cross sections interpolated at p_{loc} (*d*);
- with spectral rehomogenization of the infinite-medium cross sections interpolated at p_{nom} (*e*).

Calculation *b* is currently the most widely used approach in nodal codes. In calculation *c*, the reference spectral corrections are obtained by collapsing the 281-group macroscopic cross sections of the infinite lattice at the local conditions with the reference environmental spectrum variation from APOLLO2-A [Eq. (2.25)]. In calculation *d*, only the spectral effects of the environment are modeled by rehomogenization, as described in Chapters 2 and 3. Calculation *e* is the one that fully applies the method proposed in this chapter. In both simulations *d* and *e*, rehomogenization is applied with the diffusive leakage model (Chapter 3) and the semi-analytic basis investigated in Section 2.2.2.1 (namely, Chebyshev polynomials of the first kind combined with the

neutron emission spectrum from fission in the fast group).

In ARTEMIS, the two-group diffusion coefficient is computed from the buckling coefficient (set to the critical value by default) and the leakage cross section $\Sigma_{\text{leak},G}^{\infty} = D_G^{\infty} B^2$. The same applies to the fine-group diffusion coefficient for the calculation of the rehomogenization parameters $h_{R,D,G,j}$ and $h_{V,D,G,i,j}$ [Eq. (3.28)]. In order to be consistent with the methodology of Section 4.2.1.1, which has been derived for the zero-buckling case, the nodal data for simulations other than b are generated with the smallest user-defined value of B^2 accepted by APOLLO2-A ($B^2 = 10^{-7} \text{ cm}^{-2}$). This value is four orders of magnitude lower than the critical one in both fuel bundles ($B_{\text{crit}}^2 = 3.24 \cdot 10^{-3} \text{ cm}^{-2}$ in the unrodded assembly, and $B_{\text{crit}}^2 = -4.37 \cdot 10^{-3} \text{ cm}^{-2}$ in the rodded assembly). Compared to the zero-buckling case, the differences in all the computed cross sections are below 0.005%. Hence, with this choice no inconsistency is introduced in the application of the methodology.

Fig. 4.21 shows (i) the change in the infinite-medium spectrum due to the aforementioned perturbations in the state parameters [$\delta\Phi_{\infty,G}(u) = \Phi_{\infty,G}^{\text{loc}}(u) - \Phi_{\infty,G}^{\text{nom}}(u)$], and (ii) the deformation of the spectrum in the colorset environment at the local conditions [$\delta\Phi_{\text{env},G}(u) = \Phi_{\text{env},G}^{\text{loc}}(u) - \Phi_{\infty,G}^{\text{loc}}(u)$].

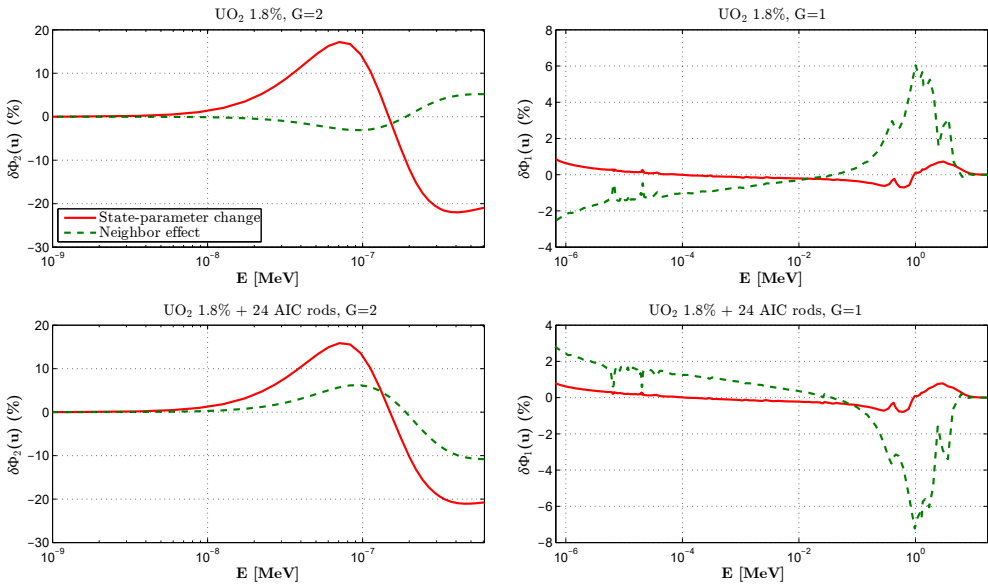


Fig. 4.21. Components of the spectrum variation (per unit u) in the unrodded and rodded assemblies of the colorset example: (i) perturbation in the infinite medium due to the transition from the nominal to the local conditions (solid lines), and (ii) perturbation in the environment due to neighbor effects (dashed lines).

The variations in both $C_{B_{10}}$ and $N_{Xe_{135}}$ from their nominal values contribute to a reduction in absorption, thus thermalizing the spectrum in the two assemblies.

4. Modeling spectral effects of local nuclide density changes

Neutron streaming hardens the spectrum in the unrodded assembly and thermalizes it in the rodded one. The neighbor-effect component is preeminent in the fast group, whereas the state-parameter change has the highest impact in the thermal group.

Fig. 4.22 depicts the overall spectrum variation $[\delta\Phi_G(u) = \Phi_{\text{env},G}^{\text{loc}}(u) - \Phi_{\infty,G}^{\text{nom}}(u)]$ estimated with calculation *e*. The computed curves accurately predict the global behavior of the reference. Minor deviations from the transport solution are mainly found in the thermal group and in the high-energy region of the fast group (at $E > 0.1$ MeV). These deviations are due partly to the use of polynomial basis functions and partly to inherent flaws of the diffusive approximation of the leakage spectrum, whose outcome is shown in Fig. 4.23. The leakage function computed with this approach is very precise in the epithermal region and in the low-energy region of the thermal group ($E < 0.25$ eV), whereas it exhibits minor inaccuracy in the range $[0.25 \text{ eV}, 0.625 \text{ eV}]$ and in the fission-emission region.

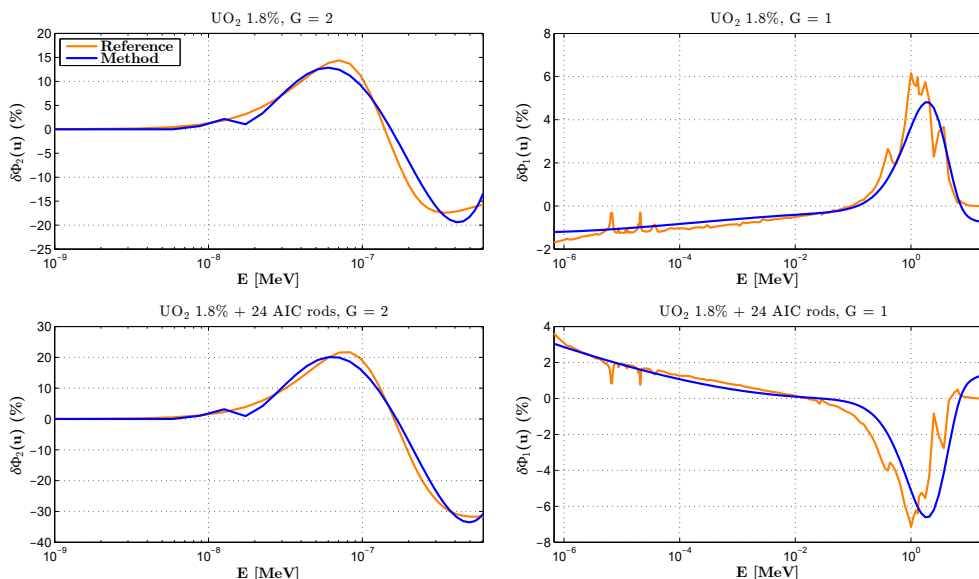


Fig. 4.22. Spectrum variation (per unit u) between the colorset environment in the local conditions and the infinite lattice in the nominal conditions, as computed by the rehomogenization-based reconstruction algorithm with the diffusive leakage model (calc. *e*).

For the above set of calculations, Table 4.10 reports the errors in the nodal cross sections of the two assemblies. The critical-buckling approach significantly overcorrects the fast-group cross sections. The corrections computed with calculation *e* go in the right direction and are close to the reference ones (calculation *c*), except for thermal absorption in the rodded assembly (for which yet the error decreases compared to the infinite-medium values). The improvement over calculations *a* and *b* is appar-

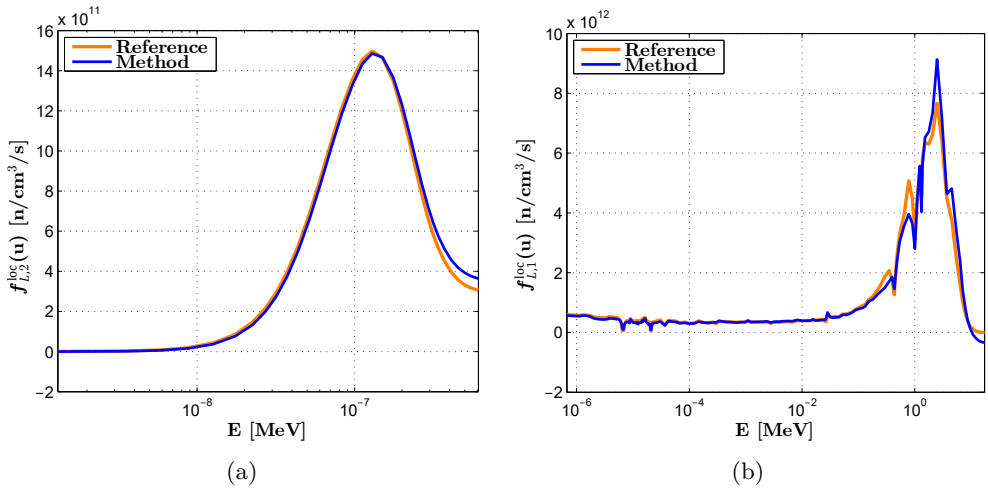


Fig. 4.23. (a) Thermal- and (b) fast-group leakage spectra in the unrodded assembly, as computed with the diffusive approximation applied to calculation *e*. The curves are normalized to the reference coarse-group, assembly-averaged leakage. Units are in neutrons/(cubic centimeters · second).

ent. Table 4.11 shows the errors in the main integral parameters and the number of power iterations for the convergence of the eigenvalue calculation. Calculation *e* produces better estimates of the integral parameters than those ensuing from standard interpolation of the infinite-medium cross sections. The method strongly reduces the overestimation of the control-rod bank worth observed with the conventional B_{crit}^2 approach (the small error found with calculation *a* is instead the result of favorable error cancellation). Similar considerations hold for the environmental rehomogenization (calculation *d*). We remark that the residual errors of our reference calculation are ascribable to the spatial component of the homogenization defects, which cannot be corrected by spectral rehomogenization. These errors are higher in k_{eff} and in the thermal fission power.

4.4 Discussion

4.4.1 Numerical features and impact on the cross-section model

For a standard PWR UO_2 assembly (as the one analyzed in this work), cross-section libraries commonly consist of about 3000 calculation points. With the rehomogenization-based model, the boron-concentration axis can be removed. Along the water-density and xenon-concentration axes, only few points must be kept, without cross calculations, to account for the effects of variations in the fine-group microscopic cross sections. The number of lattice simulations and table points decreases by a factor of approximately

4. Modeling spectral effects of local nuclide density changes

Table 4.10. Errors in the nodal cross sections of the colorset benchmark problem.

	UO ₂ 1.8%					UO ₂ 1.8% + 24 AIC rods				
	$\Sigma_{a,1}$	$\Sigma_{a,2}$	$\nu\Sigma_{f,1}$	$\nu\Sigma_{f,2}$	$\Sigma_{s,1\rightarrow 2}$	$\Sigma_{a,1}$	$\Sigma_{a,2}$	$\nu\Sigma_{f,1}$	$\nu\Sigma_{f,2}$	$\Sigma_{s,1\rightarrow 2}$
Reference [cm ⁻¹]	0.00825	0.0554	0.00483	0.0833	0.0172	0.0115	0.0810	0.00472	0.0849	0.0151
Simulation	Errors (%)									
Inf. med., no B_{crit}^2 (a)	1.39	0.55	0.36	0.60	3.40	-1.63	0.78	-0.45	-0.89	-4.42
Inf. med., B_{crit}^2 (b)	-0.82	0.41	-0.35	0.45	-1.08	1.95	0.91	0.66	-0.70	1.54
Ref. $\delta\Sigma_G^{\text{spec}}$ (c)	-0.05	0.19	-0.33	0.22	-0.28	0.47	1.37	0.43	-0.06	0.11
Rehom. at p_{loc} (d)	-0.26	0.23	-0.26	0.26	-0.23	0.54	1.20	0.31	-0.31	1.0
Rehom. at p_{nom} (e)	-0.25	0.02	-0.35	0.06	0.31	0.44	0.65	0.24	-0.38	0.04

Table 4.11. Number of power iterations (n_{iter}) and errors in the effective multiplication factor, control-rod bank worth, nodal flux, and assembly-averaged fission power of the colorset benchmark problem. The value of power error out of parentheses refers to the total power, whereas the two values within parentheses correspond to the fast- and thermal-group power, respectively.

Simulation	n_{iter}	Δk_{eff} [pcm]	Δw_{CR} (%)	UO ₂ 1.8%		UO ₂ 1.8% + 24 AIC rods	
				$\Delta\bar{\Phi}_G$ (%)	$\Delta\bar{P}_{\text{fiss}}$ (%)	$\Delta\bar{\Phi}_G$ (%)	$\Delta\bar{P}_{\text{fiss}}$ (%)
Inf. med., no B_{crit}^2 (a)	6	80	0.37	-0.47, 1.65	2.51 (0.52, 2.89)	0.62, -3.14	-3.91 (-0.61, -4.78)
Inf. med., B_{crit}^2 (b)	6	-687	-3.15	0.14, -0.51	0.41 (-0.25, 0.55)	0.083, -0.42	-0.64 (0.30, -0.92)
Ref. $\delta\Sigma_G^{\text{spec}}$ (c)	6	-425	-1.95	0.03, -0.12	0.70 (-0.07, 0.86)	0.26, -1.29	-1.10 (0.09, -1.43)
Rehom. at p_{loc} (d)	10	-387	-1.87	-0.01, 0.05	0.98 (0.04, 1.17)	0.30, -1.54	-1.53 (-0.05, -1.94)
Rehom. at p_{nom} (e)	13	-196	-0.9	-0.12, 0.42	0.77 (0.0, 0.91)	0.14, -0.73	-1.20 (0.0, -1.51)

9 if the water-density self-shielding coefficients are only computed along the burn-up axis, or 7 if they are also computed along the fuel-temperature axis. In an industrial utilization where the methodology is applied to reconstruct the cross sections directly in the real environment, the computational burden of the lattice calculations is also reduced because of the elimination of the critical-spectrum iterations. The memory requirement for the storage of the rehomogenization coefficients is negligible compared to the global memory saving.

The contraction of the interpolation hyperspace also has a beneficial effect on the on-line reconstruction phase. This step usually takes up a significant fraction of the overall run time of the nodal calculation. For example, Table 4.12 reports the run-time statistics of a 900-MW PWR reactor full-core simulation with standard six-axes interpolation in ARTEMIS. Almost half of the computing time is used by the cross-section module. This high fraction is due to the optimization of the nodal solution strategy in the flux solver (van Geemert, 2014). If the rehomogenization-based reconstruction is applied to compute the single-assembly cross sections (Section 4.2.1), the number of iterations (each of which consists of the solution of a linear system with rank 8) is generally between 6 and 8. Slower convergence is only found at very low values of the water density (Tables 4.6 and 4.9). This fraction of the core-calculation run time can

Table 4.12. Distribution of a full-core simulation run-time among the main modules for a 900-MW PWR core. The values refer to the ARTEMIS nodal code with traditional six-axes interpolation.

Module	Run time (%)
Cross-section reconstruction	48.9
Flux solver	9.58
Dehomogenization	1.17
Depletion solver	31.7
Thermal-hydraulics	0.26
Others	8.39

be easily minimized via parallelization of the algorithm. If the environmental approach is chosen (Section 4.2.2), the number of flux iterations increases. For instance, an increase by a factor of 2.17 has been observed in the colorset benchmark problem of Section 4.3.2 (Table 4.11). However, as discussed in Section 3.4.1, this value is not fully representative for an actual (i.e., coupled) core simulation, where embedding the rehomogenization updates within the thermal-feedback iterations (see Fig. 4.6) would mitigate the slowdown in convergence of the eigenvalue calculation. Moreover, as observed in Table 4.12, the contribution of the nodal flux solver to the overall run time of the core calculation is about five times smaller than that of the standard interpolation-based reconstruction phase. Therefore, the gain due to the decrease in the number of interpolation axes would prevail over the additional iterations at the flux-solver level.

Isotopic rehomogenization [Eq. (4.34)] allows modeling the spectral effects of the environment and of the local physical conditions on the microscopic cross sections of the most relevant nuclides (such as fissile elements, the main fission products and actinides, burnable absorbers, and control elements). Node-averaged history effects due to differences between the off-nominal depletion in the real environment and the single-assembly reference base depletion can therefore be fully accounted for by combining the proposed method with a microscopic depletion model.

This rehomogenization-based strategy is valid for an arbitrary number of energy groups of the nodal cross sections and can be applied to reactor types other than PWRs. For example, in BWR core analysis one could take advantage of this approach to model the spectral effects of the instantaneous coolant and moderator void fractions (or densities) and, potentially, of the coolant void (or density) history as well. When the boron concentration (which is not used for shim control in BWRs) is also retained in the cross-section parameterization for safety/transient calculations (such as the Anticipated Transient Without Scram), the interpolation hyperspace would be reduced by four to five axes. Another feature of the method is that it can be leveraged to reconstruct the cross sections in subcritical states, not only in core operation of critical

reactors, but also in the presence of a neutron source. This requires to compute the projection coefficients of the neutron-source emission spectrum $S_G(u)$ on the weighting functions $W_{G,j}(u)$:

$$\Psi_{G,j} = \int_0^1 du S_G(u) W_{G,j}(u). \quad (4.40)$$

This source term is to be added to the right-hand side of Eq. (4.15). This strategy can thus be used for safety analyses of cold shut-down states. Furthermore, it can be easily integrated into the cross-section model of accelerator-driven subcritical reactors.

4.4.2 On the modal approach

In the tests on single-assembly configurations (Section 4.3.1), we have used basis and weighting functions built with the POD approach. A similar study has been made with the semi-analytic modes (i.e., Chebyshev polynomials and the fission-emission spectrum) used for the multiassembly benchmark problem in Section 4.3.2. The results are here summarized for two sample perturbations without xenon variation: a transition to $C_{B_{10}} = 2450$ ppm (case *a* of Section 4.3.1.2), and a transition to $\rho_{H_2O} = 0.21$ g/cm³ (case *b* of Section 4.3.1.3).

The computed spectrum variations and numerical errors are shown in Fig. 4.24 and Table 4.13. A significant loss of accuracy is found in the prediction of the fast-group spectrum change, especially at high energies. In the first example, the magnitude of the perturbation is small, and the semi-analytic approach still provides reasonably accurate estimates of the cross sections and integral parameters. In the case with low moderator density, the amplitude of the deformation is high and the deviations in the computed curve result in a poor prediction of the above parameters. Hence, this set of modes cannot preserve in a generalized sense a degree of accuracy comparable to that of standard interpolation.

A basis function (such as a fission spectrum shifted toward lower values of E) could be added to better fit the high-energy double peak that characterizes water-density perturbations (Figs. 4.12 and 4.24). The first of the two peaks of opposite sign is centered at about 400 keV, which is the average energy of delayed neutrons (Stacey, 2007). Therefore, this additional mode may also be exploited to capture neutron-dynamics features in the simulation of reactor transients.

Table 4.13. Examples with the semi-analytic basis: errors in the reconstructed macroscopic cross sections and in the main integral parameters, and number of iterations.

Perturbed state	$\Delta\Sigma_{a,1}^\infty$ (%)	$\Delta\Sigma_{a,2}^\infty$ (%)	$\Delta\nu\Sigma_{f,1}^\infty$ (%)	$\Delta\nu\Sigma_{f,2}^\infty$ (%)	$\Delta\Sigma_{s,1\rightarrow 2}^\infty$ (%)	Δk_∞ [pcm]	$\Delta\Phi_{\infty,G}$ (%)	$\Delta P_{\text{fiss}}^\infty$ (%)	n_{iter}
$C_{B_{10}} = 2450$ ppm	-0.096	0.257	0.190	0.215	-0.022	41	0.049, -0.224	0.032	8
$\rho_{H_2O} = 0.21$ g/cm ³	1.107	1.084	2.89	1.071	-1.645	-549	0.211, -2.52	0.602	14

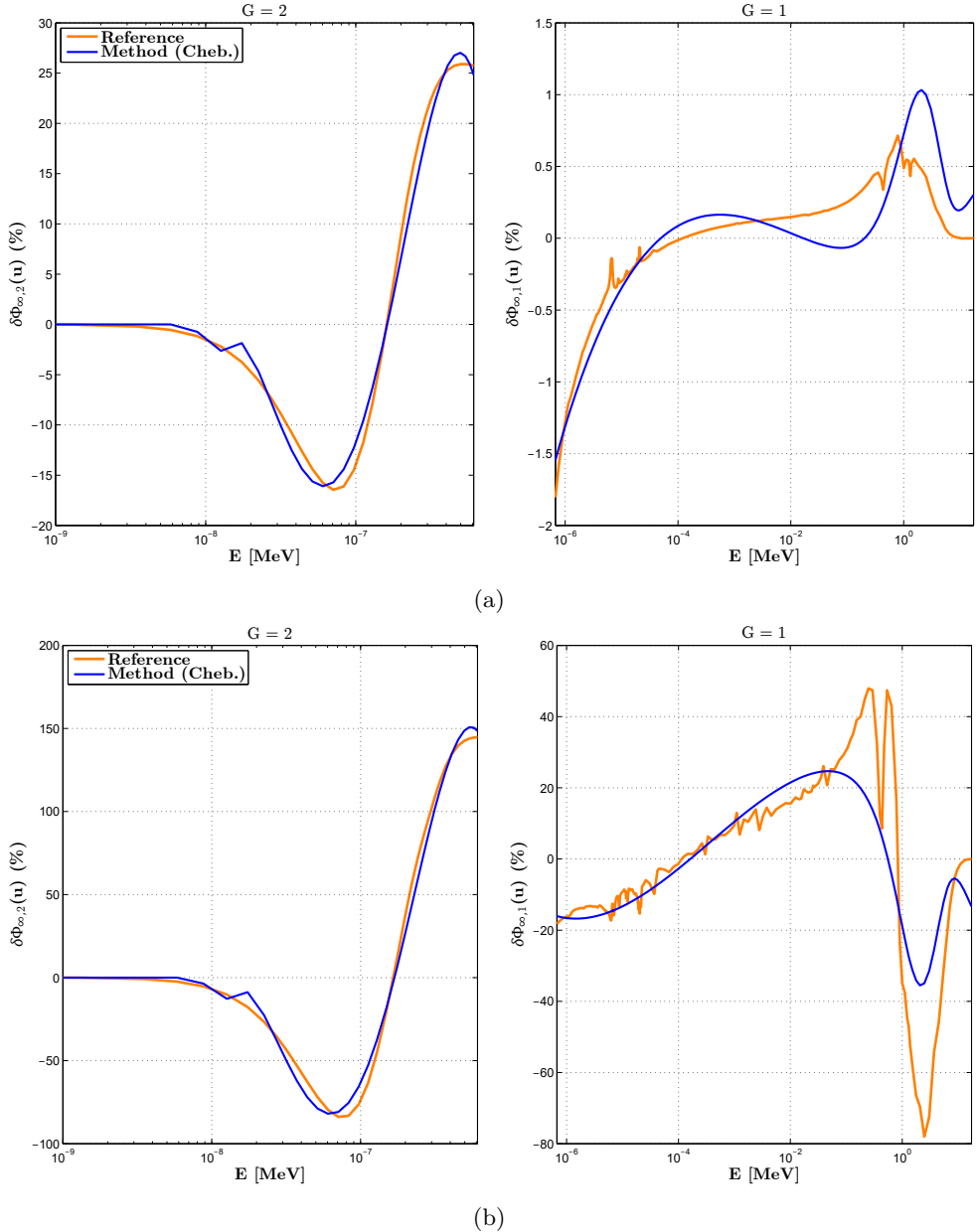


Fig. 4.24. Spectrum changes versus energy computed with the semi-analytic basis for the following transitions (without xenon variation): (a) from $C_{B_{10}} = 700$ ppm to $C_{B_{10}} = 2450$ ppm; (b) from $\rho_{H_2O} = 0.7$ g/cm³ to $\rho_{H_2O} = 0.21$ g/cm³.

4.4.3 Reconstruction of the diffusion coefficient

The diffusion coefficient is reconstructed with a procedure similar to that described for the macroscopic cross sections. Fig. 4.25 depicts the fine-group diffusion coefficient in a 1.8%-enriched UO_2 lattice at different physical conditions.

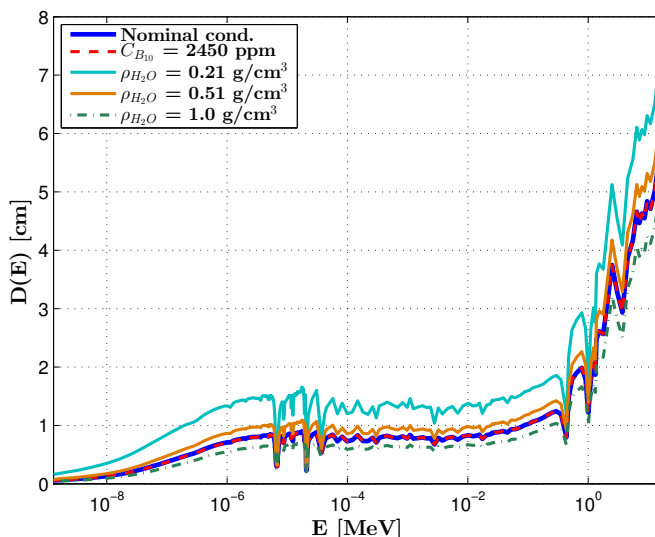


Fig. 4.25. Infinite-medium fine-group, homogenized diffusion coefficient of a 1.8%-enriched UO_2 assembly at different physical conditions. The xenon concentration is zero in conditions other than the nominal ones. The distributions have been computed with APOLLO2-A.

The distributions have been computed with the outflow transport approximation (Choi et al., 2015). Along the whole energy domain, the impact of variations in the boron and xenon concentrations is negligible. Therefore, the corresponding microscopic-effect and cross corrections $\delta D_G^{\infty,m}$ and $\delta D_G^{\infty,*}$ [Eqs. (4.11c) and (4.11d)] can be neglected. Only the moderator density has a significant impact on the diffusion-coefficient energy distribution. We account for its effect via *ad hoc* macroscopic coefficients $s_{R,D,G,j}$ and $s_{V,D,G,i,j}$ [Eq. (4.28)], which are computed with a polynomial approximation in one variable as described in Section 4.2.1.2. Eq. (4.33) is then adapted to the diffusion coefficient as

$$h_{V,D,G,i,j}^{\text{loc}} \approx h_{V,D,G,i,j}^{\text{nom}} + s_{V,D,G,i,j} , \quad (4.41)$$

where the rehomogenization parameters $h_{V,D,G,i,j}^{\text{nom}}$ are determined according to Eq. (4.17) with the nominal distribution $D_{\infty,G}^{\text{nom}}(u)$. Eq. (4.35) still holds for the few-group correction δD_G^{∞} .

It should be noted that if the diffusion coefficient is computed via the B_1 equations (Hebert, 2009), variations in the boron concentration and xenon density cause a change

in its distribution in the high-energy region (at $E > 1$ MeV). This unphysical effect is due to an inherent limitation of the B_1 methodology (Smith, 2017), which produces an increase (or decrease) in the diffusion coefficient at all energies as the lattice reactivity decreases (or increases). Because of this behavior, the contributions of boron and xenon variations to the correction terms $\delta D_1^{\infty,m}$ and $\delta D_1^{\infty,*}$ (which we have set to zero in the test case of Section 4.3.2) may no longer be negligible.

4.4.4 On the discontinuity factors and form functions

We briefly discuss the impact of variations in ρ_{H_2O} , $C_{B_{10}}$ and $N_{Xe_{135}}$ on the assembly discontinuity factors and form functions. At the library preparation stage, the discontinuity factors are usually determined and stored at the same points of the state-parameter phase space as the nodal cross sections. The form-function model often uses a simplified approach. For instance, in ARTEMIS their multivariate dependence is built with only two two-parameter cross terms.

For the UO_2 bundle considered in Section 4.3.1, Figs. 4.26 and 4.27 show the variation in the assembly-surface discontinuity factors versus the boron concentration and the water density, respectively. Changes are small (mostly $< 0.2\%$ in the fast group and $< 0.5\%$ in the thermal one) along the whole range of values of the two state parameters. This is because discontinuity factors are meant to account for intra-assembly heterogeneity, whereas perturbations in the state parameters are homogeneous within a given node. Their influence on the intranodal flux distribution is limited to changes in the fuel-to-moderator flux ratio, for the reasons discussed in Section 4.2.1.2. This can be observed, for example, in Fig. 4.28a, which shows the perturbation in the thermal-flux form function at $C_{B_{10}} = 0$ ppm and $N_{Xe_{135}} = 0$ a/ \AA^3 . The variations observed in Figs. 4.26 and 4.27 are significantly smaller than those induced by neighbor effects in the core environment. For instance, Dall’Osso (2014) found changes (compared to the infinite-medium values) of about 1.0% and 3.0% in the fast- and thermal-group environmental discontinuity factors of a rodged UO_2 assembly neighboring an unrodged assembly of the same type. As it will be shown in Chapter 5, we have found even higher variations (up to 6.0%) at UO_2/MOX interfaces.

Fig. 4.28b depicts the variation in the total-fission-power form function at $C_{B_{10}} = 0$ ppm and $N_{Xe_{135}} = 0$ a/ \AA^3 . A radial tilt is observed in the power spatial distribution. Higher perturbations in the form functions are found at very low moderator densities. For example, changes in the power distribution up to 2% occur in the assembly periphery at $\rho_{H_2O} = 0.21$ g/cm³. As observed for discontinuity factors, these variations are still modest compared to those induced by the spatial effects of the core environment.

In order to fully benefit from the reduction in the lattice-calculation computational burden and in the library memory requirements, a method should be found to reproduce the effects of local nuclide density changes on the assembly discontinuity factors and form functions. The spatial rehomogenization model described in Chapter 5 may address this aspect. This method aims to compute the variation in the 2-D spatial distribution of the neutron flux density between the real environment and the single-

4. Modeling spectral effects of local nuclide density changes

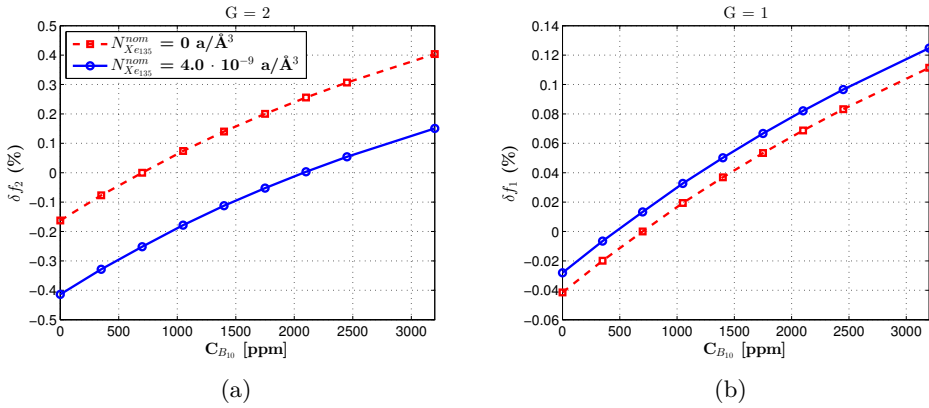


Fig. 4.26. Variations in the (a) thermal-group and (b) fast-group assembly-surface discontinuity factors versus the diluted-boron concentration.

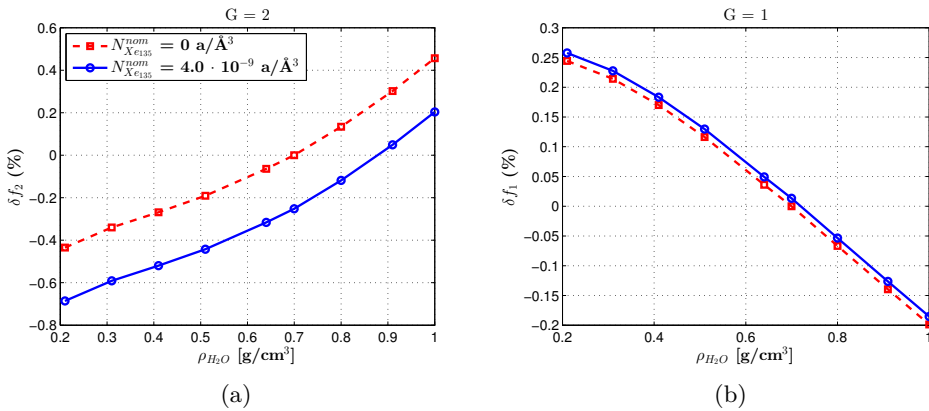


Fig. 4.27. Variations in the (a) thermal-group and (b) fast-group assembly-surface discontinuity factors versus the water density.

assembly conditions. Following an approach similar to that presented in this chapter (namely, computing the variation with respect to the infinite-lattice flux distribution in the nominal conditions), the spatial correction on the discontinuity factors could also include the state-parameter effect. Changes in the flux and power form functions may instead be estimated via empirical correlations.

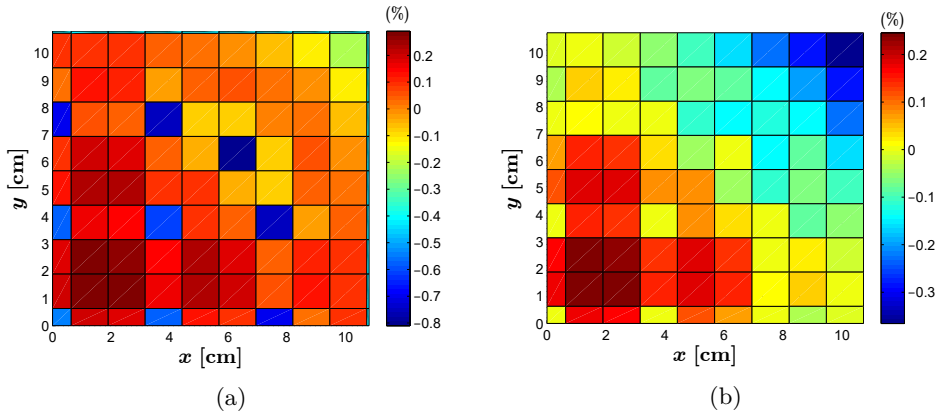


Fig. 4.28. Variation (in percentage) in the (a) thermal-flux and (b) total-fission-power form functions at $C_{B_{10}} = 0$ ppm and $N_{Xe_{135}} = 0$ a/ \AA^3 .

4.4.5 Reconstruction of the B^2 -corrected single-assembly cross sections

In the approach presented in this chapter, the cross sections are reconstructed without the critical-buckling correction. If the critical-spectrum approximation is used, Eq. (4.15) becomes

$$\begin{aligned} \bar{\Phi}_{\infty,G}^{\text{loc}} h_{R,r,G,j}^{\text{loc}} + \sum_{i=1}^{N_{Q_G}} \alpha_{\infty,G,i} h_{V,r,G,i,j}^{\text{loc}} + c_{G,j}^{\infty,\text{loc}} = \chi_{G,j} \sum_{G'=1}^{N_G} \left(\bar{\Phi}_{\infty,G'}^{\text{loc}} h_{R,f,G'}^{\text{loc}} + \right. \\ \left. \sum_{i=1}^{N_{Q_{G'}}} \alpha_{\infty,G',i} h_{V,f,G',i}^{\text{loc}} \right) + \sum_{\substack{G'=1 \\ G' \neq G}}^{N_G} \left(\bar{\Phi}_{\infty,G'}^{\text{loc}} h_{R,s,G' \rightarrow G,j}^{\text{loc}} + \sum_{i=1}^{N_{Q_{G'}}} \alpha_{\infty,G',i} h_{V,s,G' \rightarrow G,i,j}^{\text{loc}} \right), \end{aligned} \quad (4.42)$$

where $c_{G,j}^{\infty,\text{loc}}$ is the projection coefficient of the critical-leakage spectrum in the local conditions [see Eq. (4.13)]:

$$c_{G,j}^{\infty,\text{loc}} = \int_0^1 du W_{G,j}(u) L_{\infty,G}^{\text{loc}}(u). \quad (4.43)$$

Using the same approach as in Section 3.2.2, we express $L_{\infty,G}^{\text{loc}}(u)$ as

$$L_{\infty,G}^{\text{loc}}(u) = \bar{L}_{\infty,G}^{\text{loc}} f_{L,G}^{\infty,\text{loc}}(u), \quad (4.44)$$

4. Modeling spectral effects of local nuclide density changes

where $\bar{L}_{\infty,G}^{\text{loc}}$ is the infinite-medium, coarse-group critical leakage, and $f_{L,G}^{\infty,\text{loc}}(u)$ is the fundamental-mode leakage spectrum normalized to unity [Eq. (3.31)]:

$$\bar{L}_{\infty,G}^{\text{loc}} = D_G^{\infty,\text{loc}} B_{\text{crit,loc}}^2 \bar{\Phi}_{\infty,G}^{\text{loc}}, \quad f_{L,G}^{\infty,\text{loc}}(u) = \frac{D_{\infty,G}^{\text{loc}}(u) B_{\text{crit,loc}}^2 \psi_{\infty,G}^{\text{loc}}(u)}{\int_0^1 du D_{\infty,G}^{\text{loc}}(u) B_{\text{crit,loc}}^2 \psi_{\infty,G}^{\text{loc}}(u)}. \quad (4.45)$$

In Eq. (4.45) we have used the same notation as in Eq. (4.13). The few-group diffusion coefficient $D_G^{\infty,\text{loc}}$ comes from the latest iteration of the reconstruction algorithm (see Fig. 4.5 and Section 4.4.3), whereas $B_{\text{crit,loc}}^2$ and $\bar{\Phi}_{\infty,G}^{\text{loc}}$ are estimated solving the B^2 -variant of Eq. (4.19). For example, the critical zero-dimensional balance in the fast group reads

$$\left(\Sigma_{a,1}^{\infty,\text{loc}} + D_1^{\infty,\text{loc}} B_{\text{crit,loc}}^2 + \Sigma_{s,1 \rightarrow 2}^{\infty,\text{loc}} - \nu \Sigma_{f,1}^{\infty,\text{loc}} \right) \cdot \bar{\Phi}_{\infty,1}^{\text{loc}} = \left(\Sigma_{s,2 \rightarrow 1}^{\infty,\text{loc}} + \nu \Sigma_{f,2}^{\infty,\text{loc}} \right) \cdot \bar{\Phi}_{\infty,2}^{\text{loc}}. \quad (4.46)$$

Reconstructing the buckling-corrected cross sections requires the knowledge of $f_{L,G}^{\infty,\text{loc}}(u)$. A simple approach is to assume that its shape does not change significantly with the physical conditions in the node, namely

$$f_{L,G}^{\infty,\text{loc}}(u) \approx f_{L,G}^{\infty,\text{nom}}(u). \quad (4.47)$$

For the unrodded UO₂ fuel assembly considered in this chapter, Fig. 4.29 depicts the critical-leakage spectra in the nominal conditions (with $N_{X_{e135}}^{\text{nom}} = 4.0 \cdot 10^{-9} \text{ a}/\text{\AA}^3$) and in few perturbed states, all with $N_{X_{e135}} = 0 \text{ a}/\text{\AA}^3$. The differences between the local and nominal distributions are negligible in the fast group. However, the approximation of Eq. (4.47) is not warranted in the thermal range. The impact of this assumption has been quantified solving Eq. (4.42) in one step (i.e., without iterations). We have solved Eq. (4.46) with the two-group B^2 -corrected cross sections and diffusion coefficients interpolated at the local conditions (i.e., at the local values of ρ_{H_2O} , C_{B10} , and $N_{X_{e135}}$). The so obtained values of $\bar{\Phi}_{\infty,G}^{\text{loc}}$ and $B_{\text{crit,loc}}^2$ have been used in Eqs. (4.42) and (4.45). In this way, the approximation of Eq. (4.47) is the only source of inaccuracy in the solution of Eq. (4.42). For some perturbed states, Table 4.14 shows the error in the infinite-medium multiplication factor ensuing from this procedure. Significant deviations are found at low moderator densities and high boron concentrations. If the same one-step procedure is applied to the zero-buckling problem [Eq. (4.15)], the error in k_{∞} drops to 0 pcm in all sample cases. This outcome suggests that more complex modeling of $f_{L,G}^{\infty,\text{loc}}(u)$ is needed for an accurate reconstruction of the B^2 -corrected cross sections. A potential approach is to define the critical spectrum $\psi_{\infty,G}^{\text{loc}}(u)$ in Eq. (4.45) with Eqs. (4.8) and (4.14). However, this option would introduce an additional non-linearity in the rehomogenization algorithm.

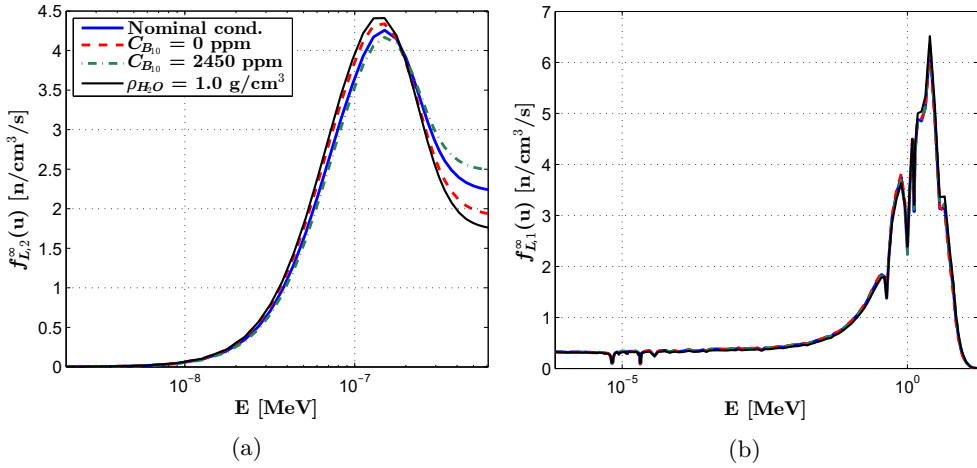


Fig. 4.29. (a) Thermal- and (b) fast-group fundamental-mode leakage spectra (normalized to unity) in the nominal state and in various perturbed conditions.

Table 4.14. Error in the multiplication factor computed with a one-step reconstruction of the B^2 -corrected single-assembly cross sections.

Local conditions	Error [pcm]
$C_{B_{10}} = 0$ ppm	-11
$C_{B_{10}} = 3000$ ppm	205
$N_{Xe_{135}} = 0$ a/Å ³ ($C_{B_{10}}^{\text{nom}}$, $\rho_{H_2O}^{\text{nom}}$)	-32
$\rho_{H_2O} = 0.81$ g/cm ³ , $C_{B_{10}} = 1000$ ppm	-13
$\rho_{H_2O} = 0.51$ g/cm ³	-47
$\rho_{H_2O} = 0.21$ g/cm ³	163

4.4.6 Spectral effects of density changes on the rehomogenization coefficients

As mentioned in Sections 2.4.2 and 3.3.1.5, in ARTEMIS the rehomogenization coefficients are only tabulated versus the burn-up, the fuel temperature and the moderator temperature. An algorithm has been developed to incorporate the effects of nuclide density changes into these parameters when rehomogenization is applied to capture only neighbor effects, such as in Chapters 2 and 3. This algorithm shares common features with the methodology described in this chapter. For the sake of completeness, it is summarized in the following.

The direct effect of density changes on the rehomogenization coefficients is taken into account with Eq. (4.24). When the spectral effects of density changes on the nodal cross sections are modeled via standard interpolation in parameterized libraries, the

reference coefficients h_R [Eq. (2.12a)] must be computed with the infinite-medium spectrum corresponding to the exact, local conditions. This spectrum is determined on the fly solving the rehomogenization problem in the infinite lattice [Eq. (4.15) or Eq. (4.42)] in one step (namely, with the cross sections interpolated at the local conditions), as explained in Section 4.4.5. Replacing Eqs. (4.8) and (4.14) into Eq. (2.12a) yields, after some algebraic manipulation, the following expression for the updated reference coefficient $h_{R,x,G,j}^{\text{loc},*}$:

$$h_{R,x,G,j}^{\text{loc},*} = h_{R,x,G,j}^{\text{loc}} + \sum_{i=1}^{N_{QG}} \alpha_{G,i}^{\infty} h_{V,x,G,i,j}^{\text{loc}}, \quad (4.48)$$

where $h_{R,x,G,j}^{\text{loc}}$ and $h_{V,x,G,i,j}^{\text{loc}}$ are the reference and variational coefficients corrected with Eq. (4.24) to take into account the direct effect of density changes. The modal coefficients $\alpha_{G,i}^{\infty}$ come from the one-step solution of Eq. (4.15) or Eq. (4.42). The spectral update of Eq. (4.48) is performed at the beginning of each rehomogenization iteration. Afterwards, the environmental rehomogenization problem [Eq. (2.13)] is solved using the coefficients $h_R^{\text{loc},*}$ and h_V^{loc} obtained with Eqs. (4.48) and (4.24), respectively. In this way, nodal cross sections are rehomogenized [by Eq. (2.15)] with the difference in the spectrum exclusively due to internodal neutron leakage. We emphasize that if only the correction of Eq. (4.24) is applied, the spectrum deformation computed with Eq. (2.13) (which becomes equivalent to Eq. (4.15)) will include the contributions of both neighbor effects and changes in the state parameters. The latter would therefore be taken into account twice (namely, via rehomogenization and the cross-section model).

The calculation with fuel depletion presented in Section 3.3.1.5 was performed with the critical-buckling approach and with the direct and spectral updates of the rehomogenization coefficients described in this section. In the solution of the one-step problem for the spectral update, Eq. (4.47) was used to approximate the critical-leakage spectrum in the local conditions. Since in this test case only the xenon concentration changes significantly compared to the nominal conditions, the impact of this approximation is small (see Table 4.14).

4.5 Summary

We have proposed a novel method to model the spectral effects of local nuclide density changes on the few-group nodal macroscopic and microscopic cross sections. The cross-section multivariate dependence on the water density, the concentration of diluted boron and the xenon level is reproduced with a rehomogenization-based approach. Our target accuracy is achieved in most of the phase space of these three state parameters. Deviations close to or slightly higher than the prescribed error bounds are only found in fast-group cross sections at very low moderator densities (below 0.3 g/cm³), which can be experienced in accidental conditions. However, these

deviations are still small compared to the homogenization errors commonly found in standard nodal simulations of strongly heterogeneous multiassembly configurations. Eventually, the rehomogenization algorithm inherently predicts the combined spectral changes due to *(i)* variations in the local physical conditions, *(ii)* interassembly neutron leakage, and *(iii)* different reactivity in the real environment and in the infinite lattice. These findings lay the groundwork for a new concept of cross-section model, featuring *(i)* a considerably smaller number of branch calculations in the lattice-physics code and of table points in the parameterized libraries, and *(ii)* a computationally less demanding on-line reconstruction of the nodal cross sections.

A TWO-DIMENSIONAL MODEL FOR SPATIAL REHOMOGENIZATION OF NODAL CROSS SECTIONS AND DISCONTINUITY-FACTOR CORRECTION

5.1 Introduction

In this chapter ¹, we propose an extension of the spatial rehomogenization technique described in Dall’Osso (2014). This method aims to compute on the fly the change in the intranodal flux shape that is used for cross-section spatial homogenization when the assembly is in the core environment. The rehomogenization problem is solved using as boundary conditions the estimates of the volume-averaged fluxes, the surface-averaged fluxes and currents, and the multiplication factor from the global (i.e., core-wide) nodal calculation. Only radial heterogeneity is addressed. The effect of axial heterogeneity is taken into account via axial homogenization or control-rod cusping models (Dall’Osso, 2002). Two significant approximations are made in the formulation presented in Dall’Osso (2014):

- The 2-D rehomogenization problem is simplified via transverse integration into two 1-D problems, which are solved sequentially in the x and y directions.
- The transverse-integrated fine-mesh cross sections (to be weighted with the computed 1-D flux change) are obtained by collapsing the 2-D pin-by-pin cross-

¹The content of this chapter has been accepted for publication in *Annals of Nuclear Energy*.

section distributions with the infinite-medium flux form function, instead of the environmental flux shape.

In the work presented in this chapter, the above assumptions are relaxed by developing a full 2-D rehomogenization model, which retains the non-separability of the flux variation in the x and y directions. In this way, the 2-D distributions of the environmental flux and directional net currents can be estimated at the nodal flux iteration level. Moving to a 2-D model is also motivated by the possibility to use the so obtained 2-D information (*i*) to compute the transverse-leakage distributions for the transverse-integrated nodal equations, and (*ii*) to reconstruct the pin-by-pin flux and power distributions directly (i.e., without the dehomogenization phase).

This chapter is structured as follows. The 2-D rehomogenization method is described in Section 5.2. Section 5.3 shows the numerical results of the PWR multiassembly configurations considered in previous chapters, in which the spatial effects of the environment are also important. The accuracy of the method is assessed on both nodal and pin-by-pin quantities. A comparison with the simplified 1-D approach is made. In Section 5.4, we discuss various aspects of interest of spatial rehomogenization. These include the correction of assembly discontinuity factors, the calculation of the transverse-leakage shape with the information from the 2-D rehomogenization, and the contributions of various environmental effects (spatial, spectral, and mixed energy-space) to the deviations of nodal cross sections from the single-assembly values. Concluding remarks follow in Section 5.5.

5.2 Description of the method

We introduce a non-dimensional coordinate u_d , where d stands for x or y . The following change of variable is applied:

$$d, \quad d \in [0, \Delta d] \quad \rightarrow \quad u_d = \frac{d}{\Delta d} - \frac{1}{2}, \quad u_d \in \left[-\frac{1}{2}, \frac{1}{2}\right]. \quad (5.1)$$

We define the 2-D intranodal distribution of the environmental neutron flux density in the coarse energy group G as

$$\Phi_{\text{env},G}(u_x, u_y) = \bar{\Phi}_G \varphi_{\infty,G}(u_x, u_y) + \delta\Phi_G(u_x, u_y), \quad (5.2)$$

where $\bar{\Phi}_G$ is the volume-averaged flux from the nodal calculation, $\varphi_{\infty,G}(u_x, u_y)$ is the infinite-medium flux distribution (normalized to unity) used for cross-section spatial homogenization in the lattice calculation, and $\delta\Phi_G(u_x, u_y)$ is the flux spatial variation between the environmental and infinite-medium conditions. The distributions $\Phi_{\text{env},G}(u_x, u_y)$ and $\varphi_{\infty,G}(u_x, u_y)$ are heterogeneous quantities, whereas $\delta\Phi_G(u_x, u_y)$ is assumed to be a smoothly varying function. The node-averaged value of $\delta\Phi_G(u_x, u_y)$ is zero to satisfy the normalization condition

$$\int_{-1/2}^{1/2} du_x \int_{-1/2}^{1/2} du_y \Phi_{\text{env},G}(u_x, u_y) = \bar{\Phi}_G. \quad (5.3)$$

The flux change is approximated with a 2-D modal expansion:

$$\delta\Phi_G(u_x, u_y) = \sum_{i_x=1}^{N_x} \alpha_{G,x,i_x} P_{G,i_x}(u_x) + \sum_{i_y=1}^{N_y} \alpha_{G,y,i_y} P_{G,i_y}(u_y) + \sum_{\substack{c_x=1 \\ c_x+c_y \leq N_c}}^{N_x} \sum_{\substack{c_y=1 \\ c_x+c_y \leq N_c}}^{N_y} \alpha_{G,xy,c_x,c_y} P_{G,c_x}(u_x) P_{G,c_y}(u_y). \quad (5.4)$$

The non-separability of the flux variation is modeled with the cross terms α_{G,xy,c_x,c_y} . In this work, for each coarse group we consider directional expansions with four basis functions (i.e., $N_x = N_y = N = 4$) and we retain four cross terms ($N_{\text{cross}} = 4$). The basis functions $P_{G,i_d}(u_d)$ are the conventional polynomial and hyperbolic functions used for the 1-D transverse-integrated flux expansion in the semi-analytic NEM, with the only exception of $P_{2,4}(u_d)$:

$$P_{G,1}(u_d) = u_d \quad (G = 1, 2); \quad (5.5a)$$

$$P_{G,2}(u_d) = u_d^2 - \frac{1}{12} \quad (G = 1, 2); \quad (5.5b)$$

$$P_{1,3}(u_d) = u_d \left(u_d^2 - \frac{1}{4} \right), \quad P_{2,3}(u_d) = \sinh(\eta u_d); \quad (5.5c)$$

$$P_{1,4}(u_d) = \left(u_d^2 - \frac{1}{4} \right) \left(u_d^2 - \frac{1}{20} \right), \quad P_{2,4}(u_d) = \cosh(\eta u_d) - \frac{2}{\eta} \sinh\left(\frac{\eta}{2}\right). \quad (5.5d)$$

In Eqs. (5.5c) and (5.5d), the coefficient η is chosen so that the hyperbolic functions $\sinh(\eta u_d)$ and $\cosh(\eta u_d)$ are particular solutions of the 1-D homogeneous diffusion equation in the thermal group:

$$\eta = \Delta d \sqrt{\frac{\Sigma_{a,2} + \sum_{G'=1}^2 \Sigma_{s,2 \rightarrow G'}}{D_2}}. \quad (5.6)$$

The basis functions of Eq. (5.5) proved to accurately reconstruct the 1-D transverse-integrated flux variation (Dall'Osso, 2014) and have been also used in this work for their generality. The above modes have zero average value in the interval $[-1/2, 1/2]$, thus satisfying Eq. (5.3). The four cross terms in Eq. (5.4) only have polynomial components, with global order up to 4 (i.e., $N_c = 4$) and directional order up to 2. The spatial distribution of the directional net neutron current $J_{\text{env},G,d}(u_x, u_y)$ is defined as

$$J_{\text{env},G,d}(u_x, u_y) = \bar{\Phi}_G J_{\infty,G,d}(u_x, u_y) + \delta J_{G,d}(u_x, u_y), \quad (5.7)$$

with

$$\delta J_{G,d}(u_x, u_y) = -\frac{D_G(u_x, u_y)}{\Delta d} \frac{\partial}{\partial u_d} \delta\Phi_G(u_x, u_y). \quad (5.8)$$

In Eq. (5.7), scaling to the volume-averaged flux $\bar{\Phi}_G$ ensues from the application of Fick's law to Eq. (5.2). In Eq. (5.8), $D_G(u_x, u_y)$ is the spatially dependent diffusion coefficient (in units of cm).

We define the environmental discontinuity factors $f_{G,d\pm}^{\text{env}}$ at the node surfaces as

$$f_{G,d\pm}^{\text{env}} = f_{G,d\pm}^{\infty} + \delta f_{G,d\pm}, \quad (5.9)$$

where the signs \pm refer to the interfaces along the positive and negative directions of the d axis.

The following nodal unknowns must be found for each coarse group [Eqs. (5.4) and (5.9)]: the directional modal coefficients α_{G,d,i_d} (4 unknowns per direction), the cross modal coefficients α_{G,xy,c_x,c_y} (4 unknowns), and the discontinuity-factor corrections $\delta f_{G,d\pm}$ (2 unknowns per direction). With the aforementioned choice of N and N_c , the number of unknowns per coarse group is 16. In order to solve for them, we identify a set of equations for the following quantities:

- the environmental surface-averaged fluxes (2 equations per direction, per group);
- the environmental surface-averaged net currents (2 equations per direction, per group);
- the environmental corner-point fluxes (4 equations per group).

The remaining four (or $[(N_x + N_y + N_{\text{cross}}) - 8]$ in a more general framework) equations per group are found applying a standard weighted-residual technique to the 2-D few-group balance equation in the environmental conditions. The procedure used to derive the aforementioned equations is explained below.

5.2.1 Equations for the environmental surface-averaged flux

The surface-averaged heterogeneous (i.e., continuous) flux in the environmental conditions $\Phi_{G,d\pm}^{\text{het}}$ can be written, for the x direction, as

$$\Phi_{G,x\pm}^{\text{het}} = \int_{-1/2}^{1/2} du_y \Phi_{\text{env},G}(u_x, u_y) \Big|_{u_x=\pm\frac{1}{2}} = f_{G,d\pm}^{\text{env}} \Phi_{G,x\pm}^{\text{hom}}, \quad (5.10)$$

where $\Phi_{G,x\pm}^{\text{hom}}$ denotes the homogeneous (i.e., discontinuous) surface-averaged flux from the nodal calculation. Introducing Eqs. (5.2) and (5.9) into Eq. (5.10) yields

$$\bar{\Phi}_G \int_{-1/2}^{1/2} du_y \varphi_{\infty,G}(u_x, u_y) \Big|_{u_x=\pm\frac{1}{2}} + \int_{-1/2}^{1/2} du_y \delta \Phi_G(u_x, u_y) \Big|_{u_x=\pm\frac{1}{2}} = (f_{G,x\pm}^{\infty} + \delta f_{G,x\pm}) \Phi_{G,x\pm}^{\text{hom}}. \quad (5.11)$$

Using the definition of single-assembly discontinuity factor and taking into account that the volume-averaged value of $\varphi_{\infty,G}(u_x, u_y)$ is unity, we rewrite the first term on the left-hand side of Eq. (5.11) as

$$\bar{\Phi}_G \int_{-1/2}^{1/2} du_y \varphi_{\infty,G}(u_x, u_y) \Big|_{u_x=\pm\frac{1}{2}} = \bar{\Phi}_G f_{G,x\pm}^{\infty}. \quad (5.12)$$

After substituting Eqs. (5.4) and (5.12) into Eq. (5.11), we obtain

$$\sum_{i_x=1}^{N_x} \alpha_{G,x,i_x} P_{G,i_x} \left(\pm \frac{1}{2} \right) = (f_{G,x\pm}^{\infty} + \delta f_{G,x\pm}) \Phi_{G,x\pm}^{\text{hom}} - f_{G,x\pm}^{\infty} \bar{\Phi}_G. \quad (5.13)$$

In Eq. (5.13), the transverse-direction (i.e., y -directional) and cross components of the surface-averaged flux variation vanish because, by definition,

$$\int_{-1/2}^{1/2} du_y P_{G,i_y}(u_y) = 0. \quad (5.14)$$

An equation analogous to Eq. (5.13) holds for the y direction.

5.2.2 Equations for the environmental surface-averaged current

We consider the simple case with homogeneous diffusion coefficient [i.e., $D_G(u_x, u_y) = D_G$]. Using Eqs. (5.7) and (5.8), the surface-averaged directional net current reads (for the x axis)

$$\begin{aligned} \int_{-1/2}^{1/2} du_y J_{\text{env},G,x}(u_x, u_y) \Big|_{u_x=\pm\frac{1}{2}} &= -\frac{D_G}{\Delta x} \int_{-1/2}^{1/2} du_y \frac{\partial}{\partial u_x} \delta \Phi_G(u_x, u_y) \Big|_{u_x=\pm\frac{1}{2}} = \\ &= -\frac{D_G}{\Delta x} \left[\sum_{i_x=1}^{N_x} \alpha_{G,x,i_x} \frac{dP_{G,i_x}}{du_x}(u_x) \Big|_{u_x=\pm\frac{1}{2}} \right]. \end{aligned} \quad (5.15)$$

In Eq. (5.15), we have used the fact that the infinite-medium current at the assembly surface is zero, namely

$$J_{\infty,G,x}(u_x, u_y) \Big|_{u_x=\pm\frac{1}{2}} = 0. \quad (5.16)$$

Eq. (5.16) is valid at the assembly outer edges and, when considering four nodes per fuel assembly, at the internal surfaces of fully symmetrically loaded fuel bundles (i.e., with octant or quadrant symmetry).

The sought equation is found equating Eq. (5.15) to the surface-averaged directional net current $J_{G,x\pm}$ from the nodal calculation:

$$-\frac{D_G}{\Delta x} \left[\sum_{i_x=1}^{N_x} \alpha_{G,x,i_x} \frac{dP_{G,i_x}}{du_x}(u_x) \Big|_{u_x=\pm\frac{1}{2}} \right] = J_{G,x\pm}. \quad (5.17)$$

5.2.3 Equations for the environmental corner-point flux

The heterogeneous (i.e., continuous) flux at a nodal corner point c is

$$\Phi_{G,c}^{\text{het}} = \Phi_{\text{env},G}(u_x, u_y) \Big|_{\substack{u_x=u_x^c \\ u_y=u_y^c}} = \bar{\Phi}_G \varphi_{\infty,G}(u_x, u_y) \Big|_{\substack{u_x=u_x^c \\ u_y=u_y^c}} + \delta \Phi_G(u_x, u_y) \Big|_{\substack{u_x=u_x^c \\ u_y=u_y^c}}, \quad (5.18)$$

where u_x^c and u_y^c denote the corner-point coordinates within the node. Introducing the single-assembly corner discontinuity factor $f_{G,c}^{\infty}$ and substituting Eq. (5.4), Eq. (5.18) becomes

$$\begin{aligned} \sum_{i_x=1}^{N_x} \alpha_{G,x,i_x} P_{G,i_x}(u_x^c) + \sum_{i_y=1}^{N_y} \alpha_{G,y,i_y} P_{G,i_y}(u_y^c) + \\ \sum_{\substack{c_x=1 \\ c_x+c_y \leq N_c}}^{N_x} \sum_{\substack{c_y=1 \\ c_x+c_y \leq N_c}}^{N_y} \alpha_{G,xy,c_x,c_y} P_{G,c_x}(u_x^c) P_{G,c_y}(u_y^c) = \Phi_{G,c}^{\text{het}} - \bar{\Phi}_G f_{G,c}^{\infty}. \end{aligned} \quad (5.19)$$

An estimate of $\Phi_{G,c}^{\text{het}}$ must be found to use Eq. (5.19) in the spatial rehomogenization algorithm. For this purpose, we use two different approaches:

- a combination of Smith's method (Rempe et al., 1989) and the Method of Successive Smoothing (MSS) (Böer and Finnemann, 1992);
- a Corner Point Balance (CPB) condition (Chang et al., 1989).

The methods mentioned above are commonly used in the context of fuel-assembly dehomogenization (Joo et al., 2009). Their application in the framework of our work is briefly explained in the following.

5.2.3.1 Smith's method and the Method of Successive Smoothing

In Smith's method, the intranodal flux distribution is considered as separable in the x and y directions. The homogeneous flux at a given node vertex is approximated using the volume-averaged flux in the node and the surface-averaged flux at the nodal edges crossing the corner. For instance, using the nodal coordinate system of Fig. 5.1, the flux in the north-east corner $\Phi_{G,NE}^{\text{hom}}$ reads

$$\Phi_{G,NE}^{\text{hom}} = \frac{\Phi_{G,x+}^{\text{hom}} \Phi_{G,y+}^{\text{hom}}}{\bar{\Phi}_G}. \quad (5.20)$$

The MSS is based on the assumption that the flux varies linearly in the neighborhood of a corner point. The homogeneous flux at a nodal vertex is estimated with a linear extrapolation in terms of the surface-averaged and volume-averaged fluxes:

$$\Phi_{G,NE}^{\text{hom}} = \Phi_{G,x+}^{\text{hom}} + \Phi_{G,y+}^{\text{hom}} - \bar{\Phi}_G. \quad (5.21)$$

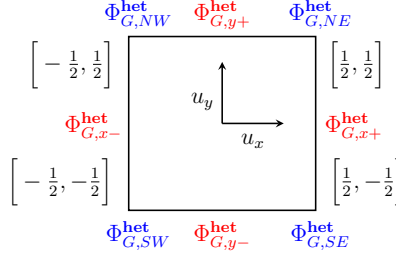


Fig. 5.1. Corner-point coordinate system in a generic node. The corner and surface-averaged fluxes are highlighted.

The heterogeneous corner flux in the environment is related to its homogeneous counterpart $\Phi_{G,c}^{\text{hom}}$ via the corner discontinuity factor:

$$\Phi_{G,c}^{\text{het}} = f_{G,c}^{\text{env}} \Phi_{G,c}^{\text{hom}}. \quad (5.22)$$

Using Eqs. (5.20) or (5.21) and Eq. (5.22), four estimates of $\Phi_{G,c}^{\text{het}}$ are available for a given corner point, one from each node surrounding the corner. The heterogeneous corner flux is thus approximated with the arithmetic average of the available estimates:

$$\Phi_{G,c}^{\text{het}} = \frac{1}{4} \left(\Phi_{G,c,i,j}^{\text{hom}} f_{G,c,i,j}^{\text{env}} + \Phi_{G,c,i+1,j}^{\text{hom}} f_{G,c,i+1,j}^{\text{env}} + \Phi_{G,c,i,j+1}^{\text{hom}} f_{G,c,i,j+1}^{\text{env}} + \Phi_{G,c,i+1,j+1}^{\text{hom}} f_{G,c,i+1,j+1}^{\text{env}} \right), \quad (5.23)$$

where we have denoted with i and j the coordinates (along the x and y axes, respectively) of the four nodes sharing the corner c . In the real environment, the corner discontinuity factors also change compared to their infinite-lattice estimates. An environmental correction on this parameter ($\delta f_{G,c}$) should therefore be introduced for each node vertex. In order not to increase the number of unknowns and equations of the rehomogenization problem, we use an approximate relation to evaluate this correction. We assume that $\delta f_{G,c}$ is proportional to the corrections on the discontinuity factors of the x - and y -directional surfaces crossing the corner ($\delta f_{G,x}$, $\delta f_{G,y}$), namely

$$\frac{f_{G,c}^{\infty} + \delta f_{G,c}}{f_{G,c}^{\infty}} = \frac{f_{G,x}^{\text{env}} + f_{G,y}^{\text{env}}}{f_{G,x}^{\infty} + f_{G,y}^{\infty}}, \quad (5.24)$$

where $f_{G,x}^{\text{env}}$ and $f_{G,y}^{\text{env}}$ are the environmental discontinuity factors estimated with Eq. (5.9) at the previous rehomogenization iteration.

Previous work (Khoshahval et al., 2014) showed that the MSS generally performs better than Smith's method, in which spatial cross effects are neglected. On the

other hand, Eq. (5.21) may lead to a negative corner flux (especially at the first nodal iterations, when the surface-averaged flux estimates are not yet accurate enough). For this reason, we use Eq. (5.21) as a default option and switch to Eq. (5.20) in case of negative corner-flux values from the MSS. Despite the ease of implementation, this approach may fail to provide accurate estimates of the corner fluxes if the flux distribution exhibits strong spatial gradients (Rempe et al., 1989; Joo et al., 2009).

5.2.3.2 The Corner Point Balance approach

The Corner Point Balance (Chang et al., 1989) is a neutron balance equation imposing the absence of net source conditions at the corner points (i.e., no accumulation of neutrons within an infinitesimally small volume). With this method, continuity of the neutron current at the vertices of a node is preserved.

We briefly review this approach with an analogy to the simple case of 1-D problem (Joo et al., 2009). From diffusion theory, the heterogeneous surface-averaged flux at the interface s between two adjacent nodes k and l is related to the inlet ($J_{G,s}^{\text{in}}$) and outlet ($J_{G,s}^{\text{out}}$) partial currents as

$$\Phi_{G,s} = 2(J_{G,s}^{\text{in}} + J_{G,s}^{\text{out}}), \quad (5.25)$$

where

$$J_{G,s}^{\text{in}} = \frac{1}{4}\Phi_{G,s} + \frac{1}{2}J_{G,s}, \quad J_{G,s}^{\text{out}} = \frac{1}{4}\Phi_{G,s} - \frac{1}{2}J_{G,s}. \quad (5.26)$$

If no continuity of the net current $J_{G,s}$ is imposed, the estimates of $J_{G,s}$ computed for the nodes k and l will be different (i.e., $J_{G,s}^k \neq J_{G,s}^l$). Inserting Eq. (5.26) into Eq. (5.25) yields

$$\Phi_{G,s}^* = \Phi_{G,s} + (J_{G,s}^k - J_{G,s}^l). \quad (5.27)$$

Eq. (5.27) defines an iterative algorithm, in which a new estimate of the surface flux $\Phi_{G,s}^*$ is obtained from the previous one and the difference in the computed net currents, which will eventually converge to zero.

A similar scheme can be applied to the neighborhood of a corner point. As illustrated in Fig. 5.2, four sets of directional net currents exist at a given nodal vertex (one for each adjacent node): $J_{x,c}^1$ and $J_{y,c}^1$ for node 1, $J_{x,c}^2$ and $J_{y,c}^2$ for node 2, etc. The currents along a certain direction must have the same value (i.e., $J_{x,c}^1 = J_{x,c}^2$, $J_{x,c}^3 = J_{x,c}^4$, $J_{y,c}^1 = J_{y,c}^3$, and $J_{y,c}^2 = J_{y,c}^4$) to ensure a zero-net-leakage balance in an infinitesimally small volume containing the corner point. However, since no condition on the corner current continuity is imposed in the nodal calculation, they may be different. Using Eq. (5.27), four new estimates of the heterogeneous corner flux are obtained (one for each node). Taking the average of them yields

$$\Phi_{G,c}^* = \Phi_{G,c} + \frac{1}{4} \left[(J_{x,c}^1 - J_{x,c}^2) + (J_{x,c}^3 - J_{x,c}^4) + (J_{y,c}^1 - J_{y,c}^3) + (J_{y,c}^2 - J_{y,c}^4) \right]. \quad (5.28)$$

This iterative scheme converges as the sum of the differences in the net currents (i.e., the term within brackets on the right-hand side of Eq. (5.28)) vanishes. Assuming

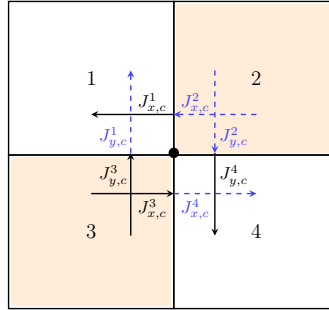


Fig. 5.2. Scheme of the directional net currents in the neighborhood of a nodal corner point. The corner is shared by four nodes of two different types in a checkerboard layout.

that Eq. (5.2) is the exact solution of the neutron balance equation in the nodes sharing the corner, an estimate of the net currents at the corner itself is obtained from Eq. (5.7). For instance, the following expression is derived for $J_{x,c}^1$ in node 1 (we use the nodal coordinate system of Fig. 5.1):

$$J_{x,c}^1 = J_{\text{env},G,x}^1 \left(\frac{1}{2}, -\frac{1}{2} \right) = -\frac{D_G^1}{\Delta x} \left(\sum_{i_x=1}^{N_x} \alpha_{G,x,i_x}^1 \frac{dP_{G,i_x}}{du_x}(u_x) \Big|_{u_x=1/2} + \sum_{\substack{c_x=1 \\ c_x+c_y \leq N_c}}^{N_x} \sum_{\substack{c_y=1 \\ c_x+c_y \leq N_c}}^{N_y} \alpha_{G,xy,c_x,c_y}^1 \frac{dP_{G,c_x}}{du_x}(u_x) \Big|_{u_x=1/2} P_{G,c_y} \left(-\frac{1}{2} \right) \right). \quad (5.29)$$

Eq. (5.29) ensues from the fact that the infinite-medium net current in a corner point is zero.

With the CPB approach, a new estimate $\Phi_{G,c}^*$ of the heterogeneous corner flux $\Phi_{G,c}^{\text{het}}$ is found at the end of each rehomogenization iteration (namely, after sweeping all the nodes) with the computed flux-variation modal coefficients. This new estimate is to be used as a known term on the right-hand side of Eq. (5.19) in the following rehomogenization update. At the first iteration, in which no estimate of the α coefficients is available, we use Eq. (5.20) or Eq. (5.21).

Compared to Smith's method and the MSS, the CPB approach has a physical foundation. Moreover, it does not involve the corner discontinuity factors, so an environmental correction on these parameters is not necessary. No further approximation is introduced when solving the rehomogenization problem. On the other hand, as it will be shown in Section 5.3, this strategy causes a slower convergence rate of the rehomogenization algorithm due to its non-linearity. This is because the heterogeneous corner fluxes depend on the flux-variation modal coefficients, which are the unknowns of the rehomogenization linear system.

5.2.4 Weighted-residual balance equations

The 2-D multigroup neutron balance equation in the real environment is

$$\frac{1}{\Delta x} \frac{\partial J_{\text{env},G,x}(u_x, u_y)}{\partial u_x} + \frac{1}{\Delta y} \frac{\partial J_{\text{env},G,y}(u_x, u_y)}{\partial u_y} + \Sigma_{t,G}(u_x, u_y) \Phi_{\text{env},G}(u_x, u_y) = \sum_{G'=1}^{N_G} \left(\frac{\chi_{G'}(u_x, u_y)}{k_{\text{eff}}} \nu \Sigma_{f,G'}(u_x, u_y) + \Sigma_{s,G' \rightarrow G}(u_x, u_y) \right) \Phi_{\text{env},G'}(u_x, u_y). \quad (5.30)$$

Following the example of spectral rehomogenization (Section 2.2.1), we project Eq. (5.30) over a set of weighting functions $W_{G,j}(u_x, u_y)$ (with $j = 1, \dots, 4$) and integrate it in the two directions. The cross-section projection term for the generic reaction rate r is

$$\int_{-1/2}^{1/2} du_x \int_{-1/2}^{1/2} du_y W_{G,j}(u_x, u_y) \Sigma_{r,G}(u_x, u_y) \Phi_{\text{env},G}(u_x, u_y) = \bar{\Phi}_G h_{R,r,G,j} + \sum_{d=x,y} \sum_{i_d=1}^{N_d} \alpha_{G,d,i_d} h_{V,r,G,d,i_d,j} + \sum_{\substack{c_x=N_x \\ c_x+c_y \leq N_c}} \sum_{\substack{c_y=N_y \\ c_x+c_y \leq N_c}} \alpha_{G,xy,c_x,c_y} h_{V,r,G,xy,c_x,c_y,j}, \quad (5.31)$$

where the rehomogenization coefficients are defined as

$$h_{R,r,G,j} = \int_{-1/2}^{1/2} du_x \int_{-1/2}^{1/2} du_y W_{G,j}(u_x, u_y) \Sigma_{r,G}(u_x, u_y) \varphi_{\infty,G}(u_x, u_y), \quad (5.32a)$$

$$h_{V,r,G,d,i_d,j} = \int_{-1/2}^{1/2} du_d P_{G,i_d}(u_d) \int_{-1/2}^{1/2} du_t W_{G,j}(u_d, u_t) \Sigma_{r,G}(u_d, u_t), \quad (5.32b)$$

$$h_{V,r,G,xy,c_x,c_y,j} = \int_{-1/2}^{1/2} du_x P_{G,c_x}(u_x) \int_{-1/2}^{1/2} du_y P_{G,c_y}(u_y) W_{G,j}(u_x, u_y) \Sigma_{r,G}(u_x, u_y). \quad (5.32c)$$

In Eq. (5.32b), the subscript t refers to the direction transverse to d .

We consider again a spatially constant diffusion coefficient within each node of the computational domain. With this assumption, the projection of the x -directional component of the current-divergence term (i.e., the first term on the left-hand side of Eq. (5.30)) yields

$$\int_{-1/2}^{1/2} du_x \int_{-1/2}^{1/2} du_y W_{G,j}(u_x, u_y) \frac{\partial J_{\text{env},G,x}(u_x, u_y)}{\partial u_x} = \bar{\Phi}_G h_{R,\text{leak},G,x,j}^- - \frac{D_G}{\Delta x} \left[\sum_{i_x=1}^{N_x} \alpha_{G,x,i_x} h_{\text{div},G,x,i_x,j} + \sum_{\substack{c_x=1 \\ c_x+c_y \leq N_c}} \sum_{\substack{c_y=1 \\ c_x+c_y \leq N_c}} \alpha_{G,xy,c_x,c_y} h_{\text{div}_x,G,xy,c_x,c_y,j} \right], \quad (5.33)$$

with the following definitions:

$$h_{R,\text{leak},G,x,j}^\infty = \int_{-1/2}^{1/2} du_x \int_{-1/2}^{1/2} du_y W_{G,j}(u_x, u_y) \frac{\partial J_{\infty,G,x}(u_x, u_y)}{\partial u_x}, \quad (5.34a)$$

$$h_{\text{div},G,x,i_x,j} = \int_{-1/2}^{1/2} du_x \frac{d^2}{du_x^2} P_{G,i_x}(u_x) \int_{-1/2}^{1/2} du_y W_{G,j}(u_x, u_y), \quad (5.34b)$$

$$h_{\text{div}_x,G,xy,c_x,c_y,j} = \int_{-1/2}^{1/2} du_x \frac{d^2}{du_x^2} P_{G,c_x}(u_x) \int_{-1/2}^{1/2} du_y P_{G,c_y}(u_y) W_{G,j}(u_x, u_y). \quad (5.34c)$$

Similar equations can be written for the projection of the y -directional component of the current divergence. The rehomogenization parameter detailed in Eq. (5.34a) is determined for the two directions from the projection of the 2-D balance equation in the infinite medium:

$$\frac{1}{\Delta x} h_{R,\text{leak},G,x,j}^\infty + \frac{1}{\Delta y} h_{R,\text{leak},G,y,j}^\infty = \sum_{G'=1}^{N_G} \frac{\bar{\Phi}_{G'}^\infty}{\bar{\Phi}_G^\infty} \left(\frac{\chi_G}{k_\infty} h_{R,f,G',j} + h_{R,s,G' \rightarrow G,j} \right) - h_{R,t,G,j}, \quad (5.35)$$

where the spectral ratio $\bar{\Phi}_{G'}^\infty/\bar{\Phi}_G^\infty$ is computed solving the single-assembly zero-dimensional (i.e., node-averaged) neutron balance equation. In a two-group framework and with neutron emission from fission only in the fast group ($\chi_1 = 1, \chi_2 = 0$), this reads

$$\frac{\bar{\Phi}_1^\infty}{\bar{\Phi}_2^\infty} = \frac{\Sigma_{a,2}^\infty + \Sigma_{s,2 \rightarrow 1}^\infty + D_2^\infty B^2}{\Sigma_{s,1 \rightarrow 2}^\infty}, \quad (5.36)$$

where $B^2 = B_{\text{crit}}^2$ with the critical-buckling approach or $B^2 = 0$ otherwise.

To summarize, with the above definitions the j -th weighted-residual equation is

$$\begin{aligned} & \bar{\Phi}_G \left(\sum_{d=x,y} \frac{h_{R,\text{leak},G,d,j}^\infty}{\Delta d} + h_{R,t,G,j} \right) + \sum_{d=x,y} \sum_{i_d=1}^{N_d} \alpha_{G,d,i_d} \left(h_{V,t,G,d,i_d,j} - \frac{D_G}{\Delta d^2} h_{\text{div},G,d,i_d,j} \right) \\ & + \sum_{\substack{c_x=1 \\ c_y=1 \\ c_x+c_y \leq N_c}}^{N_x} \sum_{c_y=1}^{N_y} \alpha_{G,xy,c_x,c_y} \left(h_{V,t,G,xy,c_x,c_y,j} - D_G \sum_{d=x,y} \frac{h_{\text{div}_d,G,xy,c_x,c_y,j}}{\Delta d^2} \right) = \\ & \sum_{G'=1}^{N_G} \left[\bar{\Phi}_{G'} \left(\frac{\chi_G}{k_{\text{eff}}} h_{R,f,G',j} + h_{R,s,G' \rightarrow G,j} \right) + \sum_{d=x,y} \sum_{i_d=1}^{N_d} \alpha_{G',d,i_d} \left(\frac{\chi_G}{k_{\text{eff}}} h_{V,f,G',d,i_d,j} + \right. \right. \\ & \left. \left. h_{V,s,G' \rightarrow G,d,i_d,j} \right) + \sum_{\substack{c_x=1 \\ c_y=1 \\ c_x+c_y \leq N_c}}^{N_x} \sum_{c_y=1}^{N_y} \alpha_{G',xy,c_x,c_y} \left(\frac{\chi_G}{k_{\text{eff}}} h_{V,f,G',xy,c_x,c_y,j} + h_{V,s,G' \rightarrow G,xy,c_x,c_y,j} \right) \right]. \end{aligned} \quad (5.37)$$

Using Eq. (5.37), we make the assumption that the nodal estimates $\bar{\Phi}_G$ and k_{eff} satisfy the neutron balance in space [Eq. (5.30)] in a weighted-integral sense.

The choice of the weighting functions $W_{G,j}(u_x, u_y)$ is, in principle, arbitrary. However, these modes must be selected carefully to avoid ill-conditioning of the rehomogenization linear system that ensues from the set of equations defined above [Eqs. (5.13), (5.17), (5.19), and (5.37)]. Using Galerkin projection, the lowest condition number of the solving matrix has been achieved with the following set of test functions in one variable:

$$W_1(u_x) = P_1(u_x), \quad W_2(u_y) = P_1(u_y), \quad W_3(u_x) = P_2(u_x), \quad W_4(u_y) = P_2(u_y). \quad (5.38)$$

With this choice, the weighting operators do not depend on the energy group.

5.2.5 Summary of the procedure

At the end of a non-linear flux iteration, the nodes are swept to solve the spatial rehomogenization problem. The rehomogenization linear system is set up independently for each node with Eqs. (5.13), (5.17), (5.19), and (5.37). In Eq. (5.19), the corner flux is determined using (i) Eqs. (5.20) to (5.24), or (ii) Eqs. (5.28) and (5.29) with the flux-variation modal coefficients from the previous rehomogenization update. After solving the system, the new estimates of the environmental discontinuity factors at the node surfaces are determined with Eq. (5.9). The spatial cross-section correction for reaction r is computed as

$$\delta\Sigma_{r,G} = \frac{1}{\bar{\Phi}_G} \int_{-1/2}^{1/2} du_x \int_{-1/2}^{1/2} du_y \Sigma_{r,G}(u_x, u_y) \delta\Phi_G(u_x, u_y) = \sum_{d=x,y} \sum_{i_d=1}^{N_d} \alpha_{G,d,i_d} h_{V,r,G,d,i_d,0} + \sum_{\substack{c_x=1 \\ c_x+c_y \leq N_c}}^{N_x} \sum_{c_y=1}^{N_y} \alpha_{G,xy,c_x,c_y} h_{V,r,G,xy,c_x,c_y,0}, \quad (5.39)$$

where the index $j = 0$ refers to the unitary weighting function [$W_{G,0}(u_d) = 1$]. When the CPB condition is applied, as the corner fluxes converge, the corrections $\delta f_{G,d\pm}$ and $\delta\Sigma_{r,G}$ also converge, and so do the multiplication factor and the nodal variables $\bar{\Phi}_G$, $\Phi_{G,d\pm}^{\text{hom}}$, and $J_{G,d\pm}$ (which are the input quantities of the rehomogenization algorithm). We exploit the information on the 2-D directional net current distributions [Eq. (5.7)] to compute the few-group transverse-leakage shape for the NEM (or ANM) equations. This approach replaces the approximation commonly adopted in industrial nodal codes, which is based on a three-node quadratic fit along the direction of interest (Lawrence, 1986). This approximation lacks a theoretical justification and introduces an inconsistency in the solution of the nodal equations, because it uses information from the adjacent nodes in the direction under consideration to determine the internodal leakage in the transverse direction. For the 1-D transverse-integrated problem along

the x direction, the transverse leakage is formulated as

$$L_{\text{env},G,y}(u_x) = \frac{1}{\Delta y} \left[J_{\text{env},G,y}(u_x, u_y) \Big|_{u_y=\frac{1}{2}} - J_{\text{env},G,y}(u_x, u_y) \Big|_{u_y=-\frac{1}{2}} \right]. \quad (5.40)$$

Introducing Eqs. (5.4), (5.7) and (5.8) into Eq. (5.40), after some algebraic manipulation we obtain

$$L_{\text{env},G,y}(u_x) = \bar{L}_{G,y} - \frac{D_G}{\Delta y^2} \sum_{\substack{c_x=1 \\ c_x+c_y \leq N_c}}^{N_x} \sum_{c_y=1}^{N_y} \alpha_{G,xy,c_x,c_y} b_{G,c_y} P_{G,c_x}(u_x), \quad (5.41)$$

where $\bar{L}_{G,y}$ is the node-averaged leakage in the y direction (i.e., the transverse direction), and b_{G,c_y} is a constant term defined as

$$b_{G,c_y} = \frac{dP_{G,c_y}(u_y)}{du_y} \Big|_{u_y=\frac{1}{2}} - \frac{dP_{G,c_y}(u_y)}{du_y} \Big|_{u_y=-\frac{1}{2}}. \quad (5.42)$$

Setting $N_c = 4$ and using directional polynomial basis functions of order up to 2 in the cross terms, we obtain $b_{G,1} = 0$ and $b_{G,2} = 2$. Eq. (5.41) becomes thus

$$L_{\text{env},G,y}(u_x) = \bar{L}_{G,y} - \frac{2D_G}{\Delta y^2} \sum_{c_x=1}^2 \alpha_{G,xy,c_x,2} P_{c_x}(u_x). \quad (5.43)$$

The transverse leakage detailed in Eq. (5.43) is still a quadratic polynomial. However, its shape retains some information on the 2-D node-to-node leakage distribution (i.e., information from the transverse direction) via the cross coefficients $\alpha_{G,xy,c_x,2}$. In this way, the unphysical feature of the standard approximation discussed above is removed.

5.3 Numerical results

We validate the method on the same test cases considered in Chapter 3 (Section 3.3.1): (i) a UO_2 colorset with Pyrex rods, (ii) a UO_2 colorset with AIC-type control rods, (iii) a UO_2 colorset with gadolinium-bearing fuel pins, and (iv) a UO_2/MOX colorset. Two-group nodal simulations are run with BRISINGR (Appendix A). The infinite-medium homogenization parameters are generated with APOLLO2-A (Martinolli et al., 2010), which is also used for the reference calculations. Since in this chapter we do not apply spectral rehomogenization, the critical-buckling correction (which is a default option in advanced nodal codes) is applied to the nodal cross sections. All the test cases are simulated in critical conditions ($k_{\text{eff}} = 1$), which are determined with a critical-boron-concentration search. Also in this analysis, we use a spatial discretization of one node per assembly quarter. We present the results of the calculations with:

- single-assembly cross sections and discontinuity factors (calc. a);

- 2-D spatial rehomogenization of cross sections and discontinuity factors, using the CPB approach (calc. *b*) and the MSS/Smith's method (calc. *c*) to determine the corner fluxes;
- 1-D spatial rehomogenization of cross sections and discontinuity factors (calc. *d*).

For the sake of convenience, from now on we will refer to the MSS/Smith's method simply as MSS. The spatial rehomogenization coefficients [Eqs. (5.32) and (5.34) for calculations *b* and *c*] are computed with the infinite-medium cell-homogenized cross sections and flux distribution. We test the accuracy of spatial rehomogenization on the main nodal parameters and on the pin-by-pin flux and fission-power distributions. In all the calculations, the 2-D heterogeneous intranodal flux is reconstructed with the dehomogenization method described in Joo et al. (2009). This approach is based on a 2-D, fourth-order Legendre-polynomial expansion of the neutron source distribution, which results in a semi-analytic solution of the 2-D, group-decoupled neutron diffusion equation. In calculations *b* and *c*, the corner fluxes computed with the 2-D rehomogenization are used as boundary conditions for the pin-flux reconstruction. The pin-power Root-Mean-Square (RMS) deviations are expressed in terms of the relative error ($RMS_{P,r}$) and of the power-weighted absolute error ($RMS_{P,wa}$), namely

$$RMS_{P,r} = \sqrt{\frac{1}{N_{fc}} \sum_{i=1}^{N_{fc}} \left(\frac{P_i^{\text{calc}} - P_i^{\text{ref}}}{P_i^{\text{ref}}} \right)^2} \cdot 100\%, \quad (5.44a)$$

$$RMS_{P,wa} = \sqrt{\frac{\frac{1}{N_{fc}} \sum_{i=1}^{N_{fc}} (P_i^{\text{calc}} - P_i^{\text{ref}})^2 \frac{P_i^{\text{ref}}}{\bar{P}_{CS}^{\text{ref}}}}{\bar{P}_{CS}^{\text{ref}}}} \cdot 100\%, \quad (5.44b)$$

where N_{fc} is the number of fuel cells, P_i^{calc} and P_i^{ref} are the computed and reference (i.e., from APOLLO2-A) values of the fission power in the i -th cell, and $\bar{P}_{CS}^{\text{ref}}$ is the reference average power in the colorset. With Eq. (5.44b), the errors in the hot spots (i.e., the fuel cells having the highest thermal load) have more weight in the accuracy assessment. We also use Eq. (5.44a) to compute the RMS deviation in the two-group flux distribution ($RMS_{\Phi_{G,r}}$).

5.3.1 Example 1: UO₂ colorset with Pyrex rods

The colorset layout can be found in Fig. 2.5 (Section 2.3.2.1). For the sake of completeness, we report here the reference absorption and production cross sections (condensed and homogenized in the colorset environment) computed with APOLLO2-A: $\Sigma_{a,1} = 0.00873 \text{ cm}^{-1}$, $\Sigma_{a,2} = 0.0686 \text{ cm}^{-1}$, $\nu\Sigma_{f,1} = 0.00483 \text{ cm}^{-1}$, and $\nu\Sigma_{f,2} = 0.0811 \text{ cm}^{-1}$ in the 1.8%-enriched assembly; $\Sigma_{a,1} = 0.0101 \text{ cm}^{-1}$, $\Sigma_{a,2} = 0.104 \text{ cm}^{-1}$, $\nu\Sigma_{f,1} = 0.00657 \text{ cm}^{-1}$, and $\nu\Sigma_{f,2} = 0.131 \text{ cm}^{-1}$ in the 3.1%-enriched assembly

with poison. The reference values of the normalized fission power are 0.92 in the 1.8%-enriched assembly and 1.08 in the assembly with Pyrex.

Fig. 5.3 depicts the reference variation in the 2-D flux distribution between the real environment and the infinite lattice in the two fuel assemblies. The percent values are computed with respect to the node-averaged flux. The coordinates $[0,0]$ (in cm) represent the assembly center, whereas the abscissas and ordinates 10.1 cm and -10.1 cm denote the center of the assembly outer pin rows.

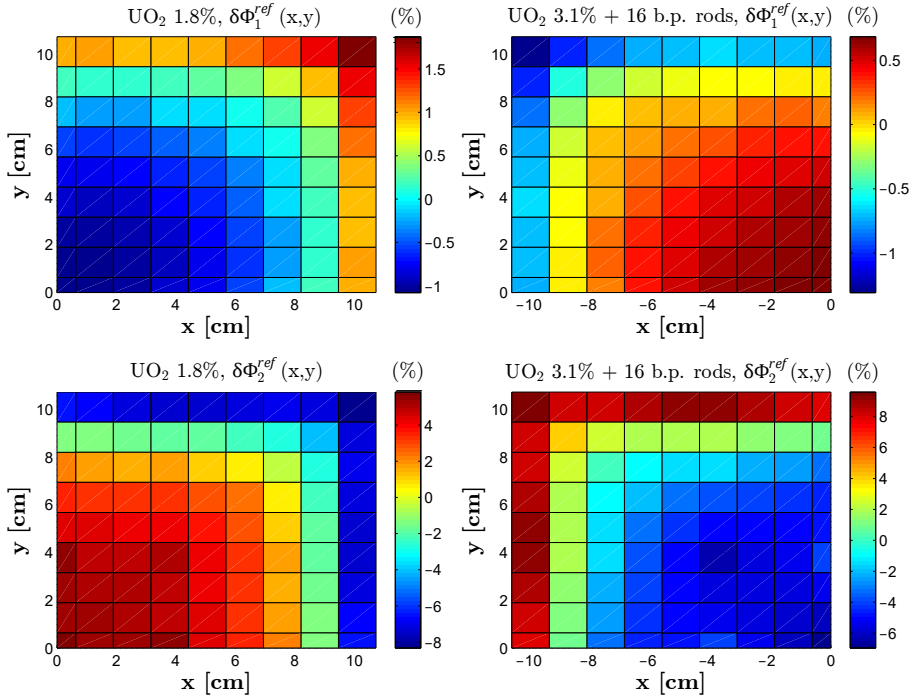


Fig. 5.3. Example 1: reference variation (in percentage) in the 2-D pin-by-pin flux between the environmental and infinite-lattice conditions in the neighboring quarters of the two dissimilar assemblies. The top and bottom plots depict the variations in the fast and thermal groups, respectively. The plots on the left side refer to the 1.8%-enriched assembly quarter, whereas those on the right side refer to the 3.1%-enriched assembly quarter. The coordinates $[0,0]$ (in cm) correspond to the assembly centers. The abscissas 10.1 cm in the 1.8%-enriched assembly and -10.1 cm in the assembly with Pyrex rods denote the centers of the outer cell rows (the water gap is not shown).

Fig. 5.4 shows the flux variation computed with the 2-D spatial rehomogenization, combined with the CPB approach for the corner-point fluxes. The result of the MSS approach is not presented because the differences are small. Rehomogenization captures the overall flux variation reasonably well. The main differences between

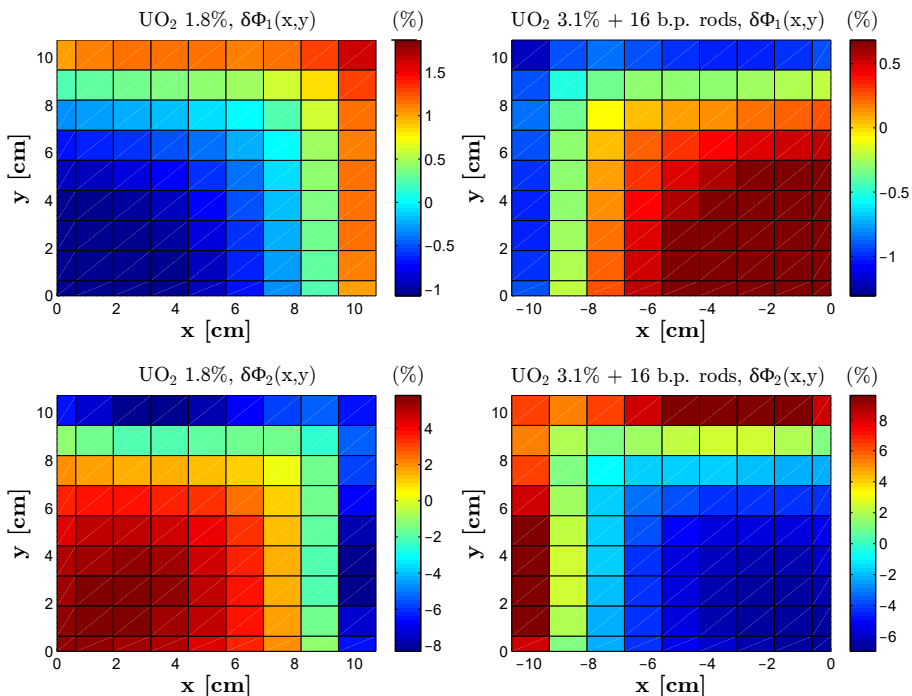


Fig. 5.4. Example 1: variation (in percentage) in the 2-D flux distribution in the neighboring quarters of the two assemblies, as computed with the CPB-based 2-D rehomogenization. The results are plotted with the same scale as in Fig. 5.3 to ease the comparison between the reference and computed variations.

the reference and computed distributions are observed in the outer pin rows of both assemblies. In the 1.8%-enriched bundle, the magnitude of the thermal flux change is overestimated at the assembly edges and underestimated in the external-corner fuel cell. The opposite is found in the assembly with Pyrex rods. Fig. 5.5 shows the variation in the transverse-integrated flux $\Phi_{G,x}(x)$ computed with the 1-D rehomogenization. For the sake of comparison, we also plot the 1-D curves obtained by transverse integration of the 2-D distributions of Fig. 5.4. The deviations between the 1-D and 2-D approaches are not significant. They are more evident in the fast group, especially in the assembly with Pyrex.

Table 5.1 reports the number of non-linear flux iterations (N_{iter}) and the errors in the integral parameters and main nodal cross sections (the errors in the discontinuity factors will be addressed in Section 5.4.2). Compared to the calculation with infinite-medium cross sections and discontinuity factors, both the 2-D and 1-D models give a significantly more accurate prediction of the multiplication factor and fission power. Much of this improvement comes from the correction of the thermal absorption cross

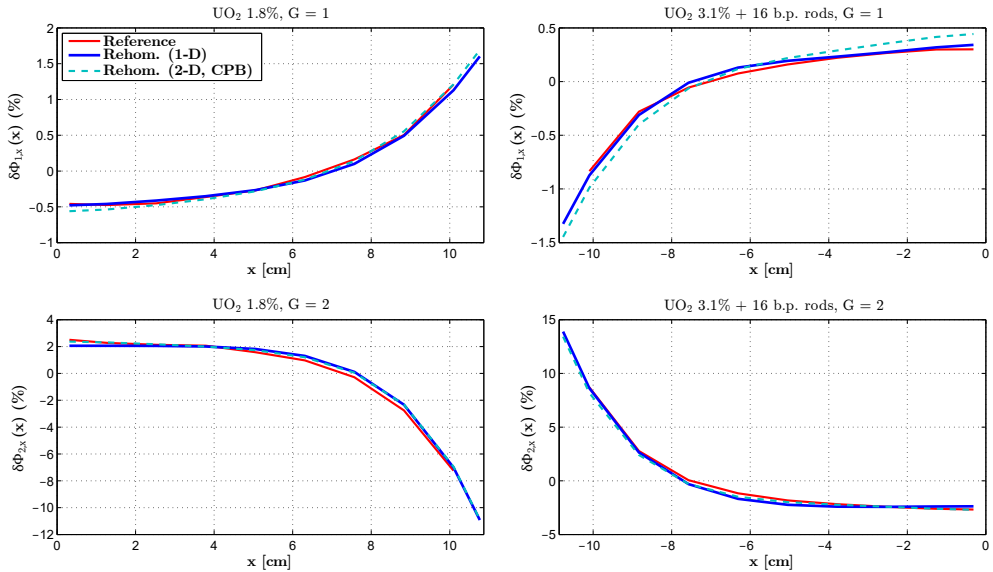


Fig. 5.5. Example 1: variation (in percentage) in the transverse-integrated flux distribution in the neighboring quarters of the two dissimilar assemblies. The computed variation in the water gap is also depicted.

section in the assembly with burnable poison, even if the corresponding error becomes higher than that of the single-assembly estimate. The increase in the error in this cross section is because of the exclusion of spectral effects, which go in the opposite direction to spatial ones (see Table 3.13 and Section 5.4.4). The improvement in the power is more apparent with the 2-D rehomogenization. The differences between the CPB and MSS strategies are negligible.

Table 5.2 compares the errors in the cross sections rehomogenized with (i) the reference 2-D flux change (Fig. 5.3) and (ii) a least-squares best fit of it. The best fit has been computed with the basis functions defined in Eq. (5.5), using the same number of directional and cross terms as in the modal reconstruction [Eq. (5.4)]. Since these two sets of cross sections do not account for the spectral effects of the environment, they can be considered as a reference to assess the accuracy of spatial rehomogenization. Comparing Tables 5.1 and 5.2, it turns out that the cross-section corrections computed with the 2-D rehomogenization go in the right direction and are very close to those obtained with a best fit of the 2-D reference. The inaccuracy in the flux-change reconstruction observed in Fig. 5.4 is therefore ascribable to the limited fitting capability of the 1-D basis functions [Eq. (5.5)] rather than to a deficiency of the method. We have verified that increasing the number of cross terms in the best fit from four to six or eight improves the computed corrections only slightly. Rehomogenization underestimates the corrections on $\Sigma_{a,2}$ and $\nu\Sigma_{f,2}$ in the 1.8%-enriched assembly and

5. A two-dimensional model for spatial rehomogenization

Table 5.1. Example 1: (a) number of non-linear flux iterations and errors in the integral parameters, and (b) errors in the absorption and production nodal cross sections.

Simulation	N_{iter}	Δk_{eff} [pcm]	UO ₂ 1.8%	UO ₂ 3.1% + 16 b.p. rods
			$\Delta \bar{P}_{\text{fiss}}$ (%)	$\Delta \bar{P}_{\text{fiss}}$ (%)
No rehom. (a)	9	-189	0.85 (0.86, 0.85)	-0.72 (-0.60, -0.76)
2-D rehom. - CPB (b)	15	26	0.19 (0.74, 0.06)	-0.16 (-0.52, -0.05)
2-D rehom. - MSS (c)	12	30	0.22 (0.78, 0.08)	-0.18 (-0.55, -0.07)
1-D rehom. (d)	13	-18	0.39 (0.87, 0.28)	-0.33 (-0.61, -0.25)

(a)

Simulation	UO ₂ 1.8%				UO ₂ 3.1% + 16 b.p. rods			
	Errors (%)							
	$\Delta \Sigma_{a,1}$	$\Delta \Sigma_{a,2}$	$\Delta \nu \Sigma_{f,1}$	$\Delta \nu \Sigma_{f,2}$	$\Delta \Sigma_{a,1}$	$\Delta \Sigma_{a,2}$	$\Delta \nu \Sigma_{f,1}$	$\Delta \nu \Sigma_{f,2}$
No rehom. (a)	-0.04	0.69	0.51	0.81	0.10	-0.50	-0.33	-1.03
2-D rehom. - CPB (b)	-0.02	0.64	0.53	0.71	0.11	-0.92	-0.34	-0.90
2-D rehom. - MSS (c)	-0.02	0.64	0.53	0.71	0.11	-0.93	-0.34	-0.90
1-D rehom. (d)	-0.03	0.64	0.53	0.70	0.11	-0.85	-0.34	-0.93

(b)

Table 5.2. Example 1: errors in the absorption and production cross sections rehomogenized with the reference 2-D flux variation and with a least-squares best fit of it.

Flux variation (2-D)	UO ₂ 1.8%				UO ₂ 3.1% + 16 b.p. rods			
	Errors (%)							
	$\Delta \Sigma_{a,1}$	$\Delta \Sigma_{a,2}$	$\Delta \nu \Sigma_{f,1}$	$\Delta \nu \Sigma_{f,2}$	$\Delta \Sigma_{a,1}$	$\Delta \Sigma_{a,2}$	$\Delta \nu \Sigma_{f,1}$	$\Delta \nu \Sigma_{f,2}$
Reference	-0.01	0.53	0.55	0.50	0.09	-0.68	-0.35	-0.71
Best fit	-0.02	0.62	0.53	0.67	0.11	-0.84	-0.34	-0.86

on $\nu \Sigma_{f,2}$ in the assembly with Pyrex (see Tables 5.1b and 5.2). It overcorrects $\Sigma_{a,2}$ in the latter. This overcorrection is due to an overly negative estimate of the flux variation in the center of the assembly, where the Pyrex rods are located and thermal absorption is higher. This mismatch is smaller with the 1-D model. The flux spatial variation has no effect on the fast-group cross sections. The same has been observed in fast-to-thermal scattering and in the diffusion coefficients of both energy groups, which are not reported in the previous tables. For these quantities, both reference and computed corrections are negligible.

Fig. 5.6 compares the relative errors in the thermal-flux pin-by-pin distribution of the 1.8%-enriched assembly, as computed with calculations *a* and *b*. A general improvement

is observed, especially in the fuel cells surrounding the assembly external vertex. The reference pin-by-pin fission power and the errors in the computed power distributions are in Figs. 5.7 and 5.8, respectively. Table 5.3 shows the RMS errors in the two-group flux and total power. The reduction in the RMS deviations is apparent in the poison-free bundle, whereas it is less evident in the assembly with Pyrex. The error in the fuel cell with the highest power (i.e., the external-corner cell in the assembly with Pyrex) increases from -0.64% to -1.71% when the 2-D rehomogenization is applied (Fig. 5.8).

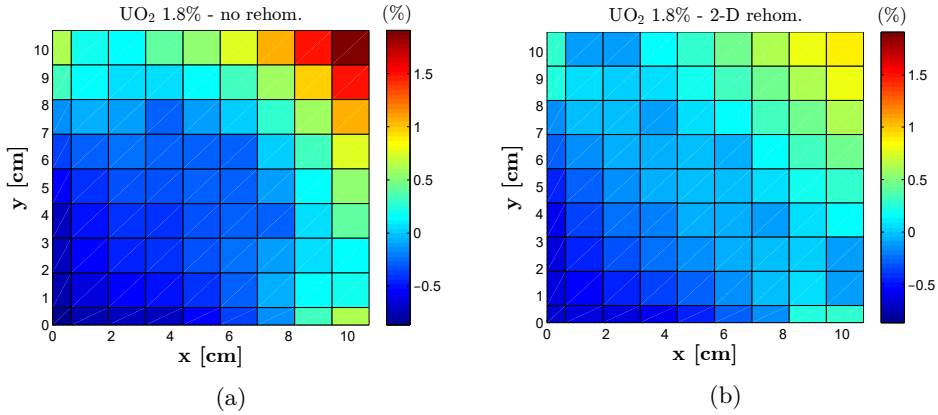


Fig. 5.6. Example 1: relative error (in percentage) in the pin-by-pin thermal flux in the 1.8%-enriched assembly quarter. The plots refer to the calculations (a) without rehomogenization and (b) with the CPB-based 2-D rehomogenization.

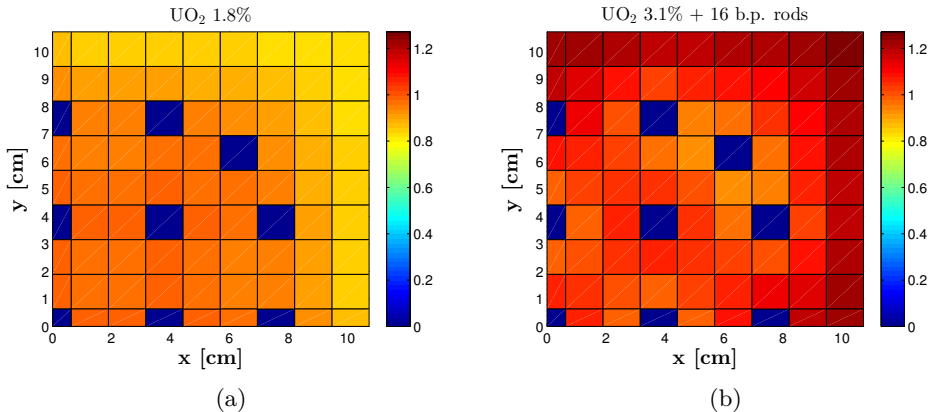


Fig. 5.7. Example 1: reference pin power (normalized to the colorset-averaged value) in (a) the 1.8%-enriched assembly and (b) the 3.1%-enriched assembly with Pyrex rods.

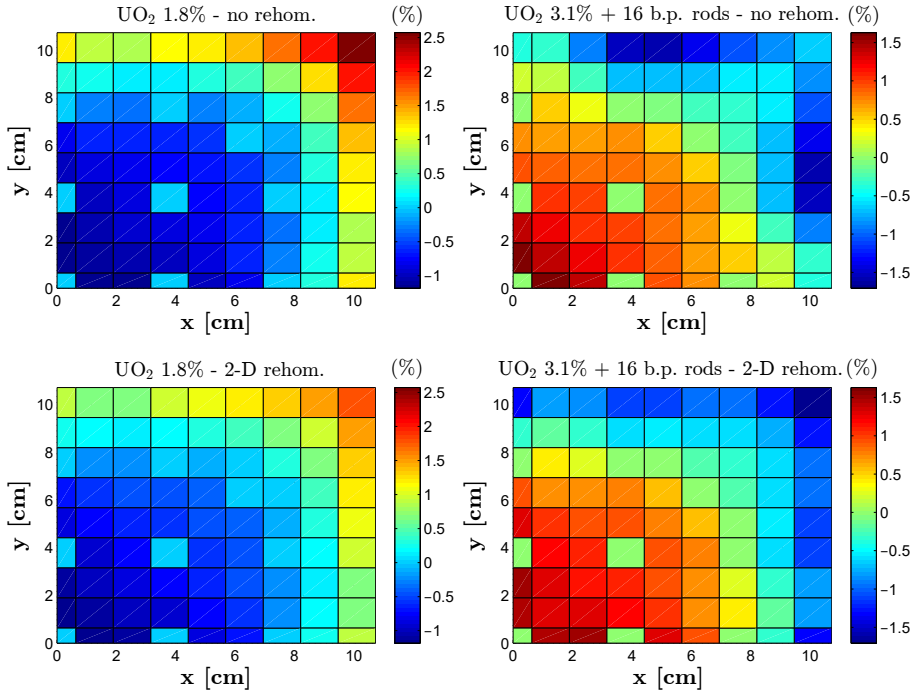


Fig. 5.8. Example 1: relative error (in percentage) in the pin-power distribution computed with calculations *a* and *b*.

Table 5.3. Example 1: RMS deviations (in percentage) in the pin-by-pin two-group flux and total fission power.

Simulation	UO ₂ 1.8%				UO ₂ 3.1% + 16 b.p. rods			
	RMS _{Φ_{1,r}}	RMS _{Φ_{2,r}}	RMS _{P_r}	RMS _{P_{,wa}}	RMS _{Φ_{1,r}}	RMS _{Φ_{2,r}}	RMS _{P_r}	RMS _{P_{,wa}}
No rehom. (<i>a</i>)	0.11	0.58	0.94	0.94	0.20	0.45	0.77	1.25
2-D rehom. - CPB (<i>b</i>)	0.14	0.36	0.77	0.66	0.27	0.43	0.91	1.06
1-D rehom. (<i>d</i>)	0.08	0.51	0.85	0.73	0.22	0.34	0.81	0.98

5.3.2 Example 2: UO₂ colorset with AIC-type control rods

The colorset layout is the same as in Fig. 2.9 (Section 2.3.2.2). In this test case, the ²³⁵U enrichment in the rodded assembly is 2.4% (instead of 1.8%). The critical configuration is achieved with a boron concentration of 222 ppm. The reference values of the normalized fission power are 1.12 in the unrodded assembly and 0.88 in the rodded one. The reference cross sections are: $\Sigma_{a,1} = 0.00833 \text{ cm}^{-1}$, $\Sigma_{a,2} = 0.0573 \text{ cm}^{-1}$, $\nu\Sigma_{f,1} = 0.00483 \text{ cm}^{-1}$, and $\nu\Sigma_{f,2} = 0.0828 \text{ cm}^{-1}$ in the unrodded assembly; $\Sigma_{a,1} = 0.0119 \text{ cm}^{-1}$, $\Sigma_{a,2} = 0.0942 \text{ cm}^{-1}$, $\nu\Sigma_{f,1} = 0.00554 \text{ cm}^{-1}$, and $\nu\Sigma_{f,2} = 0.109$

cm^{-1} in the rodded assembly.

The reference and computed 2-D flux variations are in Figs. 5.9 and 5.10. The prediction is quite accurate in the unrodded assembly. In the rodded bundle, the magnitude of the flux change is underestimated around the external corner, where it is positive, and overestimated in the control-rod cells closer to the assembly center (i.e., at the coordinates $[-3.79,0]$, $[-3.79,3.79]$ and $[0,3.79]$ cm), where it is negative. The decrease in thermal absorption in the environment is therefore overestimated (see Tables 5.4 and 5.5).

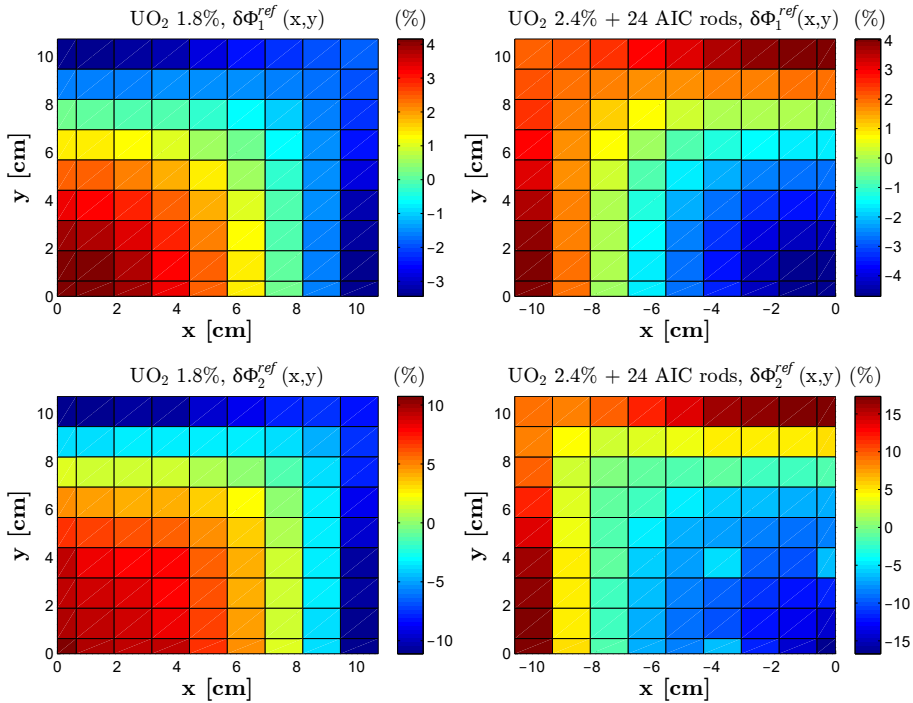


Fig. 5.9. Example 2: reference variation (in percentage) in the 2-D flux distribution.

The variation in the transverse-integrated flux is shown in Fig. 5.11. In the thermal group of the rodded assembly, the 1-D curve from the 2-D model approximates the reference better in the neighborhood of the coordinate -3.79 cm, which spans three rodded cells along the y direction (see Figs. 2.9c and 5.9). However, it provides a less accurate estimate at the periphery.

Tables 5.4 and 5.5 report the errors in the nodal quantities. Also in this case, an improvement in k_{eff} and in the fission power is observed, particularly with the 1-D rehomogenization. Calculations *b*, *c* and *d* mainly differ in the prediction of the correction $\delta\Sigma_{a,2}$ in the rodded assembly, which is overestimated to a different extent in the three cases (see Tables 5.4b and 5.5). As in the example with Pyrex rods,

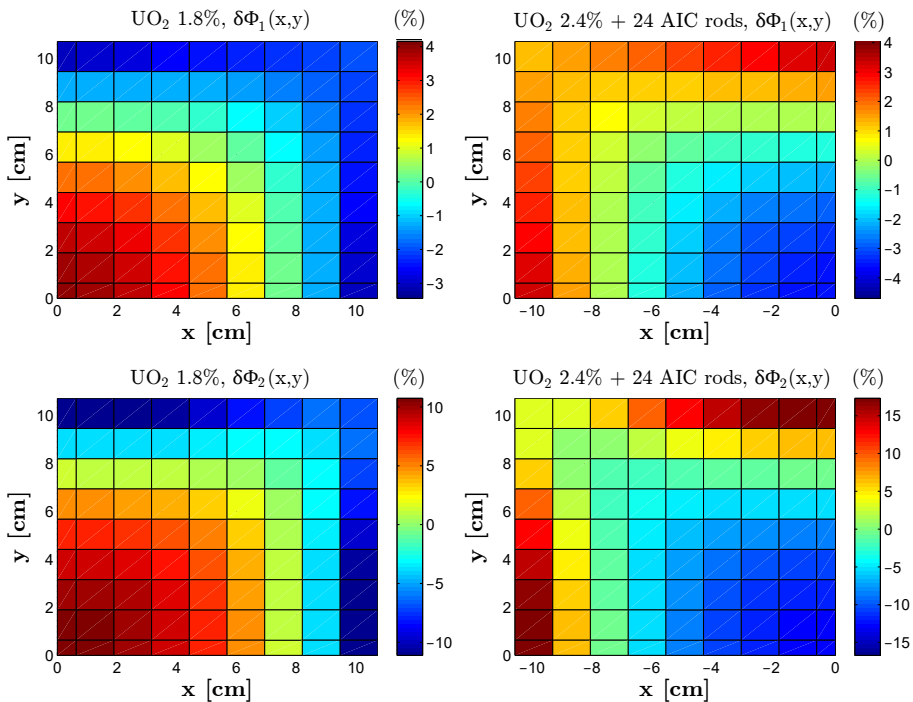


Fig. 5.10. Example 2: variation (in percentage) in the 2-D flux distribution, as computed with the CPB-based 2-D rehomogenization.

the 2-D model reproduces faithfully the corrections computed with a best fit of the reference flux change. Therefore, the overestimation of $\delta\Sigma_{a,2}$ is mostly because the basis functions cannot reconstruct the dip in $\delta\Phi_2(x,y)$ in the inner rodded cells. The relative errors in the pin-by-pin thermal flux in the unrodded assembly and in the power distribution are depicted in Figs. 5.12 and 5.14. The reference fission power is in Fig. 5.13. Table 5.6 summarizes the RMS deviations. With the 2-D model, a general improvement is only found in the unrodded bundle, even though not in the cells with higher power. Since in this assembly the 2-D rehomogenization provides a better intranodal flux distribution than calculation *a* (see Fig. 5.12), the observed increase in $\text{RMS}_{P,wa}$ is probably due in part to the inaccuracy in the infinite-medium pin-by-pin fission cross sections. With the 1-D approach, the improvement is negligible in both assemblies. The highest power (126% of the colorset-averaged value) is found in the external-corner cell of the rodded assembly and in the two cells adjacent to the empty instrumentation tube at the center of the unrodded bundle (i.e., at $[0,0]$ cm). With the 2-D rehomogenization, the power error decreases (in absolute value) from 3.38% to -1.0% in the former and increases (in absolute value) from -0.70% to -0.76% in the latter.

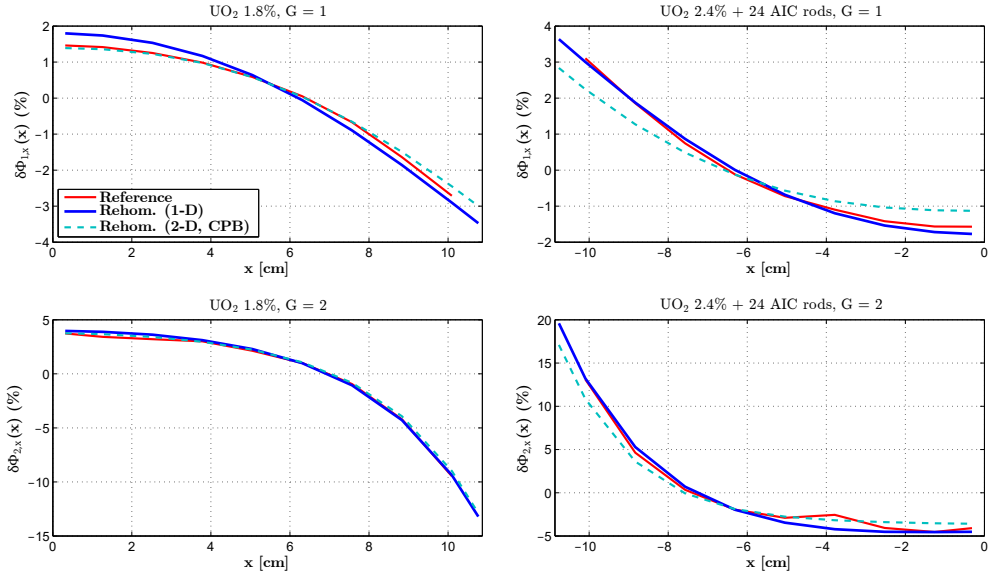


Fig. 5.11. Example 2: variation in the transverse-integrated flux distribution.

Table 5.4. Example 2: (a) number of non-linear flux iterations and errors in the integral parameters, and (b) errors in the absorption and production nodal cross sections.

Simulation	N_{iter}	Δk_{eff} [pcm]	UO ₂ 1.8%	UO ₂ 2.4% + 24 AIC rods
			$\Delta \bar{P}_{\text{fiss}}$ (%)	$\Delta \bar{P}_{\text{fiss}}$ (%)
No rehom. (a)	10	-608	1.41 (0.69, 1.57)	-1.79 (-0.66, -2.15)
2-D rehom. - CPB (b)	18	-18	-0.72 (-0.41, -0.78)	0.92 (0.40, 1.07)
2-D rehom. - MSS (c)	16	-21	-0.96 (-0.64, -1.02)	1.23 (0.61, 1.40)
1-D rehom. (d)	16	-72	0.10 (0.21, 0.08)	-0.12 (-0.20, -0.11)

(a)

Simulation	UO ₂ 1.8%				UO ₂ 2.4% + 24 AIC rods			
	Errors (%)							
	$\Delta \Sigma_{a,1}$	$\Delta \Sigma_{a,2}$	$\Delta \nu \Sigma_{f,1}$	$\Delta \nu \Sigma_{f,2}$	$\Delta \Sigma_{a,1}$	$\Delta \Sigma_{a,2}$	$\Delta \nu \Sigma_{f,1}$	$\Delta \nu \Sigma_{f,2}$
No rehom. (a)	-0.72	0.66	0.11	0.72	1.31	0.63	0.10	-1.21
2-D rehom. - CPB (b)	-0.75	0.54	0.06	0.58	1.09	-1.42	0.16	-0.98
2-D rehom. - MSS (c)	-0.75	0.55	0.07	0.59	1.08	-1.51	0.16	-0.98
1-D rehom. (d)	-0.75	0.53	0.06	0.56	1.02	-1.02	0.18	-1.08

(b)

5. A two-dimensional model for spatial rehomogenization

Table 5.5. Example 2: errors in the absorption and production cross sections rehomogenized with the reference 2-D flux variation and with a least-squares best fit of it.

	UO ₂ 1.8%				UO ₂ 2.4% + 24 AIC rods			
	Errors (%)							
Flux variation (2-D)	$\Delta\Sigma_{a,1}$	$\Delta\Sigma_{a,2}$	$\Delta\nu\Sigma_{f,1}$	$\Delta\nu\Sigma_{f,2}$	$\Delta\Sigma_{a,1}$	$\Delta\Sigma_{a,2}$	$\Delta\nu\Sigma_{f,1}$	$\Delta\nu\Sigma_{f,2}$
Reference	-0.80	0.35	0.01	0.33	1.08	-0.62	0.23	-0.81
Best fit	-0.76	0.51	0.06	0.53	1.04	-1.45	0.19	-0.91

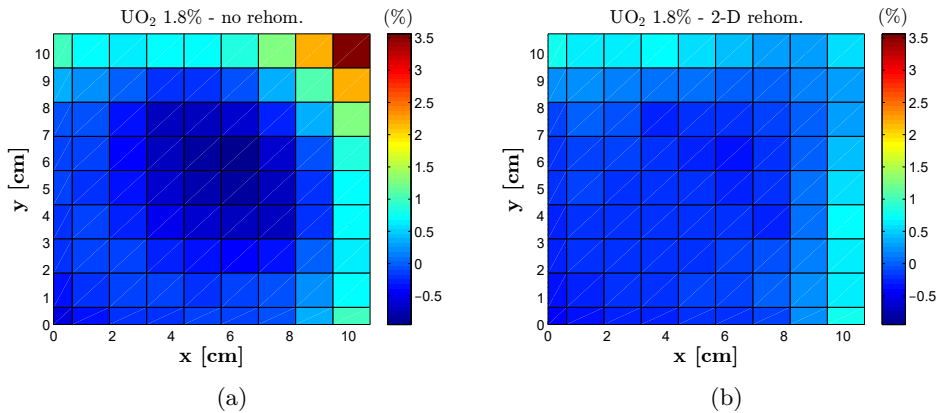


Fig. 5.12. Example 2: relative error (in percentage) in the pin-by-pin thermal flux in the unrodded-assembly quarter. The plots refer to the calculations (a) without rehomogenization and (b) with the CPB-based 2-D rehomogenization.

Table 5.6. Example 2: RMS deviations (in percentage) in the pin-by-pin two-group flux and total fission power.

	UO ₂ 1.8%				UO ₂ 2.4% + 24 AIC rods			
Simulation	RMS $\Phi_{1,r}$	RMS $\Phi_{2,r}$	RMS P_{r}	RMS P_{wa}	RMS $\Phi_{1,r}$	RMS $\Phi_{2,r}$	RMS P_{r}	RMS P_{wa}
No rehom. (a)	0.20	0.78	0.96	1.28	0.43	1.31	1.25	1.50
2-D rehom. - CPB (b)	0.18	0.33	0.68	1.81	0.54	1.45	1.60	1.75
1-D rehom. (d)	0.14	0.72	0.90	1.23	0.34	1.30	1.35	1.37

5.3.3 Example 3: UO₂ colorset with gadolinium-bearing fuel rods

This colorset has been described in Section 3.3.1.4 (Fig. 3.11). The reference normalized fission power and cross sections in APOLLO2-A are: $\bar{P}_{\text{fiss}} = 0.81$, $\Sigma_{a,1} = 0.00889 \text{ cm}^{-1}$, $\Sigma_{a,2} = 0.0723 \text{ cm}^{-1}$, $\nu\Sigma_{f,1} = 0.00483 \text{ cm}^{-1}$, and $\nu\Sigma_{f,2} = 0.0803 \text{ cm}^{-1}$ in the 1.8%-enriched assembly; $\bar{P}_{\text{fiss}} = 1.19$, $\Sigma_{a,1} = 0.0103 \text{ cm}^{-1}$, $\Sigma_{a,2} = 0.118 \text{ cm}^{-1}$, $\nu\Sigma_{f,1}$

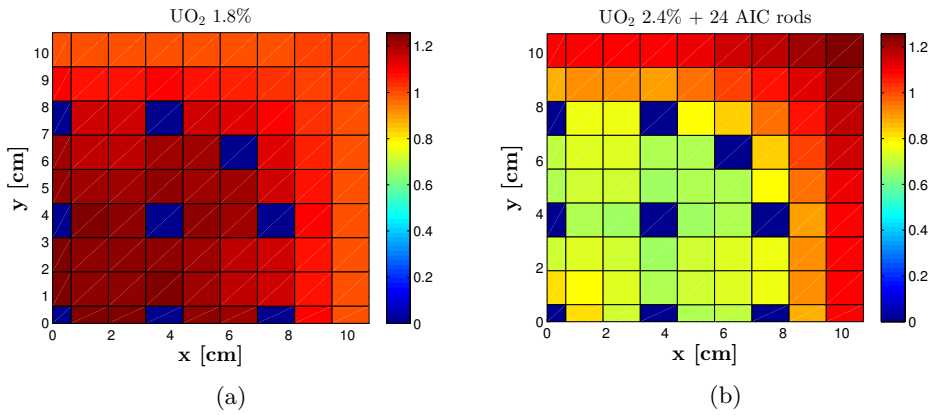


Fig. 5.13. Example 2: reference pin power (normalized to the colorset-averaged value) in the (a) unrodded and (b) rodded assemblies.

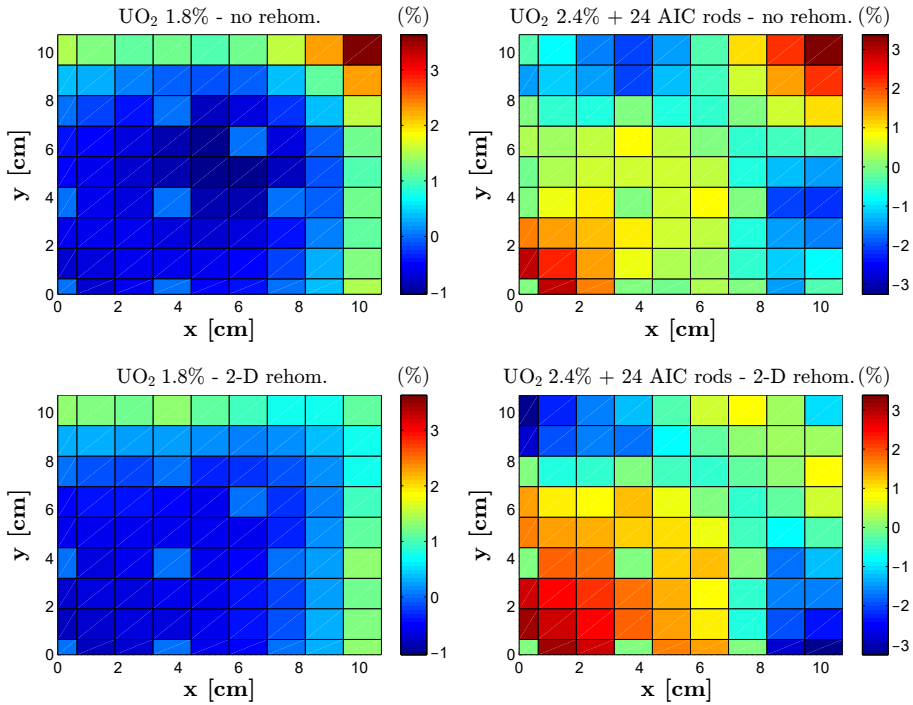


Fig. 5.14. Example 2: relative error (in percentage) in the pin-power distribution computed with calculations *a* and *b*.

5. A two-dimensional model for spatial rehomogenization

$= 0.00738 \text{ cm}^{-1}$, and $\nu\Sigma_{f,2} = 0.151 \text{ cm}^{-1}$ in the assembly with gadolinium-bearing fuel pins.

The reference and computed flux changes are shown in Figs. 5.15 to 5.17. The nodal errors are in Tables 5.7 and 5.8.

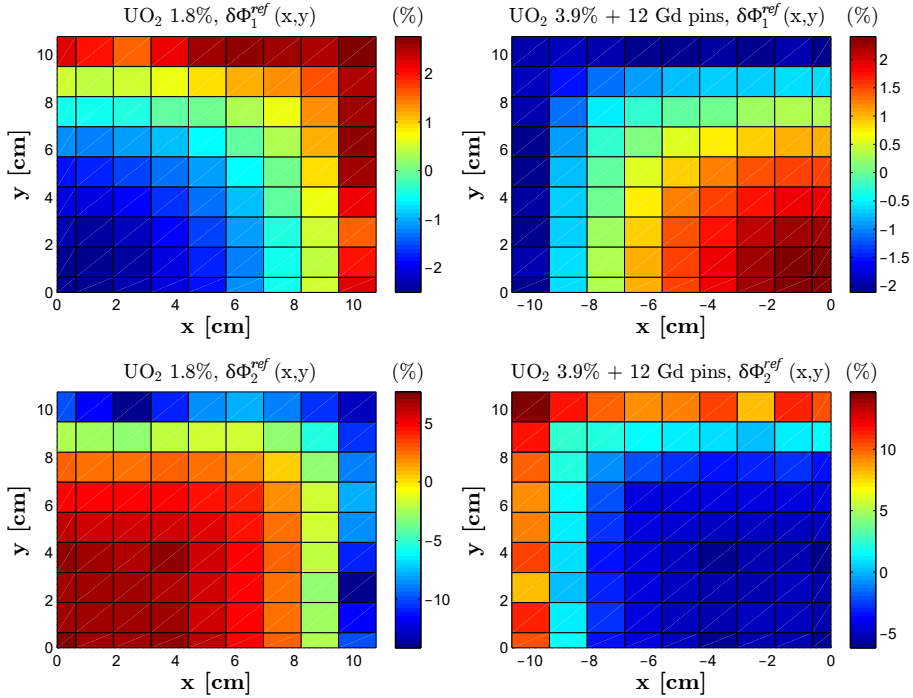


Fig. 5.15. Example 3: reference variation (in percentage) in the 2-D flux distribution.

With the 2-D model, the computed $\delta\Sigma_{a,2}$ in the 3.9%-enriched assembly is higher than the expected value. This is because the thermal-flux variation is overestimated in the gadolinium-bearing fuel pins located in the outer rows (at the coordinates $[-2.53, 10.78]$ and $[-10.78, 2.53]$ cm). In these cells the reference flux change is 8.12%, whereas the computed one is 13.4%. In the same fuel bundle, the correction on $\nu\Sigma_{f,2}$ goes in the wrong direction because of the combined underestimation and overestimation of the magnitude of $\delta\Phi_2(x,y)$ in the neighborhood of the assembly vertex and in the assembly center, respectively. Despite the above mismatches, the 2-D model significantly improves the k_{eff} and nodal-power estimates compared to the calculation without rehomogenization. These parameters improve less with the 1-D model. Figs. 5.18 and 5.19 show the reference pin-by-pin fission power and the errors in the computed power distributions. Table 5.9 lists the RMS deviations. Rehomogenization gives a better prediction in the center of the gadolinium-bearing-assembly quarter (where the power is higher), which causes a reduction in $RMS_{P,wa}$.

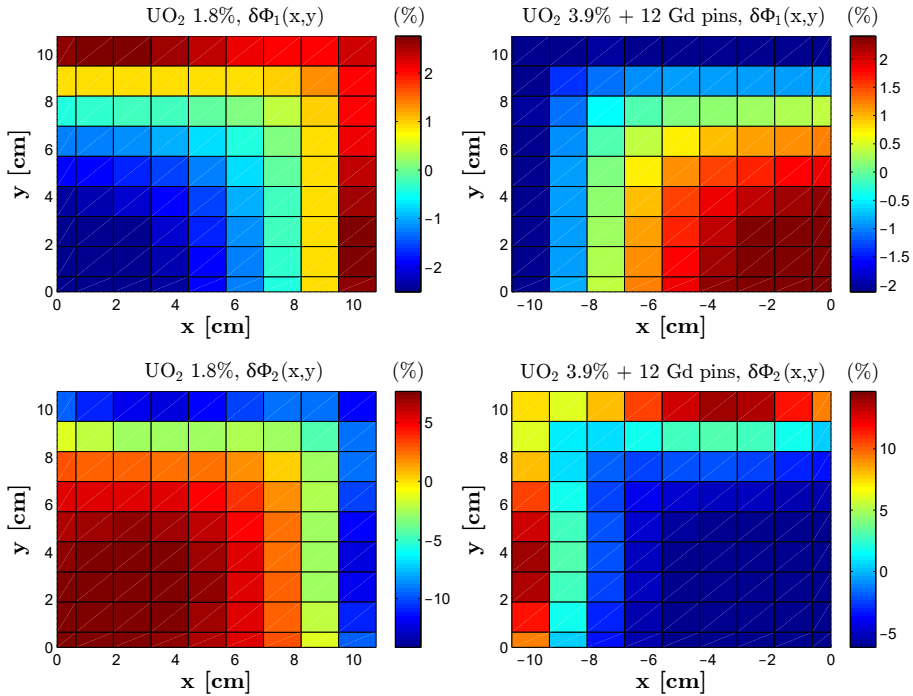


Fig. 5.16. Example 3: variation (in percentage) in the 2-D flux distribution, as computed with the CPB-based 2-D rehomogenization.

5.3.4 Example 4: UO₂/MOX colorset

The colorset and assembly layouts have been shown in Fig. 2.11 (Section 2.3.2.3). The reference normalized fission power and cross sections are: $\bar{P}_{\text{fiss}} = 0.85$, $\Sigma_{a,1} = 0.00924 \text{ cm}^{-1}$, $\Sigma_{a,2} = 0.0887 \text{ cm}^{-1}$, $\nu\Sigma_{f,1} = 0.00543 \text{ cm}^{-1}$, and $\nu\Sigma_{f,2} = 0.0974 \text{ cm}^{-1}$ in the UO₂ assembly; $\bar{P}_{\text{fiss}} = 1.15$, $\Sigma_{a,1} = 0.0143 \text{ cm}^{-1}$, $\Sigma_{a,2} = 0.258 \text{ cm}^{-1}$, $\nu\Sigma_{f,1} = 0.00994 \text{ cm}^{-1}$, and $\nu\Sigma_{f,2} = 0.372 \text{ cm}^{-1}$ in the MOX assembly.

Figs. 5.20 to 5.22 compare the results of rehomogenization with the reference flux spatial deformations. Tables 5.10 and 5.11 show the nodal errors. The 2-D model overestimates the absolute value of the thermal-flux change in the center of the MOX assembly, where it is negative. Here the plutonium content is higher (see Section 2.3.2.3), and so are the thermal-group absorption and production pin-by-pin cross sections. The corrections on the thermal cross sections are thus considerably higher than those computed with the reference flux variation and, in this case, also with a least-squares best fit of it. The error in k_{eff} increases, whereas the errors in the fission power still decrease significantly.

The pin-by-pin errors are shown in Figs. 5.23 to 5.26 and in Table 5.12. In spite

5. A two-dimensional model for spatial rehomogenization

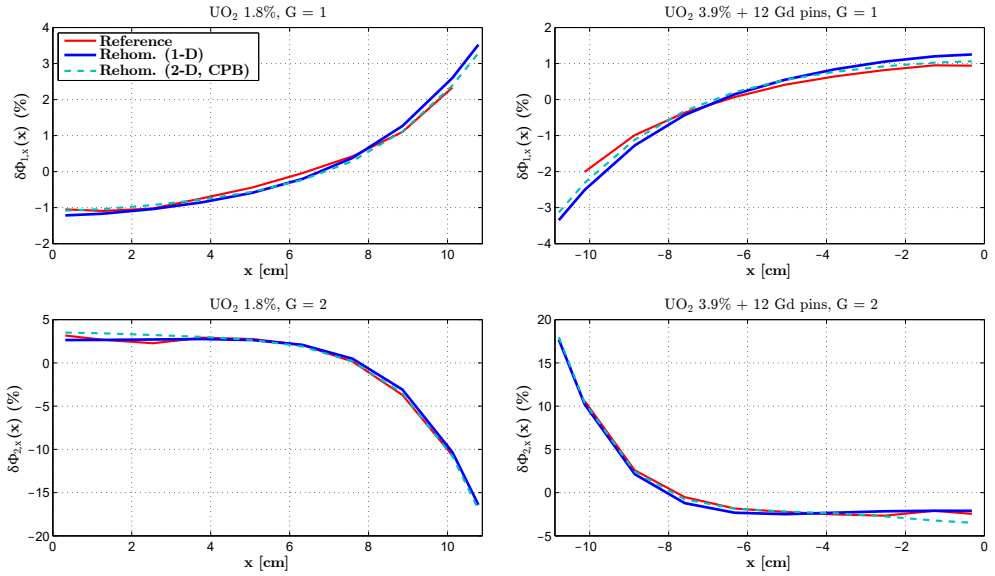


Fig. 5.17. Example 3: variation in the transverse-integrated flux distribution.

Table 5.7. Example 3: (a) number of non-linear flux iterations and errors in the integral parameters, and (b) errors in the absorption and production nodal cross sections.

Simulation	N_{iter}	Δk_{eff} [pcm]	UO ₂ 1.8%	UO ₂ 3.9% + 12 Gd pins
			$\Delta \bar{P}_{\text{fiss}}$ (%)	$\Delta \bar{P}_{\text{fiss}}$ (%)
No rehom. (a)	9	757	-0.48 (0.58, -0.78)	0.33 (-0.34, 0.56)
2-D rehom. - CPB (b)	15	-105	0.24 (0.74, 0.11)	-0.16 (-0.43, -0.08)
2-D rehom. - MSS (c)	13	-136	0.41 (0.93, 0.28)	-0.28 (-0.54, -0.20)
1-D rehom. (d)	16	358	-0.37 (0.47, -0.60)	0.26 (-0.27, 0.43)

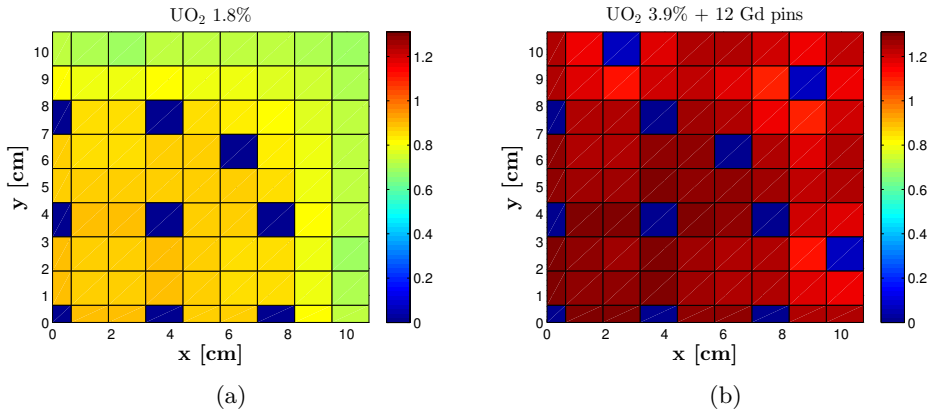
(a)

Simulation	UO ₂ 1.8%				UO ₂ 3.9% + 12 Gd pins			
	Errors (%)							
	$\Delta \Sigma_{a,1}$	$\Delta \Sigma_{a,2}$	$\Delta \nu \Sigma_{f,1}$	$\Delta \nu \Sigma_{f,2}$	$\Delta \Sigma_{a,1}$	$\Delta \Sigma_{a,2}$	$\Delta \nu \Sigma_{f,1}$	$\Delta \nu \Sigma_{f,2}$
No rehom. (a)	0.03	1.11	0.67	1.35	-0.11	-2.45	-0.48	-0.95
2-D rehom. - CPB (b)	0.07	0.98	0.73	1.10	-0.20	-0.88	-0.47	-1.23
2-D rehom. - MSS (c)	0.07	0.99	0.72	1.10	-0.19	-0.84	-0.46	-1.24
1-D rehom. (d)	0.07	0.99	0.73	1.10	-0.19	-1.62	-0.48	-0.97

(b)

Table 5.8. Example 3: errors in the absorption and production cross sections rehomogenized with the reference 2-D flux variation and with a least-squares best fit of it.

	UO ₂ 1.8%				UO ₂ 3.9% + 12 Gd pins			
	Errors (%)							
Flux variation (2-D)	$\Delta\Sigma_{a,1}$	$\Delta\Sigma_{a,2}$	$\Delta\nu\Sigma_{f,1}$	$\Delta\nu\Sigma_{f,2}$	$\Delta\Sigma_{a,1}$	$\Delta\Sigma_{a,2}$	$\Delta\nu\Sigma_{f,1}$	$\Delta\nu\Sigma_{f,2}$
Reference	0.08	0.89	0.74	0.91	-0.20	-1.27	-0.48	-0.86
Best fit	0.06	0.98	0.72	1.07	-0.18	-1.22	-0.47	-1.11

**Fig. 5.18.** Example 3: reference pin power (normalized to the colorset-averaged value) in the assemblies (a) without and (b) with gadolinium-bearing fuel pins.**Table 5.9.** Example 3: RMS deviations (in percentage) in the pin-by-pin two-group flux and total fission power.

	UO ₂ 1.8%				UO ₂ 3.9% + 12 Gd pins			
Simulation	RMS $\Phi_{1,r}$	RMS $\Phi_{2,r}$	RMS $P_{f,r}$	RMS P_{wa}	RMS $\Phi_{1,r}$	RMS $\Phi_{2,r}$	RMS $P_{f,r}$	RMS P_{wa}
No rehom. (a)	0.37	1.24	1.55	1.05	0.51	1.38	1.61	2.11
2-D rehom. - CPB (b)	0.34	1.18	1.47	1.04	0.22	1.20	1.29	1.76
1-D rehom. (d)	0.34	1.23	1.56	1.03	0.34	1.23	1.42	1.86

of the limited accuracy in the prediction of the flux variation, the flux and power distributions in the MOX assembly improve with the 2-D rehomogenization. An increase in the error is only found around the four nodal vertices, particularly in the two cells surrounding the central water-carrying instrumentation tube (in the SW corner of the shown quadrant). These observations are confirmed by the RMS deviations, which also decrease appreciably. The improvement is more significant in the UO₂ assembly with the 2-D model.

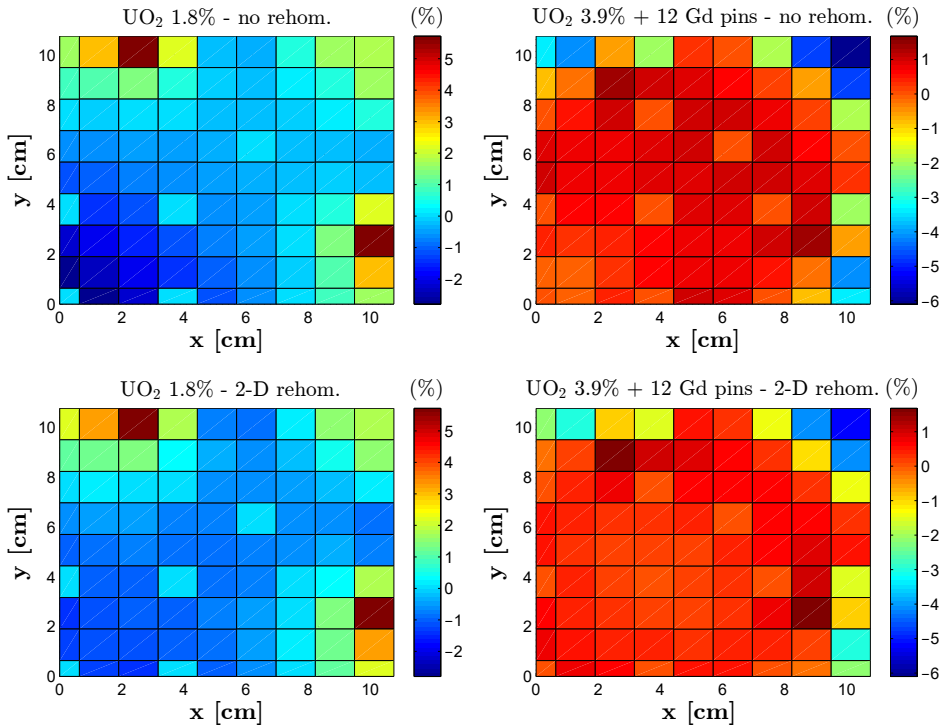


Fig. 5.19. Example 3: relative error (in percentage) in the pin-power distribution computed with calculations *a* and *b*.

In this test case, the CPB-based 2-D rehomogenization has a considerably slower convergence rate than the MSS approach and the 1-D rehomogenization (Table 5.10).

5.4 Discussion

5.4.1 On the transverse-leakage approximation

As mentioned in Section 5.2.5, the conventional three-node quadratic fit for the approximation of the transverse-leakage distribution is a non-consistent feature of nodal calculations (Lawrence, 1986). Various methods can be found in the literature to relax this approximation (Prinsloo et al., 2014). In this section, we compare the transverse-leakage distributions computed with the aforementioned standard approach and with the quadratic approximation ensuing from the 2-D rehomogenization [Eq. (5.43)]. The impact of these two strategies on the nodal simulations is also addressed.

Fig. 5.27 shows the transverse-leakage shape $L_{G,y}(x)$ in the 1.8%-enriched UO₂

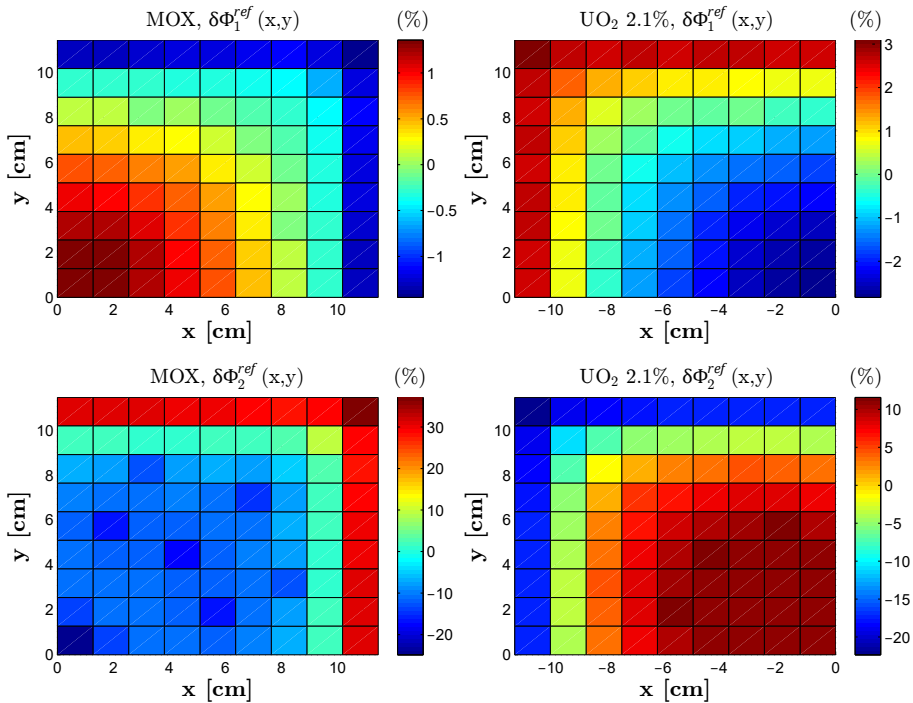


Fig. 5.20. Example 4: reference variation (in percentage) in the 2-D flux distribution.

assembly of example 1. The curves of calculations *a* and *d* have been computed with the three-node parabolic fit, whereas the curves of calculation *b* have been determined with Eq. (5.43). The distributions obtained with the 2-D rehomogenization differ significantly from those of the standard approximation, especially in the thermal group.

We have found that, when spatial rehomogenization is applied, the nodal calculation becomes insensitive to the transverse-leakage approximation. We have observed convergence to the same solution (in terms of k_{eff} , the nodal-flux distribution $\bar{\Phi}_G$, and the cross-section corrections $\delta\Sigma_{x,G}$) irrespective of the intranodal shape assumed for $L_{G,y}(x)$ and $L_{G,x}(y)$. This finding is related to the corrections on the assembly-surface discontinuity factors $\delta f_{G,d\pm}$ and can be explained as follows. The transverse-leakage approximation affects the nodal estimates of $\Phi_{G,d\pm}^{hom}$ and $J_{G,d\pm}$, which are input quantities to the spatial rehomogenization algorithm (see Section 5.2). However, the corrections $\delta f_{G,d\pm}$ vary in such a way that the modal coefficients of the flux spatial perturbation [Eq. (5.4)] converge to the same values obtained with other transverse-leakage approximations. Eventually, also the heterogeneous quantities $(f_{G,d\pm}^\infty + \delta f_{G,d\pm})\Phi_{G,d\pm}^{hom}$ and $J_{G,d\pm}$ converge to the same values. The discontinuity-factor correction acts thus as a *free parameter* that enables convergence to the unique

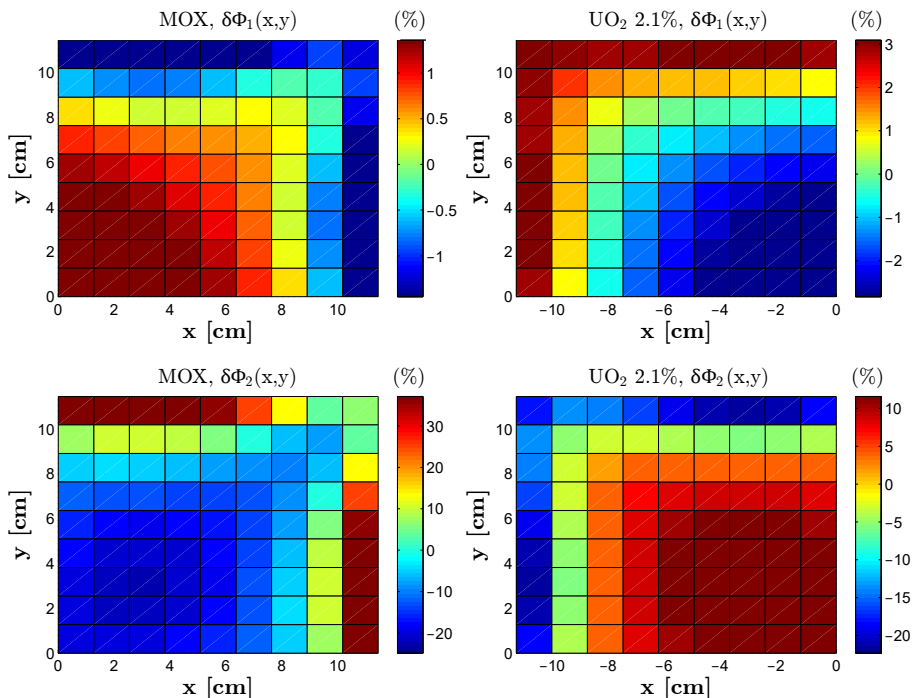


Fig. 5.21. Example 4: variation (in percentage) in the 2-D flux distribution, as computed with the CPB-based 2-D rehomogenization.

solution of the coupled nodal (i.e., CMFD + NEM) and rehomogenization fields. For example 1, Table 5.13 shows the corrections $\delta f_{G,d\pm}$ determined with calculation *b* and three different transverse-leakage distributions: the flat-leakage approximation (in which the intranodal shape is considered as uniform and equal to the node-averaged value of the transverse leakage), the standard three-node quadratic fit, and the quadratic shape from Eq. (5.43). The flat-leakage approximation leads to the highest variations in $\delta f_{G,d\pm}$, whereas Eq. (5.43) leads to the smallest.

The insensitivity to the transverse-leakage approach has also been observed with the 1-D rehomogenization. More investigation is needed to find a mathematical justification of this behavior.

5.4.2 Analysis on the discontinuity factors

In Section 5.3, we have only assessed the accuracy of the cross-section corrections. We now make a similar analysis on the discontinuity factors.

We evaluate the reference environmental discontinuity factors $f_{G,d\pm}^{\text{env,ref}}$ with a nodal-equivalence approach applied to the colorset transport calculation. We define the

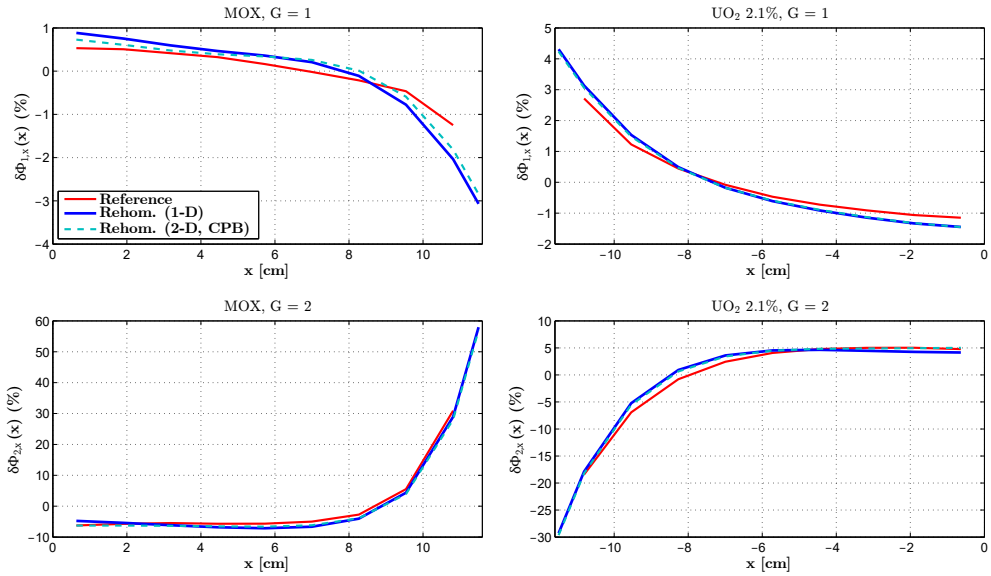


Fig. 5.22. Example 4: variation in the transverse-integrated flux distribution.

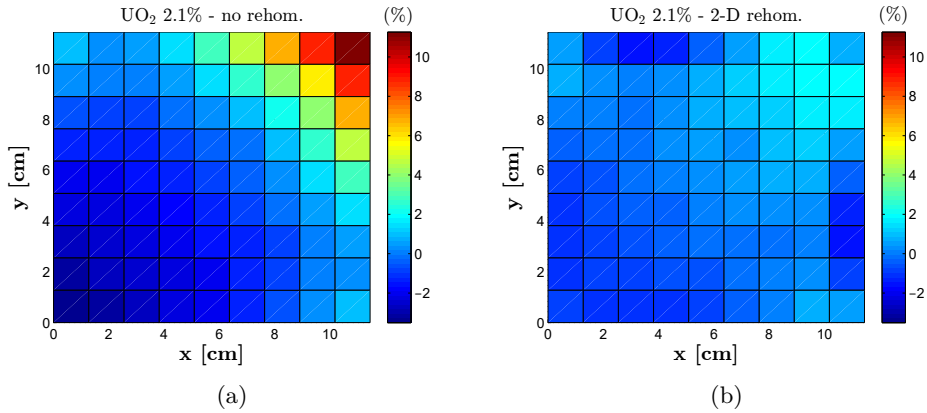


Fig. 5.23. Example 4: relative error (in percentage) in the pin-by-pin thermal flux in the UO_2 assembly. The plots refer to the calculations (a) without rehomogenization and (b) with the CPB-based 2-D rehomogenization.

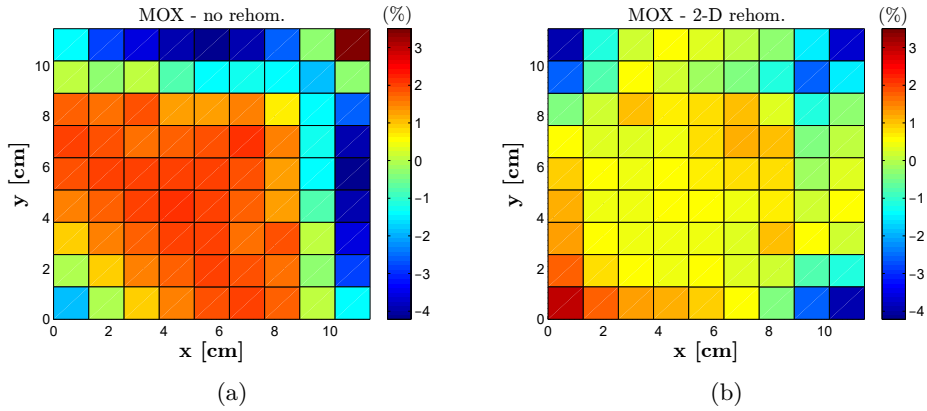


Fig. 5.24. Example 4: relative error (in percentage) in the pin-by-pin thermal flux in the MOX assembly. The plots refer to the calculations (a) without rehomogenization and (b) with the CPB-based 2-D rehomogenization.

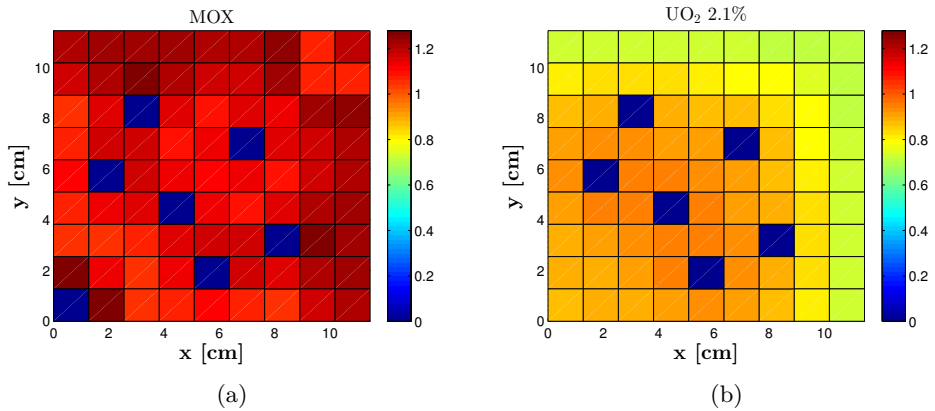


Fig. 5.25. Example 4: reference pin power (normalized to the colorset-averaged value) in the (a) MOX and (b) UO_2 assemblies.

Table 5.10. Example 4: (a) number of non-linear flux iterations and errors in the integral parameters, and (b) errors in the absorption and production nodal cross sections.

Simulation	N_{iter}	Δk_{eff} [pcm]	UO ₂ 2.1%	MOX
			$\Delta \bar{P}_{\text{fiss}}$ (%)	$\Delta \bar{P}_{\text{fiss}}$ (%)
No rehom. (a)	11	199	1.94 (0.81, 2.24)	-1.44 (-0.46, -1.86)
2-D rehom. - CPB (b)	29	276	0.38 (0.70, 0.22)	-0.28 (-0.39, -0.19)
2-D rehom. - MSS (c)	17	273	0.48 (0.89, 0.29)	-0.36 (-0.50, -0.24)
1-D rehom. (d)	17	286	0.22 (0.48, 0.10)	-0.17 (-0.27, -0.09)

(a)

Simulation	UO ₂ 2.1%				MOX			
	Errors (%)							
	$\Delta \Sigma_{a,1}$	$\Delta \Sigma_{a,2}$	$\Delta \nu \Sigma_{f,1}$	$\Delta \nu \Sigma_{f,2}$	$\Delta \Sigma_{a,1}$	$\Delta \Sigma_{a,2}$	$\Delta \nu \Sigma_{f,1}$	$\Delta \nu \Sigma_{f,2}$
No rehom. (a)	0.54	1.18	0.61	1.35	-1.05	0.31	-0.52	0.45
2-D rehom. - CPB (b)	0.54	1.17	0.62	1.31	-1.01	-1.28	-0.43	-1.40
2-D rehom. - MSS (c)	0.55	1.16	0.62	1.30	-1.0	-1.27	-0.44	-1.39
1-D rehom. (d)	0.54	1.16	0.62	1.29	-1.0	-1.19	-0.41	-1.30

(b)

Table 5.11. Example 4: errors in the absorption and production cross sections rehomogenized with the reference 2-D flux variation and with a least-squares best fit of it.

Flux variation (2-D)	UO ₂ 2.1%				MOX			
	Errors (%)							
	$\Delta \Sigma_{a,1}$	$\Delta \Sigma_{a,2}$	$\Delta \nu \Sigma_{f,1}$	$\Delta \nu \Sigma_{f,2}$	$\Delta \Sigma_{a,1}$	$\Delta \Sigma_{a,2}$	$\Delta \nu \Sigma_{f,1}$	$\Delta \nu \Sigma_{f,2}$
Reference	0.59	0.88	0.68	0.68	-1.05	-0.06	-0.49	0.07
Best fit	0.55	1.11	0.63	1.17	-1.04	-0.71	-0.48	-0.74

Table 5.12. Example 4: RMS deviations (in percentage) in the pin-by-pin two-group flux and total fission power.

Simulation	UO ₂ 2.1%				MOX			
	RMS $_{\Phi_{1,r}}$	RMS $_{\Phi_{2,r}}$	RMS $_{P,r}$	RMS $_{P,wa}$	RMS $_{\Phi_{1,r}}$	RMS $_{\Phi_{2,r}}$	RMS $_{P,r}$	RMS $_{P,wa}$
No rehom. (a)	0.35	3.0	3.1	2.68	0.73	2.10	2.59	4.09
2-D rehom. - CPB (b)	0.45	0.89	1.51	1.21	0.70	1.25	1.97	2.64
1-D rehom. (d)	0.45	2.40	2.48	1.73	0.77	1.17	1.86	2.50

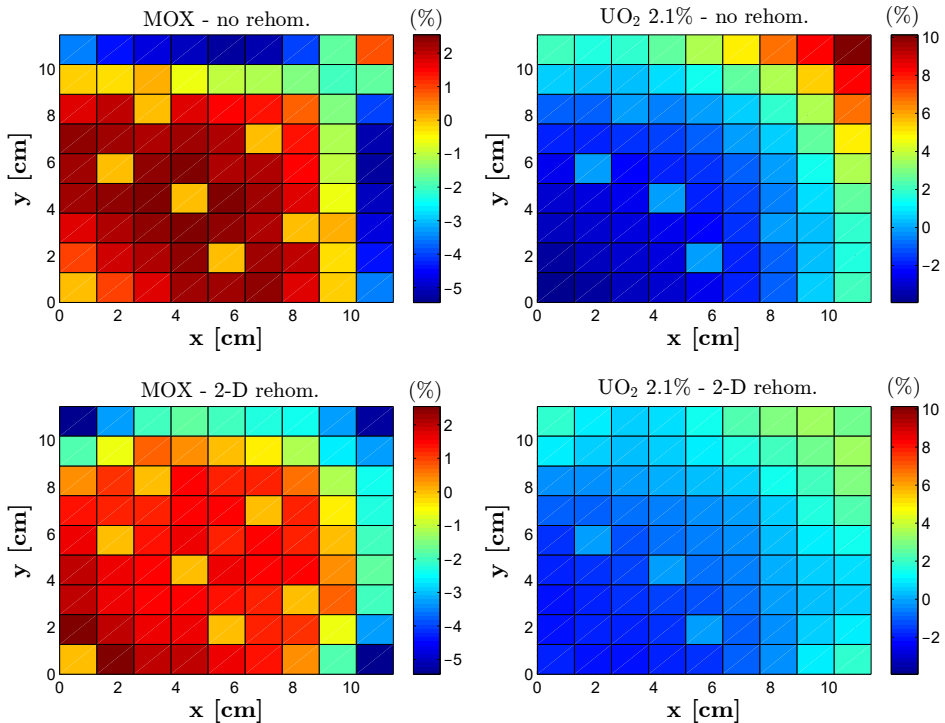


Fig. 5.26. Example 4: relative error (in percentage) in the pin-power distribution computed with calculations *a* and *b*.

Table 5.13. Example 1: corrections (in percentage) on the assembly discontinuity factors computed with calculation *b* and different transverse-leakage approximations.

	UO ₂ 1.8%		UO ₂ 3.1% + 16 b.p. rods	
Leakage approximation	δf_1 (%)	δf_2 (%)	δf_1 (%)	δf_2 (%)
Flat	-0.15	1.64	0.21	-2.87
Quadratic (standard)	0.05	0.44	0.03	-1.87
Quadratic (2-D rehom.)	-0.04	0.23	0.12	-1.70

homogeneous transverse-integrated neutron flux in the real environment with a quartic expansion, as in the conventional NEM equations:

$$\Phi_{G,d}^{\text{hom,ref}}(u_d) = \bar{\Phi}_G^{\text{ref}} + \sum_{i=1}^4 a_{G,d,i}^{\text{ref}} P_{G,i}(u_d), \quad (5.45)$$

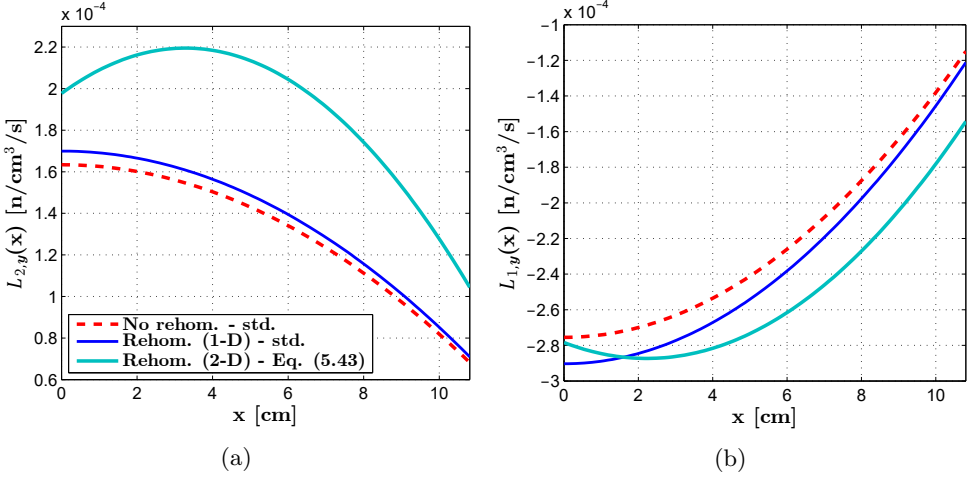


Fig. 5.27. (a) Thermal- and (b) fast-group transverse-leakage distributions in the 1.8%-enriched UO_2 assembly of example 1. The abbreviation ‘std.’ stands for ‘standard’ and refers to the conventional three-node quadratic fit. In both groups, the curves are normalized to the node-averaged transverse leakage from the nodal calculation.

where $\bar{\Phi}_G^{\text{ref}}$ is the node-averaged flux from the reference transport simulation in APOLLO2-A. The basis functions $P_{G,i}(u_d)$ are those defined in Eq. (5.5). The directional modal coefficients $a_{G,d,i}^{\text{ref}}$ in a given node are determined with a linear system of four equations per group: (i) the conservation of the reference directional net current at the left boundary of the node ($J_{G,d-}^{\text{ref}}$); (ii) the conservation of the reference directional net current at the right boundary of the node ($J_{G,d+}^{\text{ref}}$); the projection of the transverse-integrated, two-group nodal diffusion equation in the environment over the (iii) first- and (iv) second-order NEM basis functions [Eqs. (5.5a) and (5.5b)].

We exploit the symmetry of the four-assembly configurations considered in this work and determine the reference surface-averaged currents with the two-group nodal balance in the colorset:

$$|J_{G,d\pm}^{\text{ref}}| = \frac{\Delta d}{2} \left(\Sigma_{t,G}^{\text{ref}} \bar{\Phi}_G^{\text{ref}} - \frac{\chi_G^{\text{ref}}}{k_{\text{eff}}^{\text{ref}}} \sum_{G'=1}^2 \nu \Sigma_{f,G'}^{\text{ref}} \bar{\Phi}_{G'}^{\text{ref}} - \sum_{G'=1}^2 \Sigma_{s,G' \rightarrow G}^{\text{ref}} \bar{\Phi}_{G'}^{\text{ref}} \right). \quad (5.46)$$

The cross sections in Eq. (5.46) have been condensed and homogenized with the neutron flux energy spectrum and spatial distribution of the colorset environment. The j^{th} -order (with $j = 1, 2$) 1-D homogeneous equation is

$$\int_{-1/2}^{1/2} du_d P_j(u_d) \left[\frac{dJ_{G,d}^{\text{ref}}(u_d)}{du_d} + \Sigma_{t,G}^{\text{ref}} \Phi_{G,d}^{\text{hom,ref}}(u_d) - S_{G,d}^{\text{ref}}(u_d) \right] = 0, \quad (5.47)$$

where the source term $S_{G,d}^{\text{ref}}(u_d)$ includes the scattering and fission operators and the transverse leakage:

$$S_{G,d}^{\text{ref}}(u_d) = \frac{\chi_G^{\text{ref}}}{k_{\text{eff}}^{\text{ref}}} \sum_{G'=1}^2 \nu \Sigma_{f,G'}^{\text{ref}} \Phi_{G',d}^{\text{hom,ref}}(u_d) + \sum_{G'=1}^2 \Sigma_{s,G' \rightarrow G}^{\text{ref}} \Phi_{G',d}^{\text{hom,ref}}(u_d) - L_{G,t}(u_d). \quad (5.48)$$

In Eq. (5.48), the transverse-leakage distribution $L_{G,t}(u_d)$ is approximated with the conventional quadratic fit over the node under consideration and the two adjacent nodes along the direction d . The leakage expansion coefficients are computed preserving the reference volume-averaged transverse leakage $\bar{L}_{G,t}^{\text{ref}}$ (evaluated with Eq. (5.46)) in the three nodes.

After solving for the modal coefficients $a_{G,d,i}^{\text{ref}}$, the reference discontinuity factor is estimated as

$$f_{G,d\pm}^{\text{env,ref}} = \frac{\Phi_{G,d\pm}^{\text{het,ref}}}{\Phi_{G,d}^{\text{hom,ref}}\left(\pm \frac{1}{2}\right)}, \quad (5.49)$$

where $\Phi_{G,d\pm}^{\text{het,ref}}$ is the heterogeneous surface-averaged flux from the reference transport calculation. Since this quantity is not among the edits of APOLLO2-A, we make the following assumption:

$$\Phi_{G,d\pm}^{\text{het,ref}} \approx \Phi_{G,\text{wg}}^{\text{ref}}, \quad (5.50)$$

where $\Phi_{G,\text{wg}}^{\text{ref}}$ denotes the spatially averaged value of the water-gap flux from the reference calculation.

Table 5.14 reports the relative differences (in percentage) between the discontinuity-factor estimates of calculations a , b , and d and the reference values determined with Eq. (5.49). The improvement in the discontinuity factors is less apparent than that observed in the cross sections in Section 5.3. In particular, in the UO_2 and MOX assemblies of example 4 (Table 5.14d) the corrected values have significantly higher errors than the infinite-medium ones. We remark that the reference quantities in Eqs. (5.46) to (5.49) (cross sections, node-averaged fluxes, surface-averaged fluxes and currents) come from the solution of the 281-group transport equation in the colorset environment, with successive collapsing to two groups. These quantities incorporate not only the spatial effects of the environment but also the spectral ones, which are not taken into account by spatial rehomogenization. The discontinuity factors computed with Eq. (5.49), which we consider here as reference values, are therefore not fully consistent with our spatial rehomogenization approach. A more rigorous assessment should be made computing them with a reference solution that excludes the spectral effects (namely, solving the transport equation in the colorset environment directly in a two-group structure, without energy condensation).

To conclude the analysis on the discontinuity factors, we assess the impact of the reference $\delta f_{G,d\pm}$ on the nodal estimates of the multiplication factor and fission power. For this purpose, we run two nodal calculations with the cross sections rehomogenized by the reference 2-D flux variation (see Tables 5.2, 5.5, 5.8, and 5.11). The first of

Table 5.14. Relative errors (in percentage) in the infinite-medium assembly discontinuity factors and in the environmental discontinuity factors determined with rehomogenization. The errors are computed with respect to the discontinuity-factor estimates ensuing from the application of a nodal equivalence approach to the reference data from APOLLO2-A.

Example 1	UO ₂ 1.8%		UO ₂ 3.1% + 16 b.p. rods	
Simulation	Δf_1^{env} (%)	Δf_2^{env} (%)	Δf_1^{env} (%)	Δf_2^{env} (%)
No rehom. (a)	0.11	1.41	0.68	-0.69
2-D rehom. - CPB (b)	0.07	1.64	0.80	-2.38
1-D rehom. (d)	0.08	1.72	0.83	-2.15
(a)				
Example 2	UO ₂ 1.8%		UO ₂ 2.4% + 24 AIC rods	
Simulation	Δf_1^{env} (%)	Δf_2^{env} (%)	Δf_1^{env} (%)	Δf_2^{env} (%)
No rehom. (a)	0.14	0.10	0.81	3.52
2-D rehom. - CPB (b)	0.12	0.36	0.33	-1.68
1-D rehom. (d)	0.13	0.44	0.55	-0.56
(b)				
Example 3	UO ₂ 1.8%		UO ₂ 3.9% + 12 Gd pins	
Simulation	Δf_1^{env} (%)	Δf_2^{env} (%)	Δf_1^{env} (%)	Δf_2^{env} (%)
No rehom. (a)	0.41	2.95	0.66	-4.47
2-D rehom. - CPB (b)	0.31	2.97	0.27	-4.14
1-D rehom. (d)	0.34	3.22	0.22	-4.18
(c)				
Example 4	UO ₂ 2.1%		MOX	
Simulation	Δf_1^{env} (%)	Δf_2^{env} (%)	Δf_1^{env} (%)	Δf_2^{env} (%)
No rehom. (a)	0.23	5.90	0.34	2.86
2-D rehom. - CPB (b)	0.21	8.76	0.33	-10.7
1-D rehom. (d)	0.21	8.71	0.24	-9.86
(d)				

these uses the infinite-medium discontinuity factors $f_{G,d\pm}^{\infty}$, whereas the second uses the reference discontinuity factors $f_{G,d\pm}^{\text{env,ref}}$ from Eq. (5.49). The results are shown in Table 5.15. Whilst the discontinuity-factor corrections have a mild impact on the nodal simulations of examples 1 and 4, their effect is substantial in examples 2 and 3. Comparing the errors in k_{eff} and \bar{P}_{fiss} shown in Table 5.15 with those resulting from rehomogenization (Tables 5.1, 5.4, 5.7, and 5.10), the following conclusions can be

5. A two-dimensional model for spatial rehomogenization

Table 5.15. Errors in the multiplication factor and assembly-averaged fission power estimated with the reference spatial cross-section corrections ($\delta\Sigma_{r,G}^{\text{spat,ref}}$) and the infinite-medium ($f_{G,d\pm}^\infty$) or reference ($f_{G,d\pm}^{\text{env,ref}}$) discontinuity factors.

Example 1		UO ₂ 1.8%	UO ₂ 3.1% + 16 b.p. rods
	Δk_{eff} [pcm]	$\Delta \bar{P}_{\text{fiss}}$ (%)	$\Delta \bar{P}_{\text{fiss}}$ (%)
$\delta\Sigma_{r,G}^{\text{spat,ref}}, f_{G,d\pm}^\infty$	-36	0.51 (0.81, 0.43)	-0.43 (-0.57, -0.39)
$\delta\Sigma_{r,G}^{\text{spat,ref}}, f_{G,d\pm}^{\text{env,ref}}$	-43	0.65 (0.54, 0.68)	-0.55 (-0.38, -0.61)
(a)			
Example 2		UO ₂ 1.8%	UO ₂ 2.4% + 24 AIC rods
	Δk_{eff} [pcm]	$\Delta \bar{P}_{\text{fiss}}$ (%)	$\Delta \bar{P}_{\text{fiss}}$ (%)
$\delta\Sigma_{r,G}^{\text{spat,ref}}, f_{G,d\pm}^\infty$	-33	0.76 (0.38, 0.84)	-0.97 (-0.36, -1.15)
$\delta\Sigma_{r,G}^{\text{spat,ref}}, f_{G,d\pm}^{\text{env,ref}}$	-141	0.07 (-0.03, 0.095)	-0.09 (0.02, -0.13)
(b)			
Example 3		UO ₂ 1.8%	UO ₂ 3.9% + 12 Gd pins
	Δk_{eff} [pcm]	$\Delta \bar{P}_{\text{fiss}}$ (%)	$\Delta \bar{P}_{\text{fiss}}$ (%)
$\delta\Sigma_{r,G}^{\text{spat,ref}}, f_{G,d\pm}^\infty$	210	-0.24 (0.71, -0.50)	0.17 (-0.42, 0.36)
$\delta\Sigma_{r,G}^{\text{spat,ref}}, f_{G,d\pm}^{\text{env,ref}}$	137	0.95 (0.74, 1.0)	-0.65 (-0.43, -0.72)
(c)			
Example 4		UO ₂ 2.1%	MOX
	Δk_{eff} [pcm]	$\Delta \bar{P}_{\text{fiss}}$ (%)	$\Delta \bar{P}_{\text{fiss}}$ (%)
$\delta\Sigma_{r,G}^{\text{spat,ref}}, f_{G,d\pm}^\infty$	97	1.70 (0.76, 1.96)	-1.27 (-0.43, -1.62)
$\delta\Sigma_{r,G}^{\text{spat,ref}}, f_{G,d\pm}^{\text{env,ref}}$	61	2.01 (0.74, 2.37)	-1.49 (-0.42, -1.96)
(d)			

drawn for the various test cases:

- In example 1, both the 1-D and 2-D models overestimate the corrections on k_{eff} and on the fission power (especially the 2-D one).
- In example 2, similar considerations apply to the 2-D model, whereas the 1-D approach provides a very accurate result.
- In example 3, the correction on k_{eff} is overestimated with the 2-D model and underestimated with the 1-D one; both approaches underestimate the corrections on \bar{P}_{fiss} (particularly the 1-D model).

- In example 4, the computed corrections on k_{eff} and \bar{P}_{fiss} go in the wrong direction. The spatial effects have negligible impact on the assembly-averaged fission power.

5.4.3 Numerical features and implementation

As spectral rehomogenization, spatial rehomogenization also translates into an additional level of feedback in the global core calculation (Section 2.2.3). In a two-group framework with four basis functions per direction and four cross terms (see Section 5.2), the rank of the 2-D rehomogenization linear system is 32. Since the rehomogenization problem is solved independently in each node after updating the corner-point flux distribution [Eq. (5.23) or (5.28)], the corresponding computational cost can be mitigated via parallelization of the algorithm.

In the present work, the rehomogenization coefficients [Eqs. (5.32) and (5.34)] have been computed post-processing the APOLLO2-A single-assembly cell-homogenized cross sections and flux distribution. Better modeling may be achieved incorporating their calculation into the lattice-code routines, thus accounting for within-cell heterogeneity. As in the case of spectral rehomogenization, an approximation is made in the formulation of the weighted-residual equations [Eq. (5.37)]. Eq. (5.30) is valid in the real environment, whereas in practice we use the pin-by-pin cross sections of the infinite medium. In order to verify the impact of this approximation, we have repeated the calculations of Section 5.3 computing the rehomogenization coefficients of Eq. (5.32) with the colorset cell-homogenized cross sections. For examples 2 and 4, Table 5.16 shows the errors of calculation b with these improved rehomogenization parameters.

Table 5.16. Results of the CPB-based 2-D rehomogenization with environmental rehomogenization coefficients (i.e., computed with the colorset pin-by-pin cross sections).

Example 2	UO ₂ 1.8%			UO ₂ 2.4% + 24 AIC rods		
Δk_{eff} [pcm]	$\Delta \bar{P}_{\text{fiss}}$ (%)	$\Delta \Sigma_{a,2}$ (%)	$\Delta \nu \Sigma_{f,2}$ (%)	$\Delta \bar{P}_{\text{fiss}}$ (%)	$\Delta \Sigma_{a,2}$ (%)	$\Delta \nu \Sigma_{f,2}$ (%)
-32	-0.76 (-0.37,-0.84)	0.57	0.61	0.97 (0.36,1.14)	-1.34	-0.94

(a)

Example 4	UO ₂ 2.1%			MOX		
Δk_{eff} [pcm]	$\Delta \bar{P}_{\text{fiss}}$ (%)	$\Delta \Sigma_{a,2}$ (%)	$\Delta \nu \Sigma_{f,2}$ (%)	$\Delta \bar{P}_{\text{fiss}}$ (%)	$\Delta \Sigma_{a,2}$ (%)	$\Delta \nu \Sigma_{f,2}$ (%)
317	0.19 (0.66,-0.001)	1.27	1.44	-0.14 (-0.38,0.001)	-1.08	-1.18

(b)

Comparing Tables 5.16a and 5.4, we observe that the differences in the results are negligible in the colorset with control rods. In the UO₂/MOX colorset (see Tables 5.16b and 5.10), the differences are more tangible. Whilst the error in k_{eff} increases of about 40 pcm compared to the case with standard rehomogenization coefficients (i.e.,

computed with the infinite-medium pin-by-pin cross sections), the errors in the fission power are halved. However, in both cases the power errors are significantly smaller than those of calculation *a*. Moreover, the improvement in the nodal cross sections of the MOX assembly observed with the environmental rehomogenization coefficients is small if compared to the reference estimates (see Table 5.11). We have verified that the impact of the aforementioned approximation on the rehomogenization parameters is marginal also in the test cases with Pyrex rods and gadolinium-bearing fuel pins. It can therefore be concluded that using the infinite-medium fine-mesh cross sections in Eq. (5.32) does not significantly affect the performance of the method.

Intranodal depletion effects can be easily incorporated into the rehomogenization coefficients. If the environmental 1-D (i.e., transverse-integrated) or 2-D pin-by-pin cross sections are approximated with polynomial expansions (Wagner et al., 1981; Forslund et al., 2001), the generic rehomogenization parameter h can be corrected as

$$h = h^{\text{base}} + \delta h, \quad (5.51)$$

where

- h^{base} is computed with Eq. (5.32), using the cross-section distribution of the infinite-medium base depletion;
- δh is determined with the coefficients of the intranodal cross-section expansion and an additional set of rehomogenization parameters. These only depend on (i) the basis functions of the cross-section expansion, (ii) the weighting functions of the flux-variation modal synthesis, and (iii) the single-assembly flux form function.

Isotopic spatial rehomogenization coefficients can also be used (as shown in Chapter 4) to fully account for the spatial effects of the environment in fuel depletion calculations. The memory requirement for the storage of the rehomogenization coefficients in the cross-section libraries is minimized exploiting the symmetry of the fuel-assembly internal layout. For example, given the same index i_d the two directional terms of Eq. (5.32b) are equal. Moreover, with the assumption of uniform diffusion coefficient, most of the neutron-current divergence coefficients [Eqs. (5.34b) and (5.34c)] are zero due to the properties of the chosen basis functions. The rehomogenization parameters are only computed and stored for an assembly quarter. During the nodal calculation, their sign is determined based on the orientation of the node within the fuel assembly. As observed for spectral rehomogenization (Section 2.4.2), convergence of the algorithm benefits from under-relaxation, which dampens numerical oscillations. Except for the CPB approach in the UO₂/MOX benchmark problem (Table 5.10), the increase in the number of power iterations of the eigenvalue calculation is below a factor of 1.8 and, thus, acceptable. Convergence difficulties have never been encountered. To conclude, the 2-D rehomogenization method presented in this chapter can also be

viewed as an original dehomogenization approach. If Eq. (5.2) is used, the assumption is made that the 2-D flux variation is a smooth function of the x and y coordinates and is not affected by intranodal heterogeneity. The impact of this approximation on the direct reconstruction of the pin-by-pin flux and power distributions should be assessed. A successful application of the 2-D rehomogenization for assembly dehomogenization as well would increase the attractiveness of the method and largely compensate for its higher computational cost compared to the 1-D model.

5.4.4 Complementarity between the spatial and spectral effects of the environment

We briefly address the complementarity of the various environmental effects on the nodal cross sections. For the benchmark problems analyzed in Section 5.3, Table 5.17 shows: (i) the reference spectral corrections $\delta\Sigma_{r,G}^{\text{spec,ref}}$, computed with the reference spectrum variation [Eq. (2.25)]; (ii) the reference spatial corrections $\delta\Sigma_{r,G}^{\text{spat,ref}}$, computed with the reference 2-D flux spatial change; and (iii) the cross (i.e., mixed energy-space) corrections $\delta\Sigma_{r,G}^{\text{cross}}$, which have been estimated as

$$\delta\Sigma_{r,G}^{\text{cross}} = \Sigma_{r,G}^{\text{ref}} - \Sigma_{r,G}^{\infty} - \delta\Sigma_{r,G}^{\text{spec,ref}} - \delta\Sigma_{r,G}^{\text{spat,ref}}, \quad (5.52)$$

where $\Sigma_{r,G}^{\text{ref}}$ is the cross section condensed and homogenized in the colorset configuration, thus incorporating the global environmental effect. Even if the cross corrections are generally smaller than the spectral and spatial ones, they are not negligible, especially in the assemblies with the strongest heterogeneity. In particular, in the MOX assembly of example 4 (Table 5.17d), the thermal absorption and production cross terms have magnitude comparable to or larger than the spectral and spatial ones, which have opposite sign and roughly cancel each other. As discussed in Section 2.4.1, one of the reasons of this behavior is that the flux spectrum deformation varies significantly with the distance from the assembly outer edge, whereas the correction $\delta\Sigma_{r,G}^{\text{spec,ref}}$ is computed with an average deformation in the assembly. Taking into account the cross corrections is therefore important for an accurate prediction of the global cross-section variation in the environment.

From Table 5.17, some general features of the cross-section corrections can be observed:

- The spatial effects are only relevant in the thermal group, whereas the spectral ones are significant in both energy groups. There is no clear pattern for the cross effects.
- In the heterogeneous assemblies, the sign and magnitude of the spatial corrections depend on the position of the main sources of heterogeneity within the fuel bundle.

Separating the various effects on the discontinuity factors is not equally straightforward for the reasons discussed in Section 5.4.2.

5. A two-dimensional model for spatial rehomogenization

Table 5.17. Cross-section changes due to the various types of environmental effects: spectral, spatial, and cross (i.e., mixed energy-space). The variations have been computed with respect to the infinite-medium values by using the reference data from APOLLO2-A.

Example 1	UO ₂ 1.8%					UO ₂ 3.1% + 16 b.p. rods				
Variation (%)										
Type of effect	$\delta\Sigma_{a,1}$	$\delta\Sigma_{a,2}$	$\delta\nu\Sigma_{f,1}$	$\delta\nu\Sigma_{f,2}$	$\delta\Sigma_{s,1\rightarrow 2}$	$\delta\Sigma_{a,1}$	$\delta\Sigma_{a,2}$	$\delta\nu\Sigma_{f,1}$	$\delta\nu\Sigma_{f,2}$	$\delta\Sigma_{s,1\rightarrow 2}$
Spectral	0.074	-0.55	-0.34	-0.57	-0.58	-0.13	0.77	0.19	0.84	0.45
Spatial	0.028	-0.16	0.034	-0.30	-0.025	-0.007	-0.18	-0.026	0.33	0.005
Cross	-0.065	0.025	-0.15	0.067	0.045	0.034	-0.090	0.12	-0.12	-0.017
Global	0.037	-0.69	-0.46	-0.80	-0.56	-0.10	0.50	0.28	1.04	0.44

(a)

Example 2	UO ₂ 1.8%					UO ₂ 2.4% + 24 AIC rods				
Variation (%)										
Type of effect	$\delta\Sigma_{a,1}$	$\delta\Sigma_{a,2}$	$\delta\nu\Sigma_{f,1}$	$\delta\nu\Sigma_{f,2}$	$\delta\Sigma_{s,1\rightarrow 2}$	$\delta\Sigma_{a,1}$	$\delta\Sigma_{a,2}$	$\delta\nu\Sigma_{f,1}$	$\delta\nu\Sigma_{f,2}$	$\delta\Sigma_{s,1\rightarrow 2}$
Spectral	0.78	-0.44	0.056	-0.46	0.61	-0.96	0.82	-0.23	1.12	-0.53
Spatial	-0.09	-0.31	-0.10	-0.39	0.072	-0.23	-1.24	0.13	0.41	0.062
Cross	0.034	0.098	-0.008	0.13	-0.043	-0.10	-0.20	-0.048	-0.29	-0.026
Global	0.72	-0.65	-0.055	-0.72	0.64	-1.29	-0.62	-0.15	1.23	-0.49

(b)

Example 3	UO ₂ 1.8%					UO ₂ 3.9% + 12 Gd pins				
Variation (%)										
Type of effect	$\delta\Sigma_{a,1}$	$\delta\Sigma_{a,2}$	$\delta\nu\Sigma_{f,1}$	$\delta\nu\Sigma_{f,2}$	$\delta\Sigma_{s,1\rightarrow 2}$	$\delta\Sigma_{a,1}$	$\delta\Sigma_{a,2}$	$\delta\nu\Sigma_{f,1}$	$\delta\nu\Sigma_{f,2}$	$\delta\Sigma_{s,1\rightarrow 2}$
Spectral	0.0	-0.85	-0.44	-0.88	-0.92	0.082	0.80	0.32	0.84	0.98
Spatial	0.056	-0.21	0.072	-0.43	-0.056	-0.09	1.20	-0.005	0.084	0.038
Cross	-0.083	-0.030	-0.24	-0.019	0.08	0.12	0.51	0.13	0.036	-0.063
Global	-0.03	-1.09	-0.61	-1.33	-0.90	0.11	2.51	0.45	0.96	0.95

(c)

Example 4	UO ₂ 2.1%					MOX				
Variation (%)										
Type of effect	$\delta\Sigma_{a,1}$	$\delta\Sigma_{a,2}$	$\delta\nu\Sigma_{f,1}$	$\delta\nu\Sigma_{f,2}$	$\delta\Sigma_{s,1\rightarrow 2}$	$\delta\Sigma_{a,1}$	$\delta\Sigma_{a,2}$	$\delta\nu\Sigma_{f,1}$	$\delta\nu\Sigma_{f,2}$	$\delta\Sigma_{s,1\rightarrow 2}$
Spectral	-0.43	-0.98	-0.41	-1.0	-3.43	0.92	0.47	0.34	0.50	2.46
Spatial	0.05	-0.30	0.066	-0.66	-0.035	-0.002	-0.37	0.033	-0.37	0.02
Cross	-0.15	0.11	-0.35	0.33	0.10	0.13	-0.41	0.17	-0.57	-0.095
Global	-0.53	-1.17	-0.70	-1.33	-3.36	1.06	-0.31	0.54	-0.44	2.39

(d)

For example 1, we briefly compare the results obtained with the reference spatial cross-section corrections and discontinuity factors (Table 5.15a) to those obtained with the reference spectral cross-section corrections (Table 3.13). The corrections on k_{eff} and on the fission power computed in the two cases go in the same direction. Considering the magnitude of the errors in the two standalone calculations and having verified that in this configuration cross effects play a little role (Table 5.17a), it is reasonable to expect that the errors in these parameters would become close to zero if one merely summed the spatial and spectral corrections.

5.5 Summary

In this chapter, we have developed a first-principle modal method to estimate the variation in the 2-D few-group flux distribution between the core environment and the infinite lattice. This method relaxes the main approximations of the original 1-D transverse-integrated rehomogenization.

Numerical results show that the errors in the multiplication factor and assembly-averaged fission power significantly decrease compared to the calculation with infinite-medium homogenization parameters. The cross-section corrections computed by the 2-D model always go in the right direction. In most cases they match the corrections determined with a least-squares best fit of the reference flux change, but they are higher than the reference values. One of the reasons of this outcome is that the polynomial and hyperbolic basis functions used for the modal expansion cannot reproduce to a high degree of accuracy the flux variation dip in the cells hosting absorbing elements (burnable-poison rods and control rods). In the 1-D approach, the flux change dip in these cells is smoothed out by the transverse integration and is therefore better fitted by the basis functions. When applying spatial and spectral rehomogenization sequentially, the overestimation of the spatial cross-section corrections in the thermal group may affect the accuracy of the global results.

The differences between the CPB-based and MSS-based approaches are small, with the former usually performing slightly better. An apparent superiority of the 2-D model over the 1-D model has not been observed. Except for the test case with gadolinium-bearing fuel pins, in which the 2-D method is more accurate, the discrepancies between the two approaches are not significant. In general, the 1-D model overestimates the cross-section corrections to a lesser extent.

At the pin-by-pin level, on average better results are found when rehomogenization is applied. Nevertheless, the improvement in the heterogeneous flux and fission-power distributions is often not fully generalized, but limited to certain subregions of the fuel assemblies. Therefore, the accuracy of the computed fission power in the hot spots (that is, the fuel cells with the highest thermal load) is tied to their location within the fuel bundles.

We have observed that when 1-D or 2-D spatial rehomogenization is applied, the type of transverse-leakage approximation does not affect the accuracy of the nodal calcula-

tion. An analysis on the complementarity of the various environmental corrections revealed that mixed energy-space effects cannot be neglected, especially in UO_2/MOX configurations.

CONCLUSIONS AND RECOMMENDATIONS

In this thesis, rehomogenization methods have been developed to model core-environment effects on the homogenization parameters used in nodal diffusion codes. The main motivation behind this work was to enhance the accuracy of nodal simulations of current and next-generation reactor cores, where strong spatial heterogeneity invalidates the assumptions underlying conventional homogenization theory. This chapter summarizes the key contributions of this work to reactor core nodal analysis. Directions for future research are also discussed.

6.1 Conclusions

The most important findings of this research are highlighted below.

- If combined with the diffusive approximation of the neutron leakage energy distribution, the POD-based spectral rehomogenization reconstructs the environmental flux spectrum very accurately. In many benchmark problems, the accuracy of the computed spectrum perturbation is comparable to that of the reference solution from neutron transport. The spectral component of the homogenization error due to neighbor effects is therefore successfully corrected. In general, the semi-analytic modal approach gives less accurate results, while still satisfactory. This is because the polynomial basis functions cannot reproduce faithfully the details of the spectrum deformation, such as resonance absorption spikes in the epithermal range and, in UO_2/MOX configurations, strongly varying components at fission energies. With this approach, the spectral error is often corrected only partially.

In isothermal conditions (i.e., without thermal-hydraulic feedback), the number

of non-linear flux iterations increases by a factor of about 2 with the POD approach and of about 1.6 with the semi-analytic approach. However, embedding the rehomogenization cross-section updates within thermal iterations would reduce the slowdown in convergence.

- Spectral rehomogenization can also predict variations in the infinite-medium condensation spectrum due to perturbations in nuclide densities. Taking advantage of this feature, a novel approach has been developed to model the multivariate dependence of the single-assembly macroscopic and microscopic cross sections on the water density and on the concentrations of diluted boron and xenon. This approach replaces the conventional multidimensional interpolation versus these state parameters. The boron-concentration axis is eliminated. The water- and xenon-density axes cannot be removed completely, because the effects of variations in the fine-energy isotopic cross sections must also be accounted for. However, these two directions are sampled individually (i.e., discarding the cross dependences) at far fewer points than in standard polynomial and spline interpolation algorithms.

In normal operating conditions and cold-to-hot transitions, the errors in the single-assembly macroscopic cross sections reconstructed with this rehomogenization-based approach are generally well below 0.1% and, therefore, comparable to interpolation errors. The errors in the infinite-medium multiplication factor k_∞ are lower than 40 pcm. In accidental conditions (i.e., at very low values of the water density), the errors in the macroscopic cross sections and in k_∞ are below 0.5% and 100 pcm, respectively.

Compared to tensorized interpolation, this method has a dual advantage: it reduces (by a factor of 7 to 9) the number of states to be simulated in the off-line lattice transport calculation and the number of table points in the cross-section libraries, and it decreases the computational cost of the on-line cross-section reconstruction.

- Spectral rehomogenization also reproduces the effects of differences in reactivity between the core environment and the infinite medium. It therefore eliminates the need for the critical-spectrum correction at the lattice-calculation level. The use of this kind of correction is questionable when simulating non-critical conditions (Dall’Osso, 2015a; Demazière, 2016). Moreover, as observed in Sections 3.3.2 and 4.3.2, nodal calculations with buckling-corrected cross sections tend to overestimate the control-rod worth in rodded configurations. Without the critical-buckling methodology, this non-conservative feature is removed or alleviated. An additional benefit is that the critical-spectrum iterations in lattice calculations are eliminated.
- The three aforementioned properties of spectral rehomogenization can be combined together to reconstruct the overall spectrum variation between the core environment in the local physical conditions and the non-critical infinite lattice in

a predefined nominal state. This finding lays the groundwork for a new concept of cross-section model, in which all spectral effects (due to interassembly neutron streaming, local changes in the nuclide densities, and differences in multiplicative properties) are predicted by rehomogenization. The above feature makes this thesis work a significant contribution to nodal methods for core analysis.

- The 2-D spatial rehomogenization model developed in this work produces significantly better estimates of the multiplication factor and assembly-averaged fission power compared to the case with single-assembly input parameters. The spatial corrections on thermal-absorption cross sections are, however, systematically overestimated. The spatial homogenization error is therefore overcorrected with respect to the reference. Global improvements are found in the pin-by-pin flux and power density distributions. Nevertheless, the power errors in the hot spots (which commonly condition the whole thermal-hydraulic core design) do not always decrease. In general, the gain in accuracy of the assembly discontinuity factors is less tangible. It has been shown (although not mathematically proved) that spatial rehomogenization nullifies the impact of inconsistent transverse-leakage approximations, such as the three-node parabolic fit. With regard to the computational cost of the method, similar considerations hold as for spectral rehomogenization.

To summarize, the results presented in this thesis demonstrate that spectral and spatial rehomogenization succeed in enhancing the accuracy of homogenized cross sections and of the nodal estimates of the parameters of greatest interest for core design and operation. One of the main gaps in industrial routine calculations is therefore bridged or mitigated.

From a numerical point of view, the chief advantages of the methods investigated in this thesis can be summarized as follows:

- They have a solid physical basis and do not resort to *ad hoc* approximations. Practical justifications corroborate the assumptions made in the derivation of the algorithms, such as neglecting the dependence of the diffusion-coefficient energy distribution on the fuel-assembly composition in the framework of the leakage spectrum model. These aspects distinguish the developed methods from other cross-section correction techniques available in the literature, most of which rely on empirical correlations or on the tabulation of precomputed corrections.
- They are based on lattice data and information from the on-line nodal calculation. The improvement in nodal accuracy is therefore achieved preserving the single-assembly homogenization paradigm and the computational efficiency of the conventional two-step procedure.
- They proved to be robust in a wide variety of test cases chosen to validate the methodology, and in others that have not been presented in this dissertation.

- They do not substantially degrade the computing performance of nodal calculations.
- They can be easily integrated into existing nodal codes as standalone modules.
- They can be used to correct the cross sections in every homogenization-based solution strategy, i.e., irrespective of the form of the neutron transport operator used in the homogenized core model (diffusion, transport, or simplified transport). They have therefore general validity.

For the reasons stated above, these methods largely meet industry's requirements. Their suitability for implementation in nodal transport and nodal simplified P_3 (SP_3) solvers is also attractive in the light of the steadily increasing interest in whole-core deterministic transport calculations.

Below are listed the main limitations of the proposed methods.

- The spectral and spatial effects of the environment are modeled separately. In some assembly configurations, such as UO_2/MOX interfaces, these effects are tightly coupled (that is, mixed energy-space terms are important from a modeling point of view). A sequential application of the spectral and spatial rehomogenization algorithms may therefore not always fully correct the homogenization defects.
- The POD-based modal synthesis of the neutron spectrum variation demands a costly off-line phase.
- It is assumed that the homogenization error in infinite-medium assembly discontinuity factors is entirely spatial (i.e., its spectral component is neglected).
- Spatial rehomogenization tends to overcorrect spatial homogenization errors. Moreover, as presented in this work, the algorithm can only be applied to Cartesian geometries.

Some of these shortcomings leave room for further improvement in the methodology, as extensively discussed in the next section.

6.2 Perspectives and recommendations

6.2.1 Spectral rehomogenization

One of the main challenges is the application of the POD methodology at an industrial level. The development of an adaptive snapshot sampling strategy is highly recommended to retain the attractiveness of this approach. It is the author's opinion that sparse grids would be a suitable candidate to pursue this achievement. The

calculation of snapshots depends on whether rehomogenization is used to reproduce (i) the spectral effects of dissimilar neighbor assemblies, (ii) the spectral effects of the local physical conditions, or (iii) the combination of the two. Finding an effective basis for case ii is easier for three reasons: (1) the problem has lower dimension; (2) the spectrum deformations induced by changes in the state parameters depend marginally on the fuel-assembly composition; (3) only single-assembly calculations are needed to generate the snapshots, thus limiting the computational burden of the off-line phase. In the more interesting case iii (namely, when the goal of rehomogenization is to incorporate all spectral effects), the most straightforward approach would be to combine the two bases computed separately for cases i and ii, that is, defining the overall spectrum deformation as a superposition of modes from the two sets of functions. The interplay between the two types of spectral effects may, however, pose some constraints in the choice of the modes. For instance, it has been observed that in the absence of strong perturbations in the water density, the fast-group spectrum variation mostly inherits the smoother shape of the heterogeneity-induced deformation (Section 4.3.2). On the other hand, if the moderator density varies significantly, the contribution of neighbor effects becomes smaller. Therefore, the importance of the two effects may be accounted for in the modal synthesis by selecting the basis functions on the fly with an adaptive approach, based on the type of perturbation in the state parameters. With this choice, the magnitude of the moderator density variation would be the threshold parameter with which to determine the number and the order of the modes from the two sets.

Besides the POD approach, the natural next step in the investigation of spectral rehomogenization is its application to reactor problems including thermal-hydraulic feedback. The diffusive approximation of the leakage spectrum introduces a non-linearity in the rehomogenization algorithm, which adds itself a non-linearity in the solution of the nodal transverse-integrated equations. In the seemingly straightforward case of isothermal conditions, convergence issues have not been observed either at zero burn-up or with fuel depletion. It is now necessary to verify that the dual non-linearity introduced by rehomogenization is small compared to thermal-hydraulic non-linearities. In this way, the robustness of the method can be conclusively proved.

The leakage energy distribution affects not only the forward neutron spectrum, but also the adjoint one. Leakage modeling is thus of paramount importance for an accurate prediction of adjoint-dependent quantities, such as the effective delayed-neutron fraction. This kinetic parameter is commonly computed during the lattice calculation by weighting the delayed-neutron emission rate with the infinite-medium adjoint spectrum (Stacey, 2007), which may differ significantly from the environmental one, especially in the fast group. In view of the relevance of this parameter in reactor kinetics and dynamics, a method for its correction could be developed exploiting the information from rehomogenization.

It would be of great interest to investigate the effect of spatial discretization on the accuracy of spectral rehomogenization. For example, an analysis is recommended to assess the suitability of the method for nodal codes that use finer meshes with

subassembly homogenization (see Section 1.2). Exploring the limit case of direct pin-by-pin calculations would not only be of practical interest, but also give more insight into the physical foundation of rehomogenization theory. Whilst the nodal neutron continuity equation in the energy domain [Eq. (2.5)] is valid irrespective of the mesh size, the diffusive leakage model may be less accurate at the fuel-cell spatial scale, where transport effects are important and the diffusion approximation is less rigorous. More complex modeling may therefore be needed to estimate the cell-to-cell leakage spectrum.

To conclude, the rehomogenization-based cross section model investigated in Chapter 4 should be validated on other types of fuel assemblies (such as MOX assemblies and assemblies hosting control rods or burnable poison) and on calculations with fuel depletion. The reconstruction of both infinite-medium and environmental cross sections in these further test cases should be considered. Also in this case, coupled neutronics/thermal-hydraulics simulations would be the conclusive benchmark. Another topic to be addressed is modeling the spectral effects of the local physical conditions on the assembly discontinuity factors and form functions, for which some suggestions have already been given in Section 4.4.4.

6.2.2 Spatial rehomogenization

The accuracy of the 2-D spatial rehomogenization might be improved with basis functions that better fit the intranodal flux spatial variation. Based on the satisfactory outcome of the POD in the framework of spectral rehomogenization, this modal approach could be extended to the spatial problem as well. This strategy would allow the direct calculation of two-dimensional basis functions in the domain of space, thus removing the separation of the directional and cross components of the modal expansion with the one-dimensional modes $P_{G,i_d}(u_d)$. Eq. (5.4) would become

$$\delta\Phi_G(u_x, u_y) = \sum_i \alpha_{G,i} P_{G,i}(u_x, u_y). \quad (6.1)$$

The search of snapshots for the calculation of the spatial modes $P_{G,i}(u_x, u_y)$ would follow the same criteria defined for the spectral problem.

As for spectral rehomogenization, the 2-D spatial rehomogenization with the CPB approach for the corner-point fluxes also introduces a dual non-linearity, which causes slower convergence in the UO₂/MOX benchmark problem (Section 5.3). The application of the method to test cases with thermal feedback is therefore advised once again to verify the absence of numerical instabilities in coupled calculations.

A pivotal aspect to be investigated is the use of the 2-D rehomogenization model for fuel-assembly dehomogenization and pin power reconstruction. In case of a positive outcome, two important steps of the nodal calculation could be incorporated into a single algorithm, with benefits not only in the accuracy of the results, but also in software functionality.

In core configurations with strong heterogeneity in the axial direction (such as enrichment and gadolinium-concentration zoning in BWRs), the 2-D rehomogenization in the x and y coordinates may be combined with the 1-D rehomogenization along the z axis. This strategy would allow accurate modeling of axial heterogeneity while retaining coarse axial meshes for both 3-D assembly homogenization (Schneider et al., 2016), when applicable, and the on-line nodal calculation.

6.2.3 Validation on a broader spectrum of test cases

This thesis work focused on the most common assembly configurations in PWRs, with the exception of reflector boundaries. This kind of benchmark problem was not investigated because the procedure followed for reflector group-constant generation differs from that employed for fuel assemblies. For example, the Equivalent Reflector Model (Hetzelt and Winter, 1999) is used in APOLLO2-A. This feature hinders a straightforward calculation of the rehomogenization parameters in the lattice-code routines dedicated to reflector homogenization. Nevertheless, nodal interfaces between fuel assemblies and reflector nodes (where both spectral and spatial effects are very strong) remain one of the most challenging test cases for further validation of the methodology.

The application of spectral and spatial rehomogenization to calculations with thermal feedback and full-core benchmark problems would give a final answer not only on the robustness of these methods, but also on their actual impact on the computational cost of coupled calculations. The latter must be evaluated in terms of (*i*) the increase in the number of non-linear flux iterations when rehomogenization is nested in the thermal-hydraulic updates, and (*ii*) the increase in the CPU time. In this respect, investigating numerical techniques to reduce the loss in computational efficiency may also bring substantial benefits.

As a final remark, the assessment of these rehomogenization techniques would gain value from their comparison with already existing methods in reactor physics literature (Section 1.2), and from their application to the analysis of reactors that exhibit even stronger core heterogeneity than PWRs, such as BWRs and materials testing reactors. The validity of these methods for fast-reactor core analysis should also be investigated.

6.2.4 Coupled modeling of spatial and spectral effects

There exist various research paths to combine the two rehomogenization algorithms into a unified model. The simplest though least rigorous approach is to apply spatial and spectral rehomogenization sequentially and to estimate the cross-term corrections via ad hoc empirical approximations. A theoretically more sound strategy is to build upon the following expression for the variation in the space- and energy-dependent flux distribution:

$$\delta\Phi_G(\mathbf{r}, E) = \sum_i \sum_j \alpha_{G,i,j} P_{G,i}(\mathbf{r}) Q_{G,j}(E), \quad (6.2)$$

where the basis functions $P_{G,i}(\mathbf{r})$ and $Q_{G,j}(E)$ are to be computed via POD in the separate phase spaces of \mathbf{r} and E . As an alternative, considering the two phase spaces simultaneously (i.e., taking snapshots of the pin-by-pin fine-group flux variation) would generate three-variable modes $F_i(\mathbf{r}, E)$. Eq. (6.2) would thus become

$$\delta\Phi_G(\mathbf{r}, E) = \sum_i \gamma_{G,i} F_i(\mathbf{r}, E). \quad (6.3)$$

In the formulation of both coupled approaches [Eqs. (6.2) and (6.3)], attention must be paid to the numerical conditioning of the so-obtained rehomogenization system. It is remarked that the approach of Eq. (6.3) would increase significantly the numerical complexity of the problem. Our current knowledge does not allow us to evaluate *a priori* whether significant improvements (i.e., appreciable enough to justify the increase in problem complexity) may be achieved moving to this simultaneous approach, compared to a simpler sequential strategy.

To conclude, this thesis work represents a solid basis for future developments in the area of rehomogenization. Some of the refinements discussed hitherto, together with a successful application to reactor problems with thermal feedback, would allow the described methods to reach maturity and, probably, to enter the mainstream of nodal diffusion codes.

BIBLIOGRAPHY

- T. Bahadir and S. Lindahl. Studsvik's next generation nodal code SIMULATE-5. In *Proc. of Advances in Nuclear Fuel Management IV (ANFM 2009)*, Hilton Head Island, South Carolina, USA, April 12–15, 2009.
- T. Bahadir, S. Lindahl and S. P. Palmtag. SIMULATE-4 multigroup nodal code with microscopic depletion model. In *Proc. of Mathematics and Computation, Supercomputing, Reactor Physics and Nuclear and Biological Applications (M&C 2005)*, Avignon, France, September 12–15, 2005.
- Y. S. Ban and H. G. Joo. Leakage correction of homogenized few-GCS through functionalization on leakage fraction. In *Proc. of Int. Conf. PHYSOR 2016*, 1815–1824, Sun Valley, Idaho, USA, May 1–5, 2016.
- M. Becker. Incorporation of spectral effects into one-group nodal simulators. *Nuclear Science and Engineering*, **59**, 276, 1976.
- P. Benoist, J. Mondot and I. Petrovic. Calculational and experimental investigations of void effect - a simple theoretical model for space-dependent leakage treatment of heterogeneous assemblies. *Nuclear Science and Engineering*, **118**, 197, 1994.
- I. Bilodid and S. Mittag. Use of the local Pu-239 concentration as an indicator of burnup spectral history in DYN3D. *Annals of Nuclear Energy*, **37**, 1208, 2010.
- R. Böer and H. Finnemann. Fast analytical flux reconstruction method for nodal space-time nuclear reactor analysis. *Annals of Nuclear Energy*, **19**, 617, 1992.
- P. M. Bokov. Automated few-group cross-section parameterization based on quasi-regression. *Annals of Nuclear Energy*, **36**, 1215, 2009.
- P. M. Bokov, D. Botes and V. G. Zimin. Pseudospectral Chebyshev representation of few-group cross sections on sparse grids. In *Proc. of Int. Conf. PHYSOR 2012*, Knoxville, Tennessee, USA, April 15–20, 2012.

- P. M. Bokov and R. H. Prinsloo. Cross-section parameterization using quasi-regression approach. In *Proc. of Joint International Topical Meeting on Mathematics & Computation and Supercomputing in Nuclear Applications (M&C+ SNA 2007)*, Monterey, California, USA, April 15–19, 2007.
- P. M. Bokov et al. A quasi-regression method for automated cross-section parameterization: PBMR benchmark example. In *Proc. of Int. Conf. PHYSOR 2008*, 14–19, Interlaken, Switzerland, September 14–19, 2008.
- D. Botes and P. M. Bokov. Hierarchical, multilinear representation of few-group cross sections on sparse grids. In *Proc. of Int. Conf. on Mathematics and Computational Methods Applied to Nuclear Science and Engineering (M&C 2011)*, Rio de Janeiro, RJ, Brazil, May 8–12, 2011.
- D. Botes and P. M. Bokov. Polynomial interpolation of few-group neutron cross sections on sparse grids. *Annals of Nuclear Energy*, **64**, 156, 2014.
- D. Botes, S. Chifamba and P. M. Bokov. A study of the performance of a sparse grid cross section representation methodology as applied to MOX fuel. *Annals of Nuclear Energy*, **99**, 444, 2017.
- A. Bouamrhirene and S. Noceir. Performance of improved polynomial and analytical nodal diffusion methods in the treatment of the MOX-UO₂ interface. In *Proc. of the Int. Conf. on Reactor Physics and Reactor Computations*, 590, Tel-Aviv, Israel, January 23–26, 1994.
- A. G. Buchan et al. A POD reduced-order model for eigenvalue problems with application to reactor physics. *International Journal for Numerical Methods in Engineering*, **95**, 1011, 2013.
- A. G. Buchan et al. A POD reduced order model for resolving angular direction in neutron/photon transport problems. *Journal of Computational Physics*, **296**, 138, 2015.
- H.-J. Bungartz and M. Griebel. Sparse grids. *Acta Numerica*, **13**, 147, 2004.
- M. H. Chang et al. A nodal expansion method with spatially coupled effects incorporated into the transverse leakage approximation. *Nuclear Science and Engineering*, **103**, 343, 1989.
- A. Chatterjee. An introduction to the Proper Orthogonal Decomposition. *Current Science*, **78**, 808, 2000.
- S. Choi et al. Impact of inflow transport approximation on light water reactor analysis. *Journal of Computational Physics*, **299**, 352, 2015.

-
- S. Choi et al. On the diffusion coefficient calculation in two-step light water reactor core analysis. *Journal of Nuclear Science and Technology*, **54**, 705, 2017.
- K. T. Clarno and M. L. Adams. Capturing the effects of unlike neighbors in single-assembly calculations. *Nuclear Science and Engineering*, **149**, 182, 2005.
- D. V. Colameco. *Next generation iterative transport-diffusion methodology (ITDM), for LWR core analysis*. Ph.D. thesis, The Pennsylvania State University, 2012.
- F. Curca-Tivig et al. ARCADIA® - A new generation of coupled neutronics/core thermal-hydraulics code system at AREVA NP. In *Proceedings of the 2007 LWR Fuel Performance Meeting/TopFuel 2007 'Zero by 2010'*, San Francisco, California, USA, September 28 – October 3, 2007.
- A. Dall'Osso. Reducing rod cusping effect in nodal expansion method calculations. In *Proceedings of the International Conference on the New Frontiers of Nuclear Technology: Reactor Physics, Safety and High-Performance Computing, PHYSOR 2002*, Seoul, Korea, October 7–10, 2002.
- A. Dall'Osso. Introducing the migration mode method for the solution of the space and energy dependent diffusion equation. *Annals of Nuclear Energy*, **30**, 1829, 2003.
- A. Dall'Osso. Spatial rehomogenization of cross sections and discontinuity factors for nodal calculations. In *Proc. of Int. Conf. PHYSOR 2014*, Kyoto, Japan, September 28 – October 3, 2014.
- A. Dall'Osso. The influence of the neutron source spectrum on the infinite homogeneous reactor in subcritical condition. *Annals of Nuclear Energy*, **77**, 408, 2015a.
- A. Dall'Osso. Neutron spectrum kinetics in the infinite homogeneous reactor. *Annals of Nuclear Energy*, **85**, 662, 2015b.
- A. Dall'Osso, D. Tomatis and Y. Du. Improving Cross Sections via Spectral Rehomogenization. In *Proc. of Int. Conf. PHYSOR 2010*, Pittsburgh, Pennsylvania, USA, May 9–14, 2010.
- C. Demazière. Investigation of the Bias Coming from Spectrum Corrections in the Simulations of Nuclear Reactor Transients. In *Proc. of Int. Conf. PHYSOR 2016*, 3561–3570, Sun Valley, Idaho, USA, May 1–5, 2016.
- S. Douglass and F. Rahnema. Cross section recondensation method via generalized energy condensation theory. *Annals of Nuclear Energy*, **38**, 2105, 2011.
- S. Douglass and F. Rahnema. Consistent generalized energy condensation theory. *Annals of Nuclear Energy*, **40**, 200, 2012.

- T. J. Downar, C. H. Lee and G. Jiang. An assessment of advanced nodal methods for MOX fuel analysis in light water reactors. In *Proceedings of the PHYSOR 2000 ANS International Topical Meeting on Advances in Reactor Physics, and Mathematics and Computation into the Next Millennium*, Pittsburgh, Pennsylvania, USA, May 7–12, 2000.
- T. J. Downar et al. PARCS v2.7 - U.S. NRC core neutronics simulator - user manual. Technical report, Purdue University, 2006.
- J. J. Duderstadt and L. J. Hamilton. *Nuclear reactor analysis*. John Wiley & Sons, 1976.
- J. Dufek. Building the nodal nuclear data dependences in a many-dimensional state-variable space. *Annals of Nuclear Energy*, **38**, 1569, 2011.
- H. Finnemann, F. Bennewitz and M. R. Wagner. Interface current techniques for multidimensional reactor calculations. *Atomkernenergie*, **30**, 123, 1977.
- P. Forslund, E. Müller and S. Lindahl. Investigation of intranodal depletion effects. *Annals of Nuclear Energy*, **28**, 225, 2001.
- X. D. Fu and N. Z. Cho. Nonlinear analytic and semi-analytic nodal methods for multigroup neutron diffusion calculations. *Journal of Nuclear Science and Technology*, **39**, 1015, 2002.
- M. Gamarino et al. Investigation of Rehomogenization in the Framework of Nodal Cross Section Corrections. In *Proc. of Int. Conf. PHYSOR 2016*, 3698–3707, Sun Valley, Idaho, USA, May 1–5, 2016.
- M. Gamarino et al. Spectral rehomogenization of nodal cross-sections via Proper Orthogonal Decomposition. In *Proc. of Int. Conf. on Mathematics and Computational Methods Applied to Nuclear Science and Engineering (M&C 2017)*, Jeju, Korea, April 16–20, 2017.
- M. Gamarino et al. Rehomogenization of nodal cross sections via modal synthesis of neutron spectrum changes. *Nuclear Science and Engineering*, **190**, 1, 2018a.
- M. Gamarino et al. A neutron-leakage spectrum model for on-the-fly rehomogenization of nodal cross sections. *Annals of Nuclear Energy*, **116**, 257, 2018b.
- A. Gandini. A generalized perturbation method for bi-linear functionals of the real and adjoint neutron fluxes. *Journal of Nuclear Energy*, **21**, 755, 1967.
- R. van Geemert. A multi-level surface rebalancing approach for efficient convergence acceleration of 3D full core multi-group fine grid nodal diffusion iterations. *Annals of Nuclear Energy*, **63**, 22, 2014.

-
- G. H. Golub and C. F. Van Loan. *Matrix Computations*, volume 3. JHU Press, 2012.
- S. A. Groenewald, R. H. Prinsloo and O. M. Zamonsky. Practical semi-heterogeneous method in nodal core analysis. In *Proc. of Int. Conf. on Mathematics and Computational Methods Applied to Nuclear Science and Engineering (M&C 2017)*, Jeju, Korea, April 16–20, 2017.
- M. Guillo et al. COCAGNE: EDF new neutronic core code for ANDROMÈDE calculation chain. In *Proc. of Int. Conf. on Mathematics and Computational Methods Applied to Nuclear Science and Engineering (M&C 2017)*, Jeju, Korea, April 16–20, 2017.
- N. K. Gupta. Nodal methods for three-dimensional simulators. *Progress in Nuclear Energy*, **7**, 127, 1981.
- A. Hébert. A simplified presentation of the multigroup analytic nodal method in 2-D Cartesian geometry. *Annals of Nuclear Energy*, **35**, 2142, 2008.
- A. Hebert. *Applied reactor physics*. Presses Internationales Polytechnique, 2009.
- A. F. Henry. Refinements in accuracy of coarse-mesh finite-difference solution of the group-diffusion equations. In *Proc. of the Seminar on Numerical Reactor Calculations*, volume 447. International Atomic Energy Agency, Vienna, 1972.
- L. Hetzelt and H. J. Winter. Generalization of the Equivalent Reflector Model for the Siemens standard core design procedure. In *Proc. of Mathematics and Computation, Reactor Physics and Environmental Analysis in Nuclear Applications (M&C 1999)*, Madrid, Spain, September 27–30, 1999.
- G. Hobson et al. ARTEMISTM core simulator: Latest developments. In *Joint International Conference on Supercomputing in Nuclear Applications + Monte Carlo*, Paris, France, October 27–31, 2013. EDP Sciences, 2013.
- H. G. Joo, G. Jiang and T. J. Downar. Stabilization techniques for the nonlinear analytic nodal method. *Nuclear Science and Engineering*, **130**, 47, 1998.
- H. G. Joo, J. I. Yoon and S. G. Baek. Multigroup pin power reconstruction with two-dimensional source expansion and corner flux discontinuity. *Annals of Nuclear Energy*, **36**, 85, 2009.
- F. Khoshahval, A. Zolfaghari and H. Minuchehr. Effect of including corner point fluxes on the pin power reconstruction using nodal point flux scheme. *Annals of Nuclear Energy*, **69**, 25, 2014.
- W. Kim, W. Heo and Y. Kim. Improvement of nodal accuracy by using albedo-corrected parameterized equivalence constants. *Nuclear Science and Engineering*, **188**, 207, 2017.

- A. Koning et al. *The JEFF-3.1 Nuclear Data Library*. OECD, 2006.
- K. Kunisch and S. Volkwein. Galerkin Proper Orthogonal Decomposition methods for parabolic problems. *Numerische Mathematik*, **90**, 117, 2001.
- J. R. Lamarsh. *Introduction to Nuclear Reactor Theory*. Reading: Addison-Wesley, 1966.
- S. Langenbuch, W. Maurer and W. Werner. Coarse-mesh flux-expansion method for the analysis of space-time effects in large light water reactor cores. *Nuclear Science and Engineering*, **63**, 437, 1977.
- R. D. Lawrence. Progress in nodal methods for the solution of the neutron diffusion and transport equations. *Progress in Nuclear Energy*, **17**, 271, 1986.
- J. Leppänen et al. The Serpent Monte Carlo code: Status, development and applications in 2013. *Annals of Nuclear Energy*, **82**, 142, 2015.
- E. E. Lewis and W. F. Miller. *Computational methods of neutron transport*. John Wiley and Sons, Inc., New York, NY, 1984.
- Z. Liu, K. S. Smith and B. Forget. A Cumulative Migration Method for computing rigorous transport cross sections and diffusion coefficients for LWR lattices with Monte Carlo. In *Proc. of Int. Conf. PHYSOR 2016*, 2915–2930, Sun Valley, Idaho, USA, May 1–5, 2016.
- T. H. Luu et al. A new method for reconstruction of cross-sections using Tucker decomposition. *Journal of Computational Physics*, **345**, 189, 2017.
- E. Martinolli et al. APOLLO2-A - AREVA’s new generation lattice physics code: methodology and validation. In *Proc. of Int. Conf. PHYSOR 2010*, Pittsburgh, Pennsylvania, USA, May 9–14, 2010.
- M. S. McKinley and F. Rahnema. High-order boundary condition perturbation theory for the diffusion approximation. *Nuclear Science and Engineering*, **136**, 15, 2000.
- S. P. Palmtag. *Advanced nodal methods for MOX fuel analysis*. Ph.D. thesis, Massachusetts Institute of Technology, 1997.
- S. P. Palmtag and K. S. Smith. Two-group spectral corrections for MOX calculations. In *Proc. of the Int. Conf. on the Physics of Nuclear Science and Technology*, volume 1, 3, Long Island, New York, USA, October 5–8, 1998.
- D. Porsch et al. Status of verification and validation of AREVA’s ARCADIA® code system for PWR applications. In *Proc. of Int. Conf. PHYSOR 2012*, Knoxville, Tennessee, USA, April 15–20, 2012.

-
- R. H. Prinsloo, D. I. Tomašević and H. Moraal. A practical implementation of the higher-order transverse-integrated nodal diffusion method. *Annals of Nuclear Energy*, **68**, 70, 2014.
- F. Rahnema, S. Douglass and B. Forget. Generalized energy condensation theory. *Nuclear Science and Engineering*, **160**, 41, 2008.
- F. Rahnema and M. S. McKinley. High-order cross-section homogenization method. *Annals of Nuclear Energy*, **29**, 875, 2002.
- F. Rahnema and E. M. Nichita. Leakage corrected spatial (assembly) homogenization technique. *Annals of Nuclear Energy*, **24**, 477, 1997.
- K. R. Rempe, K. S. Smith and A. F. Henry. SIMULATE-3 pin power reconstruction: methodology and benchmarking. *Nuclear Science and Engineering*, **103**, 334, 1989.
- J. Rhodes, K. S. Smith and D. Lee. CASMO-5 development and applications. In *Proc. of the American Nuclear Society's Topical Meeting on Reactor Physics (PHYSOR 2006)*, 10–14, Vancouver, BC, Canada, September 10–14, 2006.
- P. J. Roache. Code verification by the method of manufactured solutions. *Journal of Fluids Engineering*, **124**, 4, 2002.
- R. Sanchez. Assembly homogenization techniques for core calculations. *Progress in Nuclear Energy*, **51**, 14, 2009.
- R. Sanchez. Prospects in deterministic three-dimensional whole-core transport calculations. *Nuclear Engineering and Technology*, **44**, 113, 2012.
- R. Sanchez and N. J. McCormick. A review of neutron transport approximations. *Nuclear Science and Engineering*, **80**, 481, 1982.
- R. Sanchez et al. APOLLO2 year 2010. *Nuclear Engineering and Technology*, **42**, 474, 2010.
- S. Sánchez-Cervera et al. Optimization of multidimensional cross-section tables for few-group core calculations. *Annals of Nuclear Energy*, **69**, 226, 2014.
- A. Sartori. *Reduced Order Methods: Applications to Nuclear Reactor Core Spatial Dynamics*. Ph.D. thesis, Politecnico di Milano, 2015.
- D. Schneider et al. APOLLO3®: CEA/DEN deterministic multi-purpose code for reactor physics analysis. In *Proc. of Int. Conf. PHYSOR 2016*, Sun Valley, Idaho, USA, May 1–5, 2016.
- Y. A. Shatilla, Y. A. Chao and Y. Tahara. Theory of Westinghouse advanced nodal code for MOX applications. *Transactions of the American Nuclear Society*, **75**, 168, 1996.

- K. S. Smith. *An analytic nodal method for solving the two-group, multidimensional, static and transient neutron diffusion equations*. Master's thesis, Massachusetts Institute of Technology, 1979.
- K. S. Smith. *Spatial homogenization methods for Light Water Reactor analysis*. Ph.D. thesis, Massachusetts Institute of Technology, 1980.
- K. S. Smith. Nodal method storage reduction by non-linear iteration. *Transactions of the American Nuclear Society*, **44**, 1983.
- K. S. Smith. Assembly homogenization techniques for Light Water Reactor analysis. *Progress in Nuclear Energy*, **17**, 303, 1986.
- K. S. Smith. Practical and efficient iterative method for LWR fuel assembly homogenization. *Transactions of the American Nuclear Society*, **71**, 238, 1994.
- K. S. Smith. Nodal diffusion methods and lattice physics data in LWR analyses: Understanding numerous subtle details. *Progress in Nuclear Energy*, **101**, 360, 2017.
- W. M. Stacey. *Modal Approximations: Theory and an Application to Reactor Physics*, volume 41. The MIT Press, 1967.
- W. M. Stacey. *Nuclear reactor physics*. John Wiley & Sons, 2007.
- T. M. Sutton. Wielandt iteration as applied to the nodal expansion method. *Nuclear Science and Engineering*, **98**, 169, 1988.
- T. M. Sutton and B. N. Aviles. Diffusion theory methods for spatial kinetics calculations. *Progress in Nuclear Energy*, **30**, 119, 1996.
- P. J. Turinsky et al. Computer code abstract: NESTLE - a few-group neutron diffusion equation solver utilizing the nodal expansion method for eigenvalue, adjoint, fixed-source steady-state and transient problems. *Nuclear Science and Engineering*, **120**, 1995.
- R. B. Turski et al. Macroscopic cross section generation and application for coupled spatial kinetics and thermal hydraulics analysis with SAS-DIF3DK. In *Proc. of the Joint International Conference on Mathematical Methods and Supercomputing in Nuclear Applications*, Saratoga Springs, New York, USA, October 6–10, 1997.
- D. L. Vogel and Z. J. Weiss. A general multigroup formulation of the analytic nodal method. In *Proc. of the Int. Topical Meeting on Advances in Reactor Physics*, Charleston, South Carolina, USA, March 8–11, 1992.
- M. R. Wagner, K. Koebke and H.-J. Winter. A non-linear extension of the nodal expansion method. In *Proc. of Int. Conf. in Advances in Mathematical Methods for the Solution of Engineering Problems*, volume 2, 43, Munich, Germany, April 27–29, 1981.

- J. K. Watson and K. N. Ivanov. Improved cross-section modeling methodology for coupled three-dimensional transient simulations. *Annals of Nuclear Energy*, **29**, 937, 2002.
- F. Wols. *Transient Analyses of Accelerator Driven Systems Using Modal Expansion Techniques*. Master's thesis, Delft University of Technology, 2010.
- L. Zhu and B. Forget. A discrete generalized multigroup energy expansion theory. *Nuclear Science and Engineering*, **166**, 239, 2010.
- L. Zhu and B. Forget. An energy recondensation method using the discrete generalized multigroup energy expansion theory. *Annals of Nuclear Energy*, **38**, 1718, 2011.
- V. G. Zimin, H. Ninokata and L. R. Pogosbekyan. Polynomial and semi-analytic nodal methods for nonlinear iteration procedure. In *Proc. of the Int. Conf. on the Physics of Nuclear Science and Technology*, 994–1002, Long Island, New York, USA, October 5–8, 1998.
- V. G. Zimin and A. A. Semenov. Building neutron cross-section dependencies for few-group reactor calculations using stepwise regression. *Annals of Nuclear Energy*, **32**, 119, 2005.

THE BRISINGR NODAL CODE: DESCRIPTION AND VALIDATION

The BRISINGR nodal diffusion solver was developed to carry out the research activity described in this thesis. This code solves the multigroup neutron diffusion equation in Cartesian geometry for external-fixed-source steady-state problems, as well as forward and adjoint eigenvalue problems.

Three types of transverse-integrated nodal methods are implemented: the Nodal Expansion Method (NEM), the Analytic Nodal Method (ANM), and the Semi-Analytic Nodal Method (SANM) (Lawrence, 1986). These nodal schemes are non-linearly coupled to a Coarse Mesh Finite Difference (CMFD) algorithm, which serves as an acceleration technique (Smith, 1983). In this solution strategy, the multidimensional diffusion equation is solved on coarse meshes with a conventional finite-difference approach. The so obtained flux distribution and core eigenvalue are inputs to the higher-order transverse-integrated nodal equations, which are solved via two-node-problem calculations (i.e., spatially uncoupled calculations spanning two adjacent nodes) for all nodes and in all directions. The two-node calculations provide an improved estimate of the net surface-averaged current at each nodal interface. Such estimate is used to correct the coarse-mesh leakage operator via update of the original CMFD diffusion coupling coefficients. This iterative strategy progressively forces the CMFD equations to yield the values of the net surface currents predicted by the higher-order nodal scheme. The node-averaged fluxes and core eigenvalue also converge to the NEM/ANM/SANM estimates. In eigenvalue calculations, power iterations are accelerated with Wielandt's eigenvalue shift (Sutton, 1988; Palmtag, 1997).

The code has been benchmarked with three different approaches: (i) the method of manufactured solutions (Roache, 2002) for external-fixed-source problems; (ii) the

comparison with the exact solution of simple eigenvalue problems; and (iii) validation against the results of Framatome’s nodal code ARTEMIS (Hobson et al., 2013) in colorset (i.e., four-assembly set) problems. In this Appendix, we show some sample results of the first two validation campaigns. Homogeneous computational domains are considered (namely, all nodes of the same type). Discontinuity factors are therefore set to unity.

A.1 Fixed-source problems

A.1.1 Finite slab geometry

The one-group diffusion equation is solved in a 1-D finite slab with vacuum boundary conditions (i.e., no reentrant current). The slab has a width of 200 cm and is subdivided into ten uniform nodes. We choose the following closed analytic form for the flux solution:

$$\Phi(x) = -x^2 + k, \tag{A.1a}$$

where k is a numerical constant. The value of k is a function of the width of the slab and is determined so that the conventional Marshak vacuum boundary condition (Stacey, 2007) is satisfied at the right and left boundaries of the slab itself. The source function that generates the flux distribution of Eq. (A.1a) is

$$S(x) = (\Sigma_r - \nu\Sigma_f)\Phi(x) - 2D. \tag{A.1b}$$

We use arbitrary values of the cross sections.

Table A.1 shows the two-norm of the relative error in the computed flux distribution, compared to the reference (i.e., manufactured) solution. The error is reported for the solutions computed with the standalone CMFD algorithm and with multiple iterations of the non-linear CMFD-NEM strategy. The nodal updates are performed after each global CMFD solution. With ten nodal updates, the error decreases by about five orders of magnitude.

Table A.1. One-group fixed-source problem in a slab geometry: two-norm of the relative error in the flux solution (in percentage) versus the number of non-linear CMFD-NEM iterations.

Solution method	Flux error two-norm (%)
CMFD	$3.15 \cdot 10^{-3}$
CMFD - NEM (1 iteration)	$8.88 \cdot 10^{-4}$
CMFD - NEM (2 iterations)	$2.60 \cdot 10^{-4}$
CMFD - NEM (5 iterations)	$6.71 \cdot 10^{-6}$
CMFD - NEM (8 iterations)	$1.73 \cdot 10^{-7}$
CMFD - NEM (10 iterations)	$1.52 \cdot 10^{-8}$

A.1.2 Three-dimensional geometry

We consider a cube with side length of 200 cm and Marshak vacuum boundary conditions. The chosen analytic solution and the corresponding source function are

$$\Phi(x, y, z) = \left(-\frac{x^2}{m} + c\right) \left(-\frac{y^2}{m} + c\right) \left(-\frac{z^2}{m} + c\right) \quad (\text{A.2a})$$

and

$$S(x, y, z) = (\Sigma_r - \nu\Sigma_f)\Phi(x, y, z) + \frac{2D}{m}f(x, y, z), \quad (\text{A.2b})$$

where m and c are numerical constants, and the function $f(x, y, z)$ is defined as

$$f(x, y, z) = \left(-\frac{x^2}{m} + c\right) \left(-\frac{y^2}{m} + c\right) + \left(-\frac{x^2}{m} + c\right) \left(-\frac{z^2}{m} + c\right) + \left(-\frac{y^2}{m} + c\right) \left(-\frac{z^2}{m} + c\right). \quad (\text{A.2c})$$

Also in this case, the constant c is determined as a function of the size of the computational domain (namely, the cube side length) and the type of vacuum boundary condition (Marshak in the case considered in this analysis).

Table A.2 reports, for various mesh sizes, (i) the minimum and maximum relative errors in the flux, and (ii) the two-norm of the 3-D flux error distributions from the CMFD and CMFD-NEM solutions. The number of non-linear iterations for the convergence of the CMFD-NEM strategy is also shown. A tight convergence criterion has been chosen (namely, a tolerance $\epsilon = 10^{-8}$ for the variation in the two-norm flux error between two consecutive nodal updates).

Table A.2. One-group fixed-source problem in a 3-D geometry: number of non-linear CMFD-NEM iterations, absolute values of the minimum and maximum local errors (in percentage), and two-norm of the error distribution (in percentage) for various discretizations. The maximum error is found in the corner nodes of the axial boundaries (i.e., the upper and lower planes), whereas the minimum error is observed at the center of the computational domain (i.e., in the nodes furthest away from the boundaries).

No. of nodes per direction	No. of non-linear iterations (CMFD-NEM)	Minimum error (%)		Maximum error (%)		Error two-norm	
		CMFD	CMFD-NEM	CMFD	CMFD-NEM	CMFD	CMFD-NEM
5	10	$6.42 \cdot 10^{-3}$	$2.15 \cdot 10^{-4}$	8.69	$3.6 \cdot 10^{-2}$	$2.16 \cdot 10^{-2}$	$1.73 \cdot 10^{-4}$
10	12	$1.6 \cdot 10^{-4}$	$1.09 \cdot 10^{-6}$	5.27	$1.79 \cdot 10^{-2}$	$5.59 \cdot 10^{-3}$	$2.92 \cdot 10^{-5}$
15	12	$1.11 \cdot 10^{-5}$	$4.54 \cdot 10^{-8}$	3.58	$1.13 \cdot 10^{-2}$	$2.49 \cdot 10^{-3}$	$8.93 \cdot 10^{-6}$
20	11	$4.04 \cdot 10^{-6}$	$1.32 \cdot 10^{-8}$	2.59	$7.48 \cdot 10^{-3}$	$1.39 \cdot 10^{-3}$	$3.58 \cdot 10^{-6}$

Compared to the 1-D case, the nodal solution is somewhat less accurate. The main source of error is the three-node quadratic fit for the transverse leakage approximation. Nevertheless, the superiority of the nodal scheme over the standalone CMFD method is still apparent.

A.2 Eigenvalue problems

The two-group diffusion eigenvalue problem is solved in the 1-D and 3-D geometries considered in Section A.1. Zero-flux boundary conditions are imposed. The eigenvalue of this simple problem can be determined analytically as

$$k_{\text{eff}}^{\text{ref}} = \frac{\chi_1 \left(\frac{\nu \Sigma_{f,1}}{\Sigma_{r,1}} P_1^{NL} + \frac{\Sigma_{s,1 \rightarrow 2}}{\Sigma_{r,1}} \frac{\nu \Sigma_{f,2}}{\Sigma_{r,2}} P_1^{NL} P_2^{NL} \right) + \chi_2 \left(\frac{\nu \Sigma_{f,2}}{\Sigma_{r,2}} P_2^{NL} + \frac{\Sigma_{s,2 \rightarrow 1}}{\Sigma_{r,2}} \frac{\nu \Sigma_{f,1}}{\Sigma_{r,1}} P_1^{NL} P_2^{NL} \right)}{1 - \frac{\Sigma_{s,1 \rightarrow 2}}{\Sigma_{r,1}} \frac{\Sigma_{s,2 \rightarrow 1}}{\Sigma_{r,2}} P_1^{NL} P_2^{NL}}, \quad (\text{A.3})$$

where P_G^{NL} is the group- G non-leakage probability, which depends on the neutron diffusion length L_G and on the geometric buckling B_h^2 :

$$P_G^{NL} = \frac{1}{1 + L_G^2 B_h^2}, \quad L_G = \sqrt{\left(\frac{D_G}{\Sigma_{r,G}} \right)}, \quad B_h^2 = \sum_{i_d=1}^{N_d} \left(\frac{\pi}{H_{i_d}} \right)^2, \quad (\text{A.4})$$

where N_d is the number of spatial dimensions of the problem ($N_d = 1$ for the slab geometry), and H_{i_d} is the width of the domain in the i_d -th direction.

With the numerical cross-section values chosen for this test case, the reference eigenvalues computed with Eq. (A.3) are 0.92719 in the homogeneous slab and 0.90884 in the homogeneous cube. We use ten uniform nodes in the slab geometry and twenty uniform nodes per direction in the cubic one. Table A.3 shows the errors in the eigenvalues computed with three solution strategies: CMFD, CMFD-NEM, and CMFD-ANM.

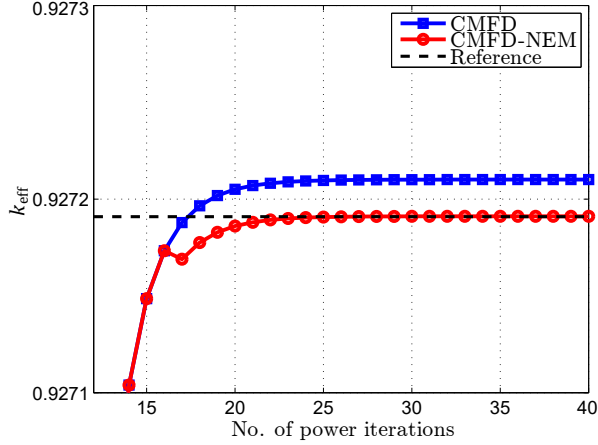
Table A.3. Two-group diffusion eigenvalue problem in slab and cubic geometries with zero-flux boundary conditions: relative error (in percentage) in the computed eigenvalues.

Geometry	Error in k_{eff} (%)		
	CMFD	CMFD-NEM	CMFD-ANM
Homogeneous slab	$8.3 \cdot 10^{-3}$	$9.7 \cdot 10^{-9}$	$9.9 \cdot 10^{-11}$
Homogeneous cube	$6.11 \cdot 10^{-3}$	$1.0 \cdot 10^{-5}$	$1.0 \cdot 10^{-5}$

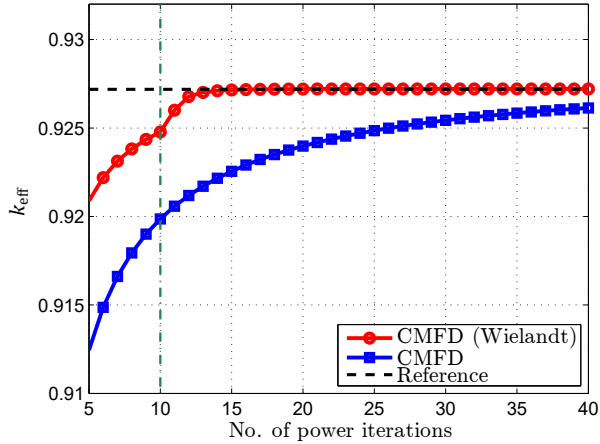
In the slab case, the ANM performs better than the NEM because it does not suffer from the spatial truncation error in the intranodal flux expansion. As observed for the fixed-source problem, in the 3-D case the accuracy of the nodal algorithms is affected by the transverse-leakage approximation, which also nullifies the superiority of the ANM solution over the NEM one.

In the CMFD-NEM calculation, the numbers of power iterations without Wielandt's acceleration are 169 and 204 in the slab and cubic geometries, respectively. These values are obtained with a tolerance $\epsilon = 10^{-8}$ for the variations in the eigenvalue and in the nodal-flux two-norm between two successive iterations. If the eigenvalue shift is applied, the numbers of iterations decrease to 21 and 22 in the two cases, respectively.

Fig. A.1 shows the impact of the NEM updates and of Wielandt's acceleration on the convergence of the coarse-mesh eigenvalue solution in the slab geometry.



(a)



(b)

Fig. A.1. Eigenvalue convergence in the finite slab geometry. (a) Comparison between the CMFD and CMFD-NEM simulations. The first NEM update is performed at the sixteenth power iteration. (b) Comparison between the CMFD simulations with and without Wielandt's acceleration. The vertical dashed line marks the power iteration at which the eigenvalue shift is activated, after partial convergence of the CMFD solution.

APPENDIX B

NOTATION

B.1 Symbols

This section reviews the notation adopted in this thesis. Focus is given to quantities for which there is no standard notation in reactor physics literature.

- $\bar{\Phi}_G$: few-group volume-averaged flux in a generic node;
- $f_{G,d\pm}$: few-group discontinuity factor at the node surface corresponding to the $d\pm$ coordinate;
- \bar{P}_{fiss} : volume-averaged fission power in a generic node;
- $\Phi_{\text{env},G}(u)$: environmental flux spectrum (per unit pseudo lethargy u) within the coarse group G ;
- $\varphi_{\infty,G}(u)$: infinite-medium flux spectrum (normalized to unity) within the coarse group G ;
- $\delta\Phi_G(u)$: variation in the G^{th} -group flux spectrum between the environmental and infinite-medium conditions;
- $L_{\text{env},G}(u)$: environmental leakage spectrum within the coarse group G ;
- $f_{L,G}(u)$: leakage spectrum function (normalized to unity) within the coarse group G ;
- $f_{L,G}^{\infty}(u)$: fundamental-mode leakage spectrum function (normalized to unity) within the coarse group G ;

- $\alpha_{G,i}$: modal coefficients of the spectrum variation between the environmental and infinite-medium conditions;
- $\alpha_{\infty,G,i}$: modal coefficients of the variation in the infinite-medium spectrum between the local and nominal physical conditions;
- $\sigma_{r,c,G}^{\infty}$: few-group infinite-medium cross section of isotope c and reaction r ;
- $\sigma_{\infty,r,c,G}(u)$: fine-group infinite-medium cross section of isotope c and reaction r ;
- $\Phi_{\text{env},G}(u_x, u_y)$: environmental 2-D pin-by-pin flux distribution within the coarse group G ;
- $\varphi_{\infty,G}(u_x, u_y)$: infinite-medium 2-D pin-by-pin flux distribution (normalized to unity) within the coarse group G ;
- $\delta\Phi_G(u_x, u_y)$: variation in the G^{th} -group 2-D pin-by-pin flux distribution between the environmental and infinite-medium conditions;
- α_{G,d,i_d} : directional (i.e., d -axis) modal coefficients of the G^{th} -group 2-D pin-by-pin flux variation between the environmental and infinite-medium conditions;
- α_{G,xy,c_x,c_y} : cross modal coefficients of the G^{th} -group 2-D pin-by-pin flux variation between the environmental and infinite-medium conditions (for the basis functions c_x and c_y along the coordinate axes x and y , respectively).

Spectral rehomogenization coefficients

- $\chi_{G,j}$: fission spectrum coefficient for the coarse group G and the weighting function j ;
- $h_{R,r,G,j}$: reference macroscopic coefficient for reaction r , coarse group G , and weighting function j ;
- $h_{V,r,G,i,j}$: variational macroscopic coefficient for reaction r , coarse group G , basis function i , and weighting function j ;
- $h_{R,r,c,G,j}$: reference microscopic coefficient for isotope c , reaction r , coarse group G , and weighting function j ;
- $h_{V,r,c,G,i,j}$: variational microscopic coefficient for isotope c , reaction r , coarse group G , basis function i , and weighting function j ;
- $s_{R,r,c,G,j}$: reference self-shielding coefficient for isotope c , reaction r , coarse group G , and weighting function j ;

- $s_{V,r,c,G,i,j}$: variational self-shielding coefficient for isotope c , reaction r , coarse group G , basis function i , and weighting function j .

Spatial rehomogenization coefficients

- $h_{R,r,G,j}$: reference coefficient for reaction r , coarse group G , and weighting function j ;
- $h_{V,r,G,d,i_d,j}$: directional variational coefficient for reaction r , coarse group G , coordinate axis d , basis function i_d , and weighting function j ;
- $h_{V,r,G,xy,c_x,c_y,j}$: cross variational coefficient for reaction r , coarse group G , basis functions c_x and c_y along the coordinate axes x and y , and weighting function j ;
- $h_{R,\text{leak},G,d,j}^\infty$: reference infinite-medium current-divergence coefficient for coarse group G , coordinate axis d , and weighting function j ;
- $h_{V,\text{div},G,d,i_d,j}$: directional current-divergence coefficient for coarse group G , coordinate axis d , basis function i_d , and weighting function j ;
- $h_{V,\text{div}_x,G,xy,c_x,c_y,j}$: x -directional, cross current-divergence coefficient for coarse group G , basis functions c_x and c_y along the coordinate axes x and y , and weighting function j .

B.2 Acronyms

- NEM: Nodal Expansion Method
- ANM: Analytic Nodal Method
- SANM: Semi-Analytic Nodal Method
- CMFD: Coarse Mesh Finite Difference
- POD: Proper Orthogonal Decomposition
- SVD: Singular Value Decomposition
- CMM: Cumulative Migration Method

Summary

This thesis develops novel first-principle methods to correct homogenization errors in nodal cross sections and discontinuity factors. Its aim is to improve the accuracy of nodal diffusion simulations of heterogeneous core configurations.

This research builds upon previous work conducted at Framatome (Paris, France). It is based on a modal reconstruction of variations in the neutron flux distribution (in space and energy) between the core environment and the infinite-medium approximation, which is typically used in lattice transport calculations for few-group constant generation. Focus is given to the correction of the nodal cross sections.

Chapter 1 provides a short introduction about nodal methods and the foundations of homogenization theory.

The choice of the basis and weighting functions for the modal synthesis of neutron flux spectrum changes is the main focus of **Chapter 2**. Two approaches are investigated. The first of these uses polynomial basis functions (Chebyshev polynomials of the first kind) and a physical mode (the neutron emission spectrum from fission). The second is based on Proper Orthogonal Decomposition (POD). It computes the optimal (in a least-squares sense) orthonormal basis functions for the space spanned by a set of snapshots of the reference spectrum perturbation. Both strategies are tested on pressurized-water-reactor benchmark problems that exhibit strong heterogeneity. In this analysis, the neutron leakage spectrum is taken as an input quantity from the reference transport calculation. Several aspects of spectral rehomogenization are discussed, such as the impact of approximations in the algorithm on the computed cross-section corrections. It is proved that the method can take into account spectral effects due not only to dissimilar neighbor assemblies, but also to different reactivity in the core environment and in the infinite lattice. This feature eliminates the need for critical-spectrum corrections at the lattice-calculation level.

Chapter 3 presents a novel method with which to approximate the spectral distribution of heterogeneity-driven interassembly neutron leakage. The proposed approach is based on Fick's diffusion law. The leakage spectrum at a nodal interface is computed as a function of the gradient of the environmental flux spectrum, which is itself determined by the rehomogenization algorithm. Extensive validation of this non-linear strategy shows that the energy dependence of streaming effects is accurately reproduced. Compared to simulations with infinite-medium homogenization parameters, when using this method fully based on nodal information significant improvements in the input nodal cross sections, fission power and multiplication factor estimates are achieved at a reasonably low computational cost (i.e., the increase in the number of non-linear flux iterations is generally below a factor of 2). The proposed model is also compared with a more straightforward approach that uses the critical-

leakage spectrum obtained from the solution of the homogeneous fundamental-mode B_1 equations. This second strategy is, however, less accurate and can only provide an adequate approximation of the environmental leakage in weakly heterogeneous systems.

In **Chapter 4**, we devise a new method, based on spectral rehomogenization, to model the dependence of nodal macroscopic and microscopic cross sections on the moderator density and on the concentrations of diluted boron and xenon. The spectral effects of changes in these state parameters are accounted for by computing the variation in the infinite-medium condensation spectrum that exists between the local conditions (with perturbed values of the aforementioned three variables) and a nominal state. This approach replaces the conventional multivariate interpolation in parameterized libraries, with substantial benefits in the computational cost of the lattice calculation, the library memory requirements, and the run time of the on-line cross-section reconstruction. The proposed strategy is applied to a sample fuel assembly, covering a wide range of the values of the state parameters mentioned above. We show that, in most cases, cross-section changes due to nuclide density perturbations are predicted with an accuracy comparable to that of standard interpolation. It is also demonstrated that this method can be combined with those described in Chapters 2 and 3 to reconstruct the spectrum variation between the perturbed real environment and the infinite lattice in the nominal state, thus modeling simultaneously the non-separable spectral effects of local physical conditions and neutron leakage.

In **Chapter 5**, a two-dimensional (2-D) modal method for spatial rehomogenization is developed. This algorithm aims to synthesize the variation in the 2-D pin-by-pin few-group flux and directional net currents between the core environment and the infinite lattice. Assembly discontinuity factors are also corrected. Validation on a broad set of benchmark problems is followed by a thorough discussion that addresses the use of the 2-D neutron current information to compute the transverse-leakage distribution for the transverse-integrated nodal equations, the potential dual application of the method for rehomogenization and dehomogenization, and the quantification of the contributions of various environmental effects to homogenization errors.

In conclusion, the findings reported in this thesis show that spectral and spatial rehomogenization are successful at reducing condensation and homogenization errors in nodal cross sections, with a marginal impact on the computational efficiency of the nodal calculation. In this way, one of the major limitations of current computational tools for core design and operation is alleviated. Throughout this work, the spectral and spatial effects of the environment have been modeled separately. However, it is shown that mixed energy-space effects can be non-negligible, which calls for a unified algorithm where the two rehomogenization methods are coupled. An overview of possible strategies with which a simultaneous approach might be developed is presented in the concluding chapter of this dissertation. Suggestions are also given for further refinements of the algorithms developed in this thesis.

Samenvatting

Modale methoden voor rehomogenisatie van nodale werkzame doorsneden in kernreactor analyse

In dit proefschrift worden nieuwe methoden ontwikkeld om homogenisatiefouten in nodale werkzame doorsneden en in discontinuïteitsfactoren te corrigeren. Het doel is om de nauwkeurigheid van nodale diffusiesimulaties van heterogene reactorkernen te verbeteren.

Dit werk bouwt voort op eerder werk dat is uitgevoerd bij Framatome (Parijs, Frankrijk). Het is gebaseerd op modale reconstructie van variaties in de neutronenfluxverdeling (in ruimte en energie) die optreedt tussen de heterogene kernsamenstelling en de oneindig-medium benadering die vaak gebruikt wordt in weinig-groeps doorsneden te bepalen in neutronen transport codes. De nadruk van het werk ligt op de correctie van de nodale werkzame doorsneden.

Hoofdstuk 1 bevat een korte inleiding over nodale methoden en de grondbeginselen van homogenisatietheorie.

De keuze van basis- en weegfuncties voor nodale synthese van neutronenflux spectrum veranderingen is het zwaartepunt van **Hoofdstuk 2**. Twee aanpakken zijn onderzocht. De eerste aanpak is gebaseerd op het gebruik van polynomen als basisfuncties (Chebyshev van de eerste soort) samen met een fysische modus (het neutronen emissiespectrum afkomstig van splijting). De tweede aanpak gebruikt de ‘Proper Orthogonal Decomposition’ (POD) methodiek en berekent de optimale (in kleinste kwadraten zin) orthonormale basis functies in een ruimte die opgespannen wordt door een set ‘momentopnames’ die genomen worden van de referentie spectrum perturbaties. Beide strategieën worden getest op benchmarkproblemen voor drukwaterreactoren die sterke heterogeniteit bevatten. In deze analyse wordt het neutronenlek-spectrum als bekend verondersteld afkomstig van een referentieberekening. Diverse aspecten van spectrale rehomogenisatie worden bestudeerd zoals de invloed van verschillende benaderingen op de resulterende correcties van de werkzame doorsneden. Aangetoond wordt dat de methode correct de spectrale effecten van de aanwezigheid van verschillende buurassemblages en van verschillende reactiviteiten in de kern t.o.v. die in de oneindig medium analyse kan voorspellen. Deze eigenschap elimineert de noodzaak voor kritische-spectrum correcties op roosterniveau.

In **Hoofdstuk 3** wordt een originele methode gepresenteerd waarmee de spectrale verdeling van de heterogeniteit-gedreven inter-assemblage neutronen stroom wordt beschreven. De voorgestelde methode is gebaseerd op het gebruik van Fick’s diffusiewet. Het lekspectrum op het nodale scheidingsvlak wordt berekend via de gradient van het flux spectrum dat op zijn beurt uit het rehomogenisatie-algoritme rolt. Een uitgebreide

validatie van deze niet-lineaire strategie laat zien dat de energie-afhankelijkheid van de neutronenstromen accuraat gereproduceerd worden. Vergeleken met simulaties waar oneindig-medium homogenisatie wordt gebruikt, leidt de huidige methode waar gebruik gemaakt wordt van nodale informatie, tot duidelijk verbeterde werkzame doorsneden, splijtingsvermogen en multiplicatiefactor tegen redelijk lage computerkosten (het aantal iteraties blijft binnen een factor 2 van de originele methode). De voorgestelde methodiek wordt vergeleken met een simpeler aanpak gebaseerd op het kritische lek-spectrum verkregen van de oplossing van de B_1 vergelijkingen. Deze alternatieve strategie is echter minder accuraat en kan slechts een adequate benadering geven in systemen met beperkte heterogeniteit.

In **Hoofdstuk 4** wordt een nieuwe rehomogenisatie-gebaseerde methode gepresenteerd om de afhankelijkheid van nodale microscopische en macroscopische werkzame doorsneden van moderatordichtheid en van Boron en Xenon concentratie te bepalen. Spectrale effecten veroorzaakt door veranderingen in deze parameters worden meegenomen door de variatie in het condensatiespectrum in lokale condities (inclusief verstoringen door bovengenoemde parameters) en in oneindig-medium condities. Deze aanpak vervangt de conventionele methode van interpolatie in databibliotheken en leidt daarmee tot duidelijke voordelen op gebied van geheugengebruik en kosten die gepaard gaan met online reconstructie van werkzame doorsneden. De voorgestelde strategie is toegepast op een voorbeeld brandstofassemblage met een breed scala aan waarden van de drie voorgenoemde parameters. Aangetoond wordt dat in de meeste gevallen de behaalde nauwkeurigheid vergelijkbaar is met standaard interpolatie. Ook wordt aangetoond dat deze methode kan worden gecombineerd met de methoden beschreven in hoofdstukken 2 en 3 die gebruikt worden om de spectrum variatie te voorspellen zodat het simultaan modelleren van zowel spectrale effecten van lokale compositie als van neutronen-lek mogelijk is.

In **Hoofdstuk 5** wordt een tweedimensionaal model voor spatiale rehomogenisatie beschreven. Dit algoritme heeft als doel de variatie in pin-vermogens te reconstrueren en de netto stroom tussen de omgeving en het oneindig-medium rooster. Assemblage-discontinuïteitsfactoren worden ook gecorrigeerd. Validatie van de methode is uitgevoerd op een uitgebreide set van benchmarkproblemen gevolgd door een diepgaande discussie van de resultaten. Beschreven worden o.a. het gebruik van 2D neutronen stroom informatie om de transversale lekdistributie te berekenen, het potentiële gebruik van de duale functie in rehomogenisatie en dehomogenisatie en de kwantificering van diverse omgevingseffecten op homogenisatiefouten.

De conclusie van dit proefschrift is dat spectrale en spatiale rehomogenisatie methoden succesvol de fouten afkomstig van condensatie en homogenisatie in werkzame doorsneden kunnen reduceren met behoud van de efficiency van de nodale methodiek. Op deze manier is een van de beperkingen van de huidige kernontwerp software weggenomen. In dit onderzoek zijn de effecten van spatiale en spectrale effecten van

de omgeving afzonderlijk gemodelleerd. Ook is geïllustreerd dat dergelijke effecten in sommige gevallen niet goed gescheiden kunnen worden en dat een volledig gekoppelde aanpak nodig is. Een overzicht van mogelijke strategieën om tot een dergelijke gekoppelde aanpak te komen is beschreven in de conclusies van dit proefschrift. Suggesties voor verdere verfijning van de ontwikkelde algoritmen worden ook beschreven.

(Dutch translation provided by Danny Lathouwers.)

Acknowledgments

I would like to thank Danny Lathouwers and Jan Leen Kloosterman for giving me the chance to do a Ph.D. at Delft University of Technology. This was a cornerstone in my professional and personal life. In particular, I am thankful to Danny Lathouwers for his close supervision in the development of the BRISINGR nodal code and for his insightful feedback in the accomplishment of part of this thesis work.

I must thank Aldo Dall’Osso for his invaluable guidance in the development of the rehomogenization methods described in this thesis. During my stays in Paris, I really enjoyed our almost daily conversations about reactor physics and related numerical methods, which strengthened my curiosity and interest in this beautiful field of science and engineering.

Of course, I would also like to thank all my colleagues in Delft and Paris, as well as the friends that I have met in the Netherlands in the past four years, who contributed to make the Ph.D. experience more enjoyable.

Grazie anche agli amici “di sempre” in Italia. Le nostre rimpatriate a Torino mi hanno fatto sentire ogni volta a casa, quasi come se non fossi mai partito.

To conclude, there are five very special people to whom I sincerely want to express my gratitude.

Gracias de corazón a Ricardo Indoval, por su amistad inmensurable y su presencia casi diaria a pesar de la distancia que nos separa. Sin un amigo como él, el mundo sería mucho más aburrido.

Grazie ai miei genitori, Giovanni e Pier Angela, e a mia sorella Cristina. Senza il loro supporto ed i loro preziosi consigli, alcune delle difficoltà incontrate in questi quattro anni sarebbero apparse ben più ardue.

Als laatste bedank ik Aldo Hennink, voor de tijd die we samen doorgebracht hebben en die we in de toekomst gaan doorbrengen. Voor mij is er niets waardevollers dan deze tijd.

List of Publications

Journal papers

M. Gamarino, A. Dall’Osso, D. Lathouwers and J.L. Kloosterman. A two-dimensional modal method for spatial rehomogenization of nodal cross sections and discontinuity-factor correction. To appear in *Annals of Nuclear Energy*, 2018.

M. Gamarino, A. Dall’Osso, D. Lathouwers and J.L. Kloosterman. A rehomogenization-based approach to model spectral effects of local nuclide density changes in nodal calculations. To appear in *Annals of Nuclear Energy*, 2018.

M. Gamarino, A. Dall’Osso, D. Lathouwers and J.L. Kloosterman. A neutron-leakage spectrum model for on-the-fly rehomogenization of nodal cross sections. *Annals of Nuclear Energy*, **116**, pp. 257-279, 2018.

M. Gamarino, A. Dall’Osso, D. Lathouwers and J.L. Kloosterman. Rehomogenization of nodal cross sections via modal synthesis of neutron spectrum changes. *Nuclear Science and Engineering*, **190**, 1, pp. 1-30, 2018.

A. Bovet, M. Gamarino, I. Furno, P. Ricci, A. Fasoli, K. Gustafson, D.E. Newman and R. Sánchez. Transport equation describing fractional Lévy motion of supra-thermal ions in TORPEX. *Nuclear Fusion*, **116**, 10, 2014.

Conference papers

M. Gamarino, A. Dall’Osso, D. Lathouwers and J.L. Kloosterman. Spectral rehomogenization of nodal cross sections via Proper Orthogonal Decomposition. In *Proceedings of the International Conference on Mathematics and Computational Methods Applied to Nuclear Science and Engineering (M&C 2017)*, Jeju, Korea, April 16-20, 2017.

M. Gamarino, D. Tomatis, A. Dall’Osso, D. Lathouwers, J.L. Kloosterman and T.H.J.J. van der Hagen. Investigation of rehomogenization in the framework of nodal cross section corrections. In *Proceedings of the International Conference on the Physics of Reactors, PHYSOR 2016*, pp. 3698-3707, Sun Valley, Idaho, USA, May 1-5, 2016.

Curriculum Vitae

Matteo Gamarino was born in Turin, Italy on June 2, 1989. He grew up in the Olympic city at the foot of the Western Alps, where he attended the Carlo Cattaneo lyceum.

After completing his high school education, in September 2008 he enrolled in the Energy Engineering Bachelor of Science at Politecnico di Torino. He received his bachelor's degree in October 2011 with the *cum laude* distinction. His bachelor's thesis focused on the experimental analysis of pressure drops in two-phase flows.

He continued his studies at Politecnico di Torino with a Master of Science in Energy and Nuclear Engineering, with a focus on nuclear technologies. In the last year of his master's, he spent eight months at the Swiss Federal Institute of Technology of Lausanne (EPFL) as part of the Erasmus student exchange program. He did his master's thesis at the Swiss Plasma Center, where he investigated numerically the turbulent transport of fast-ion beams in the magnetized plasma of the TORPEX experimental facility. His master's degree, obtained in December 2013, was awarded with the *cum laude* distinction and the European-Master-of-Science-in-Nuclear-Engineering (EMSNE) certificate delivered by the European Nuclear Education Network (ENEN). At the beginning of 2014, he did a three-month internship in the Zumaglini&Gallina construction company in Turin.

In June 2014, he joined the Faculty of Applied Sciences of Delft University of Technology as a Ph.D. student. This dissertation is the outcome of the four-year research performed jointly in the Reactor Physics and Nuclear Materials (RPNM) section of the Reactor Institute Delft and the neutronics R&D department (DTIPD-F) of Framatome (Paris, France).

In August 2018, he started working in the Fuel Management Services division of the Nuclear Research and consultancy Group (NRG) of the Netherlands.

